# Development of Dual Acid/Light-Responsive Imine-based Polymeric Nanocarriers for Drug Delivery

Kadambari Kadambari

A Thesis
In the Department of
Chemistry and Biochemistry

Presented in Partial Fulfillment of the Requirements

For the Degree of

Doctor of Philosophy (Chemistry) at

Concordia University

Montreal, Quebec, Canada

June 2025

© Kadambari Kadambari, 2025

## **CONCORDIA UNIVERSITY**

# **School of Graduate Studies**

This is to certify that the thesis

prepared by: Kadambari Kadambari

Entitled: Development of Dual Acid/Light-Responsive Imine-based Polymeric

Nanocarriers for Drug Delivery

and submitted in partial fulfillment of the requirements for the degree of

# **DOCTOR OF PHILOSOPHY (Chemistry)**

Chair

complies with the regulations of the University and meets the accepted standards with respect to originality and quality.

Signed by the final examining committee:

Cameron Skinner

<u>eumeron e</u>	ARIMICI	CHull
Yue Zhao		External Examiner
Louis Cuc	cia	Examiner
Christophe	er Wilds	Examiner
Sixu Deng		Examiner
Jung Kwoi	ı Oh	Thesis Supervisor
Approved by	Louis Cuccia Graduate Program Director	
<u>Defence date</u>	6/25/2025 Pascale Sicotte, Faculty of Arts and S	Science

#### **Abstract**

# Development of Dual Acid/Light-Responsive Imine-based Polymeric Nanocarriers for Drug Delivery

Kadambari Kadambari, Ph.D.

Concordia University, 2025

Stimuli-responsive degradable amphiphilic block copolymers (SRD-ABPs) have been extensively explored as promising building blocks in the construction of smart nanoassemblies exhibiting controlled/enhanced release of encapsulated molecules including therapeutics. A recent advance involves the development of dual SRD-ABPs designed with cleavable linkages responsive to two stimuli, typically acidic pH and light. Herein, we report a new approach to achieve dual acidic pH/light responses with a single labile linkage employing conjugated benzoic imine chemistry. As a proof-of-concept, a well-defined poly(ethylene glycol)-based SRD-ABP containing conjugated benzoic imine pendants in the hydrophobic block was synthesized by reversible deactivation radical polymerization and post-polymerization modification. The synthesized copolymer self-assembled in aqueous solution to form colloidally stable nanoassemblies, consisting of acid/light-degradable hydrophobic cores surrounded with hydrophilic coronas. Upon exposure to acidic pH and UV/visible light, the nanoassemblies degraded through change in hydrophobic/hydrophilic balance of micelle cores.

Extending this strategy, conjugated aromatic imine bonds are unique in their ability to respond to both acidic pH through acid-catalyzed hydrolysis and to visible light through photo-induced E/Z isomerization, thus enabling dual responsiveness with a single chemical group. We report a robust strategy to fabricate core-crosslinked nanogels bearing extended conjugate aromatic imine linkages, exhibiting controlled degradation in response to dual acidic pH and visible light. The strategy involves pre-crosslinking a poly(ethylene glycol)-based block copolymer bearing reactive imidazole pendants with a diol crosslinker bearing extended conjugate aromatic imine, followed by dispersion of the crosslinked polymer in aqueous solution. The fabricated nanogels are non-cytotoxic, colloidally stable, and capable of encapsulating curcumin. They exhibit controlled/enhanced release of curcumin in acidic pH and

under visible light irradiation, with synergistic release under dual stimuli. Furthermore, curcumin-loaded nanogels reduce cell viability in a controlled manner, unlike the free drug.

We further report aqueous nanocolloids based on step-growth conjugated poly(benzoic imine)s (M-PCs) bearing aromatic imine bonds on the backbones with absorption in the visible range ( $\lambda$  = 420 nm). These nanocolloids, fabricated with polymeric stabilizers, display excellent colloidal stability in physiological environments. They undergo disintegration upon degradation of the M-PC backbone under acidic pH and visible light irradiation. These results demonstrate the potential of extended aromatic imine-based nanoplatforms for dual acid/visible light-responsive therapeutic delivery with controlled/enhanced release of encapsulated drugs.

# Acknowledgements

I would like to express my deepest gratitude to my supervisor Dr. Jung Kwon Oh, for his unwavering support, invaluable guidance, and continuous encouragement throughout the course of my doctoral studies. His scientific insight and mentorship have played a crucial role in shaping my research and academic development. I would like to thank my committee members, Dr. Louis Cuccia and Dr. Christopher Wilds, for their constructive feedback during the committee meetings. I extend my sincere thanks to my examination committee members, Dr. Yue Zhao and Dr. Sixu Deng, for generously dedicating their time to review and evaluate my thesis.

To my lab mates, thank you for all the discussions, shared challenges, and happy moments. Working and learning together made this journey more enjoyable. I'm also grateful to my collaborators, whose ideas and expertise helped improve this work. This research was supported by Concordia University, the Natural Sciences and Engineering Research Council of Canada (NSERC), and the Polymer Nanoparticles for Drug Delivery (PoND) network. I truly appreciate their support.

A special thank you to my family. To my parents, Mr. Kamal Kant and Mrs. Sheela Devi, thank you for your love and support. I am grateful to my brother, Abhayesh, who has always cheered me on in challenging times. Their efforts and encouragement have been the foundation of all my achievements. Lastly, I would like to thank my friends Kamal, Karuna, Nancy, Param, Jaismine, Kirti and many others, for their constant moral support, laughter, and friendship throughout this journey. Their presence made this experience truly memorable and meaningful.

# **Dedication**

This thesis is dedicated to my parents, who hoped for and believed in this achievement even before I did, and whose unwavering faith made it possible.

## **Contribution of Authors**

This thesis is the original work of Kadambari K., conducted under the supervision of Professor Jung Kwon (John) Oh. The majority of the research presented herein was carried out by the author under Professor Oh's guidance. Chapters 3 and 4 are reproduced in full peer-reviewed publication with permission from the publisher. Chapters 5 is reproduced in full manuscript submitted for publication. The specific contributions of collaborators are detailed below.

Chapter 3: Synthesis and Dual Acid/Light-Responsive Disassembly of Amphiphilic Block Copolymer Nanoassemblies Bearing Conjugated Benzoic Imine Pendants

This chapter is the published article: Kadambari Bairagi, Jiang Tian Liu, Anna Thinphang-nga, and Jung Kwon Oh, Macromolecules, 2023, 56, 4307–4317.

Contributions: Jiang Tian Liu (Research Assistant) synthesized and characterized the M1 molecule. Anna Thinphang-nga (Undergraduate Student) conducted portions of the acid and light-responsive degradation experiments.

Acknowledgement: Sofia Nieves Casillas Popova (PhD student) for her helpful discussion in TEM studies.

**Chapter 4**: Development of Dual Acid/Visible Light-Degradable Core-Crosslinked Nanogels with Extended Conjugate Aromatic Imines for Enhanced Drug Delivery

This chapter is the published article in press: Kadambari Bairagi, Mehdi Shamekhi, Ioanna Tountas, Natasha Letourneau, Gilles H. Peslherbe, Alisa Piekny, Jung Kwon Oh, *J. Mater. Chem. B*, **2025**, DOI: 10.1039/D5TB00734H.

Contributions: Mehdi Shamekhi (Ph.D. Student in Dr. Peslherbe lab) performed DFT calculations for M2 and M3. Ioanna Tountas (M.Sc. Student in Dr. Pickney's Lab) conducted the WST-8 assay for cell viability. Natasha Letourneau (Ph.D. Student in Dr. Pickney's Lab) carried out live cell imaging using fluorescence microscopy.

**Chapter 5**: Synthesis and Dual Acid/Visible Light-Responsive Degradation of Step-Growth Conjugated Poly(benzoic imine) Nanocolloids

This chapter is the revised manuscript for publication: Kadambari Bairagi, Alondra Camacho, Jung Kwon Oh, *Journal of Polymer Science*, **2025**.

Contributions: Alondra Camacho (ELAP Scholarship Undergraduate Student in Dr. Oh's lab) assisted with the synthesis of nanocolloids and carried out parts of the acid and light-responsive degradation studies.

# **Table of Contents**

List of Figures	xiii
List of Tables	xix
List of Abbreviations	. xx
Chapter 1. Introduction	1
1.1. Drug Delivery Systems in Cancer Therapeutics	1
1.2. Polymeric Nanocarriers for Enhanced Therapeutic Delivery	2
1.3. Stimuli-Responsive Degradation	3
1.4. Imine Chemistry in Degradable Platforms	6
1.5. Research Objectives and Scope	9
Chapter 2. Progress in Block Copolymer-Based Degradable Nanoassemblies: Stimuli Sensitivand Core-Crosslinking Approaches	•
2.1. Overview of Block Copolymer-Based Stimuli-Responsive Nanoassemblies	. 11
2.2. Stimuli-Responsive Disassembly of Block Copolymer-Based Nanoassemblies	. 12
2.2.1. Endogenous Stimuli-Responsive Nanoassemblies	. 12
2.2.2. Exogenous Stimuli-Responsive Nanoassemblies	. 15
2.2.3. Dual Stimuli-Responsive Nanoassemblies	. 17
2.3. Synthetic Approaches for Stimuli-Responsive Core-Crosslinked Nanoassemblies	. 19
2.3.1. Core-Crosslinking by Conjugation via General Covalent Chemistries	. 20
2.3.2. Core-Crosslinking by Conjugation via Stimuli-Responsive Linkages	. 24
2.3.3. In Situ Core Crosslinking by Polymerization-Induced Self-Assembly (PISA)	. 27
2.4. Summary and Outlook	. 30
Chapter 3. Synthesis and Dual Acid/Light-Responsive Disassembly of Amphiphilic Bl Copolymer Nanoassemblies Bearing Conjugated Benzoic Imine Pendants	
3.1. Introduction	. 31
3.2. Experimental	. 33
3.2.1. Instrumentation	. 33
3.2.2. Materials	. 34
3.2.3. Synthesis of Small Molecule Methacrylates and Precursors	. 34
3.2.4. Synthesis of Block Copolymers	. 36
3.2.5. Aqueous Micellization through Dialysis Method	. 37
3.2.6. Studies of Acid and Light-Responsive Degradation.	. 37

3.3. Results and Discussion	38
3.3.1. Synthesis of Conjugated Benzoic Imine-Bearing Methacrylates	38
3.3.2. Direct RAFT Polymerization in Attempt to Synthesize PEG-b-PCoIm BCPs	s 40
3.3.3. Post-polymerization Modification to Synthesize PEG-PCoIm BCPs	41
3.3.4. UV/Vis Absorption Characteristics of Conjugated Benzoic Imines	44
3.3.5. Aqueous Micellization	46
3.3.6. Studies of Acid-Responsive Degradation and Disassembly	46
3.3.7. Preliminary Studies of Light-Response and Disassembly	49
3.4. Conclusion	51
Chapter 4. Development of Dual Acid/Visible Light-Degradable Core-Crosslinked Nan Extended Conjugate Aromatic Imines for Enhanced Drug Delivery	
4.1. Introduction	53
4.2. Experimental	56
4.2.1. Instrumentation	56
4.2.2. Materials	57
4.3.3. Synthesis of M3	58
4.3.4. Synthesis of PEG-b-PCIMA via RAFT Polymerization	58
4.3.5. CDI-Mediated Crosslinking to Fabricate P-Im3-DMSO Crosslinked Polyme	ers 58
4.3.6. Fabrication of Aqueous P-Im3-Aq Nanogels by Pre-crosslinking Dispersion	
4.3.7. Conventional <i>In Situ</i> Crosslinking Approach in Attempt to Fabricate Crosslinked Nanoassemblies	
4.3.8. Acid and Light-Responsive Degradation Studies	59
4.3.9. Computational Details	60
4.3.10. Preparation of Cur-Loaded Nanogels	61
4.3.11. Stimuli-Responsive Release of Cur from P-Im3-Aq/Cur Nanogels	61
4.3.12. Cell Culture	62
4.3. Results and Discussion	63
4.3.1. Synthesis and UV/Vis Absorption Characteristics of Extended Conjugat Imine-Bearing Diol Crosslinker	
4.3.2. Synthesis of Reactive PEG-b-PCIMA Copolymer Bearing Imidazole Penda	nt 64
4.3.3. Studies of CDI-mediated Crosslinking Reaction to Fabricate Crosslinked Po	olymers 65
4.3.4. Pre-crosslinking Dispersion Approach to Fabricate Aqueous Crosslinked Na	anogels 66
4.3.5. Studies of Acid-Responsive Degradation and Disassembly	68
4.3.6. Light-Responsive Degradation and Disassembly	70
X	

4.3.7. Computational Studies of E/Z Isomerization of M3 by DFT Calculations	71
4.3.8. Encapsulation and Dual Acidic pH/Light-Responsive Release of Cur	73
4.3.9. Intracellular trafficking and anti-tumor activity	75
4.4. Conclusion	77
Chapter 5. Synthesis and Dual Acid/Visible Light-Responsive Degradation of Step-G Conjugated Poly(benzoic imine) Nanocolloids	
5.1. Introduction	79
5.2. Experimental	80
5.2.1. Instrumentation	80
5.2.2. Materials	81
5.2.3. Polycondensation to Synthesize Conjugated Poly(benzoic imine)s (M-PCs)	81
5.2.4. Imine Metathesis Polymerization to Synthesize Conjugated Poly(benzoic imine) PC-D)	
5.2.5. Acid-Responsive Degradation of M-PCs	81
5.2.6. Light-Responsive Degradation of M-PCs	81
5.2.7. Fabrication of Aqueous Stabilizer-Aided Nanocolloid Dispersions (PC-Im)	82
5.2.8. Acid-Responsive Degradation of Aqueous PC-Im Nanocolloids	82
5.2.9. Light-Responsive Degradation of Aqueous Nanocolloids	82
5.3. Results and Discussion	82
5.3.1. Synthesis and UV/vis Absorption Characteristics of M-PCs	82
5.3.2. Studies of Acid- and Light-Responsive Degradation of M-PCs	86
5.3.3. Fabrication of Aqueous Stabilizer-Aided Nanocolloids	87
5.3.4. Acid- and Light-Responsive Disassembly	88
5.4. Conclusion	90
Chapter 6. Summary and Future Directions	92
6.1. Summary of Thesis	92
6.2. Future Directions	94
References	96
Appendices	112
A1. Supporting Information for Chapter 3	112
A2. Supporting Information for Chapter 4	126
A3. Supporting Information for Chapter 5	149
Summary of Achievements	151
Publications	151

Oral and Poster Presentations	
Awards and Honours	
Others	

# **List of Figures**

<b>Figure 1.1</b> . Representative polymeric nanocarriers classified by core design, self-assembled micelles, core-crosslinked nanogels, polymer-drug conjugates and stabilizer-assisted core-shell nanocolloids.
<b>Figure 1.2</b> . Schematic representation for dual acid/light-responsive block copolymers incorporating two distinct stimuli-sensitive linkages. Top: Polymer design featuring o-nitrobenzyl groups as light-cleavable moieties and benzoic imine linkages as pH-labile unitses <sup>31</sup> (Copyright 2013, American Chemical Society); Bottom: Polymer backbone with integrated o-nitrobenzyl-based light-sensitive units and ester-based acid-labile linkages. <sup>32</sup> (Copyright 2014, Wiley) 5
<b>Figure 1.3</b> . Scheme for reversible reactions involving imine chemistry, (a) formation and hydrolysis of imine bonds via condensation, (b) transimination through amine exchange, and (c) imine metathesis. (Copyright 2019, Wiley)
<b>Figure 1.4</b> . Scheme illustrating commonly employed linkages in acid- and light-responsive polymer systems, with emphasis on conjugated benzoic imines as a unique linkage capable of dual responsiveness to both stimuli.
<b>Figure 2.1</b> . Scheme showing acid-responsive cleavage of imine bonds in ImP diblock copolymers (a), pH-responsive micelle disassembly at pH 5.0 for ImP nanoassemblies (b), and %Dox release over incubation time at acidic pHs 5.0 and 6.8, compared with physiological pH 7.4 (c). (Copyright 2020, Wiley)
<b>Figure 2.2</b> . Summary of the redox-responsive block copolymer structure, micelle formation, micellar core-crosslinking with cystamine, degradation and characterization by means of DLS, TEM and SEC. <sup>77</sup> (Creative Commons Attribution 3.0 Unported License)
<b>Figure 2.3</b> . Scheme illustrating the self-assembly of the light-responsive nitrospiropyran-based triblock copolymer (a); size determination of micelles under UV and visible light by DLS (b), and its UV/vis spectral changes in water (0.5 mg/mL) following UV irradiation at $\lambda = 365$ nm (c). (Copyright 2023, Royal Society of Chemistry)
<b>Figure 2.4</b> . Schematic showing selective release of glycan ligands from APG micelles via dual stimulus-responsive linker cleavage. UV light (A) cleaves the orange linker, releasing both carbohydrate blocks A and B and disrupting the micellar structure. Acidic pH (B) cleaves the red linker, releasing block B (Man) while retaining block A (Gal), preserving micelle integrity. (Copyright 2024, Wiley)
<b>Figure 2.5</b> . Illustration for formation of diselenide core-crosslinked micelles via alkyne-azide click chemistry and NIR-induced micelle disassembly. Upon NIR irradiation in the presence of indocyanine green, ROS generation cleaves Se–Se bonds, enabling controlled release of encapsulated drug molecules. (Creative Commons Attribution (CC BY) license)
<b>Figure 2.6</b> . Schematic illustration of the synthesis of POEGMA-b-PSMA-b-PS triblock copolymers and the formation of ketal core-crosslinked micelles (CCL) via amidation between maleic anhydride units and a bifunctional ketal-containing diamine. The resulting micelles exhibit stability under physiological conditions and undergo pH-responsive disassembly for controlled doxorubicin release. <sup>134</sup> (Copyright 2020, Taylor & Francis)

<b>Figure 2.7</b> . Reversible [2+2] photocycloaddition of cinnamate (a) and coumarin (b) derivatives illustrating photo-induced dimerization. (Copyright 2025, Royal Society of Chemistry) 25
<b>Figure 2.8</b> . Schematic illustration of genetically encoded diblock polypeptides that are covalently stabilized via photo-crosslinking of para-azidophenylalanine residues in the core (a) and representative confocal images of K562 cells after 1.5 h incubation with AF488-labeled (green functionalized micelles in PBS, showing cellular uptake (b). Scale bars: 20 μm. <sup>145</sup> (Copyrigh 2021, American Chemical Society)
<b>Figure 2.9</b> . Schematic overview of the PhotoATR-PISA methodology enabling synthesis of core cross-linked nanoparticle formation without intermediate work-up (a), and GPC traces of controlled chain extensions (DP(PGMA) = 43) with temporal regulation (b, c). (Copyright 2021 American Chemical Society)
Figure 3.1. Schematic illustration of two approaches to synthesize M2 (a) and M1 (b) 38
Figure 3.2. <sup>1</sup> H NMR spectra of M1 and M2 in DMSO-d <sub>6</sub>
<b>Figure 3.3</b> . Our attempt to synthesize PEG-b-PCoIm-1 by direct RAFT polymerization of M2 in the presence of a PEG-RAFT macro-mediator, initiated with AIBN. Conditions: $[M2]_0/[PEG-RAFT]_0/[AIBN]_0 = 50/1/0.4$ and M2/anisole = 0.6/1 wt/wt; 70 °C
<b>Figure 3.4</b> . Our approach to post-polymerization modification exploring RAFT polymerization and CDI-induced coupling reaction, including the synthesis of a BA-I precursor bearing a conjugated benzoic imine, to synthesize well-defined PEG-b-PCoIm-2 (P-Im) block copolymers  42
<b>Figure 3.5</b> . Overlaid <sup>1</sup> H NMR spectra of PEG-b-PCIMA (a), BA-I (b), and P-Im (c) in DMSO-d <sub>6</sub>
<b>Figure 3.6</b> . Scheme for CDI-mediated coupling reaction of EtOH with A3 (a phenol), benzy alcohol, and BA-I (a benzyl alcohol derivative)
alcohol, and BA-I (a benzyl alcohol derivative)
alcohol, and BA-I (a benzyl alcohol derivative). 42 <b>Figure 3.7</b> . UV/Vis spectra of M2 and M1, compared with M-HX (a) as well as BA-I at 11 μM and P-Im at 0.29 μM (b) in DMF. 45 <b>Figure 3.8</b> . DLS diagram (a), digital image (b), and TEM images with different magnifications (c)
alcohol, and BA-I (a benzyl alcohol derivative)

<b>Figure 3.12</b> . Degradation progress under UV-irradiation for M1 at 340 nm (a) and P-Im at 340 nm (b) and 420 nm (c) in DMSO. Insets show overlaid UV/vis spectra over irradiation time
<b>Figure 4.1</b> . Synthesis of M3 (a diol crosslinker bearing an extended conjugate benzoic imine) by condensation reaction of ABA with TDA in DMF (a), its <sup>1</sup> H NMR spectrum in DMSO-d <sub>6</sub> (b), and its UV/vis spectrum in DMSO, compared with those of M2 (a methacrylate bearing a conjugate benzoic imine bond) and M-HX (a methacrylate bearing a benzoic imine bond) in DMF (c) 64
<b>Figure 4.2</b> . Synthesis by RAFT polymerization (a) and $^{1}H$ NMR spectrum in DMSO-d <sub>6</sub> of PEG-b-PCIMA block copolymer. Conditions: $[CIMA]_{0}/[PEG-RAFT]_{0}/[AIBN]_{0} = 100/1/0.5$ ; CIMA/anisole (w/w) = $1/0.6$
<b>Figure 4.3</b> . Schematic presentation for CDI-medicated crosslinking reaction of PEG-b-CIMA with M3 diol crosslinker to form cross-linked P-Im3-DMSO polymer network (a) and its FT-IR spectrum, compared with those of M3 and PEG-b-PCIMA precursors (b)
<b>Figure 4.4</b> . For P-Im3-Aq nanogels in aqueous solution, DLS diagram with inset TEM image (scale bar = $200 \text{ nm}$ ) (a), UV/Vis spectrum at 0.3 mg/mL, compared with that of M3 in DMSO (30 $\mu$ M) (b), and evolution of diameter with varying amount of DMSO and CI/OH mole equivalent ratio (c)
<b>Figure 4.5</b> . DLS diagrams of aqueous P-Im3-Aq nanogels incubated at pH 5.0 over 6 hrs (a); their TEM images (scale bar = 500 nm) (b,c), and digital images (d,e); and overlaid <sup>1</sup> H NMR spectra of M3 in DMSO-d <sub>6</sub> /HCl (f) and acid-catalyzed hydrolysis of benzoic imine bond in M3 (g) 70
<b>Figure 4.6</b> . UV/Vis spectra of aqueous P-Im3-Aq nanogels (a) and M3 in DMSO (b) under visible light irradiation at 420 nm over a 24-hour period, with inset plots showing the absorbance changes at 355 nm
<b>Figure 4.7</b> . Three M3 configurations as EE, EZ, and ZZ (a) and absorption spectra of EE (black), EZ (red) and ZZ (blue) configurations calculated via TD-DFT (b)
<b>Figure 4.8</b> . Digital images (upon the irradiation of UV light at 365 nm) and schematic representation of Cur encapsulated in crosslinked nanogels (P-Im3-Aq) to form P-Im3-Aq/Cur nanogels (a), DLS diagram of aqueous P-Im3-Aq/Cur (b), and %release of Cur from P-Im3-Aq/Cur upon irradiation of visible light at 420 nm, compared with in dark as a control (c), and in acidic pH = 5.0, compared in pH = 7.4, as well as both (d), by UV/Vis spectroscopy. Note that light-responsive release experiment (Figure 4.8c) was done in the greater concentration of P-Im3-Aq/Cur nanogels than acid- and dual-acid/light responsive release experiment
<b>Figure 4.9</b> . The viability of HeLa cells (%, y-axis) after incubation for 72 hrs with different concentrations of empty P-Im3-Aq nanogels ( $\mu$ g/mL, x-axis) is shown in the bar graph (a). Line graphs show the change in HeLa cell viability (%, y-axis) after incubation with different concentrations of P-Im3-Aq/Cur nanogels ( $\mu$ g/mL, top x-axis, red line) compared with free Cur ( $\mu$ g/mL, bottom x-axis, black line) (b). The averages are shown with error bars as standard deviations for all replicates (n = 9).
<b>Figure 4.10</b> . Images show HeLa cells 2 hours after incubation with free Cur (2.72 μg/mL) (top), empty P-Im3-Aq (240 μg/mL; middle), and P-Im3-Aq/Cur nanogels (240 μg/mL; bottom). DIC shows a field of cells, magenta shows the nuclei, green shows Cur, and the merged shows the three channels together. The images for each channel were collected using the same optical settings and similarly processed. The scale bar is 20 μm.

<b>Figure 5.1</b> . For conjugated M-PC, synthetic scheme with Approach I exploring polycondensation of PPD with TDA in DMSO (a), <sup>1</sup> H NMR spectrum in DMSO-d <sub>6</sub> (b), and UV/vis spectrum, compared with those of M1 (a methacrylate bearing a conjugated benzoic imine bond) and M3 (a diol bearing an extended benzoic imine bond) in DMSO (c)
Figure 5.2. Overlaid UV/vis spectra (a) and evolution of $\lambda_{max}$ (b) of M-PC with varying NH <sub>2</sub> /CHO mole equivalent ratio
<b>Figure 5.3</b> . For M-PC-D, synthetic scheme by Approach II exploring imine metathesis polymerization with two steps including i) the reaction of PPD with hexanal to form Im-precursor and ii) its imine metathesis with TDA in diglyme at 120 °C (a). UV/vis spectrum of M-PC-D in DMSO, compared with those of Im-precursor in diglyme and M-PC in DMSO (b)
<b>Figure 5.4</b> . For acid response of M-PC, acid-catalyzed hydrolysis of conjugated benzoic imine bonds (a), overlaid $^1H$ NMR spectra in DMSO-d <sub>6</sub> /HCl before and after 2 h of incubation (b), and overlaid UV/vis spectra and %change in absorbance at $\lambda = 420$ nm over incubation time (c). For light response of M-PC, overlaid UV/vis spectra in DMSO under irradiation of UV light at $\lambda = 370$ nm (d) and visible light at $\lambda = 440$ nm (e) and %change in absorbance at $\lambda = 420$ nm over 24 h of irradiation (f)
<b>Figure 5.5</b> . DLS diagram (a), TEM images with different magnifications (scale bar = 500 nm) (b), and UV/vis spectrum (c) of aqueous PC-Im nanocolloids compared with that of M-PC in DMSO.
<b>Figure 5.6</b> . Overlaid UV/vis spectra of aqueous PC-Im nanocolloids incubated at pH = 5.0 over 24 h (inset: change in absorbance at $\lambda = 365$ nm) (a) and their DLS diagrams before and after 24 h of incubation (b)
<b>Figure 5.7</b> . For light response of aqueous PC-Im nanocolloids, overlaid DLS diagrams under the irradiation of visible light at $\lambda = 440$ nm (a) and UV light at $\lambda = 370$ nm (b), their UV/vis spectra under the irradiation of visible light at $\lambda = 440$ nm (c) and UV light at $\lambda = 370$ nm (d), and %change in absorbance at $\lambda = 365$ nm over 24 h of irradiation (e).
Figure S3.1. <sup>1</sup> H-NMR spectrum of A1 in CDCl <sub>3</sub>
Figure S3.2. <sup>1</sup> H-NMR spectrum of A2 in CDCl <sub>3</sub>
Figure S3.3. <sup>1</sup> H-NMR spectrum of A3 in CDCl <sub>3</sub>
<b>Figure S3.4</b> . <sup>1</sup> H-NMR spectrum in CDCl <sub>3</sub> of a PEG-based macro-RAFT mediator after purification by precipitation from cold diethyl ether
<b>Figure S3.5</b> . <sup>1</sup> H-NMR spectrum in CDCl <sub>3</sub> for RAFT polymerization of M2 in the presence of PEG-RAFT mediator after 20 hrs, indicating no polymerization (no conversion of M2 to polymer).
<b>Figure S3.6</b> . <sup>1</sup> H-NMR spectrum in CDCl <sub>3</sub> for RAFT polymerization of MMA in the presence of CTA after 4.5 hrs
<b>Figure S3.7</b> . <sup>1</sup> H-NMR spectrum in CDCl <sub>3</sub> for RAFT polymerization of MMA in the presence of A3 after 20 hrs
Figure S3.8. DSC thermogram of P-Im.

<b>Figure S3.9</b> . <sup>1</sup> H-NMR spectrum in CDCl <sub>3</sub> for reaction mixture of PEG-b-PCIMA with A3 precursor
<b>Figure S3.10</b> . <sup>1</sup> H-NMR spectrum in DMSO-d <sub>6</sub> of Et-CI synthesized by CDI-mediated coupling reaction of EtOH. x denotes impurity
<b>Figure S3.11</b> . <sup>1</sup> H-NMR spectrum in DMSO-d <sub>6</sub> of ET1 synthesized by CDI-mediated coupling reaction of Et-CI with A3
<b>Figure S3.12</b> . <sup>1</sup> H-NMR spectrum in DMSO-d <sub>6</sub> of ET2 synthesized by CDI-mediated coupling reaction of Et-CI with benzyl alcohol. x denotes impurity
<b>Figure S3.13</b> . <sup>1</sup> H-NMR spectrum in DMSO-d <sub>6</sub> of ET3 synthesized by CDI-mediated coupling reaction of Et-CI with BA-I. x denotes impurity
Figure S3.14. Overlaid UV/Vis spectra (a) and absorbance at $\lambda_{max} = 285$ nm (b) of M2 over concentration in DMF.
Figure S3.15. Overlaid UV/Vis spectra (a) and absorbance at $\lambda_{max} = 270$ nm (b) of M1 over concentration in DMSO.
<b>Figure S3.16</b> . Overlaid UV/Vis spectra (a) and absorbance at $\lambda_{max} = 255$ nm (b) of M-HX over concentration in DMF.
Figure S3.17. Overlaid UV/Vis spectra (a) and absorbance at $\lambda_{max} = 270$ nm (b) of BA-I over concentration in DMSO.
<b>Figure S3.18</b> . Overlaid ${}^{1}$ H-NMR spectra (a) and %hydrolysis of M2 over stirring time in a mixture of $3/1 \text{ v/v CD}_{3}\text{CN/D}_{2}\text{O}$ at pD = $6.8$ .
<b>Figure S3.19</b> . Overlaid ${}^{1}$ H-NMR spectra (a) and %hydrolysis of M2 over stirring time in a mixture of $3/1 \text{ v/v CD}_{3}$ CN/D <sub>2</sub> O at pD = 7.4. 124
<b>Figure S3.20</b> . Overlaid <sup>1</sup> H-NMR spectra of M2 over irradiation time under UV light at $\lambda = 340$ nm in DMDO-d <sub>6</sub>
Figure S4.1. <sup>13</sup> C NMR spectrum of M3 in DMSO-d <sub>6</sub>
Figure S4.3. Overlaid UV/Vis spectra (a) and absorbance at $\lambda_{max} = 355$ nm (b) of M3 over its concentration in DMSO.
<b>Figure S4.4</b> . <sup>1</sup> H NMR spectrum of P-Im3-DMSO swollen in DMSO-d <sub>6</sub> . The spectrum shows no peaks presenting M3 and PEG-b-PCIMA
<b>Figure S4.5</b> . <sup>1</sup> H NMR spectrum of the supernatant in DMSO-d <sub>6</sub> after P-Im3-DMSO was precipitated from cold diethyl ether. The spectrum shows peaks presenting free imidazole as a side product that is generated by CDI-mediated crosslinking reactions
Figure S4.6. DSC thermogram of P-Im3-DMSO.
Figure S4.7. TGA thermogram of P-Im3-DMSO.
<b>Figure S4.8</b> . Digital images of aqueous dispersion fabricated through a conventional <i>in situ</i> crosslinking approach before (a) and after (b) dialysis, followed by filtration (c); DLS diagram of the dispersion after dialysis and filtration (d)

<b>Figure S4.9</b> . Schematic presentation for acid-catalyzed hydrolysis of benzoic imine bond in P-Im3-DMSO crosslinked polymer (a) and overlaid <sup>1</sup> H NMR spectra of the polymer in DMSO-d <sub>6</sub> before (b) and after (c) treatment with HCl. Insets: digital images of NMR tubes
<b>Figure S4.10</b> . Overlaid DLS diagrams of aqueous P-Im3-Aq nanogels upon irradiation of visible light at $\lambda = 420$ nm over 10 hrs (a) and their TEM images before (scale bar = 500 nm) (b) and after (scale bar = 100 nm) (c) irradiation of light
<b>Figure S4.11</b> . Relative free energy profile of EE to EZ and EZ to ZZ isomerization. TS denotes the transition state.
Figure S4.12. M3 molecular orbital configuration with possible electron transitions
<b>Figure S4.13</b> . The FMOs, HOMO-1 (a), HOMO(b), LUMO(c) and LUMO+1 (d), of EE configuration obtained via the $\omega$ B97/6–311++G(d,p) model chemistry
<b>Figure S4.14</b> . Optimized structures for different conformers of M2. The E isomer (a), transition
<b>Figure S4.15</b> . Relative enthalpy with free energies (in parenthesis) diagram of M2 E/Z isomerization with the transition state and the activation energy
<b>Figure S4.16</b> . M2 molecular orbital configuration with possible electron transitions (a) and UV/Vis spectra of E (blue) and Z (red) isomers of M2 (b)
Figure S4.17. Molecular orbital diagrams of HOMO-4 (a), HOMO-1 (b), HOMO (c), LUMO (d)
<b>Figure S4.18</b> . Overlaid UV/Vis spectrum (a) and absorbance at $\lambda_{max} = 430$ nm (b) of Cur over its concentration in water/THF (1/1 v/v).
<b>Figure S4.19</b> . UV/Vis spectrum of aqueous P-Im3-Aq/Cur nanogels at 0.27 mg/mL in water/THF (1/1 v/v)
<b>Figure S4.20</b> . Overlaid UV/Vis spectra for release of Cur from aqueous P-Im3-Aq/Cur nanogels under visible light at $\lambda = 420$ nm (a) and in dark as a control (b)
<b>Figure S4.21</b> . Overlaid UV/Vis spectra for the release of Cur from P-Im3-Aq/Cur nanogels in pH = 7.4 (a) and acidic pH = 5.0 (b)
<b>Figure S4.22.</b> Overlaid UV/Vis spectrum for the release of Cur from P-Im3-Aq/Cur nanogels in acidic pH = $5.0$ under exposure to visible light at $\lambda = 420$ nm
<b>Figure S5.1</b> . Overlaid UV/vis absorption spectra of M-PC in DMSO over polycondensation time. 149
<b>Figure S5.2</b> . Table summarizing Mass Spectroscopy analysis and chemical structures suggested for M-PC.

# **List of Tables**

Table S4.1. Recipes for a series of aqueous P-Im3-Aq nanogels.	139
<b>Table S4.2</b> . Calculated thermochemistry values with electronic energy ( $E_{DFT}$ ), zero-po (ZPE), thermal enthalpy correction ( $H_{corr}$ ) and thermal correction to free energy $G_{corr}$ (a in kcal/mol).	ll units are
<b>Table S4.3</b> . Excited state, $\lambda_{max}$ , excitation energy (E), oscillator strength (f) and	electronic
configurations for EE, EZ and ZZ conformers of M3.	140
Table S4.4. Cartesian coordinates of calculated structures (M3)	141
Table S5.1. Recipe to synthesize a series of conjugated poly(benzoic imine)s (M-PCs).	150

# **List of Abbreviations**

ABA 4-Aminobenzyl alcohol

ABP Amphiphilic block copolymer

AIBN 2,2'-Azobis(2-methylpropionitrile)

ATRP Atom transfer radical polymerization

BCP Block copolymer

CDI 1,1-Carbonyldiimidazole

CIMA Carbonyl imidazole methacrylate

CMC Critical micelle concentration

Cur Curcumin

CuAAC Copper-catalyzed azide-alkyne cycloaddition

DBU 1,8-Diazabicyclo[5.4.0]undec-7-ene

DCM Dichloromethane

DFT Density functional theory

DMAP 4-(Dimethylamino)pyridine

DMF Dimethylformamide

DMSO Dimethyl sulfoxide

DP Degree of polymerization

DSC Differential scanning calorimetry

EDC 1-Ethyl-3-(3-dimethylaminopropyl)carbodiimide hydrochloride

EPR Enhanced permeability and retention

Et<sub>3</sub>N Triethylamine

FMO Frontier molecular orbital

FT-IR Fourier transform infrared spectroscopy

GPC Gel permeation chromatography

GSH Glutathione

HCl Hydrochloric acid

HEMA 2-Hydroxyethyl methacrylate

HR-MS High resolution mass spectrometry

MWCO Molecular weight cut-off

NMR Nuclear magnetic resonance

NP Nanoparticles

PEG Poly(ethylene glycol)

PISA Polymerization-induced self-assembly

PPD p-Phenylenediamine

PTA Phosphotungstic acid

PVA Poly(vinyl alcohol)

RAFT Reversible addition fragmentation chain-transfer

ROS Reactive oxygen species

SRD Stimuli-responsive degradable

TDA Terephthaldehyde

TGA Thermogravimetric analysis

THF Tetrahydrofuran

UV/Vis Ultraviolet-visible spectroscopy

WST-8 Water soluble tetrazolium salt-8

# **Chapter 1. Introduction**

#### 1.1. Drug Delivery Systems in Cancer Therapeutics

Cancer remains one of the leading causes of morbidity and mortality worldwide, characterized by uncontrolled cell proliferation, evasion of apoptosis, angiogenesis, and potential for metastasis. Conventional cancer therapies including chemotherapy, radiotherapy, and surgery have demonstrated significant therapeutic impact but are often accompanied by severe side effects and non-specific toxicity. Chemotherapeutic agents, while potent, typically lack selectivity between malignant and healthy cells, leading to systemic adverse effects such as myelosuppression, gastrointestinal toxicity, and cardiotoxicity. Moreover, tumor microenvironment, marked by hypoxia, acidic pH, elevated levels of glutathione (GSH), and overexpressed enzymes, creates biological barriers that hinder effective drug penetration and sustained therapeutic action.<sup>1, 2</sup>

To address these challenges, the development of advanced drug delivery systems has gained prominence, aiming to improve the therapeutic index by enhancing site-specific drug accumulation, reducing off-target toxicity, and overcoming multidrug resistance. Nanocarrier-based systems, such as liposomes, dendrimers, polymeric nanoparticles, micelles, and nanogels have demonstrated the capacity to encapsulate a wide variety of anticancer agents, shielding them from premature degradation and facilitating controlled release at the tumor site.<sup>3,4</sup> The enhanced permeability and retention (EPR) effect, characterized by leaky vasculature and compromised lymphatic drainage within tumor tissues, forms the basis of the passive targeting strategy employed by numerous nanocarriers. Despite its fundamental advantage, the EPR effect exhibits significant variability across tumor types and individual patients, thereby necessitating further optimization through the integration of active targeting and stimuli-responsive delivery mechanisms.<sup>5</sup> The evolution of delivery systems for cancer treatment has advanced toward the development of polymer-based nanocarriers designed to navigate the complex tumor microenvironment and achieve controlled, site-specific drug release.<sup>6</sup>

### 1.2. Polymeric Nanocarriers for Enhanced Therapeutic Delivery

Polymeric nanoparticles have emerged as one of the most versatile platforms for drug delivery owing to their tunable size, surface chemistry, and structural architecture. Typically ranging between 10 and 500 nm in diameter, polymeric nanoparticles can be engineered from a variety of synthetic and natural polymers such as poly(lactic-co-glycolic acid) (PLGA), poly(ethylene glycol) (PEG), and polycaprolactone (PCL).<sup>7,8</sup> These systems exhibit controlled degradability, excellent biocompatibility, and substantial potential for multifunctionalization through surface conjugation or core crosslinking strategies. Polymeric nanoparticles provide precise control over key physicochemical parameters, including size, morphology, architecture, surface charge, and functionalization, facilitating their ability to traverse biological barriers, achieve site-specific targeting, encapsulate a broad spectrum of therapeutic agents, and ensure efficient drug release at the target site.<sup>9</sup>

Amphiphilic block copolymer (ABP)-based nanoassemblies have emerged as highly versatile and efficient platforms for drug delivery, particularly in the context of cancer therapeutics. These systems consist of distinct hydrophilic and hydrophobic polymer segments that spontaneously assemble in aqueous environments into well-defined nanostructures, such as micelles, nanogels, polymersomes, and hybrid nanoparticles. Driven by hydrophobic interactions and minimization of interfacial free energy, these core-shell architectures enable the encapsulation of hydrophobic drugs within the core, while the hydrophilic corona provides solubility, colloidal stability, and prolonged circulation. <sup>10, 11</sup> ABP systems offer tunable physicochemical properties through precise control of block length, composition, and architecture, allowing the optimization of particle size, critical micelle concentration, core polarity, degradation kinetics, and drug loading capacity. Functional versatility is further enhanced by end-group modification, side-chain grafting, and incorporation of cleavable linkages, enabling targeted delivery, stealth behavior, and adaptive functionality. Recent advances in controlled/living polymerization techniques, including reversible addition fragmentation chain-transfer (RAFT), atom transfer radical polymerization (ATRP), and ringopening polymerization, have enabled the synthesis of highly defined ABPs tailored for specific therapeutic applications. 12, 13

Among ABP-based nanoassemblies, polymeric micelles are most widely used for drug delivery, with a hydrophobic core for solubilizing poorly water-soluble drugs and a hydrophilic corona, often composed of PEG, for colloidal stabilization and prolonged circulation. <sup>14, 15</sup> In comparison, nanogels are crosslinked ABP networks offering superior structural integrity and controlled degradation. <sup>16</sup> Nanocolloids, although distinct from equilibrium self-assemblies like micelles, employ amphiphilic polymers or surfactants to stabilize hydrophobic cores within aqueous media, providing high drug payloads and long-term dispersion stability. <sup>17-19</sup> Collectively, these polymer nanostructures classified by their core design have shown robust preclinical and clinical performance, Core structure plays a critical role in determining the stability, drug loading, and release behavior of these assemblies (Figure 1.1).

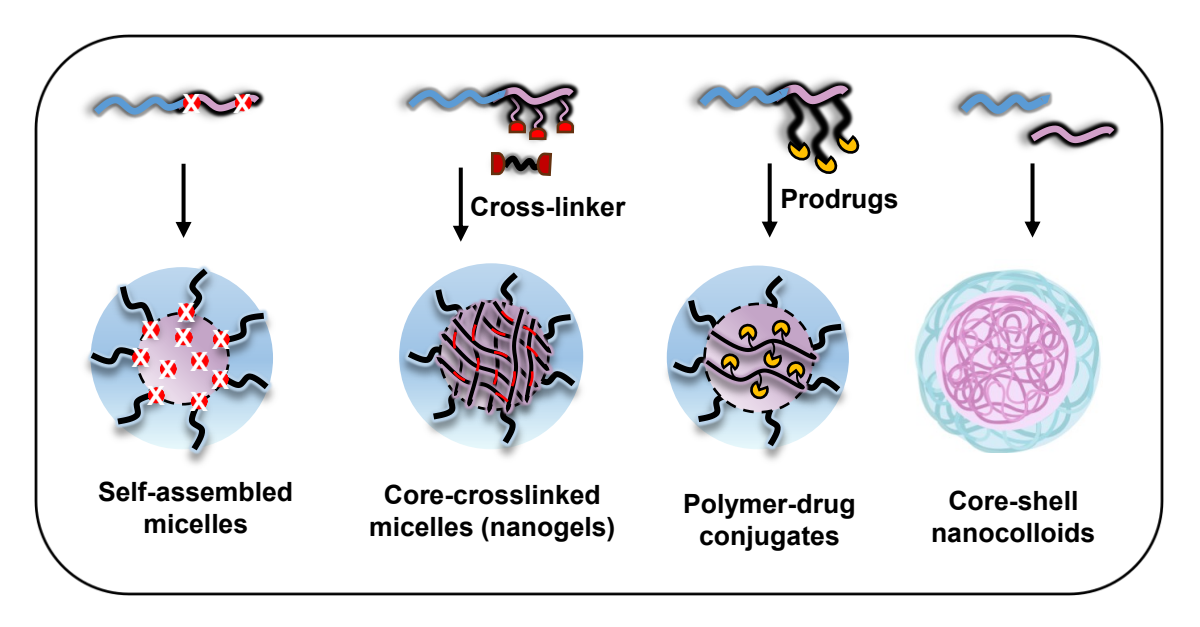


**Figure 1.1**. Representative polymeric nanocarriers classified by core design, self-assembled micelles, core-crosslinked nanogels, polymer-drug conjugates and stabilizer-assisted core-shell nanocolloids.

#### 1.3. Stimuli-Responsive Degradation

Drug release from polymeric nanoparticles can be classified broadly into diffusion-controlled, erosion-controlled, and stimuli-triggered mechanisms. Diffusion-controlled release involves the passive migration of drug molecules through the polymer matrix, governed by concentration gradients and polymer porosity. This mechanism is prevalent in hydrophilic matrices or amphiphilic block copolymer micelles. In contrast, erosion-controlled systems rely

on polymer degradation, either bulk or surface erosion to liberate encapsulated drugs.<sup>20</sup> Polyesters such as PLGA undergo hydrolytic degradation, making them ideal candidates for sustained release applications.<sup>21</sup> More recently, hybrid strategies have emerged that combine both diffusion and degradation, achieving finely tuned release kinetics.<sup>22</sup>

Despite their potential, a persistent challenge in drug delivery using polymeric nanoassemblies is the inherently slow drug release profile of ABP-based systems. To overcome this limitation, stimuli-responsive linkages have been strategically integrated into the design of block copolymers and their resulting nanoassemblies to facilitate controlled drug release. They include pH-sensitive, redox-sensitive, enzyme-responsive, and photo-responsive platforms engineered to respond to endogenous biological stimuli or externally applied stimuli. Stimuli-responsive degradation (SRD) systems represent an advanced class of nanocarriers that undergo structural disassembly or degradation upon exposure to specific stimuli, facilitating controlled drug release. These systems exploit endogenous stimuli such as acidic pH, redox gradients, enzymatic activity, and reactive oxygen species (ROS), as well as exogenous stimuli including light, ultrasound, and magnetic fields.

Notably, pH-sensitive ABP systems are designed to exploit the acidic microenvironments of pathological sites, where the extracellular pH typically drops to 6.5-7.0 in tumors and 4.5-6.0 in endosomal and lysosomal compartments, compared to ~7.4 in normal tissues. By incorporating acid-labile linkages such as hydrazone, benzoic imine, acetal, ketal, and orthoester bonds into the polymer backbone or core domains, these nanocarriers enable selective drug release under acidic conditions. <sup>25, 26</sup> Further, light as an external stimulus offers a unique advantage in drug delivery by bypassing the limitations imposed by tissue type or pathological microenvironments, which often restrict the effectiveness of systems relying solely on endogenous stimuli. Light-triggered drug release can occur through several mechanisms, including photothermal-induced physical disruption, light-driven chemical degradation, and photo-induced molecular structural transitions through light-sensitive linkages like azobenzene or coumarin derivatives. <sup>27-29</sup> Further details on their design and mechanisms are provided in Chapter 2.

Furthermore, dual-responsive ABP-based nanocarriers are engineered to respond to two independent stimuli, providing enhanced control over drug release in complex pathological environments. This is commonly achieved by combining acid-sensitive or redox-sensitive

linkages with light or temperature-responsive triggers, enabling efficient disassembly. Among these systems, acid/light-responsive nanocarriers are particularly promising, as they exploit endogenous pH gradients together with externally applied light to achieve precise and spatiotemporal drug release (Figure 1.2). However, despite their therapeutic potential, the incorporation of two distinct stimuli-sensitive linkages, such as acid-labile and light-responsive bonds, presents substantial challenges. These include premature degradation, instability during circulation, difficulty in balancing the responsiveness of each stimulus, and considerable synthetic complexity, all of which can limit clinical translation and scalability. 37-40

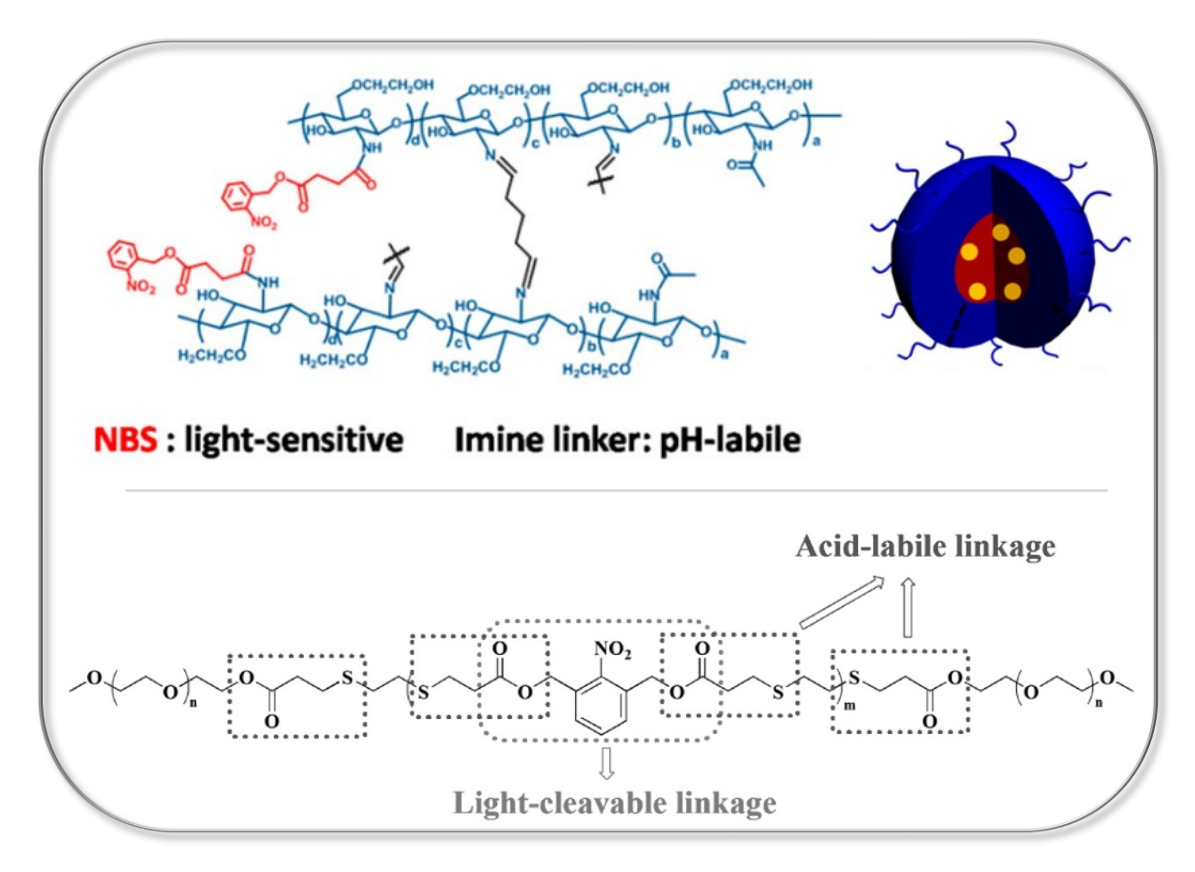


**Figure 1.2**. Schematic representation for dual acid/light-responsive block copolymers incorporating two distinct stimuli-sensitive linkages. Top: Polymer design featuring onitrobenzyl groups as light-cleavable moieties and benzoic imine linkages as pH-labile unitses<sup>31</sup>(Copyright 2013, American Chemical Society); Bottom: Polymer backbone with integrated o-nitrobenzyl-based light-sensitive units and ester-based acid-labile linkages.<sup>32</sup> (Copyright 2014, Wiley)

# 1.4. Imine Chemistry in Degradable Platforms

The imine (C=N) bond, or Schiff base, has emerged as a versatile and dynamic functional group in SRD platforms. These C=N bonds are typically synthesized through the condensation of a carbonyl group (-C=O) and a primary amine (-NH<sub>2</sub>), proceeding via a hemiaminal intermediate under mild and environmentally benign conditions without the formation of byproducts except for water molecule. Imines undergo hydrolysis in acidic environments via a dissociative mechanism, while in the absence of water, transimination can occur through amine exchange. Additionally, imine metathesis, involving the exchange between two imines, proceeds in the presence of suitable catalysts. (Figure 1.3). Among these, benzoic imine linkages are particularly notable for their tunable hydrolysis kinetics, and chemical versatility. Moreover, compared to aliphatic imines, benzoic imines exhibit enhanced hydrolytic stability at physiological pH due to their resonance stabilization with the aromatic ring. An additional feature of benzoic imines is their ability to undergo E/Z isomerization, which offers further opportunities for light-triggered structural modulation.

a) 
$$R_1$$
  $R_2$   $R_1$   $R_2$   $R_3$   $R_4$   $R_4$   $R_5$   $R_6$   $R_7$   $R_8$   $R_8$   $R_8$   $R_8$   $R_8$   $R_8$   $R_9$   $R$ 

**Figure 1.3**. Scheme for reversible reactions involving imine chemistry, (a) formation and hydrolysis of imine bonds via condensation, (b) transimination through amine exchange, and (c) imine metathesis. <sup>42</sup> (Copyright 2019, Wiley)

The acid sensitivity of benzoic imine bonds has been extensively investigated in the context of drug delivery. These linkages exhibit stability under physiological pH but undergo rapid cleavage in mildly acidic environments, such as those characteristics of tumor extracellular

matrices or intracellular compartments like endosomes and lysosomes. By modulating aromatic ring substituents, the hydrolysis kinetics of benzoic imine bonds can be finely adjusted, providing precise control over acid-catalyzed cleavage rates. This acid-labile behavior has been exploited in various delivery platforms, including polymer—drug conjugates, crosslinked hydrogels, self-assembled micelles, and polymeric nanogels. For example, Hu et al. reported acid-degradable block copolymers bearing imine pendants for tunable pH-sensitivity and doxorubicin (Dox) release. Similarly, Li et al. developed pH-responsive nanogels incorporating benzoic imine crosslinks for the controlled release of indocyanine green, improving photostability and photothermal therapeutic efficacy. In addition to single-stimulus systems utilizing acid-labile imine bonds, the incorporation of dual-responsive designs that combine imine with other endogenous-cleavable linkages has enabled synergistic degradation of nanoassemblies. Specifically, dual acid-responsive copolymers integrating benzoic imine with hydrazone or acetal bonds have been reported, demonstrating enhanced responsiveness under acidic conditions.

In addition to acid responsiveness, benzoic imines (aromatic Schiff bases) show reversible trans-cis (E/Z) isomerization under light, similar to well-known photochromic systems such as azobenzene or stilbene. However, unlike these classic molecular switches, imine isomerization has been less widely studied because the cis isomer is short-lived and rapidly relaxes back to the more thermodynamically stable trans-form. Notably, the cis isomer is higher in energy and less planar and exhibits twist of the phenyl ring on nitrogen relative to the C=N axis. This geometric distortion disrupts  $\pi$ -conjugation, explaining the energetic preference for the trans configuration and the ultrafast thermal reversion following light-induced E→Z isomerization. <sup>49,50</sup> The fundamental light-triggered process in aromatic imines is E/Z isomerization. Greb and Lehn first showed that diaryl-N-alkyl imine derivatives function as molecular motors, executing lightdriven unidirectional rotations by E/Z switching of the C=N bond.<sup>51</sup> Extending this work, Greb et al. integrated N-alkyl α-bisimine units into acyclic diene metathesis (ADMET) polymers, creating systems that altered their backbone conformation reversibly under UV light.<sup>52</sup> These principles were advanced by designing photoswitchable block copolymers containing αbisimines, which demonstrated UV-induced conformational changes, offering prospects for light-controlled soft materials and actuators.<sup>53</sup> Further depth to this field is applied by describing reversible trans—cis photoisomerization in pyrrolidene heterocyclic imines, with measurable spectral shifts during E/Z switching.<sup>50</sup>

Beyond isomerization, aromatic imines participate in dynamic covalent metathesis reactions. Visible light-induced dynamic Schiff base bonds in waterborne polyurethanes were developed, creating self-healing, reprocessable materials that operated efficiently at room temperature without external catalysts. <sup>54</sup> Complementing this work, Lei et al. elucidated the underlying mechanism of catalyst-free aromatic imine exchange, revealing the involvement of free radical intermediates and demonstrating repeated healing and reshaping of crosslinked polymers. <sup>55</sup> At the application frontier, Zheng et al. reported a triple-responsive vitrimer system incorporating oligoaniline-modified imines, which combined thermal, near-infrared (NIR), and amine solvent responsiveness. <sup>56</sup> The oligoaniline units enabled photothermal conversion, driving NIR-triggered imine bond exchange for shape memory, accelerated photohealing, and recycling.

The remarkable responsiveness of aromatic imines to both acidic and light stimuli underscore their exceptional versatility as dynamic covalent linkages. As seen in Figure 1.4, the acid-labile nature of the C=N bond, combined with its capacity for light-induced E/Z isomerization and dynamic exchange under UV or visible light, positions aromatic imines as highly promising linkages for the construction of dual acid/light-responsive materials.

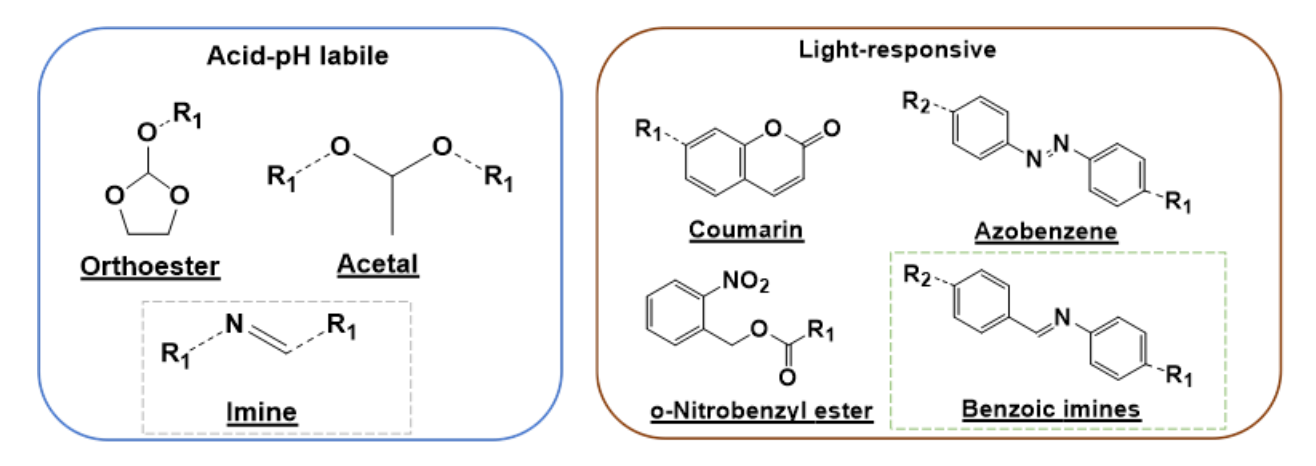


**Figure 1.4**. Scheme illustrating commonly employed linkages in acid- and light-responsive polymer systems, with emphasis on conjugated benzoic imines as a unique linkage capable of dual responsiveness to both stimuli.

#### 1.5. Research Objectives and Scope

The primary objective of this PhD research is to advance the present dual stimuli-responsive drug delivery by developing polymeric platforms with simplified synthetic strategies, focusing on acid and light stimuli. While current dual acid/light systems often rely on multiple distinct labile linkages, this work aims to achieve dual responsiveness through a single, multifunctional linkage. The inherent acid and light-responsive behavior of conjugated benzoic imines offers a powerful strategy for developing dual-responsive polymeric systems using a single labile linkage, with strong potential to overcome the synthetic complexity of existing systems and drive the next generation of smart nanocarriers and adaptive materials.

At the core of this approach is conjugated benzoic imine chemistry, enabling block copolymers and nanoassemblies that respond to both acidic pH and UV/visible light via conjugated C=N bonds. A key objective is to investigate different polymer architectures and synthetic chemistries, systematically exploring how variations in conjugated imine incorporation affect responsiveness and performance. The materials are synthesized using controlled radical polymerization, post-polymerization modification, or facile polycondensation, producing copolymers with backbone or pendant imine functionalities. These systems are designed to enable controlled disassembly and drug release under acidic and light stimuli, with performance rigorously evaluated through drug loading, release kinetics, and biological efficacy studies.

This thesis consists of six chapters, namely the introduction, a review of literature, three research projects, and a concluding chapter outlining key findings and future directions.

**Chapter 1** introduces the background, rationale, and objectives of the research.

**Chapter 2** entails a comprehensive literature review on ABP-based SRD nanoassemblies for controlled drug delivery. This chapter highlights the design principles of stimuli responsive systems, followed by synthetic strategies for core-crosslinked SRD nanoassemblies.

Chapter 3 presents a proof-of-concept study centered on the dual-responsive behavior of conjugated benzoic imine linkages, providing foundational insights into their acid and light-responsive behaviour. It further demonstrates the synthesis and characterization of ABP-based micelles bearing benzoic imine pendants, evaluating their self-assembly and stimuli-induced disassembly.

Chapter 4 expands benzoic imine-based degradation to core-crosslinked nanogels incorporating extended conjugated aromatic imines within the crosslinked core. These linkages provide structural stability and dual acid/visible light-responsive degradation. The chapter investigates the light-responsive mechanism, drug loading, release kinetics, and degradation behavior under single and combined stimuli, along with *in vitro* studies.

Chapter 5 advances the benzoic imine framework through the step-growth synthesis of poly(benzoic imine) nanocolloids, which exhibit dual acid/visible light-responsive degradation. Emphasis is placed on the formation of nanocolloids with a hydrophobic core of poly(benzoic imine)s stabilized with polymeric stabilizers, their detailed physicochemical characterization, and comprehensive evaluation of dual responsiveness.

Chapter 6 provides a comprehensive summary of the research conducted throughout the PhD program. It outlines the key findings of each research project, discusses the overall significance of the developed dual-responsive systems, and proposes potential future research directions.

# Chapter 2. Progress in Block Copolymer-Based Degradable Nanoassemblies: Stimuli Sensitivity and Core-Crosslinking Approaches

#### 2.1. Overview of Block Copolymer-Based Stimuli-Responsive Nanoassemblies

Degradable block copolymer nanoassemblies have emerged as promising platforms for controlled drug delivery, owing to their ability to undergo structural transformations in response to specific physiological or externally applied stimuli. These nanoassemblies, typically formed through the self-assembly of amphiphilic block copolymers in selective solvents, include well-defined architectures such as spherical micelles, vesicles, and nanogels. They consist of a hydrophobic core that serves as a reservoir for poorly soluble therapeutics and a hydrophilic corona that ensures colloidal stability and prolonged circulation in biological fluids. <sup>57, 58</sup>

A defining characteristic of these systems is their capacity to undergo disassembly or morphological destabilization under targeted stimuli. This is achieved by incorporating cleavable chemical linkages into the polymer backbone or at other critical regions within the nanoassembly. Stimuli such as acidic pH, intracellular reductive environments, or light exposure activate these linkages through bond cleavage or conformational changes, disrupting the coreshell interface and destabilizing the structure. Such stimulus-specific disassembly enables synergistic or sequential drug release profiles that can be tailored to complex biological environments.<sup>59, 60</sup>

Despite their advantages, conventional nanoassemblies often exhibit poor kinetic stability and rapid dissociation under physiological dilution or in the presence of serum proteins. To address this, core-crosslinking strategies have been introduced to reinforce the internal structure of the micelle without impeding its responsiveness. Crosslinking is achieved through covalent or dynamic chemistry, significantly enhances structural integrity, improves drug retention, and prolongs circulation time. Moreover, dual and multi stimuli-responsive systems incorporating orthogonal cleavable linkages allow for synergistic or sequential disassembly behavior tailored to the complexity of biological environments.

This review highlights the rational design of stimuli-responsive block copolymer nanoassemblies with a focus on their disassembly mechanisms and core-crosslinking strategies. Key design principles, synthetic methodologies, and degradation profiles are discussed, with an emphasis on how polymer architecture and crosslinking chemistry influence stability and responsiveness. The following sections provide a detailed analysis of endogenous, exogenous, and dual stimuli-responsive systems, establishing a framework for the development of next-generation smart nanocarriers.

### 2.2. Stimuli-Responsive Disassembly of Block Copolymer-Based Nanoassemblies

This section focuses on the structural design and disassembly behavior of polymeric and core-crosslinked nanoassemblies formed from amphiphilic block copolymers. It emphasizes polymer architectures incorporating cleavable or dynamic linkages that disassemble in response to physiological (e.g., pH, redox, enzyme) or external (e.g., light, temperature) stimuli. By systematically examining these triggers, we elucidate how molecular design dictates stimulus-responsive release behavior.

# 2.2.1. Endogenous Stimuli-Responsive Nanoassemblies

*pH-Responsive Systems*. Early, impactful examples of pH-cleavable linkages in amphiphilic block copolymers laid the groundwork for today's smart drug delivery systems by demonstrating how acid-labile bonds, such as imine, hydrazone, acetal, and ketal could be strategically incorporated to enable selective, environment-triggered disassembly and release. <sup>25, 64-66</sup> A notable study reported the synthesis of poly(dimethylacrylamide)-b-poly(trimethylene carbonate) (PDMAAm-b-PTMC) block copolymers featuring a pH-sensitive imine linkage at the hydrophilic–hydrophobic junction. This was achieved by preparing a vanillin-terminated PTMC block via ring-opening polymerization, introducing an imine bond through reaction with an amino-functionalized RAFT agent, followed by RAFT polymerization of the PDMAAm block.<sup>67</sup> Similarly, star-shaped amphiphilic copolymers are designed with imine bonds at the junction between the hydrophilic poly(ethylene glycol) (PEG) core and hydrophobic poly(ε-caprolactone) arms.<sup>68</sup> A foundational study in our group, employed direct RAFT polymerization to synthesize diblock copolymers (ImP) bearing pendant imine functionalities. These copolymers self-assembled into micelles that underwent disassembly under mildly acidic conditions (pH 5.0-6.8), where cleavage of the imine bonds disrupted the hydrophilic-hydrophobic balance, leading to

structural destabilization and enhanced Dox release compared to physiological pH (7.4) (Figure 2.1).<sup>45</sup>

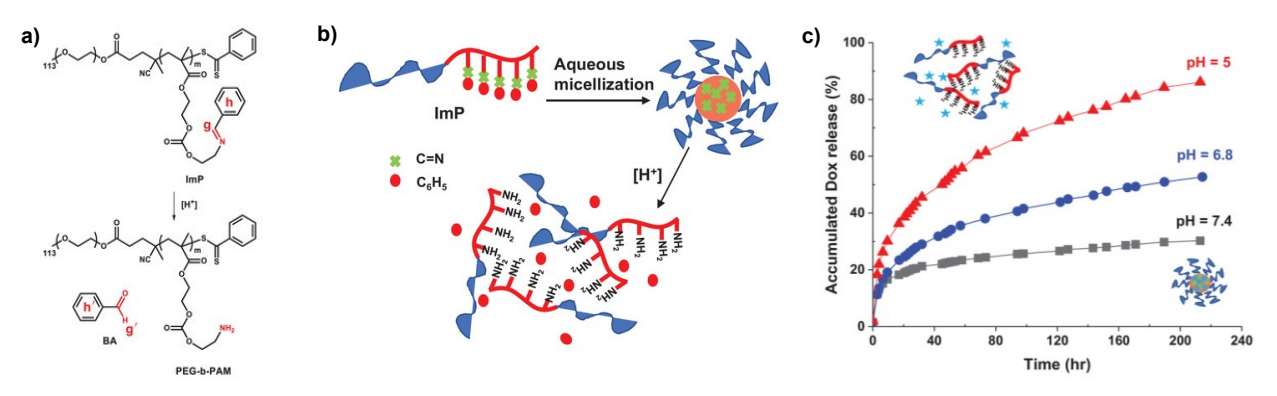


**Figure 2.1**. Scheme showing acid-responsive cleavage of imine bonds in ImP diblock copolymers (a), pH-responsive micelle disassembly at pH 5.0 for ImP nanoassemblies (b), and %Dox release over incubation time at acidic pHs 5.0 and 6.8, compared with physiological pH 7.4 (c).<sup>45</sup> (Copyright 2020, Wiley)

Another well-established example showed hydrazone chemistry in AB2-type amphiphilic block copolymer with a hydrazone linkage, which enabled pH-triggered antibiotic release. These micelles showed a two-fold increase in antibacterial activity against Methicillin-resistant Staphylococcus aureus at acidic pH, demonstrating the clinical potential of hydrazone bonds for site-specific drug delivery.<sup>69</sup> A recent design employed benzaldehyde acetal linkages at the corecorona interface of PEG-b-polymethacrylate block copolymers, positioning the acid-labile acetal precisely at the micelle boundary. This architecture enables selective acid-catalyzed hydrolysis at endosomal pH (5.0-6.5), inducing rapid shell shedding and micelle disassembly, while maintaining colloidal stability at physiological pH (7.4), thereby addressing the PEG dilemma.<sup>70</sup> Such architectural control not only enhances site-specific drug release but also offers a rational framework for overcoming biological barriers in tumor-targeted therapy.

*Redox-Responsive Systems*. Redox-responsive micelles commonly feature disulfide bonds within their structure, which are stable under physiological conditions but cleave in response to elevated intracellular glutathione (GSH) levels (~1-10 mM). This selective cleavage promotes rapid micelle disassembly and targeted drug release in the cytoplasm, while ensuring high stability during circulation and preventing premature payload leakage.<sup>71-73</sup> These systems are generally biocompatible and nontoxic at relevant concentrations, making them suitable for

clinical translation.<sup>74, 75</sup> Advances in redox-responsive micelles highlight the versatility of disulfide linkages in enabling controlled, stimuli-triggered disassembly.<sup>76-78</sup> Olszowy et al. reported a detailed investigation into the synthesis and core-crosslinking efficiency of redox-responsive polymeric micelles based on poly(2-ethyl-2-oxazoline)-block-poly(n-butyl acrylate-co-D,L-homocysteine thiolactone acrylamide). Core crosslinking was achieved through nucleophilic ring-opening of thiolactone units using diamine and triamine crosslinkers, notably cystamine, which introduced degradable disulfide bonds. The micelles showed reductive degradation in 10 mM DTT and maintained high in vitro cytocompatibility in COS-7 cells up to 0.1 mg/mL (Figure 2.2).<sup>77</sup>

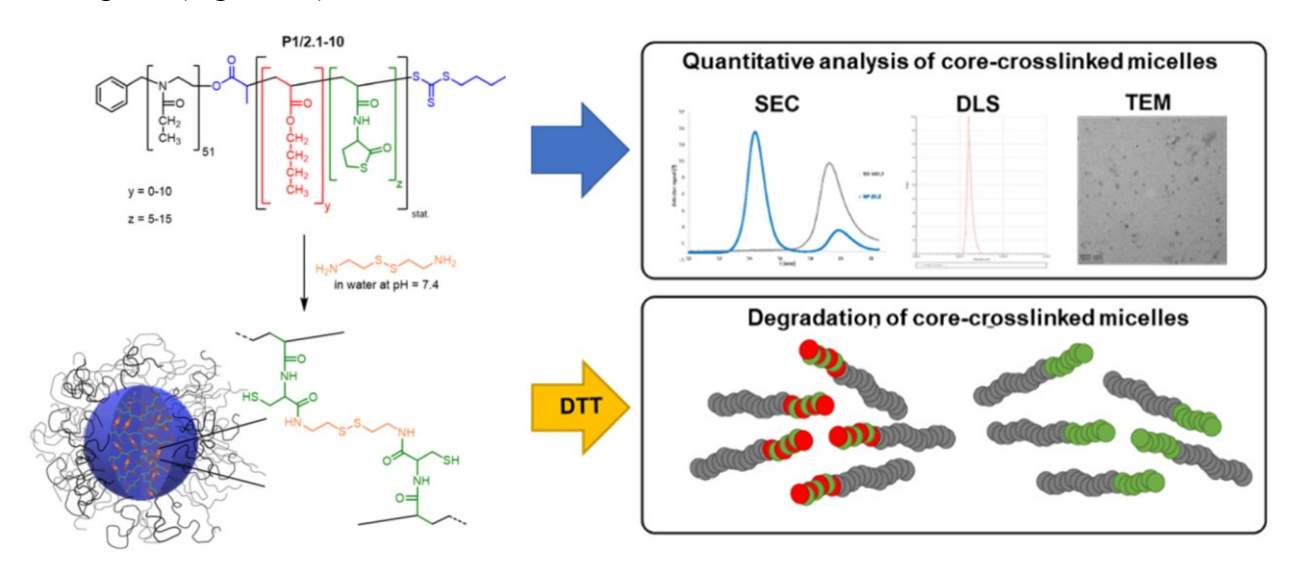


**Figure 2.2**. Summary of the redox-responsive block copolymer structure, micelle formation, micellar core-crosslinking with cystamine, degradation and characterization by means of DLS, TEM and SEC.<sup>77</sup> (Creative Commons Attribution 3.0 Unported License)

Other significant example involves poly(N-acryloylmorpholine)-b-poly(2-acryloyloxyethyl ferrocenecarboxylate) micelles, where hydrophobic ferrocene moieties undergo oxidation to hydrophilic ferrocenium, driving reversible micelle disruption and oxidation-sensitive drug release. Another system employed nonionic gemini polymeric micelles with diselenide linkages, achieving excellent colloidal stability, yet disassembling rapidly under reductive intracellular conditions. Furthermore, triblock copolymers bearing diselenide bonds at the core—shell junction form shell-shedding micelles that collapse in reductive environments, and when folate-functionalized, offer enhanced cellular uptake and tumor selectivity. It

Other Responsive Systems (Enzyme, ROS, ATP). Polymeric nanoassemblies that respond to endogenous stimuli such as enzymes, reactive oxygen species (ROS), and adenosine triphosphate (ATP) also represent powerful platforms for cancer-targeted drug delivery. Enzyme-responsive micelles are designed to degrade in the presence of tumor-overexpressed enzymes such as NAD(P)H:quinone oxidoreductase-1 (NQO1) or matrix metalloproteinases (MMPs). For instance, micelles incorporating NQO1-sensitive backbones undergo enzyme-triggered depolymerization via cascade cyclization, enabling precise intracellular drug release and enhanced therapeutic efficacy in NQO1-rich tumors.<sup>82</sup> Similarly, micelles bearing MMP-cleavable peptide linkers enable site-specific drug activation at the tumor interface.<sup>83</sup> Harnoy et al. reported PEG-dendron hybrids with variable numbers of enzyme-cleavable end-groups exhibit tunable disassembly rates, more end-groups confer greater micelle stability but hinder enzymatic degradation.<sup>84</sup> Even subtle modifications like replacing linear PEG with V-shaped PEG in dendritic micelles accelerate disassembly can modulatecleavage kinetics.<sup>85</sup>

ROS-responsive nanoassemblies utilize cleavable linkages such as diselenide, thioketal, methionine, or selenoether to achieve selective degradation in oxidative tumor environments. Diselenide-crosslinked and polypeptide-based micelles remain stable under physiological conditions but disassemble rapidly under ROS exposure, enhancing tumor suppression. <sup>86-88</sup> The location of ROS-sensitive groups is critical, corona-localized units enable partial shell shedding, while core-localized groups trigger complete micelle collapse. <sup>89</sup> Oxidation of poly(propylene sulfide) cores similarly induces hydrophilic transitions and rapid disassembly. <sup>90</sup>

# 2.2.2. Exogenous Stimuli-Responsive Nanoassemblies

External stimuli-responsive polymeric micelles have emerged as versatile platforms for ondemand drug release with enhanced spatial and temporal control. Unlike endogenous stimuli, which rely on the inherent biochemical environment of tumor tissues, exogenous stimuli such as light, heat, ultrasound, and magnetic field offer external manipulation, enabling precise regulation of drug activation at the targeted site. These systems are particularly valuable for overcoming heterogeneous tumor environments and minimizing premature release, offering flexible and controllable therapeutic strategies.<sup>24</sup> Recent research has focused on integrating photosensitive, thermoresponsive, and mechanosensitive moieties into block copolymer architectures to amplify responsiveness while ensuring safety and clinical applicability.<sup>91</sup> Light-responsive polymeric micelles are engineered through the incorporation of specific photoactive chemical groups into block copolymer architectures, enabling precise control over micelle assembly and drug release. The use of photochromic moieties such as spiropyran or azobenzene allows for reversible photoisomerization. Under UV or visible light, these groups switch between hydrophobic and hydrophilic forms, leading to micelle disassembly and drug release. 92, 93 In one study, a triblock copolymer with a nitrospiropyran middle block was synthesized via RAFT polymerization, resulting in micelles that could reversibly alter their size and catalytic properties in response to UV and visible light, demonstrating the utility of spiropyran chemistry for dynamic control of micellar behavior (Figure 2.3). 94 Another approach involves the use of photolabile groups such as 2-nitrobenzyl acrylate (NBA). In a system where NBA and a mercury(II)-detecting acrylate were copolymerized from a poly(ethylene oxide) macroinitiator via ATRP, UV irradiation cleaved the 2-nitrobenzyl moieties, converting hydrophobic PNBA to hydrophilic poly(acrylic acid), which triggered micelle dissociation. 95

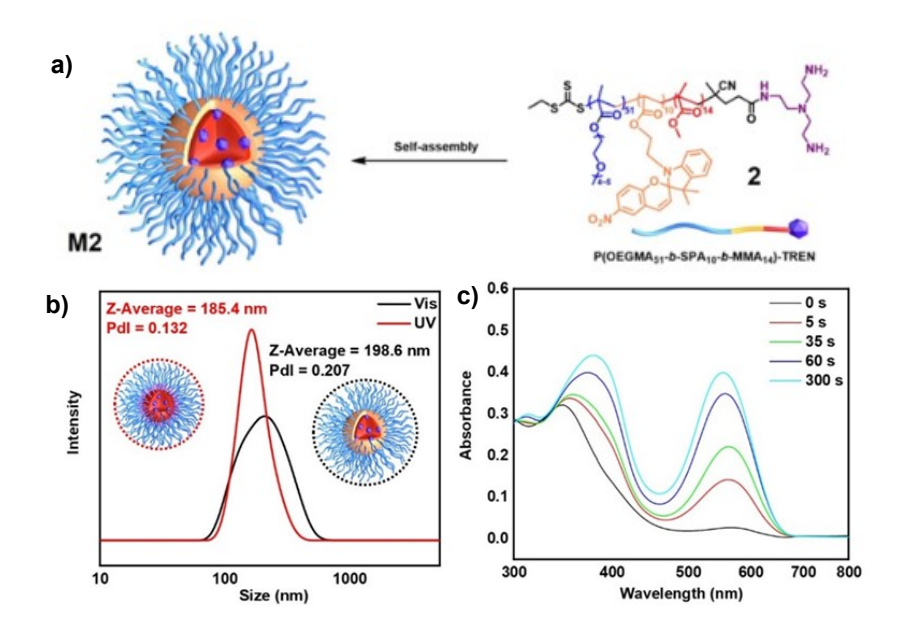


**Figure 2.3**. Scheme illustrating the self-assembly of the light-responsive nitrospiropyran-based triblock copolymer (a); size determination of micelles under UV and visible light by DLS (b), and its UV/vis spectral changes in water (0.5 mg/mL) following UV irradiation at  $\lambda = 365$  nm (c).<sup>94</sup> (Copyright 2023, Royal Society of Chemistry)

While these advances are promising, several critical challenges persist. A major limitation of UV and visible-light-responsive systems is poor tissue penetration, restricting their clinical applicability to superficial tumors or necessitating invasive light delivery methods. Upconverting nanoparticles (UCNPs) have become a transformative addition to light-responsive micellar systems, enabling deep-tissue activation using NIR light. When embedded in polymeric micelles, these emissions trigger cleavage of photocages or activation of photosensitizers, resulting in controlled drug release or phototherapy. <sup>96-98</sup> In one approach, UCNPs coated with amphiphilic diblock copolymers containing UV-sensitive poly(4,5-dimethoxy-2-nitrobenzyl methacrylate) allow NIR light to induce UV emission from the UCNPs, which cleaves the o-nitrobenzyl groups and disrupts the micelle, releasing encapsulated drugs like doxorubicin. <sup>97, 99</sup> Future research is focusing on optimizing NIR-responsive micelles, integrating imaging agents for real-time monitoring, and conducting comprehensive preclinical studies to ensure safety and efficacy for clinical translation. <sup>100, 101</sup>

Beyond light, recent advances in temperature-responsive micelles have enabled heat-responsive aggregation and *in situ* cross-linking to improve tumor retention and drug efficacy. Micelles bearing thermo-sensitive shells and reactive groups (e.g., azide–alkyne pairs) undergo dehydration and click-mediated cross-linking at 42°C, forming stable aggregates that persist post-heating. Additionally, ultrasound can trigger drug release through several mechanisms, including cavitation, shear forces, and the generation of reactive oxygen species (ROS) when sonosensitizers are present. 103, 104

# 2.2.3. Dual Stimuli-Responsive Nanoassemblies

Dual stimuli-responsive micelles represent a strategic advancement in smart nanocarrier systems, engineered to respond to two distinct environmental stimuli for enhanced site-specificity and controlled release. These systems often combine endogenous or exogenous stimuli, such as pH, redox potential, temperature, or light, to increase responsiveness under complex physiological conditions while minimizing off-target effects. Typically, dual-responsiveness is achieved by integrating orthogonal cleavable functionalities within the polymer backbone or through modular assembly of complementary copolymers. <sup>105, 106</sup>

The Oh research group has developed a series of dual stimuli-responsive degradable block copolymers engineered to disassemble under intracellular acidic and reductive conditions

through the precise placement of cleavable linkages. These systems incorporate acid-labile (ketal, acetal, or benzoic imine) and reduction-cleavable (disulfide) bonds at distinct locations such as the block junction, core, or pendant side chains. Key strategies include PEG-based copolymers with ketal junctions and pendant disulfides synthesized via ATRP, <sup>107</sup> PLA-based micelles using a double-head initiator bearing acetal/disulfide linkages for dual-junction cleavage, <sup>108</sup> and poly(oligo(ethylene oxide) methyl ether methacrylate)-based copolymers synthesized via a macroinitiator strategy combining ATRP and RAFT for orthogonal dual-site degradation. <sup>109</sup> In a more recent study, well-defined ABPs bearing pendant benzoic imine groups and a disulfide junction were synthesized via RAFT to construct dual acid/GSH-responsive nanoassemblies. These exhibited core degradation and shell detachment with tunable hydrolysis behavior influenced by para-substituents. <sup>110</sup>

Recently, Jäck et al. report the synthesis of dual stimuli-responsive amphiphilic glycomacromolecules (APGs) capable of controlled glycan release through UV and pH-sensitive cleavage. Using solid-phase polymer synthesis, the authors integrated a novel acid-labile dioxolane-benzoic acid (DBA) linker and a photo-cleavable nitrobenzyl linker (PL) into block-structured glycomacromolecules. These APGs formed micellar assemblies, whose disassembly or surface glycan modification was selectively induced under acidic (1% TFA) and UV (365 nm) conditions. *In vitro* turbidity assays and RP-HPLC-MS confirmed the selective, linker-position-dependent response for their potential as lectin targeting drug delivery applications (Figure 2.4). Similarly, Yi et al. developed micelles bearing both o-nitrobenzyl ester and disulfide linkages, where UV exposure or reducing agents independently responsive degradation. Their approach enabled sequential or combined cleavage of the core network, offering tight regulation of drug release. In another illustrative study, Zhang et al. designed dual-responsive micelles based on a RAFT-synthesized amphiphilic copolymer incorporating spiropyran methacrylate for light sensitivity and N-isopropylacrylamide (NIPAAm) for temperature responsiveness. 93

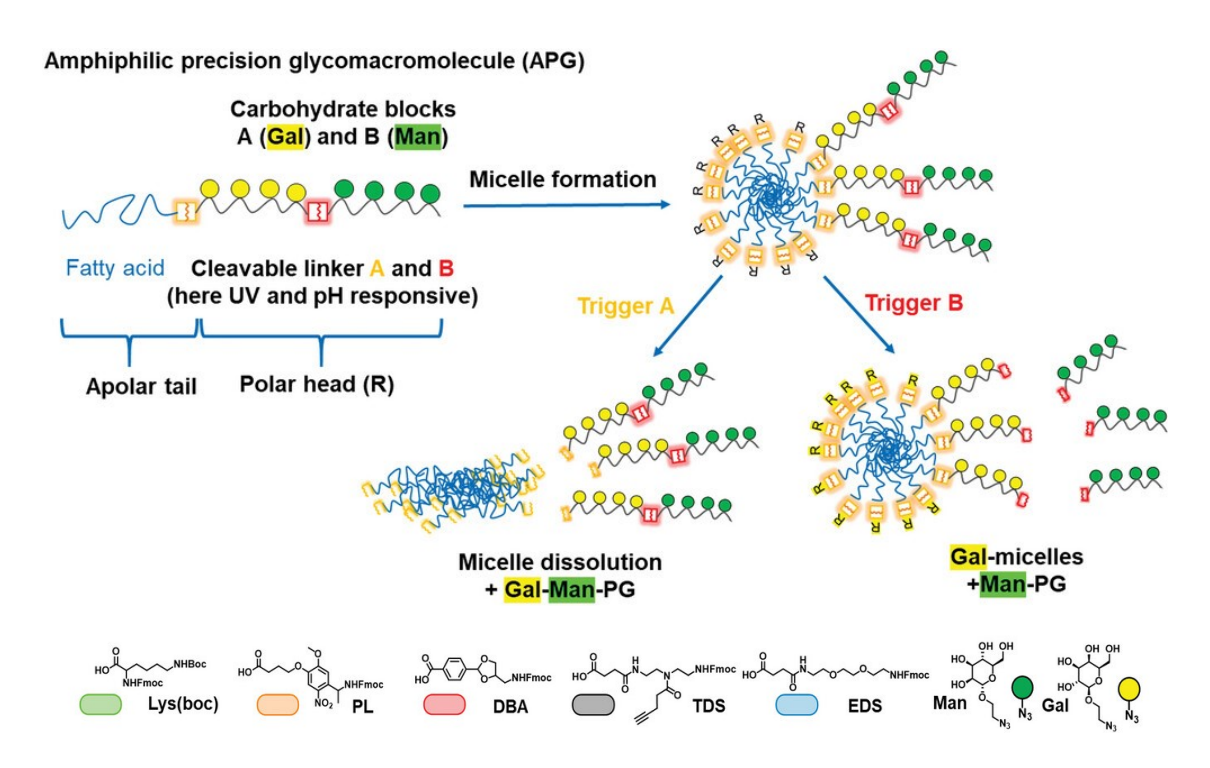


**Figure 2.4**. Schematic showing selective release of glycan ligands from APG micelles via dual stimulus-responsive linker cleavage. UV light (A) cleaves the orange linker, releasing both carbohydrate blocks A and B and disrupting the micellar structure. Acidic pH (B) cleaves the red linker, releasing block B (Man) while retaining block A (Gal), preserving micelle integrity. (Copyright 2024, Wiley)

The design of dual-stimuli responsive system must ensure that each stimulus acts selectively on its target bond without cross-reactivity. However, challenges persist in achieving true orthogonality and predictable kinetics. The rate of disassembly for each stimulus may differ, potentially resulting in incomplete or asynchronous breakdown. The dynamic interplay between chemical structure, assembly morphology, and environmental triggers is thus central to the rational design of dual stimuli-responsive amphiphilic nanoassemblies.

# 2.3. Synthetic Approaches for Stimuli-Responsive Core-Crosslinked Nanoassemblies

BCP-based nanoassemblies comprising a hydrophobic core and hydrophilic corona are formed through the self-assembly of block copolymers above their critical micelle concentration (CMC). While low CMC values enhance thermodynamic stability, micelle integrity can still be compromised *in vivo* due to dilution upon intravenous administration and interactions with serum proteins, resulting in premature drug release and reduced therapeutic efficacy. <sup>115, 116</sup> To address

this, micelle crosslinking has emerged as an effective approach to enhance structural integrity. Crosslinking can be introduced either in the corona (shell), the core, or across the entire micellar interface. Shell crosslinking has been shown to enhance colloidal stability and circulation time, but it may alter surface characteristics, potentially compromising the biological performance of the nanocarrier. In contrast, core-crosslinking is confined to the micellar interior, preserving the outer surface properties and minimizing interference with biological interactions. <sup>61, 62</sup>

A wide variety of crosslinking chemistries have been developed to achieve these objectives, ranging from purely covalent stabilization to stimuli-responsive networks. 117-119 In this section, core crosslinking strategies are categorized into three main approaches reflecting their distinct design principles and mechanisms. The first approach (Section 2.3.1), core-crosslinking by conjugation via general covalent chemistry, employs bifunctional crosslinkers that react within preformed micelles through robust coupling reactions such as click chemistry and Diels-Alder cycloadditions. While these crosslinkers incorporate cleavable motifs, the other focus is on efficient and orthogonal conjugation to enhance stability. The second approach (Section 2.3.2), conjugation by stimuli-responsive linkages, emphasizes the deliberate incorporation of labile bonds that degrade selectively under defined physiological conditions, including acidic pH, reductive environments, or light irradiation. These labile linkages, such as disulfide, acetal, thioketal, or photodimer groups, enable precise spatiotemporal control over micelle disassembly and controlled cargo release. In contrast to post-assembly conjugation, the third approach (Section 2.3.3), in situ core crosslinking by polymerization-induced self-assembly (PISA), integrates micelle formation and crosslinking into a single polymerization process. This method allows for the simultaneous generation of nanoscale morphologies and crosslinked networks, incorporating degradable linkages during polymer growth to yield nanostructures with tunable stability and responsive behavior.

# 2.3.1. Core-Crosslinking by Conjugation via General Covalent Chemistries

Core-crosslinking by conjugation via general covalent chemistries involves stabilizing preassembled micelles using bifunctional reagents that form robust covalent bonds within the hydrophobic core. This strategy focuses primarily on efficient click-type conjugation reactions such as azide-alkyne cycloaddition, Diels-Alder (DA) cycloaddition, and thiol-ene reaction, to reinforce micelle architecture under physiological conditions. The crosslinkers feature cleavable

groups, and the design criterion is the orthogonality and reliability of the conjugation mechanism. These chemistries enable precise spatial localization of crosslinks and enhance structural integrity, improving colloidal stability and reducing premature drug release.

Bifunctional click reagents have emerged as essential tools in the fabrication of corecrosslinked micelles. The copper(I)-catalyzed azide-alkyne cycloaddition (CuAAC), widely regarded as the quintessential click reaction, has been instrumental in enabling efficient core stabilization. Through the use of bifunctional azide- and alkyne-containing reagents, CuAAC facilitates the formation of covalent networks within micelle cores under mild conditions. Lacently, Zhang et al. designed redox-responsive core-crosslinked micelles by crosslinking an alkyne-terminated poly(ε-caprolactone) based A-PCL-A macromonomer containing disulfide linkages with an azide-functionalized three-arm PEG. This modular system produced micelles with a covalently stabilized hydrophobic core and hydrophilic corona, significantly improving the cytotoxicity of Dox in A549 cells, compared to free Dox, demonstrating the efficacy of disulfide-based clickable networks for intracellular drug delivery. Building on this approach, Yi et al. synthesized a dual pH- and redox-responsive micelle system based on PEG-based block copolymer, where the core-forming block contains pendant alkynyl and acetal moieties. Core crosslinking with bis(azidoethyl) disulfide via CuAAC yielded micelles that responded sequentially to endosomal acidification and cytosolic reduction.

Extending the versatility of this approach, Siboro et al. introduced diselenide-containing alkyne linkers into azide-functionalized PEO-b-poly(glycidyl methacrylate) to prepare micelles responsive to NIR light. Upon irradiation, indocyanine green produced ROS, cleaving the Se-Se bonds and triggering light-controlled drug release without thermal damage (Figure 2.5). <sup>125</sup> In a related example of ROS sensitivity, ROS-degradable core-crosslinked polycarbonate micelles were synthesized via a CuAAC reaction between poly(ethylene glycol)-poly(5-methyl-5-propargylxycar-bonyl-1,3-dioxane-2-one) (PEG-PMPC) diblock copolymers bearing pendant alkynes and a thioketal-functionalized diazide (TK-N<sub>3</sub>). The incorporation of thioketal units into the crosslinking network endowed the micelles with ROS-cleavability, making them responsive to oxidative stress in tumor microenvironments. <sup>126</sup>

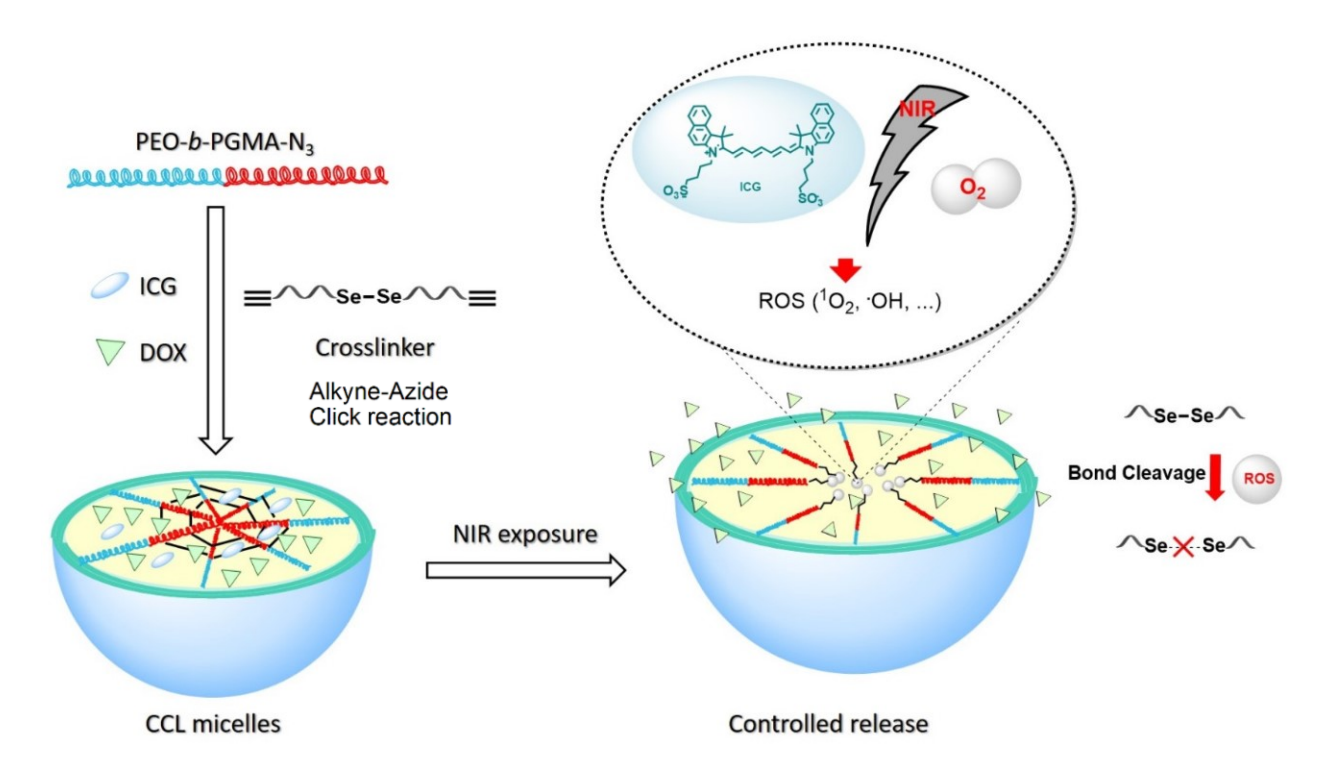


**Figure 2.5**. Illustration for formation of diselenide core-crosslinked micelles via alkyne-azide click chemistry and NIR-induced micelle disassembly. Upon NIR irradiation in the presence of indocyanine green, ROS generation cleaves Se–Se bonds, enabling controlled release of encapsulated drug molecules. (Creative Commons Attribution (CC BY) license)

To overcome limitations associated with metal catalysts in biomedical application, catalyst-free click reactions such as thiol-ene reaction have also been explored for core-crosslinking. Zhu et al. synthesized biodegradable poly(ether-ester)s bearing pendant thiol groups via melt polycondensation. These were crosslinked using a disulfide-containing diacrylate (2,2'-dithiodiethanol diacrylate) through thiol-ene reaction, forming core-crosslinked micelles (~120 nm) capable of encapsulating paclitaxel and releasing it in response to elevated intracellular GSH concentrations. The same group later expanded this method to design dual-responsive nano-prodrug micelles, where thiol-ene chemistry enabled simultaneous drug conjugation and disulfide crosslinking, allowing for integrated pH and redox-triggered release profiles. 128

In addition to azide-alkyne and thiol-ene chemistries, the DA cycloaddition has gained attraction as a metal-free, thermally reversible approach for constructing core-crosslinked micelles. The DA cycloaddition between furans and maleimides proceeds efficiently under ambient conditions, offering orthogonality and excellent biocompatibility. <sup>129, 130</sup> Salma et al.

employed this strategy to prepare diselenide-crosslinked micelles with enhanced colloidal stability. These micelles retained structural integrity upon dilution but readily degraded in the presence of reductive stimuli, demonstrating the effectiveness of DA-based networks in balancing stability and stimuli-responsiveness. <sup>131</sup> These examples illustrate the adaptability of click chemistry in designing modular core-crosslinked micelles. Whether employing CuAAC, thiol-ene, or Diels-Alder strategies, the incorporation of cleavable linkages such as disulfides, acetals, thioketals, or diselenides enables precise control over crosslinking density and stimulus-induced degradation.

Another approach involves the covalent incorporation of pre-synthesized acid-labile linkers directly into polymer backbone by amidation. Liu et al. demonstrated this strategy using ketalbridged diamine linkers to crosslink pentafluorophenyl ester-functionalized polymers through the amidation nucleophilic substitution, resulting in acid-cleavable core networks with robust stability under physiological conditions and efficient disassembly in acidic media. 132 In a related study, Nuhn et al. incorporated ketal units into micellar cores by crosslinking and conjugation through amide bond formation with bisamines to precisely regulate degradation kinetics and facilitate controlled drug release under mildly acidic conditions. 133 Expanding on this concept, Cao et al. designed a triblock copolymer, poly(oligo(ethylene glycol) methyl ether methacrylate)-block-poly(styrene-alt-maleic anhydride)-block-polystyrene (POEGMA-b-PSMAb-PS), synthesized via sequential RAFT polymerization. The anhydride-containing PSMA block provided reactive sites for crosslinking with a bifunctional ketal-containing diamine, 2,2bis(aminoethoxy)propane. As shown in Figure 2.6, upon micellization in aqueous media, this crosslinker reacted with anhydride units via nucleophilic ring-opening amidation, embedding ketal moieties at the center of each newly formed amide linkage. The resulting crosslinks were stable under neutral conditions but underwent selective cleavage under acidic pH, triggering disassembly of the micelle core. 134

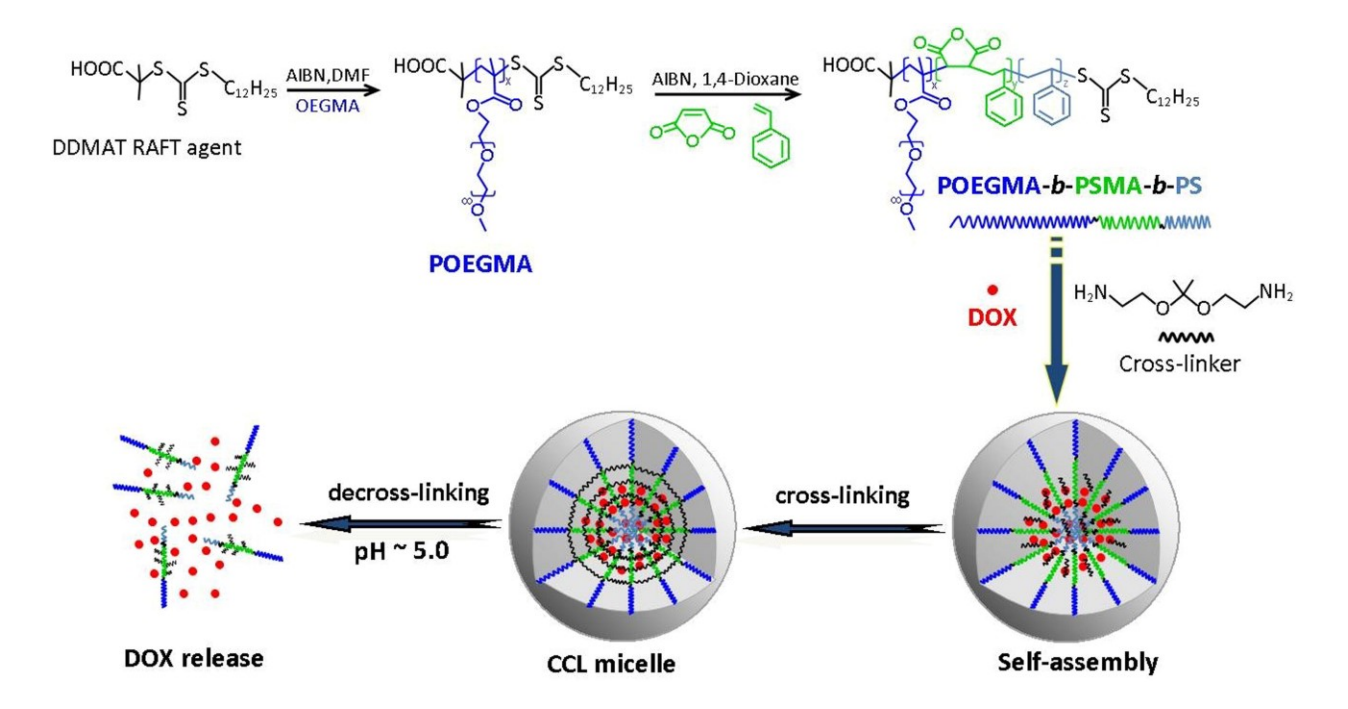


**Figure 2.6**. Schematic illustration of the synthesis of POEGMA-b-PSMA-b-PS triblock copolymers and the formation of ketal core-crosslinked micelles (CCL) via amidation between maleic anhydride units and a bifunctional ketal-containing diamine. The resulting micelles exhibit stability under physiological conditions and undergo pH-responsive disassembly for controlled doxorubicin release. (Copyright 2020, Taylor & Francis)

# 2.3.2. Core-Crosslinking by Conjugation via Stimuli-Responsive Linkages

In contrast to general covalent chemistries that primarily emphasize micelle stabilization, conjugation by stimuli-responsive linkages focuses on integrating covalent bonds that selectively degrade in response to specific biological or external stimuli. This approach enables precise spatiotemporal control over micelle disassembly and controlled drug release, enhancing therapeutic performance and reducing off-target effects. Stimuli-responsive linkages commonly incorporated into core-crosslinked networks include acid-labile imines and ketals, redox-sensitive disulfides, thioketals, and photocleavable groups.

One approach is crosslinking with bifunctional reagents to form degradable linkages. This approach involves the *in situ* formation of stimuli-cleavable links within preassembled micellar cores. For instance, Wang et al. utilized terephthaldicarboxaldehyde (TCA), a bifunctional aldehyde, to crosslink hydrazide-functionalized block copolymers through acid-labile acylhydrazone bonds, resulting in nanogels with improved colloidal stability and acid-triggered

degradation. Moreover, residual hydrazide groups allowed for post-assembly conjugation with biotin and fluorescein isothiocyanate, enabling multifunctional applications. Similarly, Azuma et al. employed a tailor-made methacrylate monomer labeled with both urea and aniline functionalities (ApUMA) that was polymerized into a diblock copolymer, forming poly(methyl methacrylate)-based PMMA-b-PApUMA. The resulting copolymers self-assembled in organic solvents via hydrogen bonding among urea pendants, forming micelles with cores enriched in aniline groups. TCA diffused into the micellar core and selectively reacted with these aniline groups to form imine linkages through a dehydration condensation reaction. This strategy enabled the creation of microgel star polymers that degrade selectively in mildly acidic environments, demonstrating precise control over pH-responsive disassembly. 136

Furthermore, photo-induced crosslinking strategies offer a powerful and precise method for stabilizing micellar architectures via light-triggered covalent bond formation. Unlike conventional chemical crosslinking, this approach utilizes the spatiotemporal control of light to induce core crosslinking *in situ*, often without the need for external crosslinkers or initiators. <sup>137,</sup> Among various photo crosslinkable moieties, cinnamic acid, coumarin, and thymine have attracted considerable interest due to their ability to undergo reversible [2+2] cycloaddition upon UV irradiation, forming cyclobutane linkages that can be cleaved under different light wavelengths (Figure 2.7). <sup>139, 140</sup>

(a) 2 
$$R_1$$
  $OR_2$   $R_2OOC$   $R_1$   $COOR_2$ 

**Figure 2.7**. Reversible [2+2] photocycloaddition of cinnamate (a) and coumarin (b) derivatives, illustrating photo-induced dimerization. (Copyright 2025, Royal Society of Chemistry)

A notable example is the work by Zhang et al., who introduced a dual-wavelength irradiation strategy using amphiphilic diblock copolymers functionalized with phthalimide esters

and coumarin groups. <sup>141</sup> This design enabled simultaneous photo-cleavage and photo-crosslinking, allowing for on-demand destabilization and solubilization of the micelles under selective UV light at  $\lambda = 365$  and 254 nm. The study demonstrates that the amphiphilic balance and crosslinking density of the micelles can be modulated through wavelength-specific photoreactions, a critical mechanism underlying responsive behavior in such systems. Alemdar et al. developed a light-sensitive hydrogel by incorporating coumarin-functionalized amphiphilic diblock terpolymers into Pluronic F127 micelles. Here, the pendant coumarin moieties underwent efficient UV-induced photodimerization at  $\lambda = 350$  nm, contributing to enhanced hydrogel integrity. <sup>142</sup> Beyond the classic [2+2] photocycloaddition, visible light-mediated strategies have expanded the toolbox for micellar crosslinking under milder and more biocompatible conditions. Cheng et al. designed a triblock copolymer bearing pendant diselenolane groups, which underwent visible light-induced Se–Se metathesis to generate diselenide crosslinks within the micellar core. <sup>143</sup> Notably, this method not only improves biocompatibility by avoiding UV exposure but also imparts redox-responsiveness for targeted delivery.

Alternative photo-crosslinking chemistries have also been explored. Baysoy et al. synthesized PEG-b-poly(styrene-r-4-(azidomethyl)styrene) PEG-b-P(St-r-AMS) random copolymers bearing pendant azido groups, which enabled efficient UV-induced crosslinking via nitrene insertion reactions. The resulting micelles exhibited improved drug retention and acid-sensitive doxorubicin release. Have a biologically inspired approach, Weber et al. incorporated the unnatural amino acid para-azidophenylalanine into recombinant elastin/resilin-like polypeptides. Upon UV irradiation, these azide-functional polypeptides underwent intramicellar crosslinking, yielding micelles which maintained their structural integrity in 7.2 M guanidinium hydrochloride, while uncrosslinked micelles disassembled. As shown in Figure 2.8, in ανβ3-positive K562 cells, confocal microscopy confirmed superior internalization of crosslinked micelles even at 70 nM (sub-CMC). Overall, the chemistry of photocrosslinking in micellar systems, [2+2] Cycloadditions, diselenide metathesis, and nitrene insertion each offer distinct crosslinking mechanisms, dictated by the electronic structure and reactivity of the pendant groups.

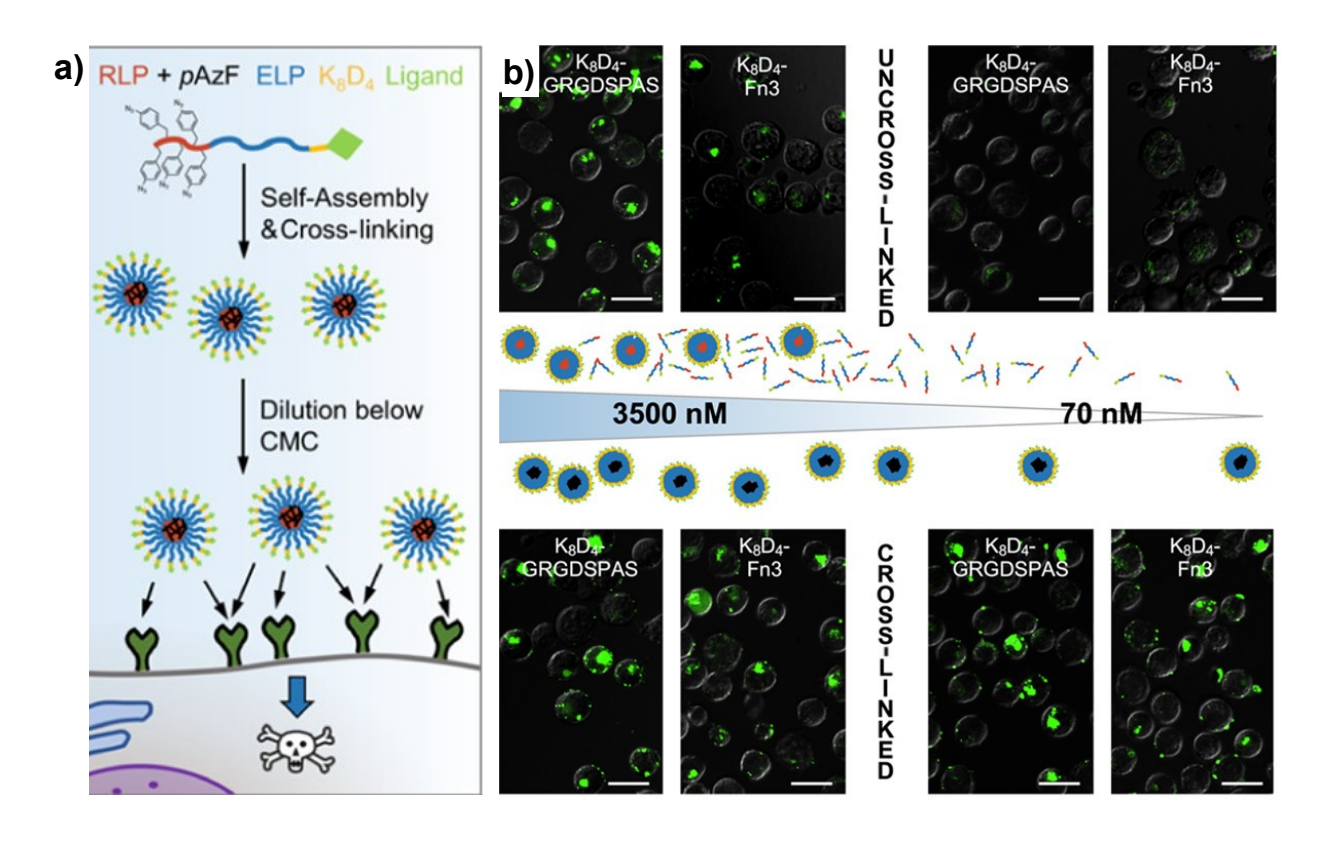


**Figure 2.8**. Schematic illustration of genetically encoded diblock polypeptides that are covalently stabilized via photo-crosslinking of para-azidophenylalanine residues in the core (a) and representative confocal images of K562 cells after 1.5 h incubation with AF488-labeled (green) functionalized micelles in PBS, showing cellular uptake (b). Scale bars: 20 μm. <sup>145</sup> (Copyright 2021, American Chemical Society)

Collectively, these photoresponsive systems illustrate how external irradiation can be harnessed to achieve precise control over micelle crosslinking and degradation, offering adaptable strategies for controlled drug delivery and responsive nanocarriers. While bifunctional crosslinkers bearing labile bonds and photo-triggered chemistries offer precise mechanisms for controlled micelle disassembly, they still require pre-assembly or post-assembly functionalization steps. In contrast, *in situ* crosslinking strategies such as PISA integrate polymerization, micelle formation, and network stabilization into a single streamlined process, providing unique advantages in scalability and morphological control.

# 2.3.3. In Situ Core Crosslinking by Polymerization-Induced Self-Assembly (PISA)

Distinct from post-assembly conjugation strategies, *in situ* core crosslinking by polymerization-induced self-assembly (PISA) enables simultaneous formation, crosslinking, and

stabilization of block copolymer nanostructures in a single process. PISA relies on controlled or living polymerization techniques to grow a solvophobic block from a soluble macro-chain transfer agent (macro-CTA), driving spontaneous micellization as the polymerization progress. By incorporating crosslinkable monomers or multifunctional crosslinkers during polymerization, this approach achieves efficient intramicellar crosslinking, affording nanostructures with tunable morphology, enhanced colloidal stability, and programmable responsiveness.

Since the initial development of PISA by Pan and colleagues, this one-pot strategy, based on phase separation and structural reorganization of block copolymers, has received considerable attention to achieve specific stimulus-responsive controlled release, and crosslinking and discrosslinking. 146-149 Among various functional strategies, the incorporation of disulfide-containing difunctional monomers into PISA formulations has proven particularly effective, enabling both the stabilization of nanoassemblies and their selective cleavage under reductive environments. These redox-responsive systems show significant promise for intracellular drug delivery, although careful consideration of factors such as cytocompatibility, redox potential, and environmental stability remains essential. 150, 151 Warren and Armes reported aqueous dispersion RAFT polymerization of 2-hydroxypropyl methacrylate (HPMA) using PEG-based macromolecular chain transfer agents, where *in situ* micelle formation and core crosslinking with *N,N'*-bis(acryloyl)cystamine yielded disulfide-bridged micelles that disassembled rapidly under reducing intracellular conditions. 151

A prominent work by Zhao et al. employed intramicellar crosslinking during PISA to fabricate micelle-crosslinked hydrogels with tunable mechanical properties and adaptive strain-stiffening behavior. Spherical micelles with variable core crosslinking densities were generated via aqueous RAFT-mediated PISA using allyl acrylamide (ALAM) as a delayed-reactivity crosslinker. Similarly, Shahrokhinia et al. developed a Photo-controlled atom transfer radical polymerization (PhotoATR-PISA) system that enables one-pot synthesis of redox- and pH-responsive nanoparticles by integrating UV-mediated polymerization with *in situ* disulfide crosslinking. Using poly(oligo(ethylene oxide) methyl ether methacrylate)-b-poly(glycidyl methacrylate) (POEGMA-b-PGMA) copolymers and cystamine bismethacrylamide as a degradable crosslinker, the system allows for controlled nanoparticle formation and dual stimuli-responsive disassembly via disulfide cleavage and epoxide hydrolysis. Gel permeation

chromatography (GPC) revealed distinct monomodal shifts toward higher molecular weights after each UV-exposure cycle, confirming successful chain growth with preserved end-group fidelity as shown in Figure 2.9.<sup>153</sup> Notably, during dark periods between UV cycles, no increase in molecular weight was observed, demonstrating effective temporal regulation of polymerization.

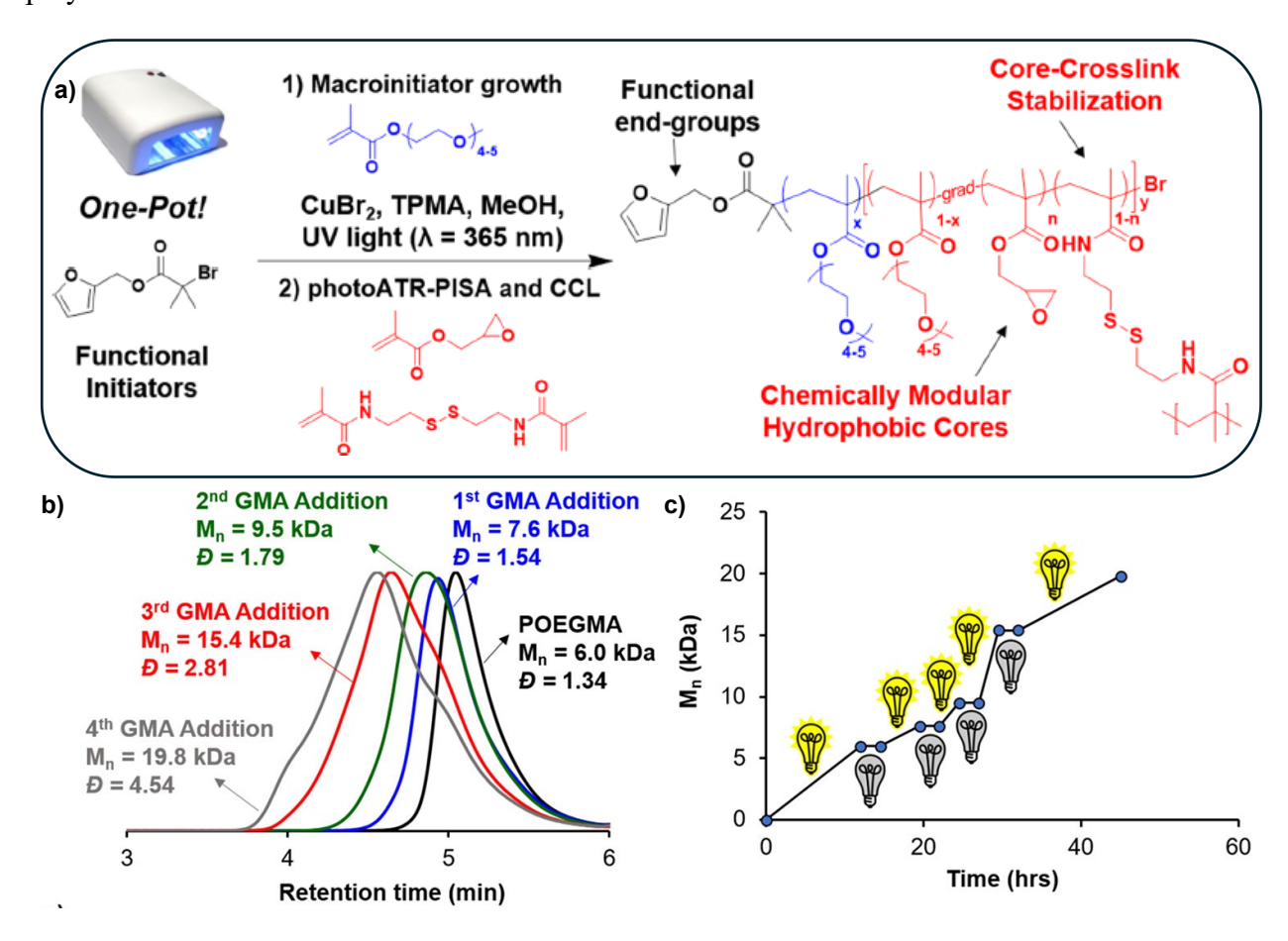


**Figure 2.9**. Schematic overview of the PhotoATR-PISA methodology enabling synthesis of core cross-linked nanoparticle formation without intermediate work-up (a), and GPC traces of controlled chain extensions (DP(PGMA) = 43) with temporal regulation (b, c). (Copyright 2021, American Chemical Society)

Complementing these approaches, Park et al. employed RAFT-mediated PISA in acetonitrile to copolymerize styrene with divinylbenzene (DVB) or 1,2-bismaleimidoethane (BMI), enabling *in situ* formation of core-crosslinked star micelles. DVB facilitated anisotropic growth via flexible crosslinking, while BMI yielded compact spherical micelles due to its alternating copolymerization behavior. The resulting high-molecular-weight assemblies

exhibited strong core stability, confirming efficient intramicellar network formation.<sup>154</sup> By judiciously selecting monomer composition, crosslinker reactivity, and polymerization technique (e.g., RAFT or Photo ATRP), it is possible to engineer nanostructures tailored for drug delivery, stimuli-triggered degradation, or load bearing nanoassemblies.

Overall, *in situ* core crosslinking by PISA represents a powerful and modular strategy to achieve robust, responsive nanocarriers through a streamlined synthetic process. Its ability to integrate polymer growth, self-assembly, and network formation in a single step holds significant promise for scalable manufacturing of advanced drug delivery systems.

# 2.4. Summary and Outlook

The development of core-crosslinked block copolymer nanoassemblies has advanced significantly through a diverse array of conjugation and polymerization strategies. General covalent chemistries utilizing click-type reactions such as azide-alkyne cycloaddition, DA cycloaddition, and thiol-ene reaction have enabled robust stabilization of micelles while preserving surface properties. In parallel, the incorporation of stimuli-responsive linkages, including disulfide, diselenide, acetal, thioketal, and photocleavable groups, has facilitated precise spatiotemporal control over micelle disassembly in response to endogenous and exogenous triggers. More recently, *in situ* crosslinking via polymerization-induced self-assembly has emerged as a powerful and scalable approach to integrate self-assembly and network formation within a single step.

Despite these advances, several challenges remain. Optimizing the balance between colloidal stability and rapid degradation, enhancing the efficiency of crosslinking reactions under mild conditions, and achieving high drug-loading capacities without compromising micelle integrity are ongoing areas of focus. Future efforts are likely to explore combinatorial strategies that integrate multiple stimuli-responsive motifs within a single platform, as well as the development of greener synthetic protocols and clinical translation of these systems. As the field evolves, core-crosslinked polymeric micelles are poised to play a pivotal role in next-generation drug delivery technologies.

# Chapter 3. Synthesis and Dual Acid/Light-Responsive Disassembly of Amphiphilic Block Copolymer Nanoassemblies Bearing Conjugated Benzoic Imine Pendants

#### 3.1. Introduction

Well-controlled amphiphilic block copolymers (ABPs) exhibiting stimuli-responsive degradation (SRD) have been extensively explored as controlled/enhanced drug delivery systems for disease sites (desirably tumors). The intrinsic amphiphilic character of SRD-ABPs as they consist of both hydrophilic and hydrophobic blocks, allows them to self-assemble into colloidally stable nanometer-sized micelles (called nanoassemblies) in aqueous solutions. The formed nanoassemblies are composed of hydrophobic cores encapsulating drug molecules, surrounded by hydrophilic coronas, endowing compatibility with aqueous environments. Furthermore, these SRD-ABPs are designed with labile linkages that are cleaved through chemical transition or integrated with functional groups that undergo physical transition such as cis-trans isomerism. In response to stimuli, the SRD-ABPs and their nanoassemblies could be degraded or disintegrated, leading to the enhanced release of encapsulated drug molecules. The stransition of the enhanced release of encapsulated drug molecules.

Among many stimuli, acidic pH is a promising endogenous stimulus that is found in the body, thus attaining biodegradation. Acidic pH is found at 6.5-6.9 in tumor tissues (tumoral pH) and 4.5-5.5 in endosomes and lysosomes (endo/lysosomal pH). Due to these features, various SRD-ABPs degradable in cellular acidic pH have been synthesized with the incorporation of acid-labile linkages such as ketal, acetal, imine, and β-thioester groups. Light is also a promising trigger that allows for on-demand degradation upon the irradiation of light. Photo-cleavable o-nitrobenzyl and coumarin linkages have been integrated in photo-degradable SRD-ABPs. These acid-labile and photo-cleavable linkages are positioned on backbones or as pendant groups in hydrophobic blocks as well as at the junction of hydrophilic and hydrophobic blocks of ABPs; consequently, they are found either in micelle cores or at core/corona interfaces of nanoassemblies.

Further to such a single stimulus approach, advanced SRD-ABPs that respond to dual acidic pH and light stimuli have been synthesized. A general strategy involves the integration of both an acid-labile and a light-responsive linkages in the design of SRD-ABPs. A poly(ethylene glycol) (PEG)-based triblock copolymer micelles degradable in response to light and acidic pH were synthesized with both o-nitrobenzyl (light-responsive) and β-thioester (acid-responsive) linkages at the block junctions.<sup>178</sup> Dual pH/light-responsive crosslinked micelles were fabricated by self-assembly of amphiphilic glycol chitosan-o-nitrobenzyl succinate conjugates, followed by crosslinking with glutaraldehyde through the formation of imine (acid-responsive) linkage.<sup>31</sup> Recently, triple pH/glutathione/light-responsive triblock copolymer micelles were designed with both acetal and disulfide in the center of the copolymer on the backbone and o-nitrobenzyl pendants in the hydrophobic block.<sup>179</sup>

Benzoic imine is one of the Schiff bases that is formed by the reaction of an aldehyde and a primary amine. It undergoes acid-catalyzed hydrolysis, resulting in the cleavage of C=N double bond to generate the corresponding aldehyde and amine. 44, 180, 181 In addition to their acid response, benzoic imine derivatives can also respond to light. Reports describe that C=N imine bonds underwent E/Z isomerization upon exposure to UV/vis light. Lehn et al reported, upon the irradiation of UV light, the E/Z isomerization of C=N double bonds in diaryl-N-alkyl imine derivatives as molecular motors. 182 Later, Lehn et al and Barner-Kowollik et al synthesized acyclic diene metathesis (ADMET)-polymers containing N-alkyl α-bisimine as main-chain functional groups. Upon the irradiation of UV light, the ADMET homopolymers <sup>183</sup> and block copolymers<sup>184</sup> underwent their conformational changes through the E/Z isomerization of C=N bonds. Further reports describe that conjugate imine bonds undergo dynamic exchange reaction through imine metathesis in covalent adaptive network materials upon exposure to visible or NIR light. Du et al fabricated self-healable and reprocessable polyurethanes containing aromatic Schiff-base bonds as N,N'-(4-hydroxybenzylidene)aniline methane that exhibited dynamic exchange imine metathesis upon irradiation of visible-light. <sup>185</sup> Zhang et al fabricated a thermal, near-infrared light, and amine solvent triple-responsive polyimine vitrimer by incorporating oligoaniline (e.g. aniline trimer) into a traditional imine-type vitrimer. <sup>186</sup> The formed vitrimer containing conjugated imine bonds shows a unique photothermal conversion property. Based on these reports, we envisage that conjugated benzoic imine linkages can be incorporated into the

design of SRD-ABPs in order to achieve dual responses to acidic pH and light with only one linkage. To the best of our knowledge, no reports describe SRD-ABPs that display dual acidic pH/light response with a single labile linkage.

In this work, as a proof-of-concept to explore our hypothesis for dual acid/light-responsive drug delivery, we synthesized a well-defined SRD-ABP containing conjugated benzoic imine pendants (abbreviated as P-Im) degradable both in acidic pH and upon irradiation of light. Two approaches utilizing reversible addition fragmentation chain transfer (RAFT) polymerization were explored: direct polymerization of a novel methacrylate bearing a conjugated benzoic imine group and post-polymerization modification using a carbonyldiimidazole coupling chemistry. To prove their adaptability toward drug delivery systems, the P-Im synthesized uniquely by post-polymerization modification was characterized for UV/vis absorption characteristics and aqueous micellization. Furthermore, both acid and light responses of the conjugated benzoic imine linkage were comprehensively studied with methacrylates, P-Im, and nanoassemblies, all of which bear the conjugated benzoic imine bond(s).

## 3.2. Experimental

### 3.2.1. Instrumentation

<sup>1</sup>H-NMR spectra were recorded using 500 MHz Varian spectrometer. The CDCl<sub>3</sub> singlet at 7.26 ppm, DMSO-d<sub>6</sub> quintet at 2.5 ppm and CD<sub>3</sub>CN at 1.94 ppm were selected as the reference standard. UV/vis spectra on Agilent Cary 60 UV/vis spectrometer were recorded using a 1 cm wide quartz cuvette. The size and size distribution of nanoassemblies in hydrodynamic diameter were measured by dynamic light scattering (DLS) at a fixed scattering angle of 175° at 25 °C with Malvern Instruments Nano S ZEN1600 equipped with a 633 nm He-Ne gas laser.

Transmission Electron Microscopy (TEM) images were obtained using FEI Tecnai G2 F20 200 kV Cryo-STEM with Gatan Ultrascan 4000 4kx4k CCD Camera System Model 895. To prepare the specimens using negative staining, an aqueous 1% stain solution was first prepared by mixing phosphotungstic acid (5 mg) with deionized water (0.5 mL) for 5 min. The resulting solution was then mixed with sodium hydroxide (5  $\mu$ L, 1 M) and filtered with a 0.45  $\mu$ m PES membrane. Then, aliquots (5  $\mu$ L) of aqueous dispersions were dropped on a 300 mesh TEM Cu grid and allowed to sit for 2 min. After excess dispersion was blotted off the grid using filter

paper, a drop of stain was applied. The grid was again blotted to remove excess stain and allowed to dry in fume hood before TEM measurements.

#### 3.2.2. Materials

2-Hydroxyethyl methacrylate (HEMA, 99%), methanesulfonyl chloride (MsCl, >99.7%), triethylamine (Et<sub>3</sub>N, 99.5%), 1,1'-carbonyldiimidazole (CDI, 97%), 1,8-diazabicyclo[5.4.0]undec-7-ene (DBU, 98%), 4-(methylamino)pyridine (DMAP, 99%), 4-cyano-4 (phenylcarbonothioylthio) pentanoic acid (CTA, 97%), 4-aminobenzyl alcohol (ABA, 98%), 4-hydroxybenzaldehyde (HBA, 98%), aniline (>99.5%), potassium carbonate (K<sub>2</sub>CO<sub>3</sub>, >99%), methacryloyl chloride (> 97%), benzaldehyde (>99%), methoxy-terminated poly(ethylene glycol) (PEG, MW = 5000 g/mol, dried by an azeotropic distillation with anhydrous toluene prior to use), methyl methacrylate (MMA, purified by passing through a column filled with basic aluminum oxide to remove the inhibitor), and 2,2'-azobis(2-methylpropionitrile) (AIBN, 98%) from Sigma-Aldrich and 1-ethyl-3-(3 dimethylaminopropyl) carbodiimide•HCl (EDC) from Matrix Innovation were purchased and used as received. A carbonyl imidazole-bearing methacrylate (CIMA)<sup>179</sup> and a CTA-functionalized PEG (PEG-RAFT)<sup>187</sup> were synthesized as described elsewhere.

#### 3.2.3. Synthesis of Small Molecule Methacrylates and Precursors

Small molecule methacrylates and precursors were synthesized and purified by standard methods.

M2. In the first step to synthesize A1, MsCl (2.4 g, 46 mmol) was added dropwise to a solution containing HEMA (5.0 g, 38 mmol) and Et<sub>3</sub>N (10.9 g, 57 mmol) dissolved in anhydrous THF (100 mL) in an ice-bath for 20 min. The resulting mixture was stirred at room temperature for 6 hrs. After the removal of THF by vacuum filtration, ethyl acetate (50 mL) was added, and the resulting mixture was washed with 0.1 M aqueous HCl solution three times, further washed with brine and deionized water (150 mL) three times, and then dried over sodium sulfate. After solvents were removed by rotary evaporation, the product was dried in a vacuum oven for 12 hrs. Colorless oil with yield = 7.1 g (90%);  $R_f = 0.2$  on silica (3/2 v/v hexane/ethyl acetate).

In the second step to synthesize A2, K<sub>2</sub>CO<sub>3</sub> (0.66 g, 4.8 mmol) was added to a clear solution containing HBA (0.48 g, 3 mmol) and anhydrous DMF (13 mL) placed in 80 °C in an oil bath

for 20 mins under nitrogen atmosphere. The resulting mixture was mixed with A1 (1 g, 4.8 mmol) and stirred vigorously for 18 hrs at room temperature. It then was diluted with ethyl acetate, washed with brine and deionized water (50 mL) three times, and then dried over sodium sulfate. After the removal of the solvent by rotary evaporator, the product was dried in vacuum oven for 13 hrs. Pale-white residue with yield= 0.7 g (65%);  $R_f$  = 0.59 on silica (3/2 v/v hexane/ethyl acetate).

In the last step to synthesize M2, aniline (1.95 g, 21 mmol) was added dropwise to a solution containing A2 (4.94 g, 21 mmol) dissolved in ethanol (EtOH, 45 mL). The resulting mixture was stirred under reflux for 18 hrs. After the removal of the solvent by rotary evaporation the product was crystallized from hexane at -20 °C. Residual solvent was removed by filtration and the resulting product was dried in vacuum oven for 13 hrs. Yellow residue with yield = 5.8 g (90%);  $R_f = 0.71$  on Et<sub>3</sub>N treated silica (3/2 v/v hexane/ethyl acetate).

*M1*. In the first step to synthesize A3, aniline (5 g, 53 mmol) was added dropwise to a solution of HBA (6.47 g, 53 mmol) dissolved in EtOH (100 mL). After the addition of anhydrous MgSO<sub>4</sub> (1 g), the resulting mixture was stirred under reflux for 48 hrs. Solvents were removed by rotary evaporation and the resulting solution was filtered through silica plug to remove MgSO<sub>4</sub>. The product was further recrystallized from acetone at -20 °C. Yellow residue with yield = 7.3 g (70%);  $R_f = 0.23$  on silica (10/1 v/v hexane/ethyl acetate).

In the second step to synthesize M1, methacryloyl chloride (0.25 mL, 3 mmol) was added dropwise into an organic solution containing A3 (0.5 g, 2.5 mmol) and Et<sub>3</sub>N (1.73 ml, 12.5 mmol) in anhydrous THF (25 mL) in an ice-bath under stirring for 20 hrs. After the removal of the solvent by rotary evaporation, the mixture was diluted with ethyl acetate, washed with brine and distilled water (150 mL) four times, and dried over sodium sulfate. The residual solvent was removed by rotary evaporation and the product was purified by silica gel column chromatography using Et<sub>3</sub>N treated silica and hexane/ethyl acetate (50/1 v/v). The product was collected as the first of the total two bands off a silica gel column and then dried in vacuum oven for 24 hrs. White residue with yield = 0.4 g (61%);  $R_f = 0.42$  on (9/1v/v hexane/ethyl acetate).

**BA-I**. ABA (1.5 g, 12.2 mmol) and benzaldehyde (1.29 g, 12.2 mmol) were dissolved in EtOH (25 mL) and mixed with sodium sulfate (1 g) under stirring at room temperature for 12

hrs. The resulting mixture was filtered under vacuum to remove solids. Solvent was evaporated by rotary evaporation to yield yellow colored solid: Yield = 2.2 g (70%);  $R_f = 0.2 \text{ on } Et_3N$  treated silica (5/2 v/v hexane/ethyl acetate).

*Et-CI*. EtOH (0.2 g, 4.34 mmol) was added dropwise to a clear solution of CDI (0.84 g, 5.2 mmol) in anhydrous DCM (20 mL) in an ice-bath for 20 min under stirring. After being stirred for 18 hrs at room temperature, the resulting mixture was washed with deionized water (100 mL) three times and then dried over sodium sulfate. Solvents were removed by rotary evaporation and the product was dried by vacuum oven for 12 hrs. Colorless oil with yield = 0.46 g (76%);  $R_f = 0.2$  on silica (5/1 v/v hexane/ethyl acetate).

# 3.2.4. Synthesis of Block Copolymers

General procedure for RAFT polymerization. Methacrylate monomer, RAFT mediator, and AIBN were dissolved in solvent in a 10 mL Schlenk flask. The mixture was purged with nitrogen for 45 min and then placed in an oil bath pre-heated at 70 °C for the desired time. The polymerization was stopped by cooling to room temperature in an ice bath. For purification, assynthesized polymers were precipitated from cold hexane (excess) three times. The precipitates were dried in a vacuum oven set at 40 °C for 24 hrs.

M2 (1 g, 3.2 mmol), PEG-RAFT (0.34 g, 64 μmol), and AIBN (3.2 mg, 19 μmol) in anisole (1.8 mL) for an attempt to synthesize PEG-b-PCoIm-1; MMA (0.3 g, 2.9 mmol), CTA (8.4 mg, 29 μmol), and AIBN (2.3 mg, 11 μmol) with and without A3 (0.59 g, 2.9 mmol) in DMSO-d<sub>6</sub> (0.5 mL) for control experiments; and CIMA (1 g, 4.5 mmol), PEG-RAFT (0.24 g, 45.6 μmol), AIBN (3.7 mg, 22.8 μmol) in anisole (1.7 mL) for the synthesis of PEG-b-PCIMA were used.

General procedure for CDI-mediated Coupling Reaction. Alcohol-precursor was added to a solution containing CI-precursor and DBU dissolved in DCM under stirring at room temperature for 24 hrs. The resulting mixture was washed with deionized water (30 mL) three times and then dried over sodium sulfate. After the removal of solvents by rotary evaporation, the product was dried by vacuum oven for 12 hrs.

For control experiments, Et-CI (0.12 g, 0.85 mmol), A3 (0.16 g, 0.85 mmol), and DBU (26 mg, 0.17 mmol) in DCM (4 mL) to synthesize ET1; Et-CI (0.3 g, 2.14 mmol), benzyl alcohol (0.23 g, 2.14 mmol), and DBU (65 mg, 0.42 mmol) in DCM (5 mL) to ET2; and Et-CI (0.39 g,

2.79 mmol), BA-I (0.59 g, 2.79 mmol), and DBU (85 mg, 0.55  $\mu$ mol) in DCM (7 mL) to ET3 were used.

A3 (0.37 g, 1.89 mmol), PEG-b-PCIMA (0.1 g, 2.8 μmol), and DBU (11 mg, 75 μmol) in DCM (2 mL) for an attempt to synthesize PEG-b-PCoIM BCP and BA-I (1.45 g, 6.9 mmol), PEG-b-PCIMA (0.68 g, 32.5 μmol), and DBU (69.3 mg, 0.45 mmol) in DCM (20 mL) for the synthesis of PEG-b-PCoIm-2 were used. PEG-b-PCoIm-2 was purified by precipitation from cold diethyl ether before being dried.

# 3.2.5. Aqueous Micellization through Dialysis Method

An organic solution consisting of P-Im (6 mg) in DMF (2 mL) was added to deionized water (10 mL) at a rate of 60 mL/hr using a syringe pump under magnetic stirring at room temperature. The resulting mixture was placed in a dialysis tubing (MWCO = 11-13 kDa) for dialysis over distilled water (1 L) for 24 hrs. The resulting mixture was filtered through a 0.45  $\mu$ m PES membrane to remove any precipitate, resulting in P-Im micelle solution of 0.5 mg/mL.

# 3.2.6. Studies of Acid and Light-Responsive Degradation

*Acid-responsive Degradation of Aqueous Nanoassemblies*. Aliquots of aqueous nanoassemblies (2 mL, 0.5 mg/ml) were mixed with aqueous sodium acetate buffer (0.2 M, pH 5.0, 3 mL) under stirring at room temperature. Samples were taken at given times for DLS and TEM analysis.

Investigation of Acid-Triggered Degradation of Conjugated Imines Using <sup>1</sup>H NMR spectroscopy. Aqueous stock solutions of KH<sub>2</sub>PO<sub>4</sub> (0.2 M) and K<sub>2</sub>HPO<sub>4</sub> (0.2 M) in D<sub>2</sub>O were prepared and mixed at different volume ratios to prepare phosphate buffered (PB) solutions in D<sub>2</sub>O (0.2 M) at pD = 5, 6.8, and 7.4. Their pH values were measured using a glass electrode pH meter standardized with aqueous buffer solutions at pH = 4, 6 and 10. The equation pD = pH (measured) + 0.41 was used to determine pD values. M2 (6.2 mg) dissolved in CD<sub>3</sub>CN (0.6 mL) was mixed with the as-prepared PB solutions in D<sub>2</sub>O (0.2 mL, 0.2 M) at pD = 5, 6.8 and 7.4. To study the hydrolysis kinetics of P-Im block copolymer, the purified PEG-b-PCoIm-2 (9 mg) dissolved in DMSO-d<sub>6</sub> (0.5 mL) was mixed with a solution of acetic acid in DMSO-d<sub>6</sub> (0.15 mL) at pH = 5 and pD = 5.4.

Light-Responsive Degradation of Aqueous Nanoassemblies. Aqueous P-Im nanoassemblies (3 mL) in a 1 cm wide quartz cuvette were exposed to 340 nm light at a distance of 5 cm from light source. Aliquots were taken at given time intervals for DLS and TEM analysis.

Investigation of Light-Response of Conjugated Imines Using UV/Vis Spectroscopy. A solution of M1 in DMSO (3 mL, 30  $\mu$ M) in a 1 cm wide quartz cuvette was placed under the irradiation of light at 340 nm in the distance of 5 cm from light source. Its absorbances were monitored at given time intervals using UV/Vis spectrometer. A similar procedure was followed with PEG-b-PCoIm-2 dissolved in DMSO (3 mL, 0.42  $\mu$ M) at both 340 nm and 420 nm.

#### 3.3. Results and Discussion

# 3.3.1. Synthesis of Conjugated Benzoic Imine-Bearing Methacrylates

Figure 3.1 depicts our approach to synthesize novel methacrylate derivatives of conjugated benzoic imine groups with (M2) and without (M1) an ethylene oxide spacer between methacrylate and conjugated benzoic imine groups.

Figure 3.1. Schematic illustration of two approaches to synthesize M2 (a) and M1 (b).

As illustrated in Figure 3.1a, M2 was synthesized with three steps. The first step was the activation of OH group in HEMA with MsCl in the presence of Et<sub>3</sub>N as a base. This reaction allowed for the formation of HEMA-MS adduct (A1) at an isolated yield as high as 90%. The formed A1 then reacted with HBA in the presence of K<sub>2</sub>CO<sub>3</sub>, yielding A2 precursor bearing a terminal aldehyde group at 65% yield through the formation of a carbonate bond. The last step was the reaction of the purified A2 with aniline to yield M2 through the formation of a conjugated benzoic imine bond. All three steps appeared to be straightforward, with no need of column chromatography for purification and isolation of the products. Each step was followed by <sup>1</sup>H NMR analysis (see Figures S3.1-S3.2 for precursors A1 and A2 and Figure 3.2 for M2). Typically, <sup>1</sup>H NMR of M2 shows the appearance of the new peak at 8.5 ppm being equivalent to an imine proton and disappearance of the peak at 9.8 ppm corresponding to aldehyde proton shown in <sup>1</sup>H NMR of A2 precursor. This result confirms the successful synthesis of M2 with conjugated benzoic imine bonds being intact.

M1 was synthesized with two steps (Figure 3.1b). The first step was the reaction of aniline with HBA (1.1 mole equivalent excess) in EtOH under a reflux condition at 90 °C. The formed conjugated benzoic imine precursor (A3) was purified by recrystallization from acetone at 70% yield. <sup>1</sup>H NMR in Figure S3.3 shows the presence of imine bond at 8.6 ppm, the integral of which corresponds to the quantitative conversion. The next step was the reaction of the purified A3 with methacryloyl chloride to yield M1 with no evidence of the undesired cleavage of imine bond, confirmed by <sup>1</sup>H NMR analysis (Figure 3.2).

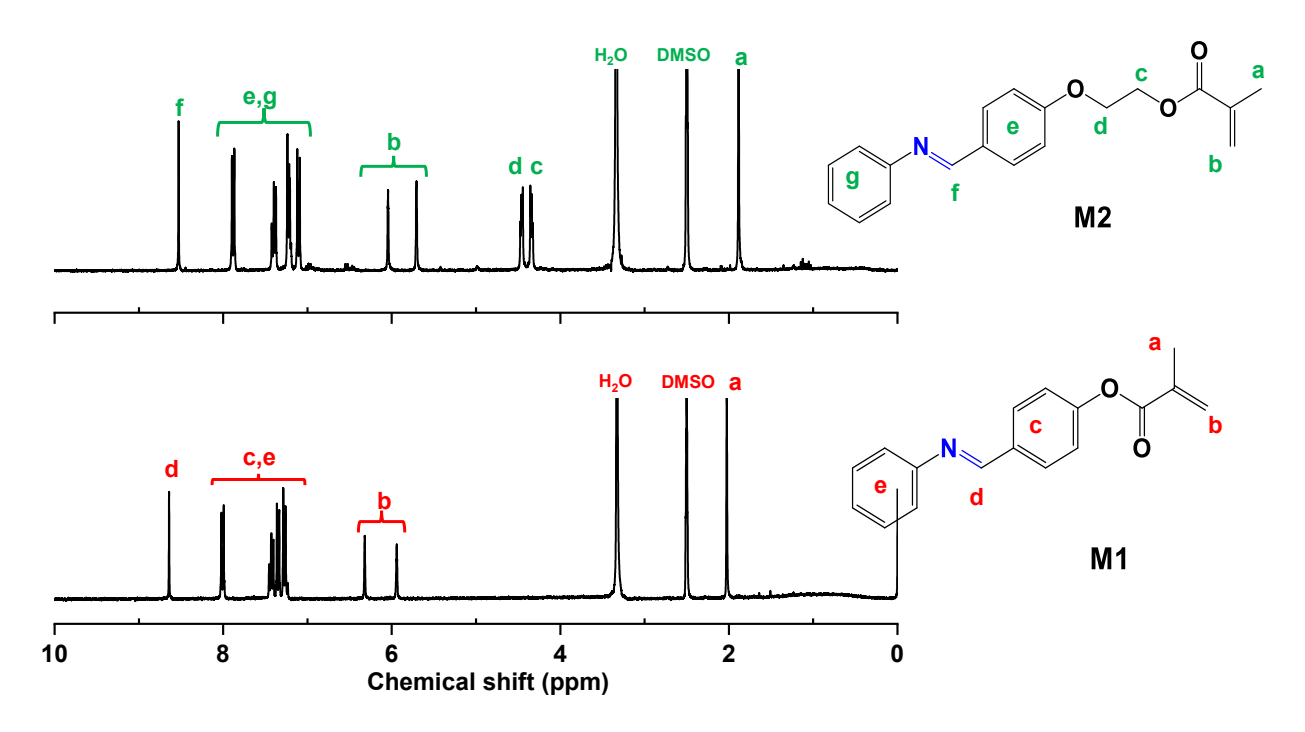


Figure 3.2. <sup>1</sup>H NMR spectra of M1 and M2 in DMSO-d<sub>6</sub>.

# 3.3.2. Direct RAFT Polymerization in Attempt to Synthesize PEG-b-PCoIm BCPs

Given our successful synthesis and structural analysis of conjugated benzoic imine-bearing methacrylates, we attempted to synthesize an amphiphilic block copolymer consisting of a hydrophilic PEG block and a hydrophobic methacrylate block having pendant conjugated benzoic imine bonds (called, PEG-b-PCoIm). A PEG-RAFT mediator was synthesized by a facile EDC-mediated coupling reaction of CTA RAFT agent with PEG as described in our previous publication.<sup>187</sup> Its structure was confirmed by <sup>1</sup>H NMR (Figure S3.4). As depicted in Figure 3.3, RAFT polymerization was explored with a choice of M2 in the presence of PEG-RAFT. The polymerization was initiated with AIBN, an azo-type initiator, at 70 °C in anisole under the conditions of [M2]<sub>0</sub>/[PEG-RAFT]<sub>0</sub>/[AIBN]<sub>0</sub> = 50/1/0.4 and M2/anisole = 0.6/1 wt/wt. After 4 hrs, <sup>1</sup>H NMR spectrum of the polymerization mixture did not show the characteristic peaks at 0.7-1.2 ppm, which correspond to methyl protons on the backbones of polymethacrylates (indicated with a dotted circle in Figure S3.5). This suggests that no polymerization occurred under the conditions. Our further efforts with increase of the amount of AIBN, polymerization temperature and time could not improve polymerization kinetics.

**Figure 3.3**. Our attempt to synthesize PEG-b-PCoIm-1 by direct RAFT polymerization of M2 in the presence of a PEG-RAFT macro-mediator, initiated with AIBN. Conditions:  $[M2]_0/[PEG-RAFT]_0/[AIBN]_0 = 50/1/0.4$  and M2/anisole = 0.6/1 wt/wt; 70 °C.

We have hypothesized that radical polymerization could be interfered with the presence of a conjugated benzoic imines. To test our hypothesis, RAFT polymerization of MMA (a common methacrylate) was conducted with and without A3 precursor (a conjugated benzoic imine compound) in DMSO-d<sub>6</sub> at 70 °C under the conditions of [MMA]<sub>0</sub>/[CTA]<sub>0</sub>/[AIBN]<sub>0</sub> = 100/1/0.4. After 4.5 hrs, conversion reached to 50% in the absence of A3 (Figure S3.6), while no conversion was observed in the presence of A3 even after 20 hrs (Figure S3.7). These results confirm that the presence of conjugated benzoic imine interferes with radical-driven polymerization.

# 3.3.3. Post-polymerization Modification to Synthesize PEG-PCoIm BCPs

Given unsuccess with direct RAFT polymerization for M2 bearing conjugated benzoic imine, a post-polymerization modification method was explored. CDI-mediated coupling reaction has been known to be facile and quantitative in mild conditions. Figure 3.4 illustrates our approach utilizing a combination of RAFT polymerization with CDI-mediated coupling reaction with an OH-bearing conjugated benzoic imine precursor.

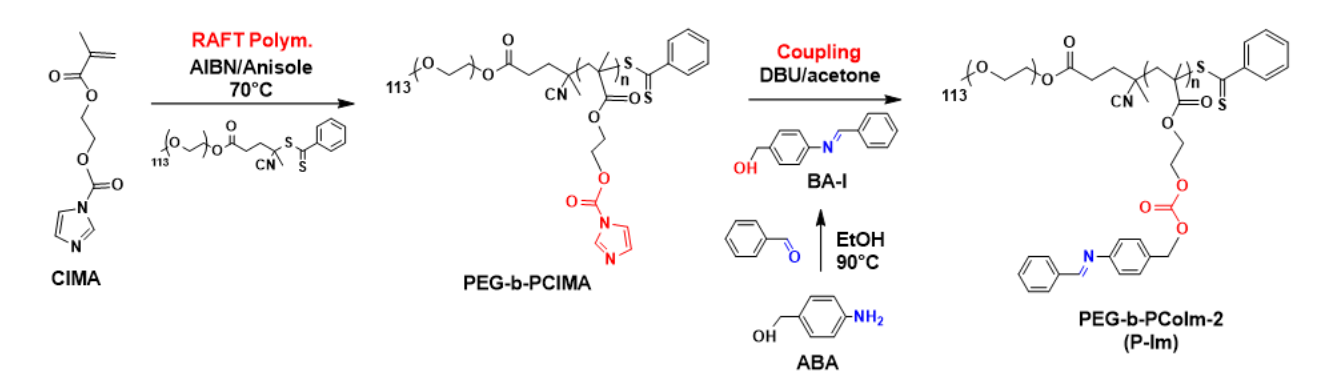


**Figure 3.4**. Our approach to post-polymerization modification exploring RAFT polymerization and CDI-induced coupling reaction, including the synthesis of a BA-I precursor bearing a conjugated benzoic imine, to synthesize well-defined PEG-b-PCoIm-2 (P-Im) block copolymers.

Our approach began with the synthesis of well-defined PEG-based block copolymers bearing pendant imidazole groups (PEG-b-PCIMA) as the first step. RAFT polymerization was employed for CIMA in the presence of PEG-RAFT macro-mediator, initiated with AIBN in anisole at 70 °C with the conditions of [CIMA]<sub>0</sub>/[PEG-RAFT]<sub>0</sub>/[AIBN]<sub>0</sub> = 100/1/0.5. The synthesized polymers were purified by precipitating in hexane to remove unreacted CIMA at 70% monomer conversion. <sup>1</sup>H NMR spectrum in Figure 3.5a shows the presence of PEG at 3.6 ppm and pendant imidazole rings at 7.0-8.2 ppm. Their integral ratio with the DP of PEG = 113 allows us to determine the DP of PCIMA block to be 67, thus forming PEG<sub>113</sub>-b-PCIMA<sub>67</sub>. Importantly, our <sup>1</sup>H NMR analysis confirms no significant cleavage of CI groups in the PCIMA block under our RAFT condition at 70 °C.

Next, a new benzyl alcohol precursor bearing a conjugated benzoic imine (BA-I) was designed and synthesized. As depicted in Figure 3.4, ABA reacted with benzaldehyde at a stoichiometric balance in EtOH at room temperature, yielding as high as 70%. <sup>1</sup>H NMR spectrum in Figure 3.5b shows the peak at 8.7 ppm corresponding to imine proton, 4.5 ppm to benzyl methylene protons, and 7-8 ppm to aromatic protons. Their integral ratio is quantitative.

Given our synthesis of PEG-b-PCIMA and BA-I, their CDI-mediated coupling reaction was conducted in the presence of DBU, a base catalyst, at room temperature. After purification by precipitation from diethyl ether three times, <sup>1</sup>H NMR spectrum of Figure 3.5c shows the presence of aromatic conjugated benzoic imine moieties at 8.5 ppm, PEG at 3.5 ppm, polymethacrylate at 0.7-1.2 ppm. More importantly, the new peak at 5.2 ppm corresponds to

benzyl protons adjacent to carbonyl ester. Further, its integral is quantitative to other characteristic peaks, suggesting high efficiency of coupling reaction. Our <sup>1</sup>H NMR analysis firmly confirms the synthesis of well-defined PEG-b-PCoIm-2 (called P-Im). Further, P-Im was characterized for its thermal property using DSC. As seen in Figure S3.8, the copolymer shows a single transition at 23.1 °C.

The use of DBU, instead of butylamine, in excess was reported for aminolysis to cleave phenylthiocarbonylthio RAFT species to the corresponding thiol groups. An interesting question is whether aminolysis can occur during the CI-mediated coupling reaction of PEG-b-PCIMA with BA-I, catalyzed with DBU. Promisingly, our <sup>1</sup>H NMR analysis did not show the significant cleavage of phenylthiocarbonylthio RAFT species in P-Im copolymers. This is plausibly attributed to the usage of DBU in less excess and the CI-mediated coupling reaction being more efficient over aminolysis.

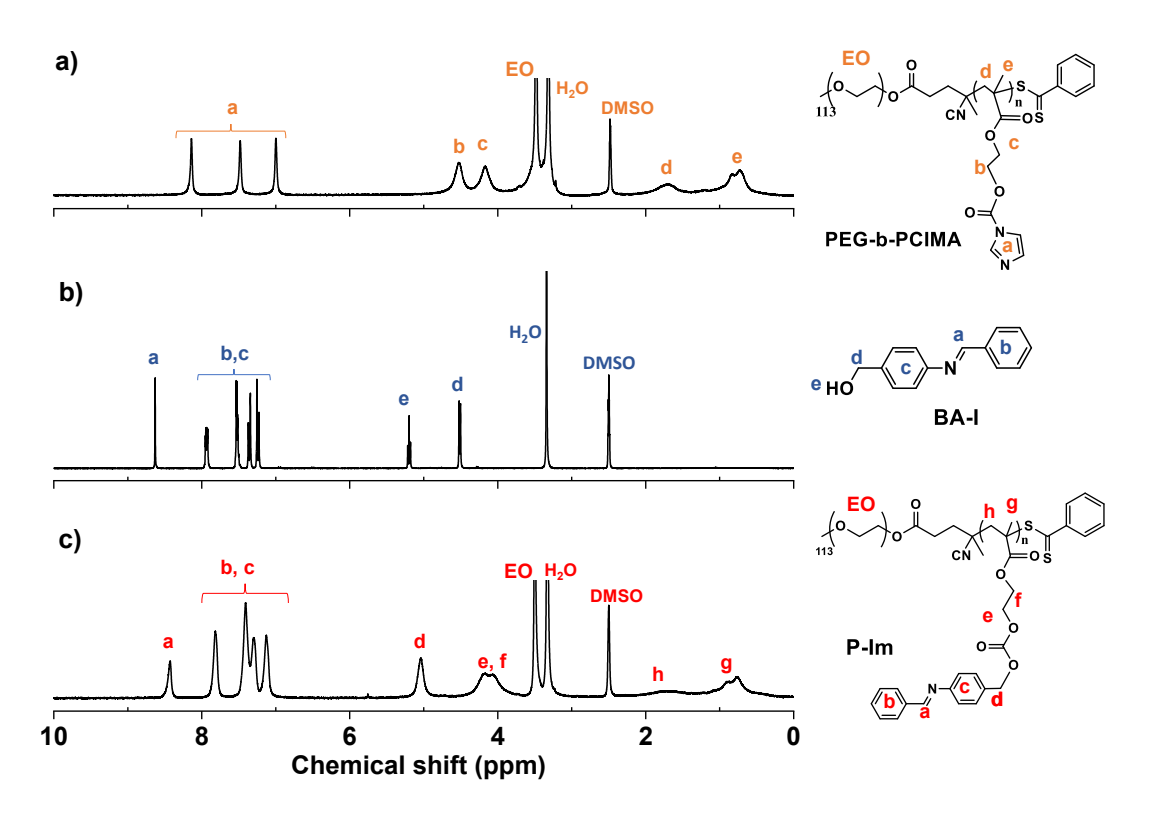


**Figure 3.5**. Overlaid <sup>1</sup>H NMR spectra of PEG-b-PCIMA (a), BA-I (b), and P-Im (c) in DMSO-d<sub>6</sub>.

In our further experiments, we found the notable result that CDI coupling reaction is specific to the types of alcohols. We initially conducted the CDI coupling reaction for PEG-PCIMA with A3, a phenol-type conjugated benzoic imine (see its chemical structure in Figure 3.1b) under the similar condition. Interestingly, our NMR analysis shows the occurrence of no reaction (Figure S3.9). To get an insight, we conducted control experiments with a small molecule CI precursor. As illustrated in Figure 3.6, EtOH was activated with CDI. After the confirmation by <sup>1</sup>H NMR analysis (Figure S3.10), the formed Et-CI reacted in the presence of DBU, a strong base, with various types of alcohols, including A3 (a phenol), benzyl alcohol, and BA-I (a benzyl alcohol derivative bearing a conjugated benzoic imine). Our <sup>1</sup>H NMR analysis confirms no reaction with A3, while quantitative conversions with other alcohols (Figure S3.11-S3.13). Our results are consistent with the reports in literature that phenol-type alcohols slow down CDI-induced coupling reaction with low yield, compared with benzyl-type alcohols.<sup>190, 191</sup>

**Figure 3.6**. Scheme for CDI-mediated coupling reaction of EtOH with A3 (a phenol), benzyl alcohol, and BA-I (a benzyl alcohol derivative).

# 3.3.4. UV/Vis Absorption Characteristics of Conjugated Benzoic Imines

Figure 3.7a compares the UV/vis absorption characteristics of M2 bearing a conjugated benzoic imine moiety with M-HX bearing a benzoic imine bond in DMF. Their extinction coefficients were determined from their UV spectra recorded over their various concentrations in DMF (Figure S3.14 for M2, S3.15 for M1, and S3.16 for M-HX). M-HX was synthesized as reported in our publication and its chemical structure is shown in the inset of Figure 3.7a.

M1 had its absorption up to 400 nm with two bands for aromatic imines: a strong band at 270 nm and a less intense band at 315 nm. Its extinction coefficient was determined to be 25,700  $M^{-1}$  cm<sup>-1</sup> at 285 nm in DMSO. Similarly, M2 had absorption up to 400 nm with a strong absorption at 285 nm at which its extinction coefficient was 20,100  $M^{-1}$  cm<sup>-1</sup> and a less intense band at 320 nm in DMF. Furthermore, BA-I bearing similar conjugated benzoic imine moieties had its absorption up to 400 nm with the strong band at 270 nm (extinction coefficient of 40,420  $M^{-1}$  cm<sup>-1</sup>, see Figure S3.17) and a less intense band at 320 nm in DMSO. According to literature, <sup>50, 192</sup> these bands are characteristic to aromatic imines, corresponding to  $\sigma \rightarrow \sigma^*$  transition for the strong absorption and  $\pi \rightarrow \pi^*$  transitions for the less intense band. In contrast, M-HX had its absorption up to 300 nm with its maximum absorption at 255 nm at which its extinction coefficient was 2,200  $M^{-1}$  cm<sup>-1</sup> in DMF, with no evidence of absorption band at >300 nm. These results clearly confirm that the UV absorption is shifted to longer wavelength with more conjugation of the benzoic imine bonds.

Promisingly, P-Im block copolymer had its UV/vis absorption characteristics similar to BA-I precursor, suggesting that the chemical structure of conjugated benzoic imine moieties was not changed during modification process (Figure 3.7b).

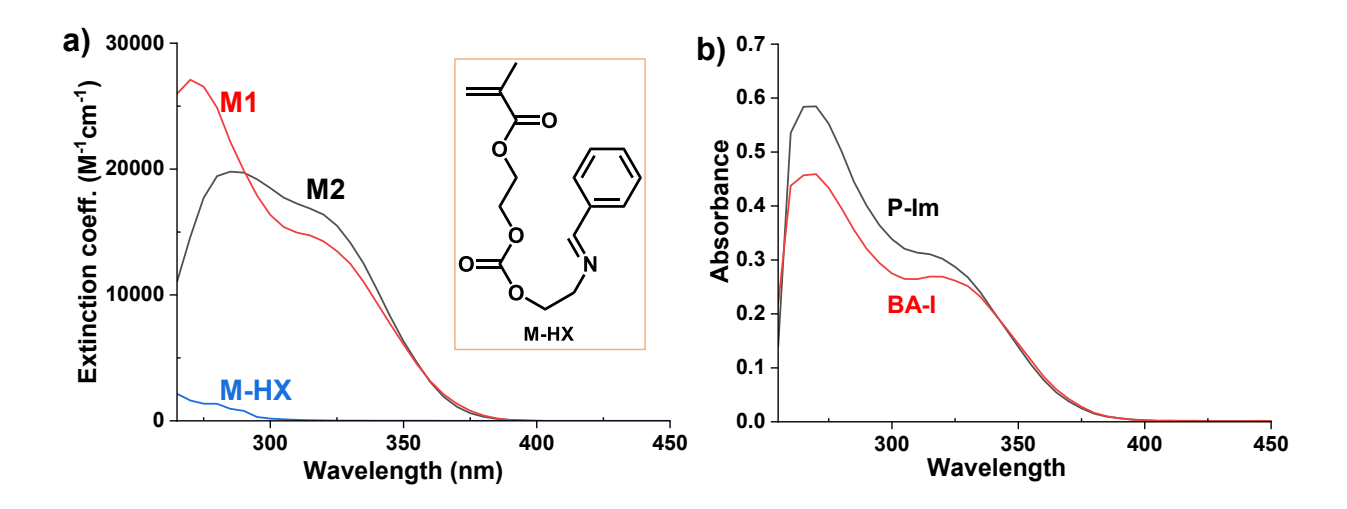


**Figure 3.7**. UV/Vis spectra of M2 and M1, compared with M-HX (a) as well as BA-I at 11  $\mu$ M and P-Im at 0.29  $\mu$ M (b) in DMF.

## 3.3.5. Aqueous Micellization

The synthesized P-Im is an amphiphilic block copolymer consisting of a hydrophilic PEG block and a hydrophobic methacrylate block bearing conjugated benzoic imine pendants. It self-assembles in aqueous solution to form colloidally stable micelles (called nanoassemblies) with hydrophobic cores having acid/light-responsive benzoic imine linages, surrounded with PEG corona. Here, aqueous micellization was examined using a dialysis method to fabricate aqueous dispersion of nanoassemblies at 0.6 mg/mL (Figure 3.8). DLS analysis confirms that the nanoassemblies had their hydrodynamic diameter by intensity to be 153.8 nm on average. TEM analysis confirms that the nanoassemblies in dried state are spherical with their average diameter to be  $69 \pm 32 \text{ nm}$ .

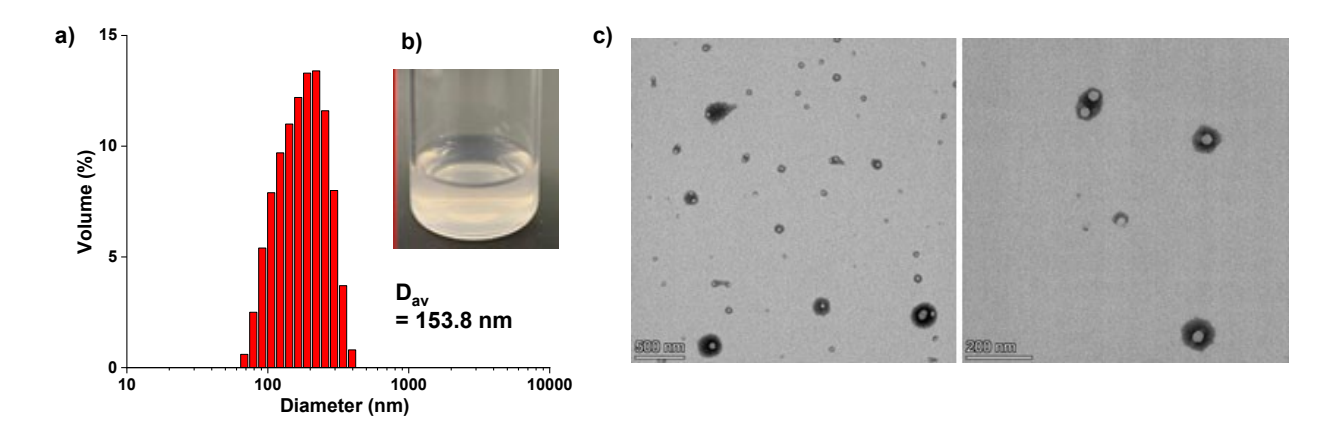


**Figure 3.8**. DLS diagram (a), digital image (b), and TEM images with different magnifications (c) of aqueous nanoassemblies self-assembled from well-defined P-Im in aqueous solution.

# 3.3.6. Studies of Acid-Responsive Degradation and Disassembly

The formed nanoassemblies contain conjugated benzoic imine linkages in hydrophobic cores. Their acid-responsive degradation was investigated using DLS and TEM techniques. Aliquots of aqueous nanoassemblies were incubated in acidic buffer at pH = 5.0. DLS diagrams show that their size distribution became multimodal with the occurrence of large aggregation over incubation time (Figure 3.9a). Interestingly, no population of aggregates was presented in the DLS diagram after 20 hr incubation, which could be because large aggregates were precipitated. TEM images also show the presence of large aggregates (Figure 3.9b). These changes in sizes and size distributions could be attributed to the destabilization (or disintegration) of nanoassemblies.

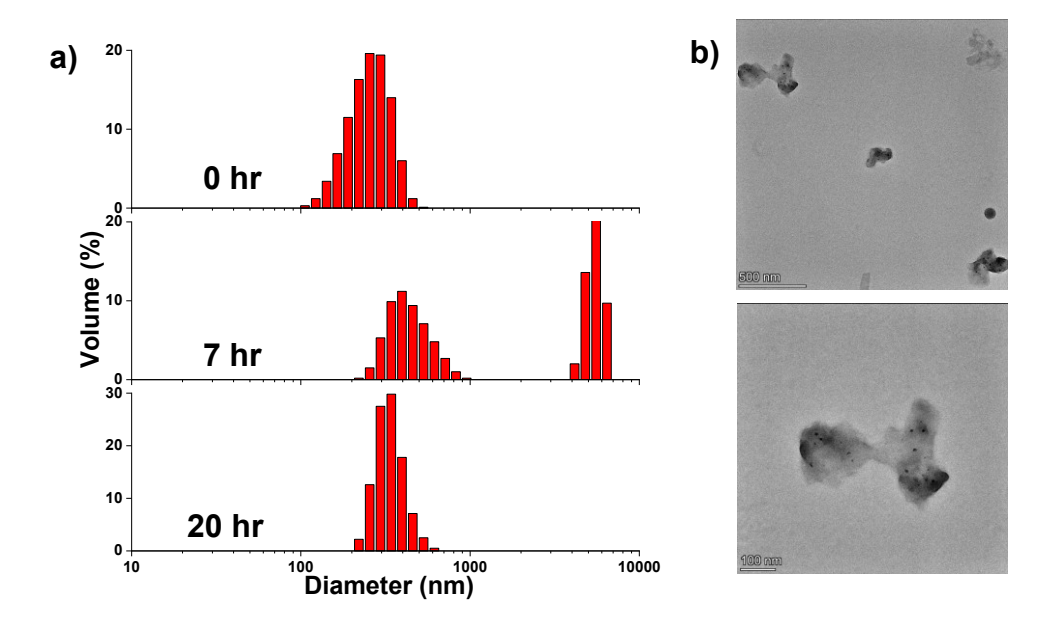


**Figure 3.9**. Evolution of DLS diagrams (a) and TEM images with different magnification (b) of aqueous nanoassemblies of P-Im incubated at pH = 5.0.

Acid-catalyzed hydrolysis of conjugated benzoic imine bonds were studied in organic homogenous solution using <sup>1</sup>H NMR spectroscopy. First, M2 was chosen to examine its hydrolysis in a mixture of 3/1 v/v CD<sub>3</sub>CN/D<sub>2</sub>O at different acidic pDs of 5.0 (endo/lysosomal pH), 6.8 (tumoral pH), and 7.4 (physiological pH). Their <sup>1</sup>H NMR spectra over incubation time are recorded as shown in Figure 3.10a for pD = 5.0 as a typical example as well as Figure S3.18 for pD = 6.8 and S3.19 for pD = 7.4. The peak at 8.6 ppm corresponding to imine proton (a) decreased, while the new peak at 9.2 ppm corresponding to aldehyde proton (b) increased. Such change is caused from the cleavage of imine bonds to the corresponding aldehyde and amine precursors through acid-catalyzed hydrolysis (Figure 3.10b). Their integral ratios were used to determine the %degradation of conjugated benzoic imine bonds over incubation time at different pDs. As seen in Figure 3.10c, percentage degradation increased over incubation time at all three pDs. As expected, %degradation turned out to be faster at lower acidic pDs. For example, it reached as high as 82% within 10 min at pD = 5.0. At pD = 6.5, it gradually increased and reached 90% (similar maximum at pD = 5.0) in 90 min. However, %degradation slowly increased to reach 30% in 80 min at pD = 7.4.

Given the results with M2, P-Im block copolymer was further examined for acid-catalyzed hydrolysis. Because the copolymer did not turn to be dissolved in CD<sub>3</sub>CN/D<sub>2</sub>O mixture, <sup>1</sup>H NMR analysis of its hydrolysis was conducted in DMSO-d<sub>6</sub> mixed with a trace amount of acetic acid at pH = 5.0. Similar to M2, <sup>1</sup>H NMR spectra of P-Im in Figure 3.10d shows the appearance and increase of the peak at 10 ppm corresponding to aldehyde proton while the decrease of the peak at 8.6 ppm corresponding to imine proton, confirming the cleavage of benzoic imine bonds in the copolymer in acidic condition (Figure 3.10e). Hydrolysis gradually increased over incubation time, reaching 80% in 110 min, which turned to be slower than M2 at the same pH (Figure 3.10f). Such difference could be attributed to the larger size of P-Im compared with M2 and also the use of different solvents (DMSO-d<sub>6</sub> vs CD<sub>3</sub>CN/D<sub>2</sub>O).

These results obtained from <sup>1</sup>H NMR analysis with M2 and P-Im confirm that the disintegration of nanoassembly in acidic environments is attributed to the cleavage of conjugated benzoic imine bonds through acid-catalyzed hydrolysis. Known acid-catalyzed E/Z isomerization of aromatic imines in non-aqueous solution such as dioxane, <sup>193</sup> a possible mechanism for acid-responsive disassembly of the nanoassemblies involves the isomerization of the conjugated imine bonds in the presence of acid. Despite this mechanism, the cleavage of the conjugated imine bonds through acid-catalyzed hydrolysis could be the main mechanism for the disintegration of the P-Im nanoassemblies in aqueous acidic solutions.

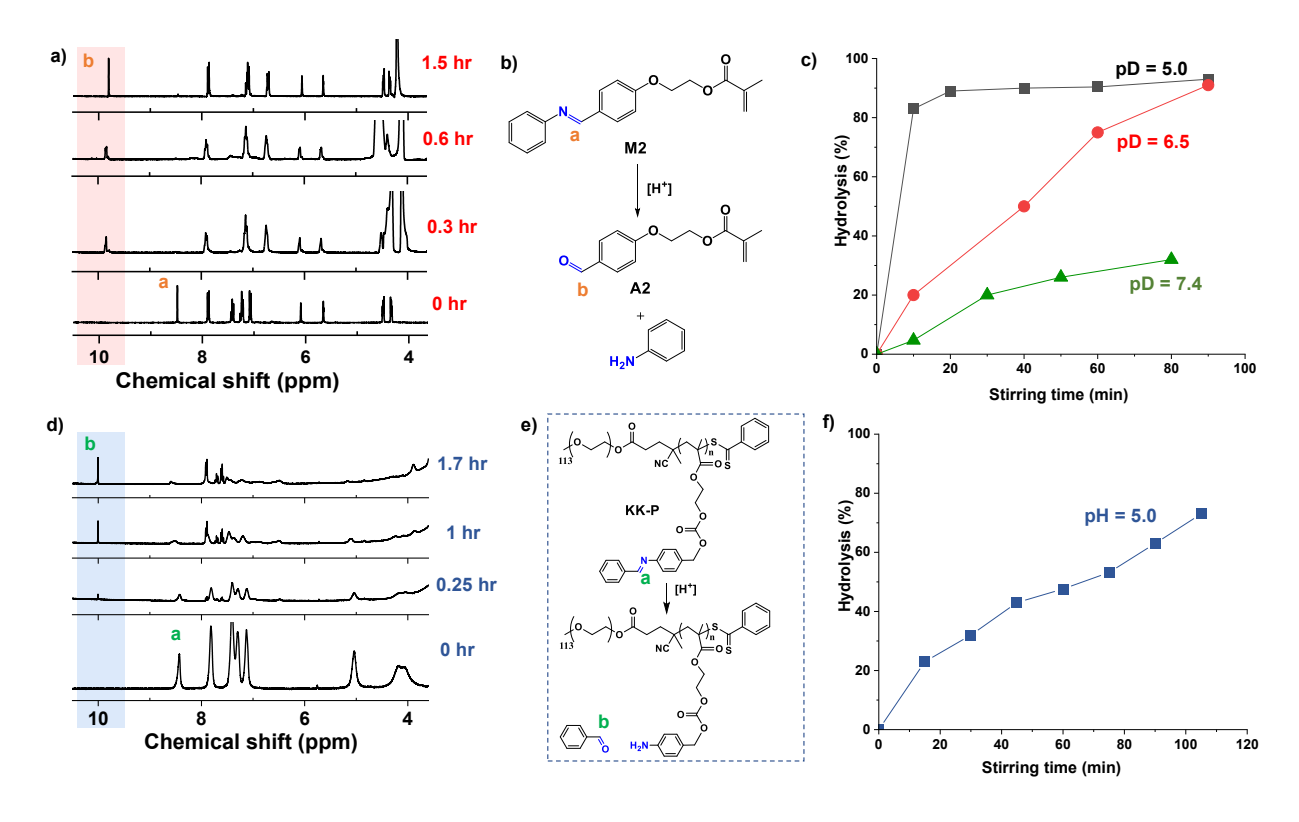


**Figure 3.10**. For M2, overlaid  $^1H$  NMR spectra over stirring time incubated at pD = 5.0 as a typical example (a), schematic illustration of acid-catalyzed hydrolysis of benzoic imine bond (b), and %hydrolysis over stirring time incubated at various acidic pDs = 5.0, 6.8, and 7.4 in a mixture of 3/1 v/v CD<sub>3</sub>CN/D<sub>2</sub>O (c). For P-Im block copolymer, overlaid  $^1H$  NMR spectra over stirring time (d), schematic illustration of acid-catalyzed hydrolysis of benzoic imine bond (e), and %hydrolysis over stirring time incubated in DMSO-d<sub>6</sub> containing a trace amount of acetic acid at pH = 5.0 (f).

#### 3.3.7. Preliminary Studies of Light-Response and Disassembly

Light response of nanoassemblies were examined upon the irradiation of light with a 340 nm band filter (Figure 3.11). DLS diagrams show that their size distributions became multimodal with not only large aggregates but also smaller species (diameter < 10 nm) over irradiation time. TEM images also confirmed that core-shell structure had disappeared and translated into irregular aggregation over irradiation time. These results suggest that the nanoassemblies could be disintegrated upon exposure to UV light.

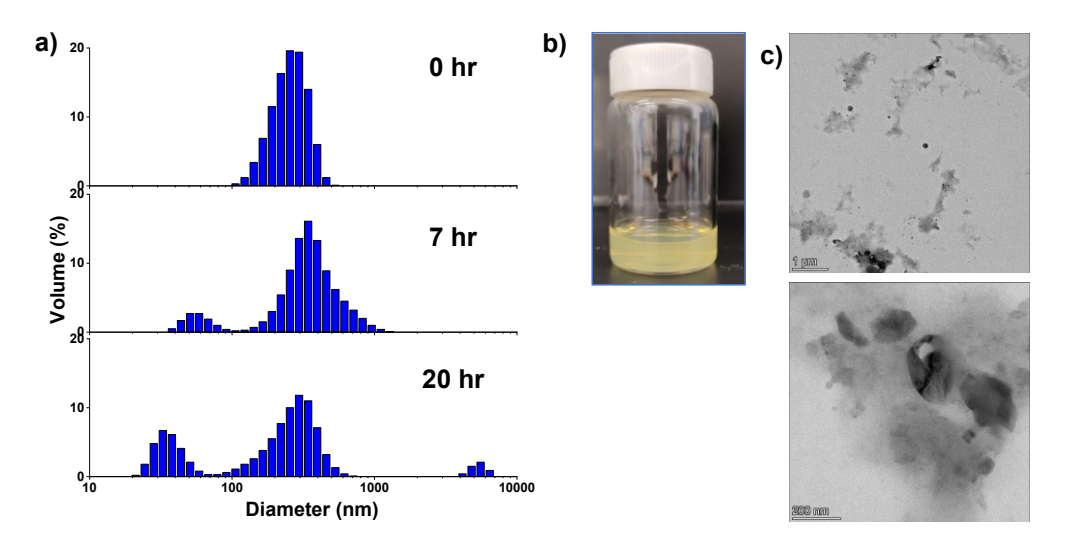


**Figure 3.11**. Evolution of DLS diagrams (a), digital image (b), and TEM images with different magnifications (c) of aqueous nanoassemblies of P-Im upon irradiation of light with a band filter of 340 nm.

Light response of conjugated benzoic imine bonds was further investigated using UV/Vis spectroscopy in organic solutions. With M1 dissolved in DMSO at 30 µM, its UV/Vis spectra were recorded as a function of irradiation time with a 340 nm band-filter. As seen in the inset of Figure 3.12a, the absorption decreased with an increasing irradiation time up to 5 hrs. Furthermore, the band at 270 nm was blue-shifted to ca. 255 nm and the band at 315 nm was redshifted to ca. 325 nm. Such changes are reported due to E/Z isomerization of aromatic imines.<sup>50</sup> For quantitative analysis, the absorbance at 270 nm was used to calculate the change in absorbance ( $\Delta A$ ). As seen in Figure 3.12a,  $\Delta A$  increased to as high as 90% in 5 hrs. Next, P-Im block copolymer was examined for photo-induced response in DMSO at 0.42 µM. Similar to small molecule M1, the absorption of copolymer decreased with irradiation time upon irradiation with 340 nm (UV) and further 420 nm (visible) band-filters (insets of Figure 3.12b and 3.12c). Upon irradiation at 340 nm, the copolymer reached  $\Delta A$  up to 50% in 5 hrs and 60% in 6 hrs, which is somewhat slower, compared with M1 that reached  $\Delta A$  up to 80% in 5 hrs. As expected, the change in absorption appeared to be slower at 420 nm, compared with 370 nm, which is attributed to the lower power. These results obtained from our UV/Vis spectroscopy analysis with M1 and P-Im could imply that the destabilization of nanoassemblies upon the exposure of

UV/Vis light are plausibly attributed to the change in UV absorption through photo-induced E/Z isomerization of conjugated imine bonds.

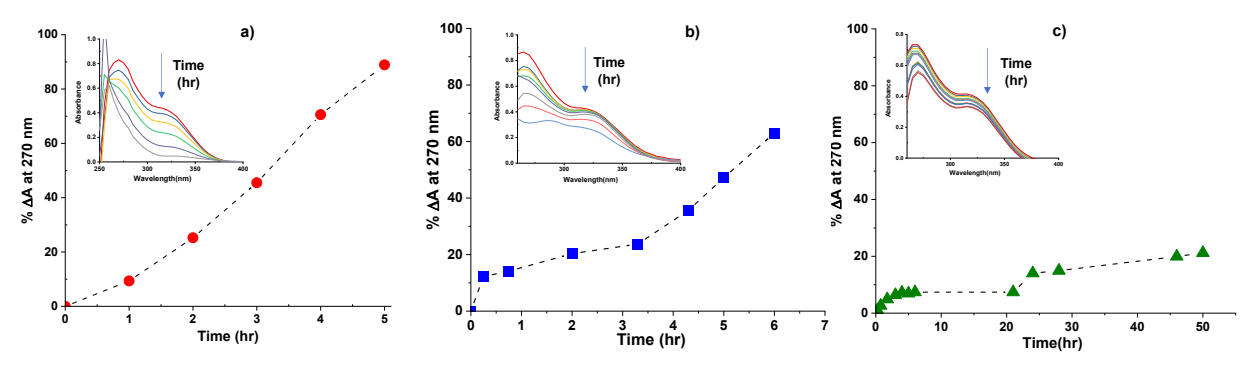


**Figure 3.12**. Degradation progress under UV-irradiation for M1 at 340 nm (a) and P-Im at 340 nm (b) and 420 nm (c) in DMSO. Insets show overlaid UV/vis spectra over irradiation time.

To further examine this phenomenon, <sup>1</sup>H NMR spectra of M2 dissolved in DMSO-d<sub>6</sub> at 32 mM were recorded as a function of irradiation time using 340 nm band-pass filter. As shown in Figure S3.20, no appreciable changes in chemical shifts, peak splitting, or integrals were observed under these conditions. This lack of detectable NMR evidence could be attributed to relatively high sample concentration and timescale of isomer interconversion, which may have broadened the signals and obscured subtle changes in coupling patterns or chemical shifts associated with E/Z isomerization by conventional 1D-<sup>1</sup>H NMR spectroscopy.

# 3.4. Conclusion

We have developed an effective approach that allows for the synthesis of a well-defined PEG-based ABP with conjugated benzoic imine pendants P-Im). The approach includes the RAFT polymerization of CIMA mediated with a PEG-RAFT, yielding well-defined PEG-b-PCIMA, followed by CDI-coupling reaction with BA-I precursor. Interestingly, an alternative approach exploring direct RAFT polymerization of M2 methacrylate bearing a conjugated benzoic imine group resulted in no polymerization. The plausible reason is the presence of conjugated benzoic imine moieties that interfere with radical polymerization mechanism, based on our control experiments. The formed P-Im self-assembled to form nanoassemblies with conjugated benzoic imine cores surrounded with PEG corona in water through aqueous self-assembly. The conjugated benzoic imine bonds in M2 and P-Im underwent acid-catalyzed

hydrolysis to corresponding amine moieties and benzaldehyde and their rates were strongly relied on acidic pH. More interestingly, the conjugated benzoic imine had its absorption up to 400 nm, confirmed by UV/vis spectroscopy analysis of P-Im, along with small molecules including M methacrylates and BA-I precursor. Upon the exposure of UV/Vis light, their absorptions decreased over time, which could be caused by the isomerization of conjugated benzoic imine bonds. Through the acid-catalyzed hydrolysis and photo-response of conjugated benzoic imine bonds, the P-Im based nanoassemblies degraded when being incubated in acidic pH and exposed to light, while they were colloidally stable in physiological condition, confirmed by DLS and TEM analysis.

# Chapter 4. Development of Dual Acid/Visible Light-Degradable Core-Crosslinked Nanogels with Extended Conjugate Aromatic Imines for Enhanced Drug Delivery

#### 4.1. Introduction

Development of well-defined amphiphilic block copolymers (ABPs) and their nanoassemblies has emerged as a promising platform for effective intracellular delivery of anticancer therapeutics to tumors. <sup>161-165, 194</sup> They consist of hydrophobic cores, enabling the encapsulation of hydrophobic drugs and hydrophilic corona endowing them with biocompatibility and structural stability. <sup>195</sup> After being intravenously administered, the nanoassemblies extravasate into tumor tissues primarily through the Enhanced Permeability and Retention (EPR) effect. <sup>196-203</sup> Following endocytosis to cancer cells, they are expected for the controlled release of anticancer drugs. However, conventional nanoassemblies present a critical drawback of the uncontrol over the release of therapeutics from conventional nanocarriers in tumor sites.

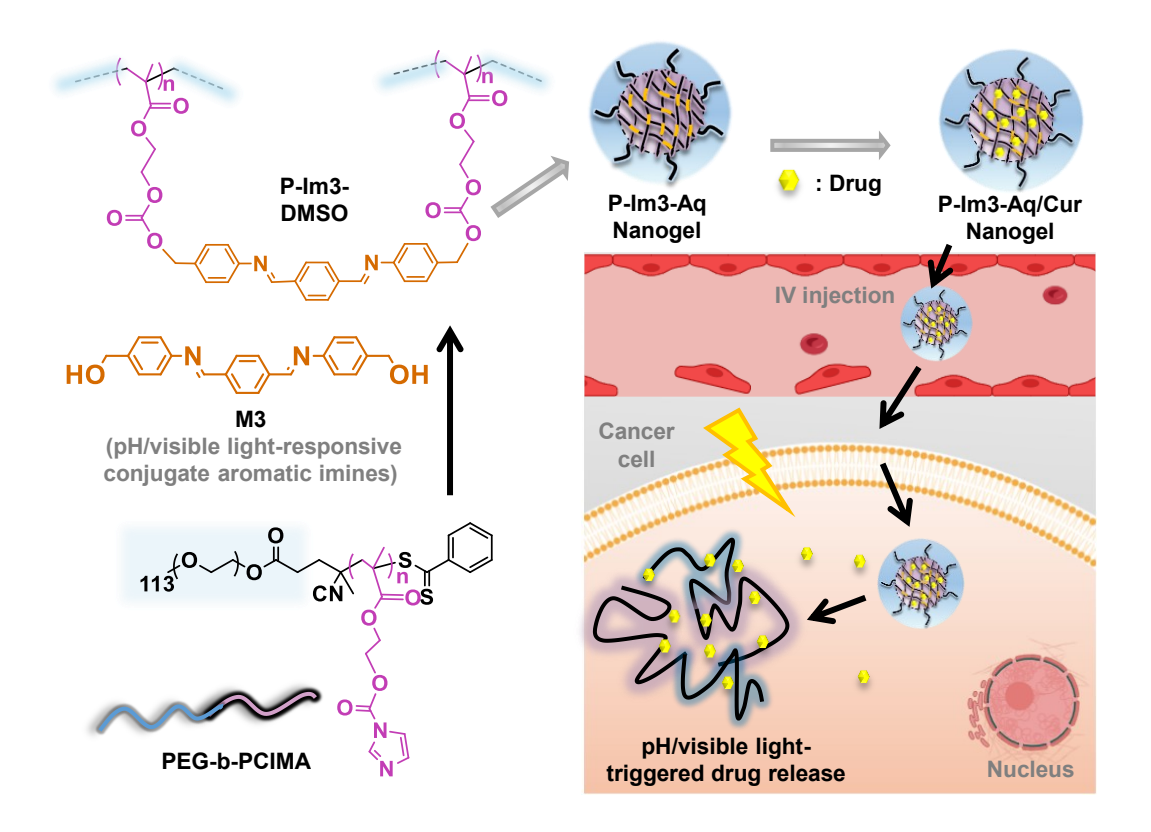
To overcome this drawback, stimuli-responsive degradation (SRD) has been integrated in the design of ABPs and their nanoassemblies. <sup>156, 158, 159, 166-168</sup> SRD-exhibiting nanoassemblies have been designed with degradable (or labile) covalent bonds, which are cleaved in response to stimuli, preferably endogenous stimuli found cellular environments. <sup>14, 114, 204</sup> The degradation causes the disintegration of nanoassemblies, leading to controlled/enhanced release of encapsulated drugs, thus improving the biodistribution of small drug molecules thereby enhancing therapeutic efficacy and minimizing off-target cytotoxicity. Acidic pH is a typical endogenous stimulus because of pH = 6.5-6.9 in tumoral extracellular cellular compartment and pH = 4.5-5.5 in endo/lysosomes. <sup>169-171</sup> In addition to endogenous acidic pH stimulus, light is considered as a promising exogenous stimulus to achieve on-demand delivery. Typically, imine, acetal and ketal groups as acid-labile linkages <sup>44, 172-174, 177, 205-207</sup> and o-nitrobenzyl and coumarin dimer groups as photo-cleavable linkages <sup>138, 175, 176</sup> have been incorporated into ABP-based nanoassemblies for single stimulus acid- and light-responsive degradation and response. Moreover, a combination of two distinct linkages, typically including o-nitrobenzyl group (light-

responsive) with β-thioester, <sup>178</sup> acetal, <sup>179</sup> and imine<sup>31</sup> groups (acid-responsive), has been formulated to achieve dual acid/light-response. Despite these advances, the conventional strategies could increase synthetic complexity, limit scalability, or cause instability issues. Our recent proof-of-concept studies demonstrate the versatility of our approach exploring single conjugate benzoic imine chemistry that enables dual response to acidic pH through acid-catalyzed hydrolysis and UV light through photo-induced E/Z isomerization. <sup>208</sup> However, the approach could be limited for tumor-targeting drug delivery because conjugate benzoic imine bond has its main absorption in UV region which is harmful to tissues. We have envisioned that extending the conjugation of benzoic imine bond can enhance its light absorption toward visible light region. To prove, we have explored an advanced approach that centers on the integration of extended conjugate benzoic imine bond into SRD-ABP-based nanoassemblies to achieve dual acidic pH/visible light response.

Another drawback of conventional nanoassemblies involves their nature of self-assembly through physical entanglement of ABPs in aqueous solution. Upon dilution in blood (4 L), they could be destabilized or disintegrated to the corresponding unimers, causing undesired premature release of drug molecules during blood circulation. To circumvent this drawback, stimuliresponsive degradable core-crosslinked nanoassemblies have been developed.<sup>209-211</sup> They endow structural stability upon dilution, while they facilitate the enhanced release of encapsulated drugs in response to endogenous or exogenous stimulus. A prevalent approach to fabricate corecrosslinked nanoassemblies (or nanogels) is called *in situ* crosslinking. This approach involves the fabrication of aqueous nanoassemblies of reactive ABPs bearing pendant functional groups, followed by their crosslinking induced with external crosslinkers. Click-type reactions such as azide-alkyne cycloaddition, <sup>212-214</sup> conjugation, <sup>77, 215-217</sup> and *in situ* imine formation <sup>135, 218-220</sup> allowed for the fabrication of reduction or acid-degradable core-crosslinked nanogels labeled with disulfide, 77, 213, 214, 217 imine, 135, 218-220 and ketal/acetal 212, 215, 216 linkages. This approach has been proved to be effective; however, when hydrophobic crosslinkers are required for use, this approach remains a critical challenge due to their limited solubility in aqueous dispersion of nanoassemblies. We have recently explored an alternative, but robust approach that centers on pre-crosslinking of a reactive ABP with a crosslinker in organic solvent, followed by the mechanical dispersion of the formed crosslinked polymers in aqueous solution, yielding welldefined core-crosslinked nanogels. This approach has allowed for the precise control over sizes and functionalities of SRD-exhibiting nanoassemblies with varying ratios of ABP/solvent and reactive functional groups.

In this work, we explored the robust pre-crosslinking dispersion approach to fabricate colloidally stable, core-crosslinked nanogels exhibiting dual acid/visible light response with a single extended conjugate aromatic imine bond (Scheme 1). A diol bearing extended conjugate benzoic imine bond (M3) was newly synthesized as an effective crosslinker for a well-defined PEG-based ABP bearing reactive imidazole pendants (PEG-b-PCIMA). The formed crosslinked polymers (P-Im3-DMSO) were mechanically dispersed in aqueous solution, yielding well-defined core/shell nanogels (P-Im3-Aq) with hydrophobic crosslinked cores, surrounded with hydrophilic PEG corona. They were characterized for dual acid/visible light-responsive degradation through acid-catalyzed hydrolysis and photo-induced E/Z isomerization, confirmed by spectroscopic and computational studies. Further, curcumin-loaded nanogels (P-Im3-Aq/Cur) were evaluated for the uptake and release of encapsulated curcumin, which is an anticancer drug, in HeLa cells.

**Scheme 1**. A robust approach exploring pre-crosslinking and dispersion techniques that allow for the fabrication of colloidally-stable, core-crosslinked nanogels exhibiting dual acid/visible light response with a single extended conjugate aromatic imine bond, exhibiting controlled/enhanced release of encapsulated Cur drug inside cancer cells. The nanogels are predicted to enter cells via endocytosis, where they can release Cur in the lower pH environments and/or after fusion to form the endo/lysosome, and exposure to light.



# 4.2. Experimental

#### 4.2.1. Instrumentation

<sup>1</sup>H NMR spectra were recorded on a 500 MHz Varian spectrometer. CDCl<sub>3</sub> singlet at 7.26 ppm and DMSO-d<sub>6</sub> quintet at 2.5 ppm were selected as reference standards. Exact mass of M3 was analyzed by High Resolution Mass Spectroscopy using a Thermo LTQ Orbitrap Velos mass spectrometer equipped with a heated electrospray ion source. A full MS spectrum (m/z 150-600) was acquired in the Orbitrap at positive mode at a resolution of 100000. Fourier-transform infrared (FT-IR) spectra were collected on a Thermo Scientific Nicolet iS5 spectrometer with an iD5 attenuated total reflection (ATR) accessory. UV/vis spectra were obtained using an Agilent

Cary 60 spectrometer with a 1 cm quartz cuvette. The hydrodynamic diameter and size distribution of aqueous nanogels were analyzed by dynamic light scattering (DLS) using a Malvern Nano S ZEN1600 system, equipped with a 633 nm He-Ne laser, at a fixed scattering angle of 175° and a temperature of 25 °C.

Light-responsive experiments were conducted with a PR160L-440nm Gen 2 LED lamp (Kessil, USA) at  $\lambda = 440$  nm (60 mW/cm<sup>2</sup>) and a MAX-302 xenon arc lamp (Asahi Spectra) at  $\lambda = 420$  nm (1.7 mW/cm<sup>2</sup>) at a distance of 15 cm from their light sources.

Transmission Electron Microscopy (TEM) images were acquired using a FEI Tecnai G2 F20 200 kV Cryo-STEM with Gatan Ultrascan 4000 4kx4k CCD Camera System Model 895. For negative staining, a 1% phosphotungstic acid solution was prepared by dissolving 5 mg of phosphotungstic acid in 0.5 mL of deionized water, followed by the addition of 5  $\mu$ L of 1 M sodium hydroxide and filtration through a 0.45  $\mu$ m PES membrane. Aqueous dispersions (5  $\mu$ L) were drop-cast onto a 300-mesh copper TEM grid and left undisturbed for 2 min. Excess liquid was blotted with filter paper before applying a drop of stain. The grid was blotted again and dried under a fume hood before imaging.

Differential scanning calorimetry (DSC) analysis was conducted to investigate thermal properties including glass transition temperature (Tg) of crosslinked polymers with a TA Instruments DSC Q20 Differential Scanning Calorimeter. Polymer samples were dried in vacuum oven for 24 hrs to remove residual solvents. Temperature ranged from –80 to 200 °C with heating and cooling cycles at a rate of 10 °C/min (cycles: cool to –80 °C and heat up to 200 °C (1st run), cool to –80 °C and heat up to 200 °C (2nd run), and cool to 25 °C. Tg values were determined from the 2nd heating run. Thermogravimetric analysis (TGA) was conducted with a TA Instruments Q50 Analyzer. Dried polymer samples (10 mg) were placed in a platinum pan inside a programmable furnace and then heated from 25 to 800 °C at a heating rate of 20 °C/min under nitrogen flow.

### 4.2.2. Materials

2-Hydroxyethyl methacrylate (HEMA, 99%, purified by passing through a column filled with basic aluminum oxide to remove the inhibitor), 1,1'-carbonyldiimidazole (CDI, 97%), 1,8-diazabicyclo[5.4.0]undec-7-ene (DBU, 98%), 4-(methylamino)pyridine (DMAP, 99%), 4-cyano-

4 (phenylcarbonothioylthio) pentanoic acid (CTA, 97%), 4-aminobenzyl alcohol (ABA, 98%), terephthalaldehyde (TDA, 98%), curcumin (Cur, 99%), methoxy-terminated poly(ethylene glycol) (PEG, MW = 5000 g/mol, dried by an azeotropic distillation with anhydrous toluene prior to use), and 2,2′-azobis(2-methylpropionitrile) (AIBN, 98%) from Sigma-Aldrich and 1-ethyl-3-(3 dimethylaminopropyl) carbodiimide•HCl (EDC) from Matrix Innovation were purchased and used as received. A carbonyl imidazole-bearing methacrylate (CIMA)<sup>179</sup> and a CTA-functionalized PEG (PEG-RAFT)<sup>187</sup> were synthesized as described elsewhere.

## 4.3.3. Synthesis of M3

ABA (0.73 g, 6.0 mmol) was mixed with TDA (0.40 g, 3.0 mmol) in DMF (7 mL) in an oilbath preset at 100 °C under stirring for 18 hrs. The resulting mixture was purified by precipitation from cold diethyl ether. The precipitate was dried in a vacuum oven at room temperature for 24 hrs to yield yellow solid. Yield = 0.70 g (67%).  $^{1}$ H NMR (DMSO-d<sub>6</sub>, ppm): 8.7 (s, 2H, -NCHC<sub>6</sub>H<sub>4</sub>CHN-), 8.06 (m, 4H, NCHC<sub>6</sub>H<sub>4</sub>CHN), 7.32-7.25 (m, 8H, -C<sub>6</sub>H<sub>4</sub>NCH C<sub>6</sub>H<sub>4</sub>CHN C<sub>6</sub>H<sub>4</sub>-), 5.22 (s, 2H, -C<sub>6</sub>H<sub>4</sub>CH<sub>2</sub>OH), 4.5 (s, 4H, -C<sub>6</sub>H<sub>4</sub>CH<sub>2</sub>OH).  $^{13}$ C NMR (DMSO-d<sub>6</sub>, ppm): 159.8, 150.1, 141.3, 138.9, 129.3, 127.8, 63.0. Mass calculated for C<sub>22</sub>H<sub>20</sub>N<sub>2</sub>O<sub>2</sub> [M+H]  $^{+}$ : 345.1598 and found: 345.1600.

### 4.3.4. Synthesis of PEG-b-PCIMA via RAFT Polymerization

CIMA (1 g, 4.5 mmol), PEG-RAFT (0.24 g, 45.6 µmol), and AIBN (3.7 mg, 22.8 µmol) were mixed with anisole (1.7 mL) in a 10 mL Schlenk flask. The mixture was purged with nitrogen for 45 min and then placed in an oil-bath preset at 70 °C to start polymerization. After 3 hrs, the mixture was cooled down to room temperature to stop polymerization. For purification, as-synthesized polymers were precipitated from cold hexane and isolated by vacuum filtration. The procedure was repeated three times and then the polymer was dried in a vacuum oven at 40 °C for 24 hrs.

# 4.3.5. CDI-Mediated Crosslinking to Fabricate P-Im3-DMSO Crosslinked Polymers

M3 (26 mg, 74.3 μmol, 149 μmol equivalent of OH groups) was mixed with PEG-b-PCIMA (52.5 mg, 3.6 μmol, 149 μmol equivalent of CIMA units) and DBU (4.5 mg, 30 μmol) in DMSO (6 mL) under stirring at room temperature for 24 hrs. The formed crosslinked polymers were precipitated from cold diethyl ether and then dried in a vacuum oven at 40 °C for 24 hrs.

# 4.3.6. Fabrication of Aqueous P-Im3-Aq Nanogels by Pre-crosslinking Dispersion Approach

Typically, to fabricate P-Im3-Aq at 0.31 mg/mL, M3 (1.7 mg, 5  $\mu$ mol) was mixed with PEG-b-PCIMA (3.5 mg, 0.2  $\mu$ mol) and DBU (0.3 mg, 2  $\mu$ mol) in DMSO (2 mL) under stirring at room temperature for 24 hrs. Deionized water (10 mL) was then added dropwise at 60 mL/hr using a syringe pump under stirring. The resulting dispersion was dialyzed against water (1 L) using a dialysis tubing with MWCO = 11–13 kDa for 24 hrs and then filtered with a 0.45  $\mu$ m PES filter.

The similar procedure was examined with the varying amounts of DMSO and water to investigate DMSO/water ratio (called P-Im3-Aq-A, B, and C) as well as the varying amounts of PEG-b-PCIMA and M3 to investigate CI/OH mole equivalent ratio (called P-Im3-Aq-D and E). The recipes are summarized in Table S4.1.

# 4.3.7. Conventional *In Situ* Crosslinking Approach in Attempt to Fabricate Aqueous Crosslinked Nanoassemblies

Typically, deionized water (10 mL) was added dropwise to an organic solution consisting of M3 (4.8 mg, 14.0  $\mu$ mol) and PEG-b-PCIMA (10 mg, 0.7  $\mu$ mol) in DMSO (2 mL) at a rate of 60 mL/hr using a syringe pump under magnetic stirring at room temperature. The resulting dispersion was dialyzed against water (1 L) using a dialysis tubing with MWCO = 11–13 kDa for 24 hrs. DBU (0.8 mg, 5.6  $\mu$ mol) was added, and the resulting mixture was stirred at room temperature for another 24 hrs.

### 4.3.8. Acid and Light-Responsive Degradation Studies

Acid-Responsive Degradation of Aqueous Nanoassemblies. Aqueous P-Im3-Aq nanogels (2 mL, 0.31 mg/mL) were mixed with 0.2 M sodium acetate buffer solution at pH = 5.0 (2 mL) under stirring at room temperature. Aliquots were taken for DLS and TEM analysis.

Acid-Responsive Degradation of M3 in DMSO using  $^{1}H$  NMR Spectroscopy. To investigate acid-catalyzed hydrolysis of benzoic imine bonds, M3 (10 mg, 30  $\mu$ mol) was dissolved in DMSO-d<sub>6</sub> (1 mL) and then mixed with HCl (5  $\mu$ L, 60  $\mu$ mol) at a 1/1 mole equivalent ratio of C=N/H<sup>+</sup> (equivalent to pH = 1.2 or pD = 1.6, calculated using pD = pH + 0.4).  $^{1}H$  NMR spectra of the resulting mixtures were recorded for given time intervals. Similar

procedure was used for P-Im3-DMSO polymer, except with the use of P-Im3-DMSO (10 mg) swollen in DMSO-d<sub>6</sub> (1 mL).

Light-Responsive Degradation of Aqueous Nanoassemblies. Aqueous P-Im3-Aq nanogels (3 mL) in a quartz cuvette were exposed upon the irradiation of visible light with  $\lambda = 440$  nm (60 mW/cm²). Their UV/Vis spectra were recorded to follow change in absorbance at  $\lambda = 355$  nm.

Light-Responsive Degradation of M3 in DMSO via UV/Vis Spectroscopy. A solution of M3 (31 µg) dissolved in DMSO (3 mL) at 30 µM in a quartz cuvette was exposed upon the irradiation of visible light with  $\lambda = 440$  nm (60 mW/cm<sup>2</sup>). Their UV/Vis spectra were recorded to monitor change in absorbance at  $\lambda = 355$  nm over irradiation time.

#### 4.3.9. Computational Details

Density functional theory (DFT) calculations with the range-separated hybrid exchangecorrelation (XC) functional based on B97 exchange (ωB97XD) are performed to evaluate the structural and electronic properties of the molecular structures.<sup>221</sup> The molecular geometries were fully optimized at the  $\omega$ B97XD level of theory along with the 6–311++G(d,p) split-valence triple-ζ Pople basis set<sup>222</sup> Vibrational frequency analysis was carried out to confirm that each configuration was a minimum on the potential energy surface (zero imaginary frequencies), and thermodynamic properties were evaluated within the rigid-rotor harmonic oscillator approximation. The STON method was used to locate the transition states for the interconversion of structures. Three structure specifications are required in this method: the reactants (EE for EE  $\rightarrow$  EZ and EZ for EZ  $\rightarrow$  ZZ), the products (EZ for EE  $\rightarrow$  EZ and ZZ for EZ  $\rightarrow$  ZZ), and an initial guess for the transition state structure. The energies of the highest occupied molecular orbital (HOMO), lowest unoccupied molecular orbital (LUMO), and the electronic bandgap (Eg) between these orbitals were determined through analysis of frontier molecular orbitals (FMOs). The energies of the singlet-excited-state transitions were calculated using time-dependent DFT (TD-DFT) for optimized molecular structures. We note that ωB97XD is a reliable XC functional to accurately capture the UV/Vis light absorption spectra for the structures due to the partitioning of short and long range components, compared to traditional hybrid XC functionals such as the Becke three-parameter hybrid methods with the Lee-Yang-Parr correlation functional

(B3LYP).<sup>223</sup> For all the calculations the Gaussian 16 (revision C.01) software package of programs was used along with the GaussView6 interface for structure and orbital manipulations.<sup>224</sup> The enthalpy and free energy of the reaction was calculated as summarized in Table S4.2.

### 4.3.10. Preparation of Cur-Loaded Nanogels

An organic solution of Cur (1 mg) dissolved in DMSO (2 mL) was added dropwise to aqueous P-Im3-Aq nanogel dispersion (0.31 mg/mL, 12 mL) under stirring for 1 hr. The resulting mixture was transferred to dialysis tubing with MWCO = 11-13 kDa for dialysis against water (1 L) for 24 hrs. The dispersion was filtered through a 0.45  $\mu$ m PES filter to remove unencapsulated (free) Cur, yielding aqueous Cur-loaded nanogels (P-Im3-Aq/Cur) at 0.27 mg/mL.

To determine the loading level of Cur in nanogels, a series of solutions containing different amounts of Cur in a mixture of THF and water (1/1 v/v) were prepared, and their UV/Vis spectra were recorded to determine the extinction coefficient of Cur at  $\lambda = 430 \text{ nm}$ . Then, aliquots of P-Im3-Aq/Cur (1 mL) were mixed with THF (1 mL) and filtered through a 0.45  $\mu$ m PTFE filter. UV/Vis spectrum of the filtrate was recorded to quantify encapsulated Cur using the predetermined extinction coefficient.

### 4.3.11. Stimuli-Responsive Release of Cur from P-Im3-Aq/Cur Nanogels

For light-responsive release, aliquots of P-Im3-Aq/Cur (2 mL) were irradiated with visible light with  $\lambda = 420$  nm (1.7 mW/cm²). Other aliquots were kept in dark as control. For acidic pH-responsive release, aliquots of P-Im3-Aq/Cur (2 mL) were mixed with 0.2 M sodium acetate buffer solution (2 mL) at pH = 5.0 and 7.4 under stirring. For dual acidic pH/light-responsive release, aliquots of P-Im3-Aq/Cur (2 mL) mixed with 0.2 M sodium acetate buffer solution (2 mL) at pH = 5.0 were exposed to visible light with  $\lambda = 420$  nm (1.7 mW/cm²) at room temperature under stirring. To determine the %release of Cur from nanogels, UV/Vis spectra of supernatants were recorded for given time intervals and the absorbance at  $\lambda = 430$  nm was monitored.

#### **4.3.12.** Cell Culture

HeLa cervical cancer cells were cultured in DMEM (Dulbecco's modified Eagle's medium) containing 10% CCS (cosmic calf serum) and were kept at 37 °C with 5% CO<sub>2</sub> in a HERAcell Vios 160i incubator (ThermoFisher Scientific).

*Viability Assay.* HeLa cells were plated at  $2.5\times10^3$  cells per well in a 96-well plate and incubated for 24 hrs in 100 μL of DMEM with 10% CCS for 24 hrs at 37 °C with 5% CO<sub>2</sub>. Various concentrations of aqueous P-Im3-Aq/Cur nanogels as well as aqueous P-Im3-Aq nanogels (empty, e.g. Cur-free) and free Cur as controls were added to the cells for 72 hrs. Due to the poor solubility of Cur in aqueous media, aliquots of Cur dissolved in DMSO were diluted with cell culture media to keep DMSO to be as low as 1% for all control samples. Cell viability was measured using the WST-8 proliferation assay kit as per manufacturer's instructions (Cayman Chemicals). Briefly, the medium containing samples was carefully removed and 100 μL of the prepared colorimetric reagent WST-8 (0.5 mM, 5-(2,4-disulfophenyl)-3-(2-methoxy-4-nitrophenyl)-2+(4-nitrophenyl)-2H-tetrazolium, inner salt, monosodium salt) was added to each well. After 2hrs, aTecan Infinite M200 Pro plate reader was used to measure the absorbance at  $\lambda$  = 450 nm for each well. Wells with untreated cells were measured as a positive control, while WST-8 reagent alone was measured to have a 'blank' reference. Each treatment was replicated 3 times. Cell viability was calculated as the percent ratio of absorbance of mixtures with nanogels to control (untreated cells).

Live Cell Imaging by Fluorescence Microscopy. HeLa cells were plated in DMEM with 10% CCS at  $2.5 \times 10^5$  cells/mL in a μ-slide 4-well dish. The cells were treated with  $240 \mu g/mL$  of P-Im3-Aq/Cur nanogels,  $2.72 \mu g/mL$  free Cur solution ( $2.72 \mu g/mL$ ) or  $240 \mu g/mL$  of P-Im3-Aq and SYTO Deep Red Nucleic Acid Stain (Thermo Fisher) for 2 hrs at 37 °C with 5% CO<sub>2</sub>. Live cells were visualized on a Nikon Ti2 microscope equipped with a Yokogawa CSU-X1 spinning disk, a Gataca Live-SR unit, an Andor Zyla 4.2 (Oxford instruments, UK), 60x/1.45NA PlanApo objective lens and DIC optics. Cur was excited with a  $\lambda = 488$  nm laser (18% power, 200 ms exposure time), and SYTO Deep Red was excited with a 638 nm laser (10% power, 200 ms exposure time). Images were acquired with Micro-Manager. Images were viewed and analyzed on ImageJ.

#### 4.3. Results and Discussion

# 4.3.1. Synthesis and UV/Vis Absorption Characteristics of Extended Conjugate Benzoic Imine-Bearing Diol Crosslinker

Figure 4.1a depicts our approach to synthesize a new diol crosslinker bearing two conjugate benzoic imine bonds (called extended conjugate benzoic imine bonds), labelled as M3. The approach utilizes a facile condensation reaction of an amine group of ABA with two aldehyde groups of TDA at an elevated temperature through the formation of benzoic imine bonds. <sup>1</sup>H NMR spectrum in Figure 4.1b shows the new peak at 8.72 ppm (a) corresponding to imine proton, along with the peak at 4.53 ppm (e) corresponding to methylene protons in benzyl moieties and the peaks at 7.35 ppm (b) and 8.07 ppm (c) corresponding to aromatic protons. Their integrals were quantitative to the numbers of protons. This result, combined with <sup>13</sup>C NMR spectrum (Figure S4.1) and HR-MS (Figure S4.2), confirms the successful synthesis of M3.

Given the synthesis of M3, its UV/Vis absorption characteristics was investigated in DMSO and compared with M-HX (a methacrylate bearing a benzoic imine bond). As seen in Figure 4.1c, M3 exhibits an extended absorption up to 450 nm, with a distinct absorption at  $\lambda = 355$  nm corresponding to  $n\rightarrow\pi^*$  transition and a secondary absorption at  $\lambda = 310$  nm attributed to  $\pi\rightarrow\pi^*$  transition. Its extinction coefficient at  $\lambda = 355$  nm was determined to be 32,000 M<sup>-1</sup> cm<sup>-1</sup> (Figure S4.3). Promisingly, its absorption was red-shifted because of the extended benzoic imine conjugation, compared with M2 having its maximum absorption at  $\lambda = 285$  nm ( $\epsilon = 20,100$  M<sup>-1</sup>cm<sup>-1</sup> in DMF) and further to M-HX having its maximum absorption at  $\lambda = 255$  nm ( $\epsilon = 2,200$  M<sup>-1</sup>cm<sup>-1</sup> in DMF).

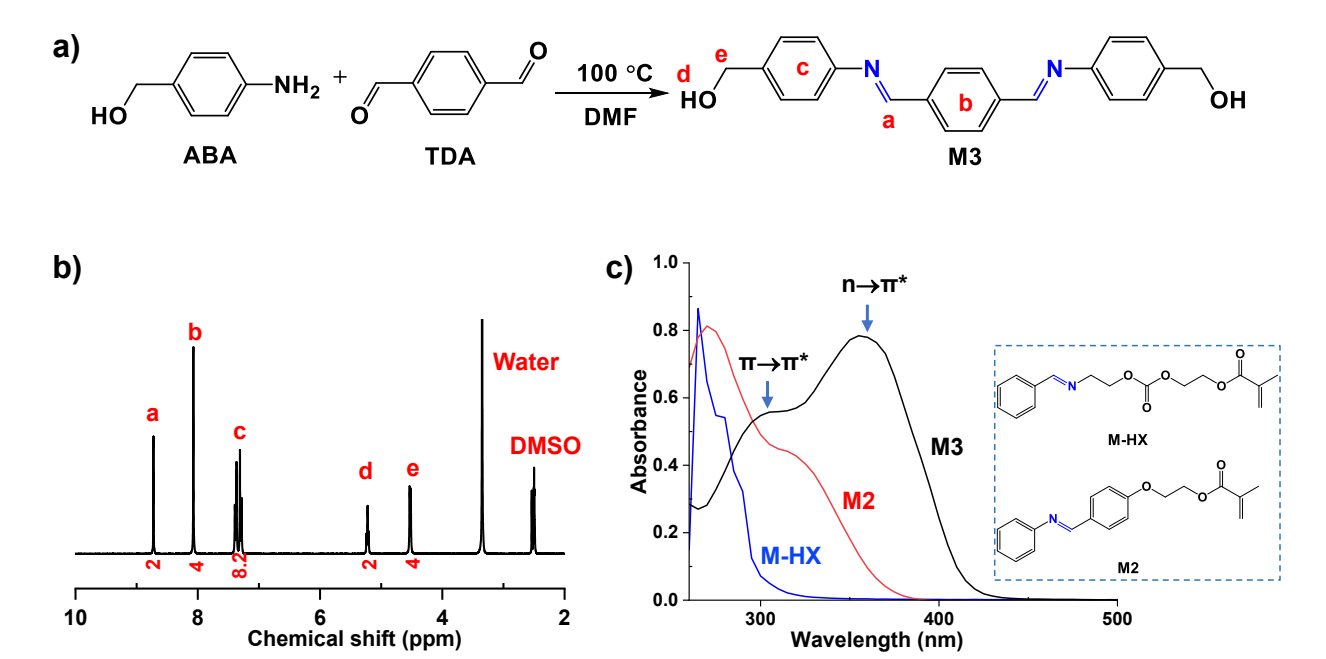


**Figure 4.1**. Synthesis of M3 (a diol crosslinker bearing an extended conjugate benzoic imine) by condensation reaction of ABA with TDA in DMF (a), its <sup>1</sup>H NMR spectrum in DMSO-d<sub>6</sub> (b), and its UV/vis spectrum in DMSO, compared with those of M2 (a methacrylate bearing a conjugate benzoic imine bond) and M-HX (a methacrylate bearing a benzoic imine bond) in DMF (c).

## 4.3.2. Synthesis of Reactive PEG-b-PCIMA Copolymer Bearing Imidazole Pendant

As illustrated in Figure 4.2a, RAFT polymerization was examined for CIMA in the presence of PEG-RAFT, a PEG-based macro-RAFT mediator, initiated with AIBN in anisole at 70°C, to synthesize a well-defined PEG-based block copolymer bearing reactive imidazole pendants (PEG-b-PCIMA). The conditions include the initial mole ratio of [CIMA]<sub>0</sub>/[PEG-RAFT]<sub>0</sub>/[AIBN]<sub>0</sub> = 100/1/0.5 with the targeted degree of polymerization (DP) = 100 at complete monomer conversion. The synthesized copolymer was purified by precipitation from hexane to remove unreacted CIMA at 40% conversion. <sup>1</sup>H NMR spectrum in Figure 4.2b shows the presence of PEG at 3.6 ppm and pendant imidazole rings at 7.0-8.2 ppm. Their integral ratio, with the DP of PEG = 113, allows to determine the DP of the PCIMA block to be 41, thus forming PEG<sub>113</sub>-b-PCIMA<sub>41</sub>.

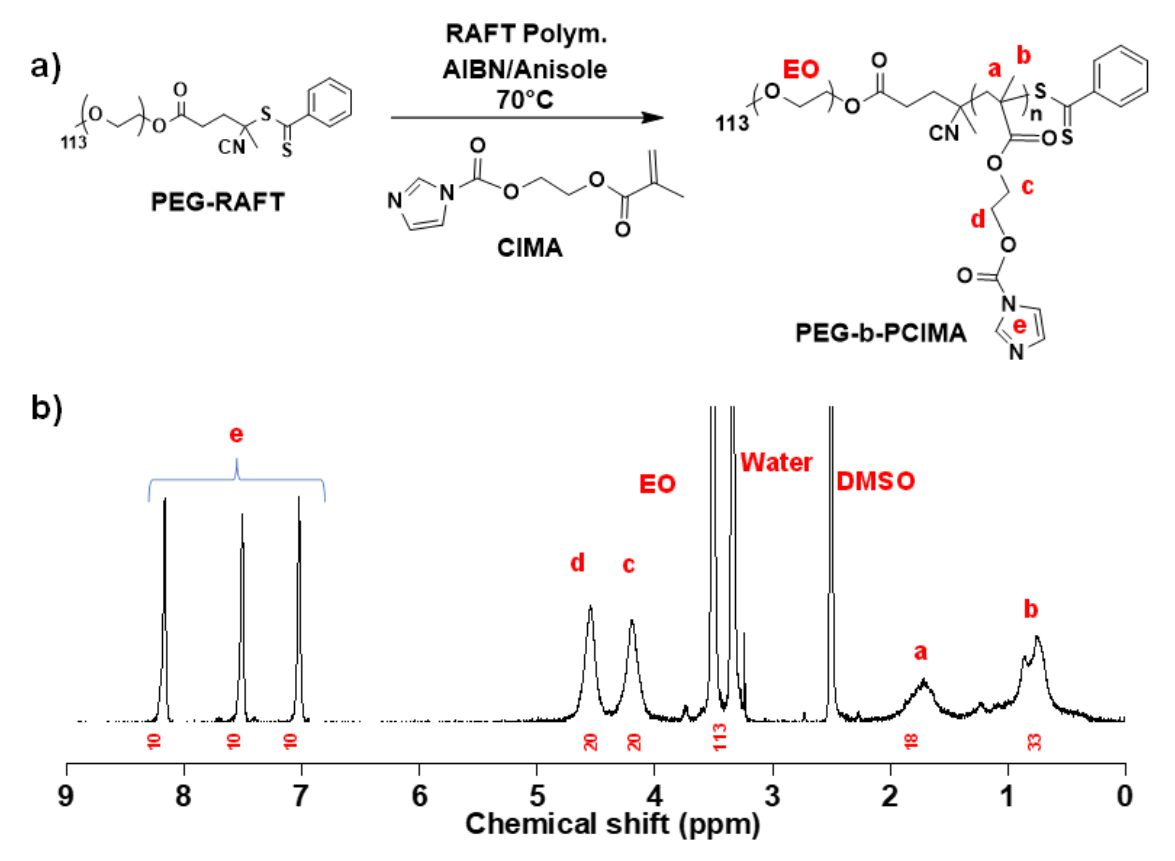


**Figure 4.2**. Synthesis by RAFT polymerization (a) and  ${}^{1}H$  NMR spectrum in DMSO-d<sub>6</sub> of PEG-b-PCIMA block copolymer. Conditions:  $[CIMA]_{0}/[PEG-RAFT]_{0}/[AIBN]_{0} = 100/1/0.5$ ; CIMA/anisole (w/w) = 1/0.6.

# 4.3.3. Studies of CDI-mediated Crosslinking Reaction to Fabricate Crosslinked Polymers

Given the synthesis of well-defined PEG-PCIMA and M3 diol crosslinker, their CDI-mediated coupling reaction between pendant CI groups with OH groups were investigated in an organic solvent (Figure 4.3a). DMSO was chosen because it was found to be a good solvent to both PEG-PCIMA and M3 precursors. With a choice of CI/OH mole equivalent ratio = 1/1, aliquots of PEG-PCIMA and M3 were mixed in DMSO at 50 mg/mL to induce CDI-mediated crosslinking. The formed PEG-PCIMA/M3 crosslinked polymer (called P-Im3-DMSO) was isolated by precipitation from diethyl ether and then analyzed by solubility, <sup>1</sup>H NMR and FT-IR spectroscopies for chemical structure, and DSC and TGA for thermal properties.

The polymer turned out to be insoluble in any organic solvents including DMSO and its gel content to measure insoluble species in DMSO was greater than 84%. Given the polymer being swollen in DMSO-d<sub>6</sub>, <sup>1</sup>H NMR spectrum in Figure S4.4 shows no peaks corresponding to

protons in copolymer. In addition, <sup>1</sup>H NMR spectrum of supernatant in Figure S4.5 shows two peaks at 7.0 and 7.6 ppm presenting imidazole which could be generated as a side product during CDI-mediated crosslinking. Moreover, its FT-IR spectrum in Figure 4.3b shows the characteristic C=N stretching vibration at 1620 cm<sup>-1</sup>, along with C-H stretching vibration at 2800-3000 cm<sup>-1</sup> and carbonyl vibration at 1700-1750 cm<sup>-1</sup>. These results confirm the formation of crosslinked polymer network through the formation of carbonate bonds by CDI-medicated crosslinking reaction of PEF-b-PCIMA with M3. The crosslinked polymer had a single glass transition at -21 °C and a single melting transition at 55.2 °C, by DSC analysis (Figures S4.6). It also had the temperature at which its mass loses half to be 407 °C with 15% residue, by TGA analysis (Figure S4.7).

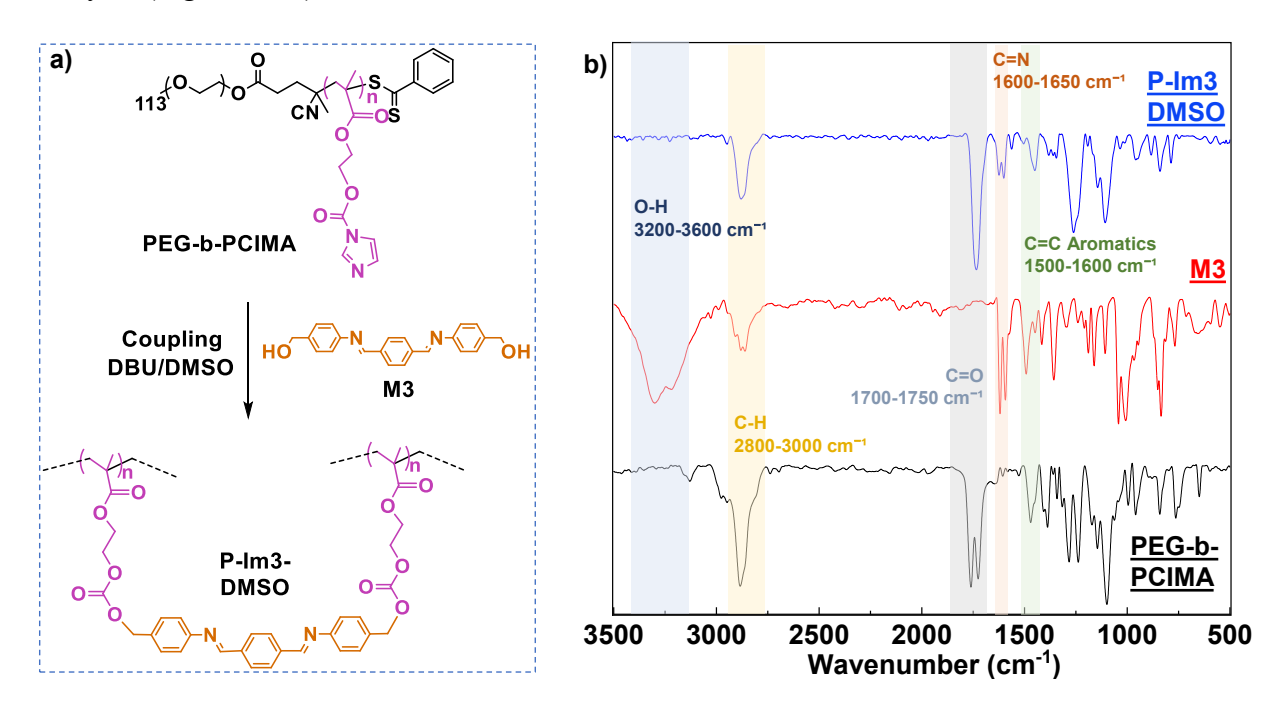


**Figure 4.3**. Schematic presentation for CDI-medicated crosslinking reaction of PEG-b-CIMA with M3 diol crosslinker to form cross-linked P-Im3-DMSO polymer network (a) and its FT-IR spectrum, compared with those of M3 and PEG-b-PCIMA precursors (b).

#### 4.3.4. Pre-crosslinking Dispersion Approach to Fabricate Aqueous Crosslinked Nanogels

A new approach centered on pre-crosslinking in a homogeneous solution was explored to fabricate colloidally stable crosslinked nanogels dispersed in aqueous solution. The approach consists of two steps, including i) the synthesis of P-Im3-DMSO crosslinked polymer from a

mixture of PEG-b-PCIMA and M3 at CI/OH = 1/1 in DMSO and ii) its spontaneous self-assembly in water to yield nanogel dispersion. Because of the amphiphilic nature of P-Im3-DMSO polymer, the formed nanogels consist of crosslinked hydrophobic cores surrounded with hydrophilic PEG corona in water.

After being purified by dialysis, the resulting dispersion was determined to be 0.31 mg/mL, which is close to that (0.36 mg/mL) in the recipe, suggesting the loss of polymeric species during pre-crosslinking/dispersion process could be negligible. The purified aqueous nanogels were characterized for size and size distribution as well as morphology. As seen in Figure 4.4a, the nanogels had a diameter of 119 nm and their size distribution appeared to be narrow and monomodal, based on DLS analysis. No visible aggregates were observed. TEM analysis reveals that they had a diameter  $87 \pm 21$  nm in the dried state, which is smaller than that by DLS analysis (inset in Figure 4.4a). Furthermore, the nanogels were characterized for UV/Vis absorption characteristics. As compared in Figure 4.4b, it had an absorption at  $\lambda = 355$  nm, which is similar to M3 crosslinker, indicating that extended conjugate benzoic imine bonds are intact on the course of the fabrication of nanogels. These results confirm that pre-crosslinking/dispersion approach is robust and enables the fabrication of colloidally stable nanogels in aqueous solution.

Important parameters that significantly influence colloidal stability and sizes were systematically investigated by DLS analysis. Figure 4.4c shows the change in diameter of P-Im3-Aq nanogels in water. One parameter is CI/OH mole equivalent ratio. When the ratio increased (e.g. decreasing the number of crosslinks), the diameter increased. Another parameter is the amount of PEG-b-PCIMA in DMSO as DMSO/PEG-b-PCIMA v/wt ratio for CDI-mediated crosslinking reaction. The diameter increased with an increasing ratio (e.g. amount of DMSO). These results and trends of change in sizes indicate that the size of core-crosslinked nanogels greatly relies on crosslinking density and thus highly crosslinked networks are likely to produce more compact hydrophobic cores.

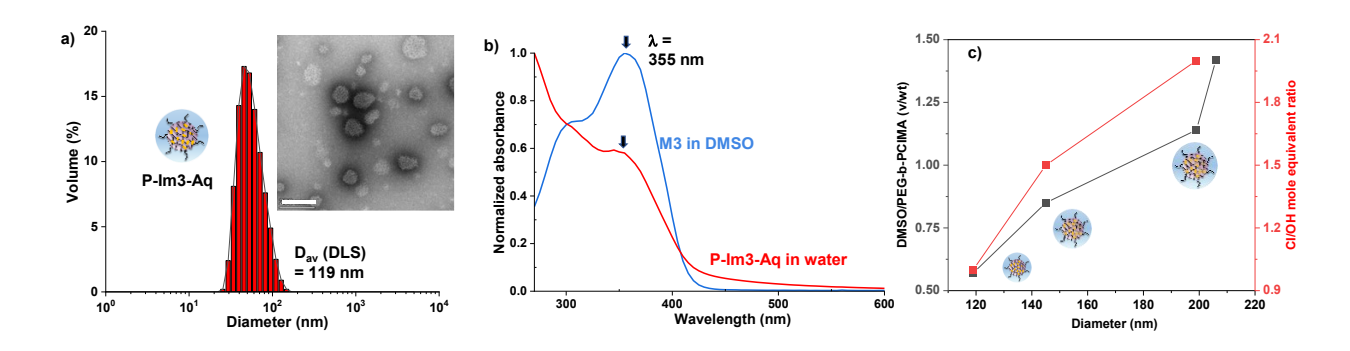


**Figure 4.4**. For P-Im3-Aq nanogels in aqueous solution, DLS diagram with inset TEM image (scale bar = 200 nm) (a), UV/Vis spectrum at 0.3 mg/mL, compared with that of M3 in DMSO (30  $\mu$ M) (b), and evolution of diameter with varying amount of DMSO and CI/OH mole equivalent ratio (c).

In our separated experiment, a conventional *in situ* crosslinking approach was examined in an attempt to fabricate aqueous crosslinked nanoassemblies. The approach involves the fabrication of aqueous nanoassemblies consisting of PEG-b-PCIMA and M3 through self-assembly, followed by the addition of water-soluble DBU as a catalyst in aqueous solution. The resulting dispersion was white-colored with visible aggregates (Figure S4.8). The dispersion was subjected to dialysis and filtration to remove significant amount of white aggregates. The resulting dispersion turned out to be blue-tinted with the average diameter of 125 nm by DLS. When being characterized by UV-Vis spectroscopy, the dispersion shows no absorption at  $\lambda = 355$  nm corresponding to  $n \rightarrow \pi^*$  transition, characteristic of M3, in its UV/Vis spectrum. Our attempts with the variation of the amounts of PEG-b-PCIMA and M3 over DMSO and water were not straightforward toward the fabrication of colloidally-stable aqueous dispersion of crosslinked nanoassemblies by this approach.

## 4.3.5. Studies of Acid-Responsive Degradation and Disassembly

Aqueous P-Im3-Aq nanogels contain extended conjugate benzoic imine bonds in the crosslinks of hydrophobic cores which could be cleaved in an acidic environment. Aliquots of the nanogels were incubated in acidic buffer at pH = 5.0, and their acid-responsive degradation was investigated using DLS and TEM techniques. DLS analysis reveal that their size distribution became multimodal with appearance of large aggregates in 6 hrs of incubation (Figure 4.5a). TEM analysis further confirms the occurrence of large aggregates (Figure 4.5b, 5c) and the digital images of the aqueous nanogel dispersion show the change in color from turbid white to

visibly clear after 24 hrs of incubation in acidic buffer (Figure 4.5d, 4.5e). Further, precipitates were visible in the bottom of the vials. These results could be attributed to the disintegration of P-Im3-Aq nanogel cores via the cleavage of benzoic imine bonds to corresponding aldehyde and amine under an acidic condition.

Further to get insights, acid-responsive degradation of M3 and crosslinked polymer (P-Im-DMSO) through acid-catalyzed hydrolysis of benzoic imine bonds was quantitatively investigated using <sup>1</sup>H NMR spectroscopic analysis. First, M3 dissolved in DMSO-d<sub>6</sub> was incubated with HCl (an acid) for 2 hrs. <sup>1</sup>H NMR spectrum in Figure 4.5g shows the disappearance of the peak at 8.6 ppm corresponding to imine proton (a), and appearance of a new peak at 9.2 ppm corresponding to aldehyde proton (b). These changes confirm the cleavage of imine bonds into the corresponding aldehyde and amine precursors through acid-catalyzed hydrolysis (Figure 4.5f). Their integral ratio allows the %hydrolysis to be 82%. Next, P-Im3-DMSO swollen in DMSO-d<sub>6</sub> was treated with HCl. As compared in Figure S4.9, <sup>1</sup>H NMR spectrum of P-Im3-DMSO/HCl mixture shows the peaks in greater than 7 ppm, which could be attributed to the cleavage of partial imine bonds in the presence of acid, which could improve the relaxation of protons in degraded network polymers.

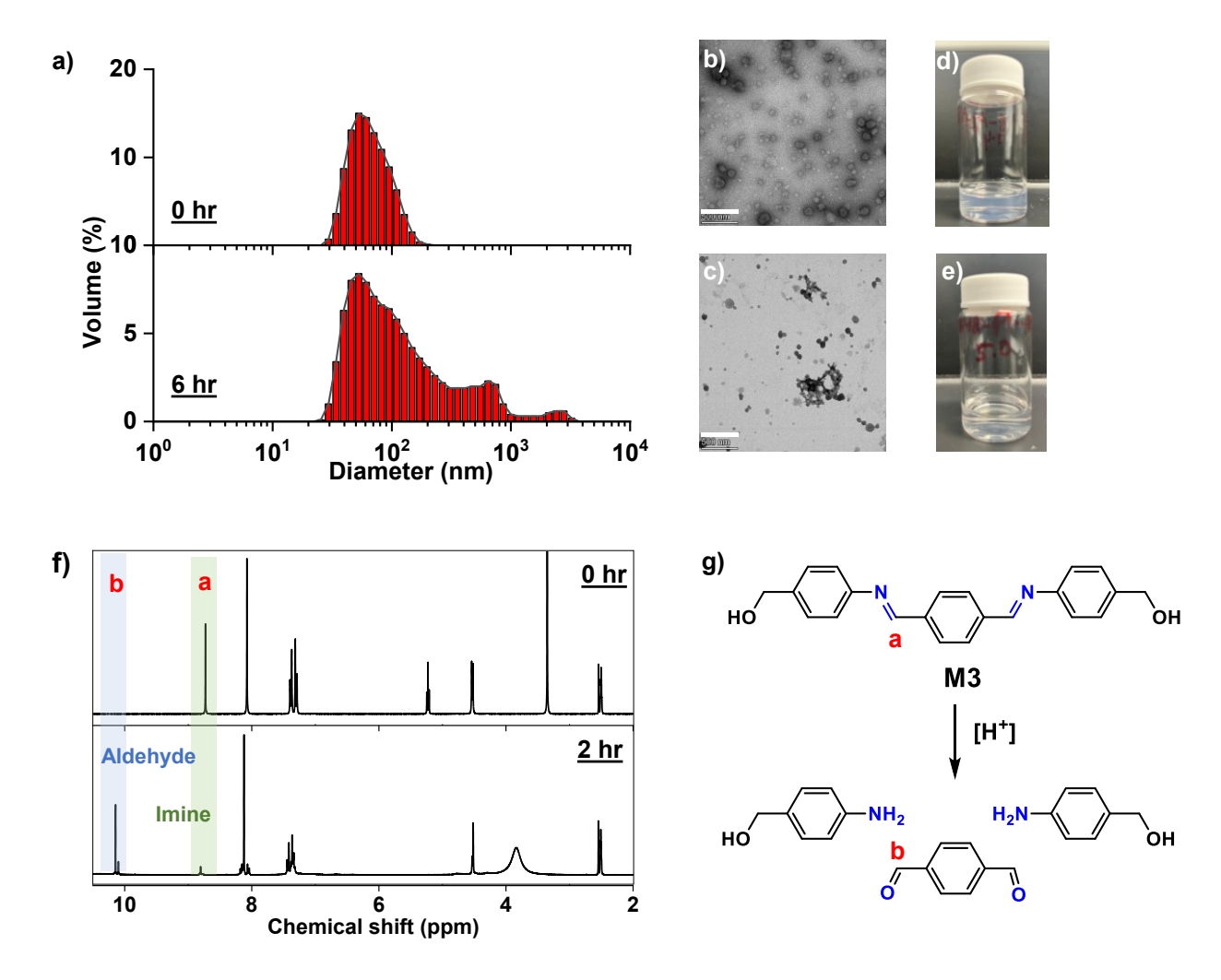


**Figure 4.5**. DLS diagrams of aqueous P-Im3-Aq nanogels incubated at pH 5.0 over 6 hrs (a); their TEM images (scale bar = 500 nm) (b,c), and digital images (d,e); and overlaid <sup>1</sup>H NMR spectra of M3 in DMSO-d<sub>6</sub>/HCl (f) and acid-catalyzed hydrolysis of benzoic imine bond in M3 (g).

## 4.3.6. Light-Responsive Degradation and Disassembly

The light response of aqueous P-Im3-Aq nanogels was investigated using UV/Vis spectroscopy upon the irradiation of visible light at  $\lambda = 440$  nm. As seen in Figure 4.6a, the absorption gradually decreased over irradiation time. The absorbance at  $\lambda = 355$  nm was monitored to determine %degradation. It decreased to 40% over 24 hrs. Additionally, the DLS diagrams and TEM images show no change in size distribution over the irradiation time, suggesting that only cores could be disintegrated through E/Z isomerization of conjugate benzoic imines, with no chemical cleavages (Figure S4.10).

To get insight into the plausible mechanism of decrease in absorption, M3 dissolved in DMSO (30 uM) was examined for the light response of the conjugate benzoic imine bonds. As seen in Figure 4.6b, absorbance at  $\lambda = 355$  nm decreased to >90% in 24 hrs. Interestingly, maximum absorption wavelength was blue-shifted over irradiation time, which could be attributed to the photochemical E/Z isomerization of two C=N bonds under visible light. 50, 208 Notably, the degradation of P-Im3-Aq nanogels appeared to be slower than that of M3, which is attributed to the delayed penetration of visible light to crosslinked cores in nanogels. Our results obtained from UV/Vis spectroscopic analysis of M3 and P-Im3-Aq suggest that the destabilization of nanogels upon exposure to visible light could be attributed to change in UV absorption due to photo-induced E/Z isomerization.

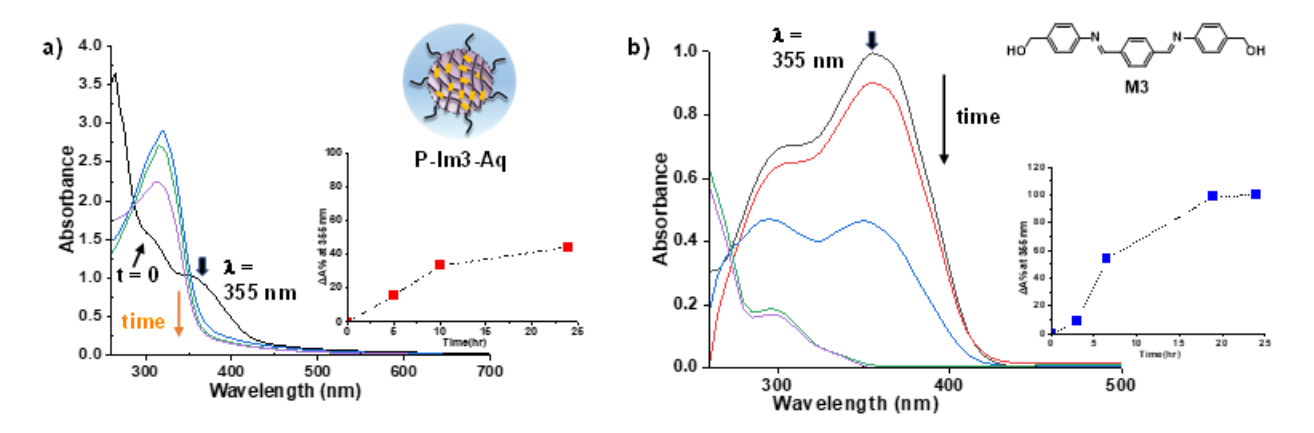


**Figure 4.6**. UV/Vis spectra of aqueous P-Im3-Aq nanogels (a) and M3 in DMSO (b) under visible light irradiation at 420 nm over a 24-hour period, with inset plots showing the absorbance changes at 355 nm.

# 4.3.7. Computational Studies of E/Z Isomerization of M3 by DFT Calculations

M3 labeled with two conjugate benzoic imine bonds could be presented with three ground state configurations as shown in Figure 4.7a (e.g. EE, EZ, and ZZ). Their transitions as EE  $\rightarrow$  EZ  $\rightarrow$  ZZ are assumed to be achieved through a photo-induced E/Z isomerization of benzoic imine bonds. We scanned the potential energy surface to characterize the ground states of EE, EZ and ZZ configurations of M3 and the transition states TS1 and TS2 for EE  $\rightarrow$  EZ and EZ  $\rightarrow$  ZZ isomerization pathways, respectively. DFT calculations show that EE is the most stable configuration, compared to EZ and ZZ, while ZZ is the least stable configuration. The ground state energy of EE calculated through DFT is 3 kcal/mol and 11 kcal/mol lower compared to EZ

and ZZ configurations (Figure S4.11). The STQN method implemented in Gaussian 16 was used to locate these transition states. The estimated activation energy for EE  $\rightarrow$  EZ ( $\Delta G^{\ddagger}_{EZ}$ ) and EZ  $\rightarrow$  ZZ ( $\Delta G^{\ddagger}_{ZZ}$ ) was calculated to be 19 and 21 kcal/mol, respectively.

We used TD-DFT calculations to predict the absorption spectra of EE, EZ and ZZ configurations. The vertical excitation energy for three different configurations of M3 was calculated and the excitation energies, oscillator strength and possible electron transitions are summarized in Table S4.3 and Figure S4.12, respectively. Figure 4.7b shows the absorption spectra of EE (black), EZ (red) and ZZ (blue) configurations calculated via TD-DFT (Table S4.4). The calculated  $\lambda_{max} = 337$  nm for the EE configuration is in good agreement with the experimental result ( $\lambda_{max} = 355$  nm). The EZ and ZZ configurations had progressively lower absorbance values. The EZ demonstrates a decrease in absorbance and a blue shift, while the ZZ exhibits the lowest absorbance, signifying substantial disruption in the conjugate structure. The similarity in spectral features between experimental and computational studies indicates that the light-responsive degradation of M3 (shown in Figure 4.6b) could be attributed to stepwise transformation to EZ and ZZ forms upon exposure to light.

Frontier molecular orbital (FMO) is crucial for electrical and optical properties and chemical reactions. Figure S4.13 shows the HOMO-1, HOMO, LUMO and LUMO+1 of EE configuration. Yellow and cyan regions show FMO with opposite phases. The positive phase of the molecule is represented in yellow color and the negative phase in cyan color. The HOMO is localized mainly on aromatics, while the LUMO is relocated on the whole system. Moreover, electron orbital delocalization can be seen across imine bonds for HOMO. The LUMO is antibonding orbital ( $\pi^*$ ) with respect to the C=N which justifies the  $\pi \to \pi^*$  excitation according to FMO of EE configuration.

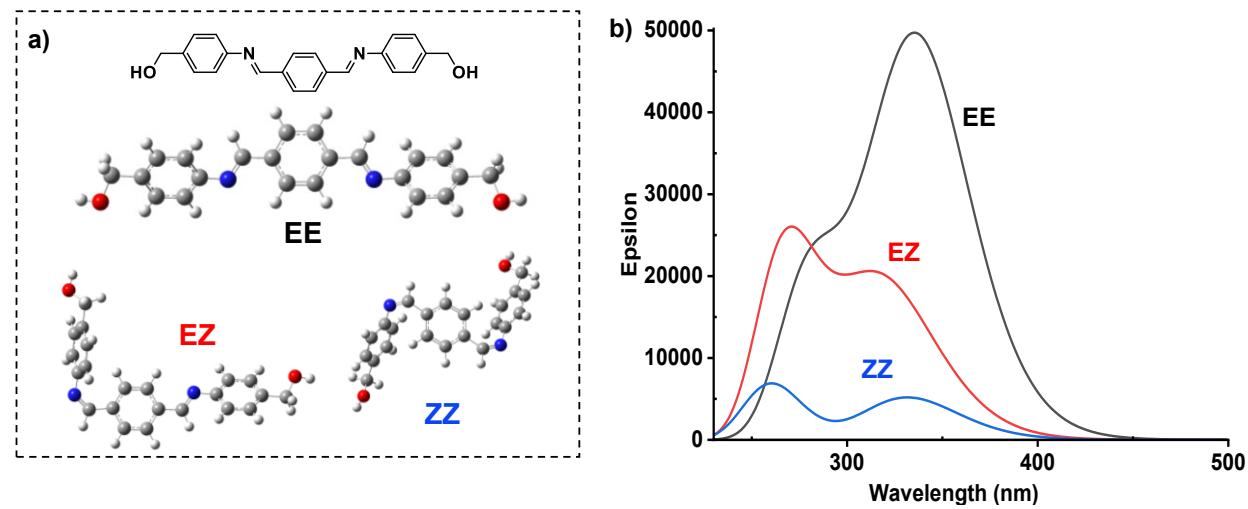


**Figure 4.7**. Three M3 configurations as EE, EZ, and ZZ (a) and absorption spectra of EE (black), EZ (red) and ZZ (blue) configurations calculated via TD-DFT (b).

The light-responsive degradation was also investigated for the M2 structure shown in Figure S4.14. Based on the PES of M2, the E configuration of M2 conjugated system is the more stable compared to the Z configuration due to the steric effect between two aromatic groups (Figure S4.15). DFT calculations estimate an activation energy ( $\Delta G^{\dagger}_{Z}$ ) of 17 kcal/mol for the transition from E to Z configuration. Figure S4.16 shows the absorption spectra of E (blue) and Z (red) configurations calculated via TD-DFT where exists two peaks for the E isomer with  $\lambda_{max} = 288$  nm and  $\lambda_{max} = 336$  nm which are in good agreement with the experimentally obtained UV-Vis spectra. The red curve in Figure S4.17 shows the UV/Vis spectra for the Z isomer with a peak at  $\lambda_{max} = 272$  nm. The blue shift and decrease in absorbance are predicted upon isomerization of C=N in M2 that follows a similar trend to M3 conjugated system.

## 4.3.8. Encapsulation and Dual Acidic pH/Light-Responsive Release of Cur

Cur is a potent bioactive agent with therapeutic effects against various diseases, including cancer. Since being hydrophobic, Cur could be encapsulated in hydrophobic cores of P-Im3-Aq nanogels mainly through hydrophobic-hydrophobic interaction. Here, Cur-loaded aqueous nanogels (P-Im3-Aq/Cur) in colloidally stable, yellow suspension were fabricated by the addition of a solution of Cur in DMSO to aqueous P-Im3-Aq dispersion, followed by purification with dialysis and filtration (Figure 4.8a). With the pre-determined extinction coefficient of Cur ( $\epsilon$  = 55,000 M-1cm-1) in THF/water (1/1 v/v) (Figure S.18) and UV/Vis spectrum of aqueous P-

Im3-Aq/Cur dispersion (Figure S4.19), the loading level of Cur to be 4.7 wt% and its loading efficiency to be 24.5% were determined. DLS analysis reveals that it had an average diameter of 130 nm (Figure 4.8b).

The fabricated P-Im3-Aq/Cur was next evaluated for *in vitro* release of Cur in acidic pH, upon the irradiation of visible light, and both, using UV/Vis spectroscopy. For light responsive release, aliquots in quartz cuvette were exposed to visible light at  $\lambda$  = 420 nm. Due to poor solubility in water, Cur released from nanogels was precipitated from the solution. UV/Vis spectra of supernatants were recorded for given time intervals (Figure S4.20). The absorbance at  $\lambda$  = 430 nm was used to determine the amount of released Cur and thus %release. As seen in Figure 4.8c, %release significantly increased to reach 80% within 8 hrs. Compared with negligible release of Cur under dark conditions, such enhanced release of Cur under visible light could be attributed to structural change of benzoic imine bonds through photo-induced E/Z isomerization, causing the destabilization of Cur-loaded cores. Although the empty P-Im3-Aq nanogels did not exhibit noticeable distortion of the structural integrity under visible light (Section 4.3.6), this can be attributed to the chemically crosslinked nature of the core network. Consequently, E/Z isomerization alone could be experienced in large-scale disassembly of the nanogels but remains effective in locally perturbing the microenvironment surrounding the encapsulated drug, thereby promoting its release.

For pH-responsive release, aliquots were incubated at endo/lysosomal pH = 5.0 and physiological pH = 7.4 for comparison. UV/Vis spectra of supernatant were recorded at given time intervals (Figure S4.21). As compared in Figure 4.8d, %release was less than 10% at pH = 7.4 up to 25 hrs, which could be attributed to natural loss. At pH = 5.0, %release increased to 51% in 20 hrs, which could be attributed to acid-responsive degradation of nanogels through acid-catalyzed hydrolysis of benzoic imine bonds. More promisingly, when P-Im3-Aq/Cur was irradicated by visible light in acidic pH = 5.0, % release was synergistically accelerated, reaching 70% within 15 hrs (Figure S4.22). Such rapid release results from the dual-responsive degradation mechanism, involving both the cleavage of conjugate benzoic imine linkages within the crosslinked core and the destabilization of the core structure through benzoic imine isomerization.

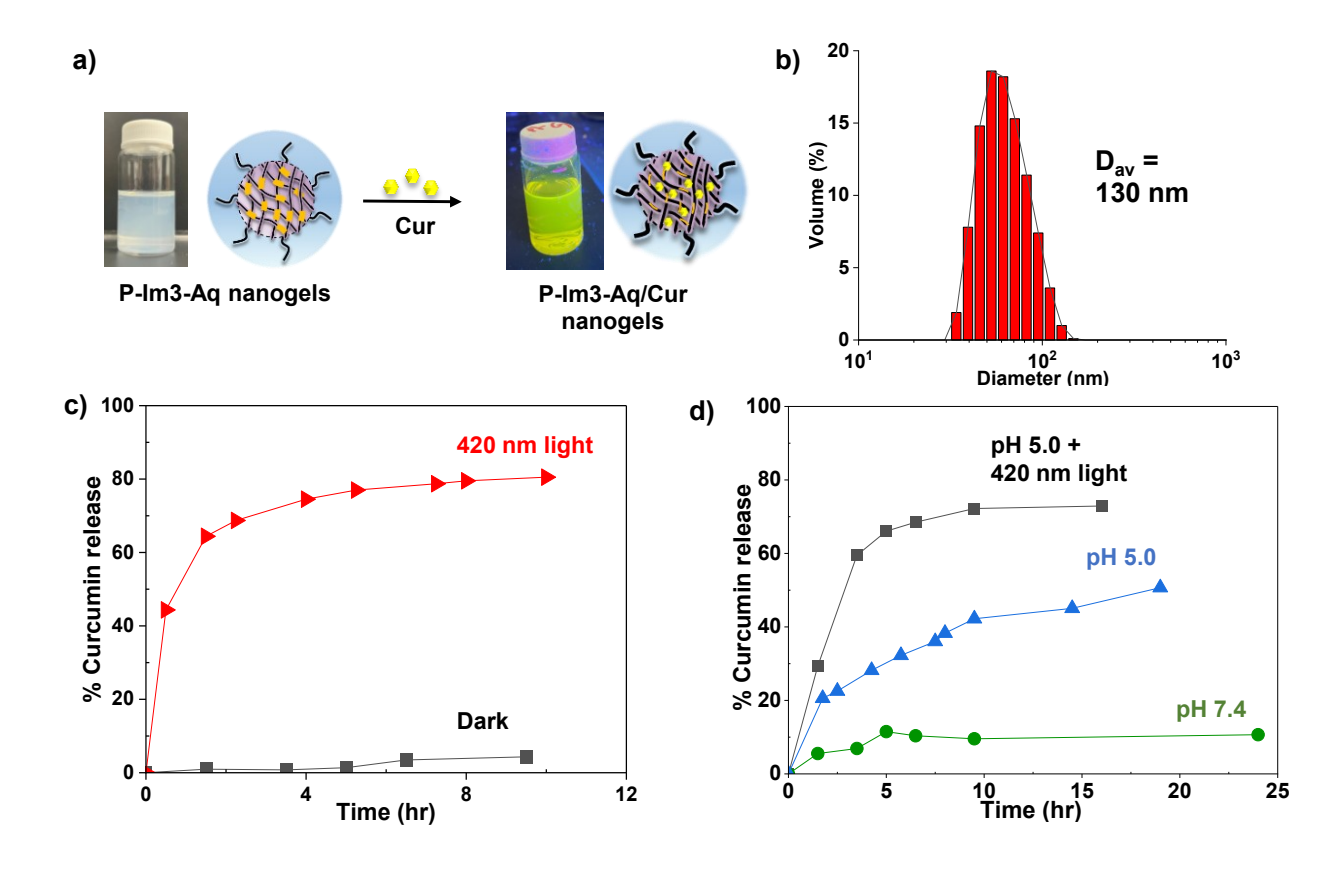


**Figure 4.8**. Digital images (upon the irradiation of UV light at 365 nm) and schematic representation of Cur encapsulated in crosslinked nanogels (P-Im3-Aq) to form P-Im3-Aq/Cur nanogels (a), DLS diagram of aqueous P-Im3-Aq/Cur (b), and %release of Cur from P-Im3-Aq/Cur upon irradiation of visible light at 420 nm, compared with in dark as a control (c), and in acidic pH = 5.0, compared in pH = 7.4, as well as both (d), by UV/Vis spectroscopy. Note that light-responsive release experiment (Figure 4.8c) was done in the greater concentration of P-Im3-Aq/Cur nanogels than acid- and dual-acid/light responsive release experiment.

# 4.3.9. Intracellular trafficking and anti-tumor activity

Given the promising results with dual acid/light-responsive degradation and Cur release, the P-Im3-Aq/Cur nanogels were evaluated as a mechanism for effective intracellular drug delivery of Cur. Figure 4.9a shows the viability of HeLa (human cervical adenocarcinoma) cells to be >90% when incubated with empty nanogels up to 240  $\mu$ g/mL, which suggests that they are not toxic to cells and are biocompatible. As shown in Figure 4.9b, the viability of HeLa cells decreased to 50% when incubated with increasing concentrations of P-Im3-Aq/Cur nanogels up to 240  $\mu$ g/mL (equivalent to 11.2  $\mu$ g/mL). The viability of HeLa cells dropped to below 10% with >5  $\mu$ g/mL of free Cur, and the IC50 was calculated to be 2.72  $\mu$ g/mL (equivalent to 7.39

 $\mu$ M), which is in the range of literature values (3.36-13.8  $\mu$ M for HeLa cells). The linear reduction in the viability of HeLa cells with increasing concentrations of P-Im3-Aq/Cur nanogels suggests that there is controlled release of Cur.

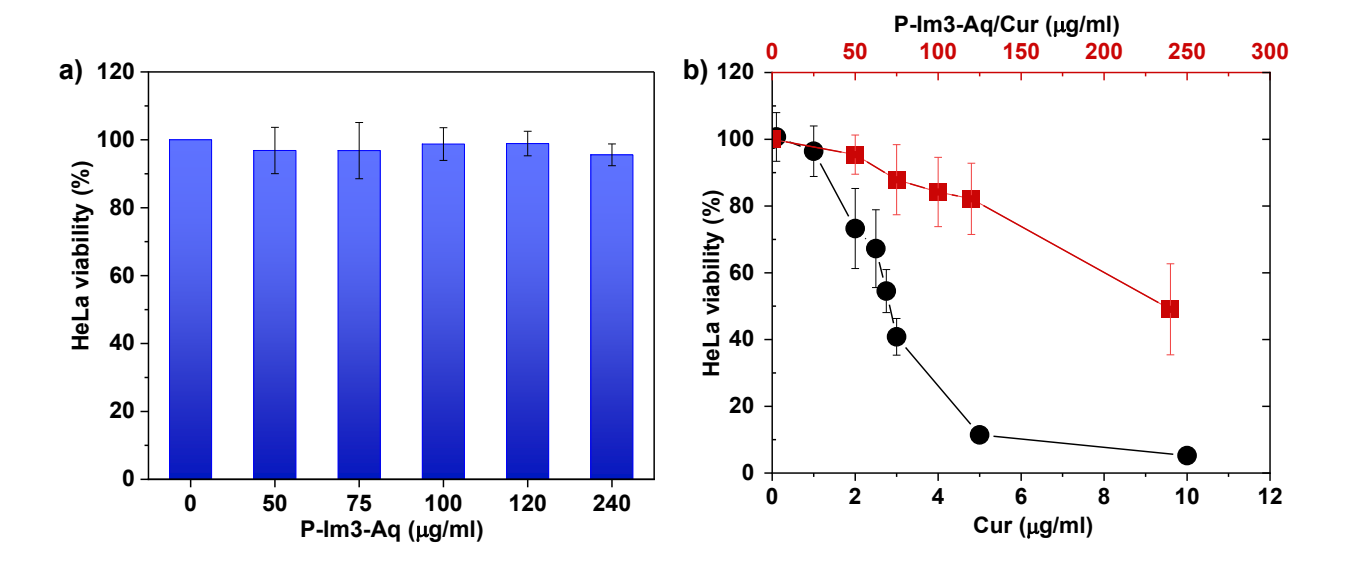


**Figure 4.9**. The viability of HeLa cells (%, y-axis) after incubation for 72 hrs with different concentrations of empty P-Im3-Aq nanogels ( $\mu$ g/mL, x-axis) is shown in the bar graph (a). Line graphs show the change in HeLa cell viability (%, y-axis) after incubation with different concentrations of P-Im3-Aq/Cur nanogels ( $\mu$ g/mL, top x-axis, red line) compared with free Cur ( $\mu$ g/mL, bottom x-axis, black line) (b). The averages are shown with error bars as standard deviations for all replicates (n = 9).

Next, the cellular uptake of P-Im3-Aq/Cur nanogels was evaluated in HeLa cells using live-cell imaging with a spinning disk confocal microscope. Figure 4.10 shows fluorescence images of HeLa cells after incubation with P-Im3-Aq/Cur nanogels for 2 hrs (bottom), compared with empty P-Im3-Aq nanogels (middle) and free Cur (top). The nuclei shown in magenta were stained with SYTO Deep Red Nucleic Acid Stain and Cur fluorescence is shown in green. Free Cur and P-Im3-Aq/Cur nanogels exhibited a distinct perinuclear accumulation, indicating efficient cellular uptake by the endomembrane network. In contrast, cells with empty nanogels showed no detectable fluorescence for Cur. These results support that P-Im3-Aq/Cur nanogels can enter cells allowing for the delivery of Cur.

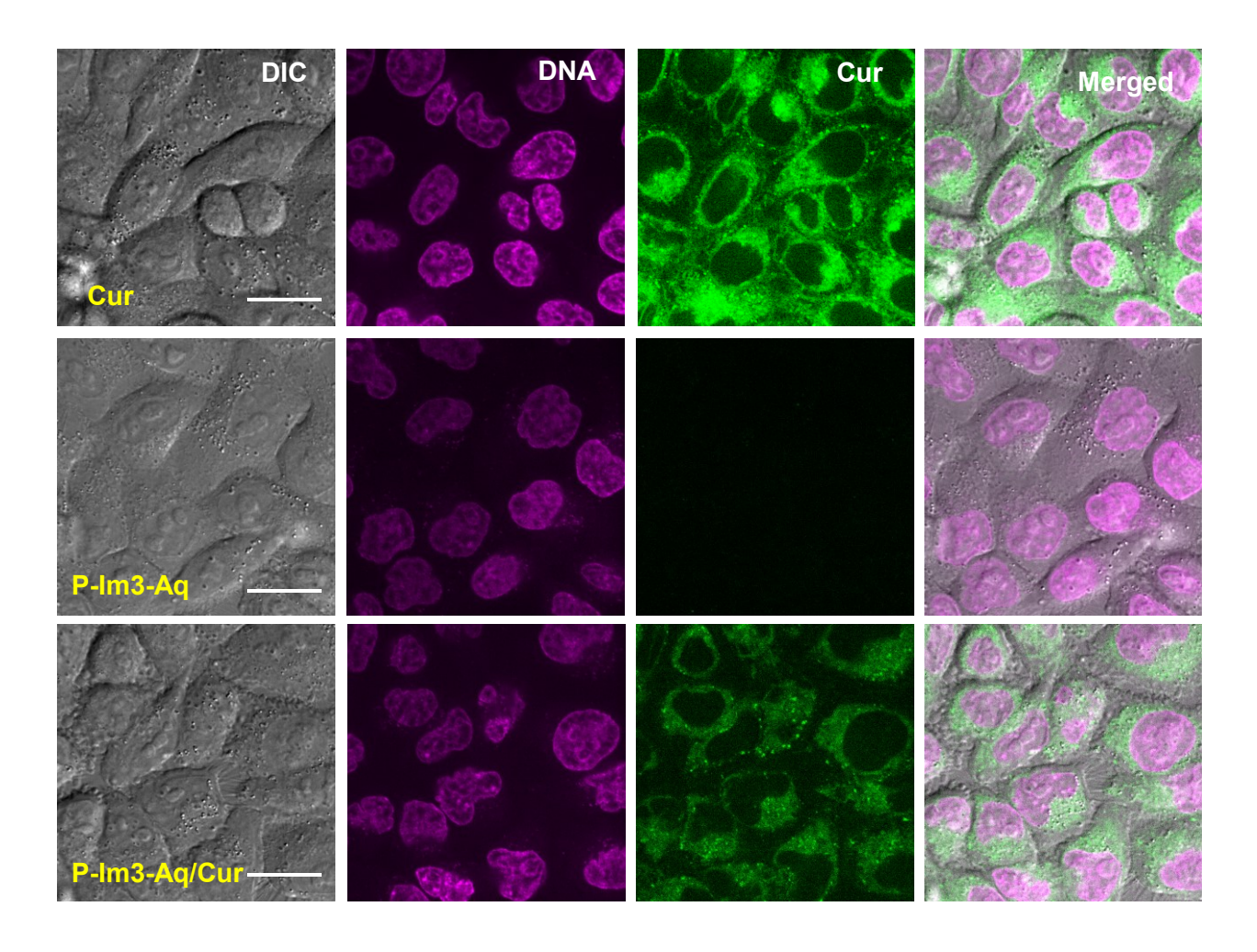


**Figure 4.10**. Images show HeLa cells 2 hours after incubation with free Cur (2.72  $\mu$ g/mL) (top), empty P-Im3-Aq (240  $\mu$ g/mL; middle), and P-Im3-Aq/Cur nanogels (240  $\mu$ g/mL; bottom). DIC shows a field of cells, magenta shows the nuclei, green shows Cur, and the merged shows the three channels together. The images for each channel were collected using the same optical settings and similarly processed. The scale bar is 20  $\mu$ m.

### 4.4. Conclusion

We developed a robust approach exploring pre-crosslinking dispersion to fabricate colloidally stable, core-crosslinked nanogels exhibiting dual acid/visible light response with a single extended conjugate aromatic imine bond. A well-defined PEG-b-PCIMA block copolymer synthesized by RAFT polymerization reacted with a novel M3 diol crosslinker bearing extended conjugate benzoic imine bond through a CDI-mediated coupling reaction in an organic solvent. Following mechanical dispersion of the formed crosslinked polymers in aqueous solution allows for the fabrication of well-defined core/shell nanogels with hydrophobic cores crosslinked

through the formation of carbonate linkages, surrounded with hydrophilic PEG corona. The nanogels were spherical with monomodal distribution and were non-cytotoxic. When exposed to acidic pH and visible light, the nanogels (e.g., crosslinked cores) degraded, confirmed by DLS and TEM analyses. Such degradation could be attributed to the acid-catalyzed hydrolysis in acidic pH, while photo-induced E/Z isomerization of aromatic imine bonds upon the irradiation of visible light, confirmed by <sup>1</sup>H NMR spectroscopy and computational DFT studies. The nanogels were capable of encapsulating up to 4.6% of the Cur anticancer drug. They exhibited the accelerated and synergistic release of Cur in a combination of acidic pH and visible light, and entered HeLa cells, reducing their viability. Notably, compared to free Cur, the linear reduction in cell viability suggests that Cur was released in a controlled manner, which could be highly desired as a method to reduce the side-effects caused by treatments using free drug. These findings underscore the potential of the core-crosslinked nanogels bearing extended conjugate aromatic imine bonds as a promising platform for dual stimuli-responsive drug delivery, where dual acidic pH and visible light response enable enhanced control for advanced cancer therapy.

# Chapter 5. Synthesis and Dual Acid/Visible Light-Responsive Degradation of Step-Growth Conjugated Poly(benzoic imine) Nanocolloids

#### 5.1. Introduction

Stimuli-responsive degradable (SRD) polymeric nanomaterials have attracted considerable attention in recent years due to their tremendous potential for site-specific, controlled drug delivery.  $^{229-237}$  Toward tumor-targeting drug delivery, biodegradation in response to endogenous stimulus found in cancer cells and tumor tissues is highly desired for the controlled/enhanced release of encapsulated therapeutics.  $^{14, 156, 158, 159, 166-168, 204, 210}$  Acidic pH is a typical endogenous stimulus found in tumoral compartment at pH = 6.5-6.9 and in endo/lysosomes at pH = 4.5-5.5.  $^{169-171}$  In addition to endogenous stimulus, visible or near infrared light is an exogenous, non-invasive, and precisely tunable stimulus capable of spatiotemporal control for the on-demand release of therapeutics.

Ketal, acetal, and imine are typical acid-labile groups, while o-nitrobenzyl and coumarin dimer are photo-cleavable moieties. A common approach involves the incorporation of these cleavable groups individually to single acid- 44,172-174,177,205-207 and light-degradable 138,175,176 nanomaterials and further dual acid/light-degradable 131,178,179,238-240 nanomaterials. Distinct from these approaches, an elegant approach to achieve dual acid/light responsive degradation with single conjugate benzoic imine through acid-catalyzed hydrolysis and photo-induced E/Z isomerization has been reported with poly(ethylene glycol) (PEG)-based block copolymer nanoassemblies bearing conjugate benzoic imine pendants 208 and core-crosslinked nanogels with extended conjugate benzoic imine groups. Given our promising findings, we have expanded our concept to macromolecular systems and investigated if the further extension of conjugation of aromatic imine bonds can respond to visible and even near infrared light.

In this work, we explored a dual acid/visible light-responsive nanoplatform based on extended conjugate poly(benzoic imine) (M-PC) with backbone aromatic benzoic imine bonds. The M-PCs were synthesized by step-grow polycondensation of aromatic diamines and

dialdehydes. They turned to be linear, highly conjugated, and limited of solubility in organic solvents, while enabled to absorb visible light. They were fabricated to colloidally-stable aqueous nanocolloids with an aid of polymer stabilizers of a mixture of poly(vinyl alcohol) (PVA) with PEG. Owing to acid/visible light-response of conjugate benzoic imine bonds in M-PC polymers, the fabricated nanocolloids degraded in acidic pH and upon the irradiation of visible light.

# 5.2. Experimental

#### **5.2.1.** Instrumentation

 $^{1}$ H NMR spectra were recorded on a 500 MHz Varian spectrometer, using the quintet of DMSO-d<sub>6</sub> at 2.5 ppm as reference standard. UV/vis spectra were recorded on an Agilent Cary 60 spectrometer with a 1 cm quartz cuvette. The hydrodynamic diameter and size distribution of aqueous nanocolloids were analyzed by dynamic light scattering (DLS) on a Malvern Nano S ZEN1600 system, equipped with a 633 nm He-Ne laser at a fixed scattering angle of 175° and a temperature of 25 °C. Mass Spectroscopy (MS) analysis for M-PC was conducted using a Thermo LTQ Orbitrap Velos mass spectrometer equipped with a heated electrospray ion source. A full MS spectrum (m/z 150-2000) was acquired in the Orbitrap at positive mode at a resolution of 100000. Light-responsive experiments were performed using a PR160L Gen 2 LED lamp (Kessil, USA) at  $\lambda = 440$  nm (60 mW/cm²) and  $\lambda = 370$  nm (41 mW/cm²), with samples positioned 15 cm from the light source.

Transmission Electron Microscopy (TEM) images were obtained using a FEI Tecnai G2 F20 200 kV Cryo-STEM equipped with a Gatan Ultrascan 4000 4kx4k CCD Camera System Model 895. Aqueous dispersions (5 μL) were dropped onto 300-mesh copper TEM grids and incubated for 2 minutes. Excess liquid was gently blotted with filter paper. For negative staining, a 1% phosphotungstic acid solution was prepared by dissolving 5 mg of phosphotungstic acid in 0.5 mL deionized water, followed by the addition of 5 μL of 1 M sodium hydroxide and filtration through a 0.45 μm poly(ethylene sulfone) membrane. A drop of the staining solution was then applied to the grid, blotted again, and the grid was left to dry under a fume hood before imaging.

#### 5.2.2. Materials

Phenylenediamine (PPD, 98%), terephthaldehyde (TDA, 99%), poly(ethylene glycol) (PEG, MW = 1350-1595 g/mol), poly(vinyl alcohol) (PVA, Mw = 89,000-98,000 g/mol, 99% hydrolysed), and hexanal (98%) were purchased from Sigma-Aldrich and used as received.

#### 5.2.3. Polycondensation to Synthesize Conjugated Poly(benzoic imine)s (M-PCs)

Typically, a solution of PPD (18 μmol, 2 mg) dissolved in DMSO (2.9 mL) was mixed with a solution of TDA (18 μmol, 2.48 mg) dissolved in DMSO (3.5 mL) containing molecular sieves under stirring at room temperature for 24 h, yielding an orange-colored M-PC suspension in DMSO at 0.6 mg/mL. Similar procedure was examined with various amounts of PPD and TDA as mole equivalent ratio of NH<sub>2</sub>/CHO. The detailed recipe is summarized in Table S1.

# 5.2.4. Imine Metathesis Polymerization to Synthesize Conjugated Poly(benzoic imine)s (M-PC-D)

A solution of PPD (5.0 mmol, 541 mg) dissolved in diglyme (8.3 mL) was mixed with hexanal (10.0 mmol, 1.2 mL) and heated at 100 °C for 1 h under nitrogen. After cooled to room temperature, an aliquot of the mixture (0.2 mL) was mixed with a solution of TDA (0.1 mmol, 13.4 mg) dissolved in diglyme (2.8 mL). The resulting mixture was kept at 120 °C for 1 h, yielding a dark red-colored M-PC-D solution in diglyme.

#### 5.2.5. Acid-Responsive Degradation of M-PCs

A solution of M-PC dissolved in DMSO-d<sub>6</sub> (3 mL, 0.6 mg/mL) for  $^{1}$ H NMR spectroscopy and M-PC dissolved in DMSO (3 mL,18 µg/mL) for UV/Vis spectroscopy was mixed with HCl (3 µL, 10 mM) (equivalent to pH = 5 or pD = 5.4, calculated using pD = pH + 0.4). In addition to their  $^{1}$ H NMR spectra, UV/vis spectra were recorded to monitor change in absorbance at  $\lambda$  = 420 nm over irradiation time.

### 5.2.6. Light-Responsive Degradation of M-PCs

A solution of M-PC dissolved in DMSO (3 mL, 18  $\mu$ g/mL) in a quartz cuvette was exposed to visible light at  $\lambda = 440$  nm (60 mW/cm²) and UV light at  $\lambda = 370$  nm (41 mW/cm²). Their UV/vis spectra were recorded to monitor change in absorbance at  $\lambda = 420$  nm over irradiation time.

#### 5.2.7. Fabrication of Aqueous Stabilizer-Aided Nanocolloid Dispersions (PC-Im)

M-PC (0.6 mg) dissolved in DMSO (1 mL) was mixed with PEG (1 mg) dissolved in DMSO (1 mL) and then PVA (12.5 mg) dissolved in water (5 mL). The resulting dispersion was sonicated using a Branson sonifier for 30 sec (2 sec pulse on and 2 sec pulse off). The resulting dispersion was dialyzed with a dialysis tubing (MWCO = 12,000 Da) for 24 h against water to remove DMSO and then purified by filtration with a disk-type PES filter (0.45  $\mu$ m pores), yielding aqueous PC-Im nanocolloid dispersions.

# 5.2.8. Acid-Responsive Degradation of Aqueous PC-Im Nanocolloids

Aqueous PC-Im (2 mL, 2 mg/mL) was mixed with 0.2 M sodium acetate buffer solution at pH = 5.0 (2 mL) under stirring at room temperature. Aliquots were taken for given time periods for UV/vis spectroscopy, DLS, and TEM analysis.

# 5.2.9. Light-Responsive Degradation of Aqueous Nanocolloids

Aqueous PC-Im (3 mL) in a quartz cuvette was exposed to visible light at  $\lambda = 440$  nm (60 mW/cm<sup>2</sup>) and UV light at  $\lambda = 370$  nm (41 mW/cm<sup>2</sup>). Their UV/vis spectra were recorded to follow any change in absorbance at  $\lambda = 365$  nm. Aliquots were taken for DLS and TEM analysis.

#### 5.3. Results and Discussion

#### 5.3.1. Synthesis and UV/vis Absorption Characteristics of M-PCs

Approach I by Polycondensation. As depicted in Figure 5.1a, our Approach I explores the polycondensation of PPD with TDA in DMSO at room temperature, eliminating water molecules as a side product, through the formation of extended benzoic imine bond, thus yielding poly(PPD-TDA)-based M-PCs. DMSO was chosen because it is a good solvent for both aromatic amines and aldehydes. Initially, designed with the mole equivalent ratio of NH<sub>2</sub>/CHO = 1/1 of TDA and PPD in DMSO at 0.7 mg/mL, polymerization was followed by UV/vis spectroscopy. As seen in Figure S5.1, the absorption at  $\lambda = 420$  nm which corresponds to a  $\pi \rightarrow \pi^*$  transition of conjugated benzoic imine bonds increased while the absorption at  $\lambda = 310$  nm decreased over time up to 25 h. Furthermore, the color of the polymerization mixture changed from pale yellow to orange, which could be attributed to the formation of conjugated benzoic imine bonds. The synthesized M-PC was purified by precipitation from diethyl ether.

Figure 5.1b of  $^{1}$ H NMR spectrum shows the characteristic peaks at 8.7 ppm (b) corresponding to benzoic imine protons and 6-8 ppm (c) to aromatic protons in M-PC backbone as well as 10 ppm (a) corresponding to terminal aldehyde protons. Their integral ratio (a and c) could allow to estimate the degree of polymerization (DP) of the formed poly(benzoic imine) to be 3-6, in assumption that all polymer chains are terminated with both aldehyde and amino groups. The DP appeared to be consistent with that of 2-5 determined by MS analysis (Figure S5.2). GPC analysis was not straightforward because of the low solubility of the polymer in DMF. Figure 5.1c compares the UV absorption of M-PC with M1 (a conjugated benzoic imine) $^{208}$  and M3 (an extended benzoic imine). Promisingly, M-PC exhibits the absorption at  $\lambda = 340$ -540 nm with the maximum absorption at  $\lambda = 420$  nm, which is red-shifted, compared with M1 and M3.

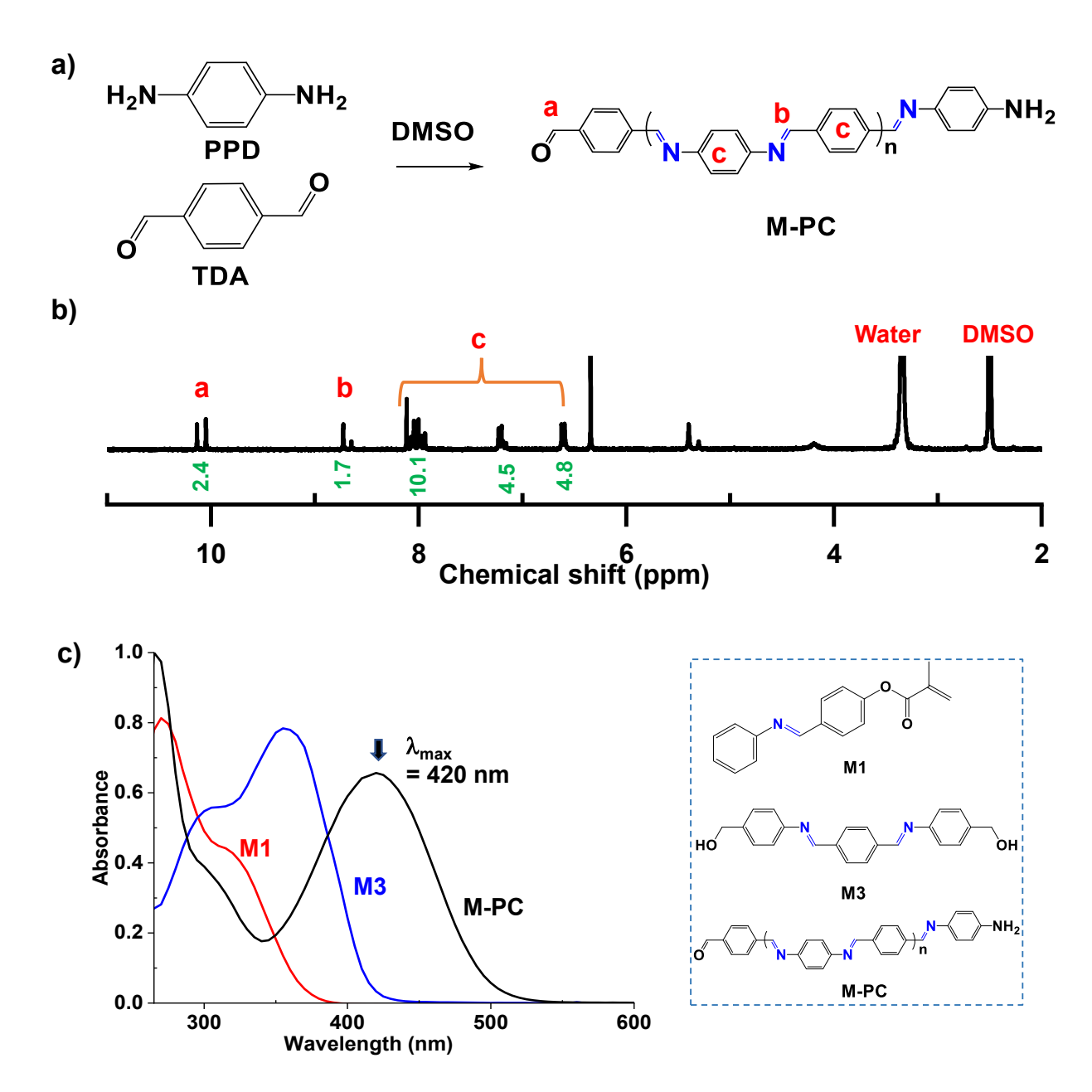


**Figure 5.1**. For conjugated M-PC, synthetic scheme with Approach I exploring polycondensation of PPD with TDA in DMSO (a), <sup>1</sup>H NMR spectrum in DMSO-d<sub>6</sub> (b), and UV/vis spectrum, compared with those of M1 (a methacrylate bearing a conjugated benzoic imine bond) and M3 (a diol bearing an extended benzoic imine bond) in DMSO (c).

In a separate experiment, the mole equivalent ratio of NH<sub>2</sub>/CHO was varied in DMSO at as high as 20 mg/mL concentration of TDA and PPD, where the formed polymers were precipitated during polymerization. This could be because the poly(benzoic imine) has a highly conjugated, rigid backbone. The precipitated polymers were characterized for their absorption characteristics.

As seen in Figure 5.2a and 2b, the maximum absorption was red shifted from  $\lambda = 405$  to 425 nm, when the ratio increased from 0.8/1 to 1.5/1. According to Carothers theory, a major population could be M-PC terminated with CHO groups at both ends with NH<sub>2</sub>/CHO = 0.8/1 (i.e. CHO excess), while M-PC terminated with NH<sub>2</sub> at both ends with NH<sub>2</sub>/CHO = 1.25/1 (i.e. NH<sub>2</sub> excess). Given this prediction, the plausible reason for the ref-shift could be the electronic effect of terminal NH<sub>2</sub> (electron-donating group) vs CHO (electron-withdrawing group).

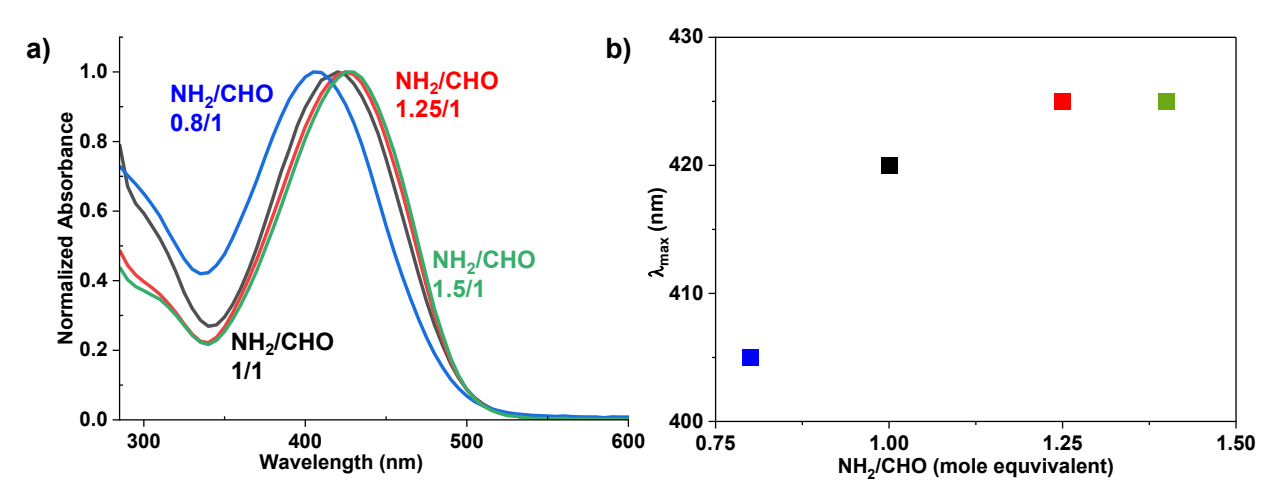


**Figure 5.2**. Overlaid UV/vis spectra (a) and evolution of  $\lambda_{max}$  (b) of M-PC with varying NH<sub>2</sub>/CHO mole equivalent ratio.

Approach II by Imine Metathesis Polymerization. The challenge of M-PC prepared by polycondensation is its low solubility in DMSO. The plausible reason could be because M-PC is a linear and highly conjugated aromatic imine. Inspired from literature,<sup>242</sup> imine metathesis polymerization was explored (Figure 5.3a), which consists of two steps including i) the reaction of PPD with hexanal to form Im-precursor and ii) its imine metathesis with TDA in diglyme at 120 °C, yielding M-PC-D extended poly(benzoic imine).

M-PC-D had better solubility in DMSO. However, as compared in Figure 5.3b, M-PC-D had a maximum absorption at  $\lambda_{max} = 355$  nm, which is lower than that ( $\lambda_{max} = 420$  nm) of M-PC prepared by polycondensation. This spectral difference could be attributed to the less conjugation of benzoic imine bonds in M-PC-D.

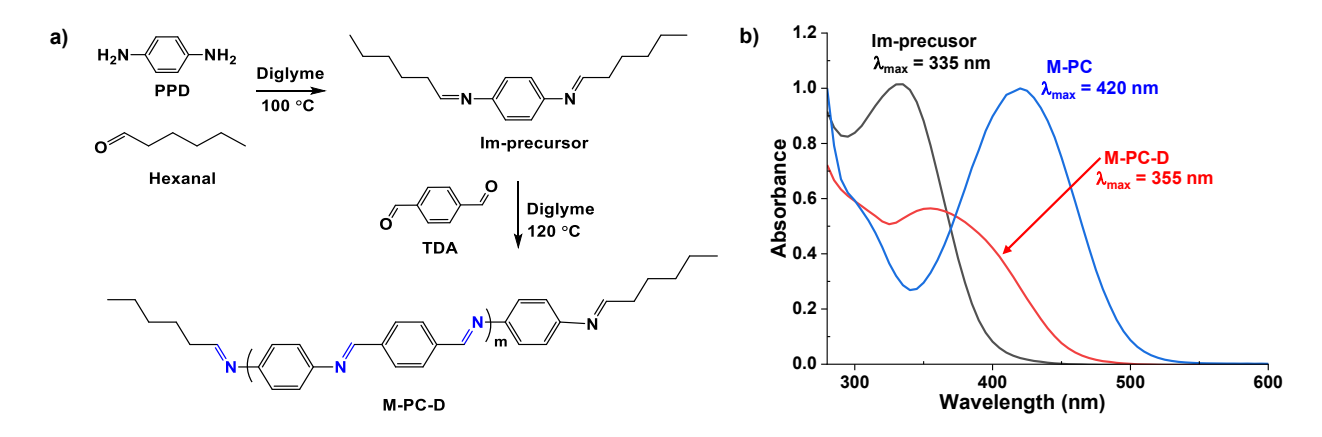


**Figure 5.3**. For M-PC-D, synthetic scheme by Approach II exploring imine metathesis polymerization with two steps including i) the reaction of PPD with hexanal to form Imprecursor and ii) its imine metathesis with TDA in diglyme at 120 °C (a). UV/vis spectrum of M-PC-D in DMSO, compared with those of Im-precursor in diglyme and M-PC in DMSO (b).

# 5.3.2. Studies of Acid- and Light-Responsive Degradation of M-PCs

Conjugated benzoic imine bonds in M-PC could be cleaved in acidic pH through acid-catalyzed hydrolysis to corresponding aldehyde and amine, as depicted in Figure 5.4a. <sup>1</sup>H NMR spectroscopy was used in DMSO-d<sub>6</sub> containing HCl (equivalent to pH = 5) for 2 h. <sup>1</sup>H NMR spectrum in Figure 5.4b shows the disappearance of the peak at 8.7 ppm (a) corresponding to imine protons and the appearance of a new peak at 10.1 ppm (b) corresponding to aldehyde protons. Their integral ratio confirms the 80% cleavage of imine bonds. Because of the loss of conjugation, its UV/vis absorption rapidly decreased within 30 min in DMSO containing HCl (Figure 5.4c).

Conjugated benzoic imine bonds could respond to light. UV/vis spectroscopy was used in DMSO at 18  $\mu$ g/mL. Upon the irradiation of UV light at  $\lambda$  = 370 nm, the maximum absorption at  $\lambda$  = 420 nm decreased to >90% and interestingly was blue-shifted over 24 h, indicating a significant change in electronic structure of conjugated benzoic imine bonds (Figure 5.4d and 4f). Upon the irradiation of visible light at  $\lambda$  = 440 nm, the maximum absorption slowly decreased by 20% with no substantial blue shift in the wavelength (Figure 5.4e and 4f). This disparity in response to UV and visible light highlights the selective sensitivity of conjugated imine bonds to higher energy UV photons. The spectral changes under UV/vis light could be

attributed to photo-induced E/Z isomerization of conjugated benzoic imine bonds present in the M-PC backbone. <sup>208</sup>

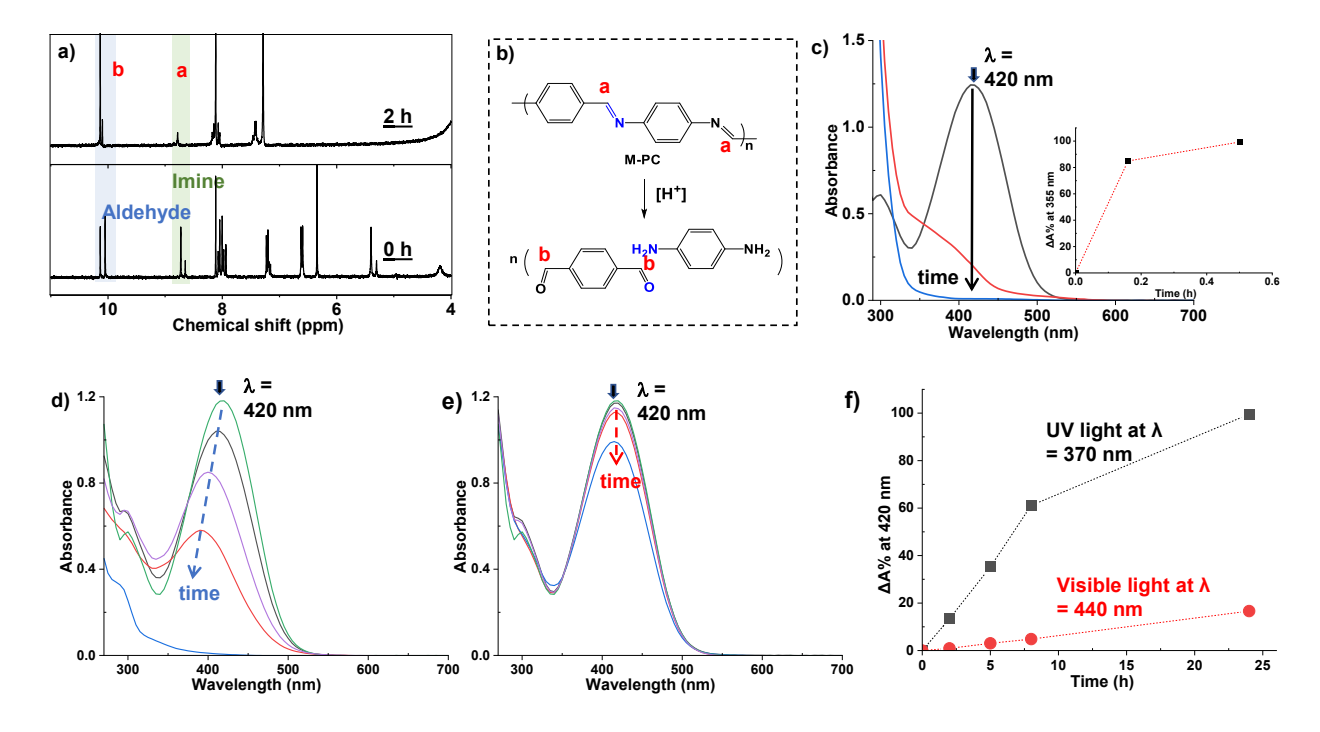


**Figure 5.4.** For acid response of M-PC, acid-catalyzed hydrolysis of conjugated benzoic imine bonds (a), overlaid  $^1H$  NMR spectra in DMSO-d<sub>6</sub>/HCl before and after 2 h of incubation (b), and overlaid UV/vis spectra and %change in absorbance at  $\lambda = 420$  nm over incubation time (c). For light response of M-PC, overlaid UV/vis spectra in DMSO under irradiation of UV light at  $\lambda = 370$  nm (d) and visible light at  $\lambda = 440$  nm (e) and %change in absorbance at  $\lambda = 420$  nm over 24 h of irradiation (f).

#### 5.3.3. Fabrication of Aqueous Stabilizer-Aided Nanocolloids

The M-PC polymers synthesized by polycondensation are hydrophobic and thus require external stabilizers to form colloidally stable nanocolloids in aqueous solution. A mixture of low molecular weight PEG (MW = 1,300 g/mol) with high molecular weight PVA (MW  $\approx$  85 kg/mol) were employed as polymeric stabilizers. PEG offers biocompatibility and anti-fouling properties; however, its low molecular weight limits surface tension reduction. The addition of PVA as a co-stabilizer to PEG is known to facilitate to fabricate aqueous colloidal dispersions.

An organic solution of M-PC and PEG dissolved in DMSO was mixed with aqueous solution of PVA under the conditions of M-PC = 0.6 mg/mL, (PEG+PVA)/M-PC = 22.5/1 w/w, and PVA/PEG = 12.5/1 wt/wt. After sonicated, the resulting dispersion was subjected to dialysis

against water, yielding aqueous M-PC nanocolloids surrounded with PEG and PVA stabilizers (PC-Im). The formed nanocolloids had a hydrodynamic diameter of  $203 \pm 2$  nm in a wet state, by DLS analysis (Figure 5.5a), while  $131 \pm 38$  nm in a dry state, by TEM analysis (Figure 5.5b). They had good shelf stability over four weeks. The colloids were further characterized for their UV/vis absorption characteristics (Figure 5.5c). They had the absorption maximum at  $\lambda = 365$  nm, which turns to be blue-shifted from that ( $\lambda = 420$  nm) of M-PC precursor in DMSO. The plausible reason could be attributed to the gradual degradation of M-PC in aqueous solution (which is slightly acidic) during the storage for several days.

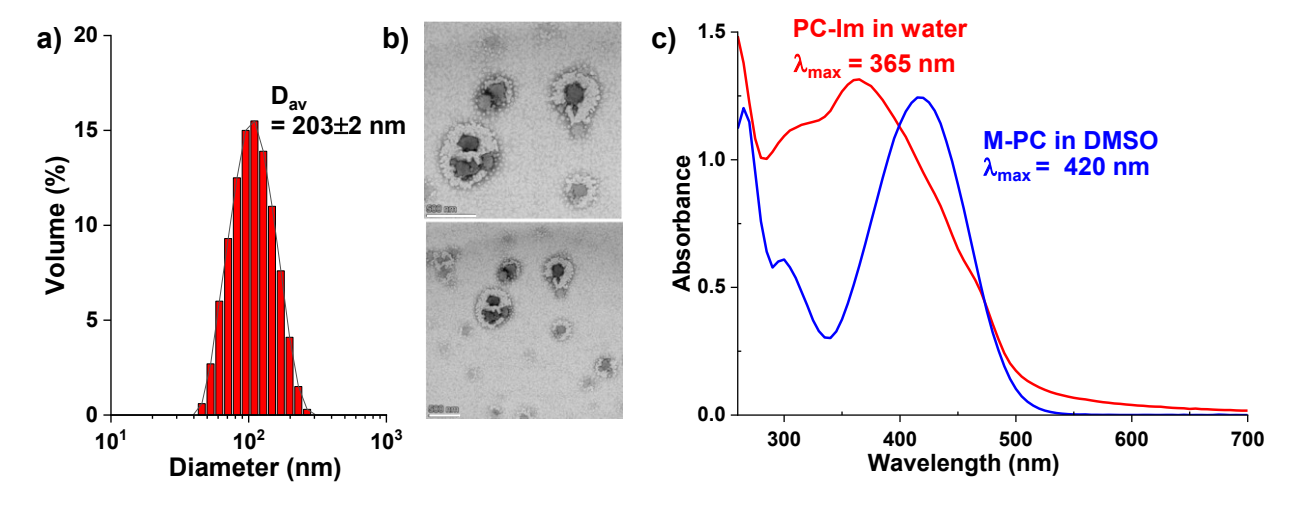


**Figure 5.5**. DLS diagram (a), TEM images with different magnifications (scale bar = 500 nm) (b), and UV/vis spectrum (c) of aqueous PC-Im nanocolloids compared with that of M-PC in DMSO.

#### 5.3.4. Acid- and Light-Responsive Disassembly

Given our studies on acid- and light-responses of M-PC polymers, the disassembly of PC-Im nanocolloids in response to acidic pH and light was investigated.

For acid-responsive disassembly, nanocolloids were incubated in acidic buffer at pH = 5.0 and their stability and degradation were followed by UV/vis spectroscopy and DLS. As seen in Figure 5.6a, their absorption decreased over incubation time and the absorbance at  $\lambda = 365$  nm decreased by >40% in 24 h, which could be attributed to the cleavage of conjugated benzoic imine bonds through their acid-catalyzed hydrolysis. Interestingly, their hydrodynamic diameter remained nearly unchanged over incubation time (e.g.  $D_{av} = 203$  nm at 0 h and 210 nm at 24 h)

(Figure 5.6b). This unexpected result could be attributed to the hydrophobic nature of degraded products (likely PPD with TDA). As a consequence, nanocolloids did not appear to be completely disintegrated, even though a majority of benzoic imine bonds on the backbones could be cleaved in acidic pH.

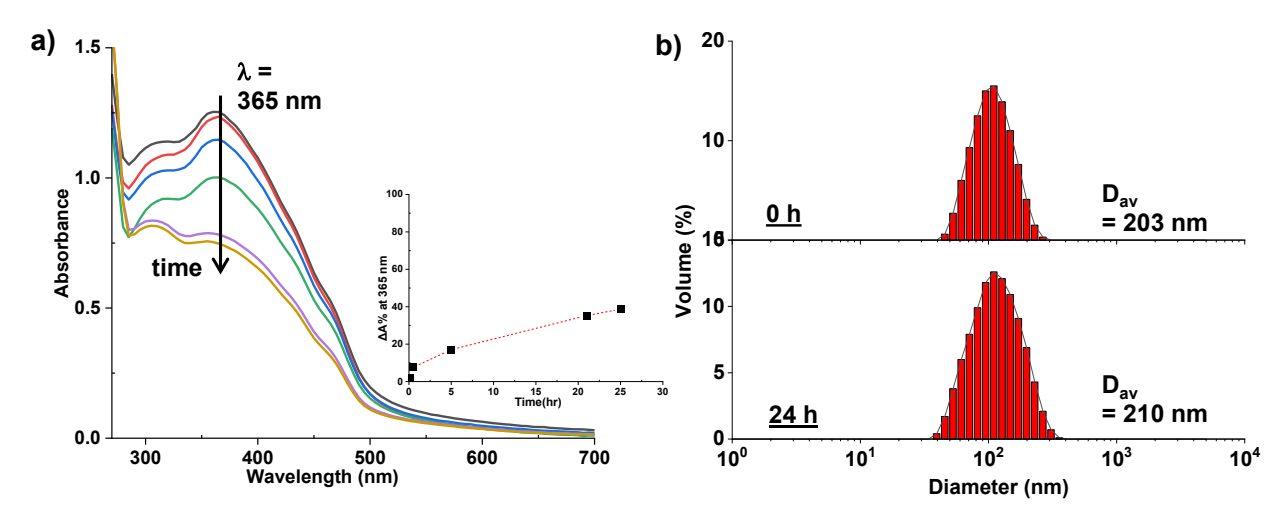


**Figure 5.6**. Overlaid UV/vis spectra of aqueous PC-Im nanocolloids incubated at pH = 5.0 over 24 h (inset: change in absorbance at  $\lambda = 365$  nm) (a) and their DLS diagrams before and after 24 h of incubation (b).

For light-triggered disassembly, the colloids were exposed to visible light at  $\lambda = 440$  nm and UV light at  $\lambda = 370$  nm. DLS analysis reveals that their diameter decreased from 205 nm to 180 nm over 24 h under visible light (Figure 5.7a), while it decreased more significantly from 205 nm to 134 nm under UV light (Figure 5.7b). Notably, absorption at  $\lambda = 365$  nm decreased by >50% over 24 h of visible light exposure, while it more pronouncedly decreased by >75% under UV irradiation (Figure 5.7c, 7d and 7e).

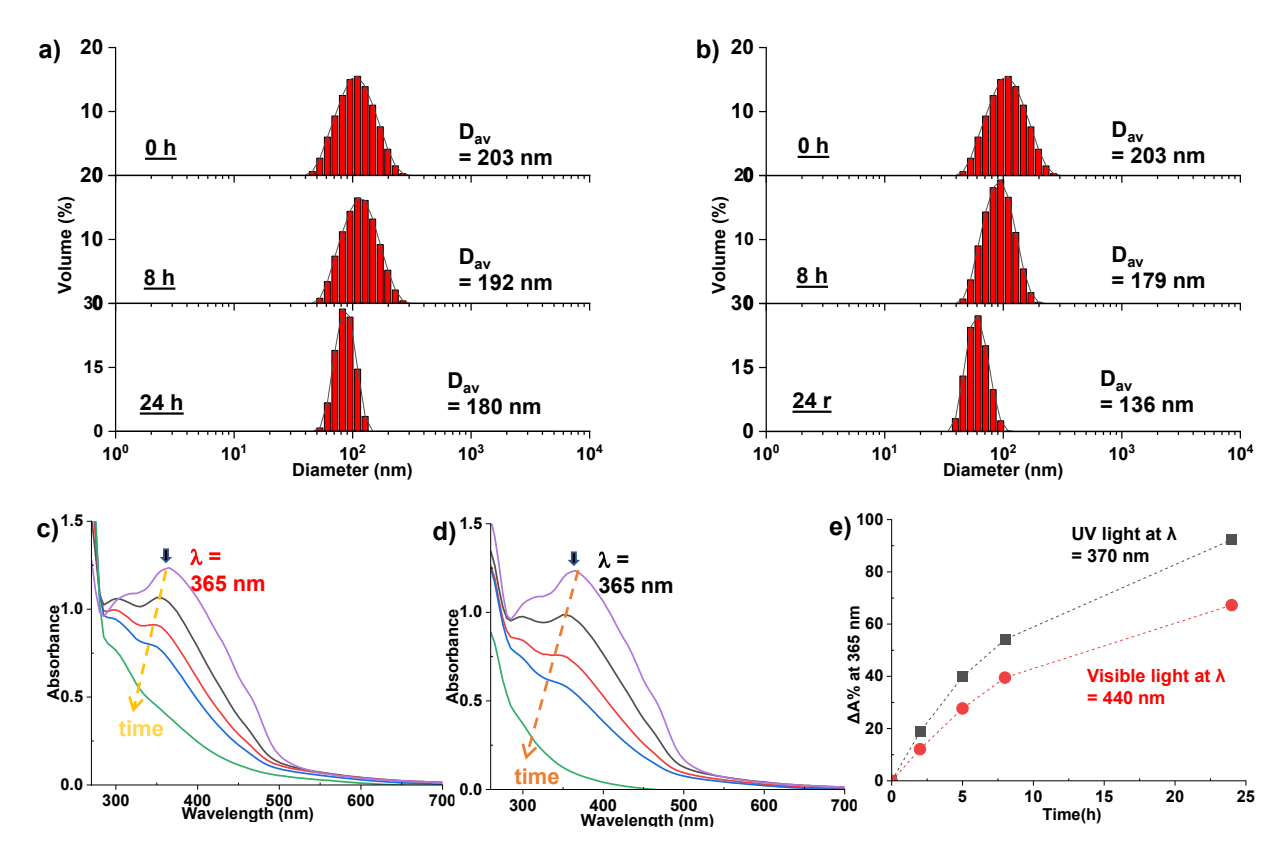


**Figure 5.7**. For light response of aqueous PC-Im nanocolloids, overlaid DLS diagrams under the irradiation of visible light at  $\lambda = 440$  nm (a) and UV light at  $\lambda = 370$  nm (b), their UV/vis spectra under the irradiation of visible light at  $\lambda = 440$  nm (c) and UV light at  $\lambda = 370$  nm (d), and %change in absorbance at  $\lambda = 365$  nm over 24 h of irradiation (e).

#### 5.4. Conclusion

Step-growth M-PCs polymers with conjugated benzoic imine bonds on the backbones were synthesized by polycondensation or imine metathesis polymerization approach. The M-PCs synthesized by polycondensation had the absorption in visible light region with the maximum at  $\lambda = 420$  nm. Because of their intrinsic hydrophobicity and limited solubility in organic solvents, PEG/PVA polymeric stabilizers were used for the fabrication of aqueous nanocolloids with good colloidal stability. The M-PC polymers and nanocolloids not only degraded upon the cleavage of backbone benzoic imine bonds in acidic environment but also in response to visible light ( $\lambda = 440$  nm). Given the promising dual acid and light response imparted by a single benzoic imine bond, this approach, together with forthcoming cytotoxicity assessments to evaluate the

cytocompatibility of the nanocolloids, holds considerable potential as an effective smart drug delivery.

## **Chapter 6. Summary and Future Directions**

#### 6.1. Summary of Thesis

Advancements in the development of stimuli-responsive degradable nanocarriers have propelled the development of dual-responsive systems which rely on distinct chemical functionalities to respond independently to acidic pH and light, thereby increasing synthetic complexity. Within this framework, conjugated benzoic imine chemistry offers a unique opportunity to integrate dual responses with a single labile linkage, eliminating the need for multiple cleavable moieties and thus simplifying synthetic design. This PhD research focused on the development of degradable polymeric nanocarriers that respond synergistically to acidic pH and UV/visible light through benzoic imine-based dynamic covalent linkages, with the aim of enabling controlled disassembly and effective intracellular drug delivery.

The central objective of this research was to design and evaluate PEG-based block copolymers and nanostructures bearing conjugated aromatic imine moieties, enabling controlled degradation under intracellular acidic conditions and visible or UV light. Three complementary polymer architectures were developed using synthetic strategies including RAFT polymerization, carbonyldiimidazole (CDI)-mediated post-polymerization conjugation, and step-growth imine polycondensation.

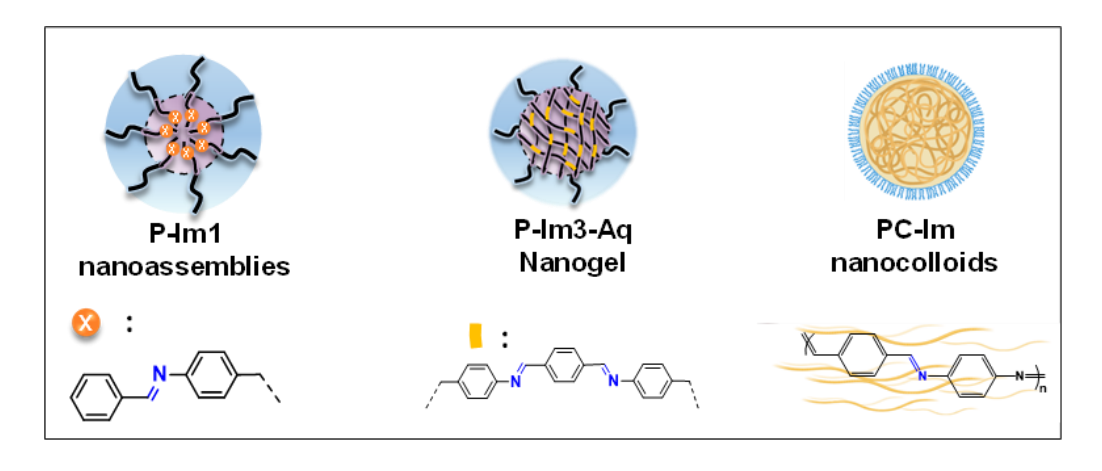
Chapter 3 presents a proof-of-concept study on the synthesis of PEG-b-PCIMA block copolymers bearing conjugated benzoic imine pendants, prepared by RAFT polymerization and post-polymerization conjugation. These amphiphilic polymers self-assembled into micelles with hydrophobic cores enriched in imine moieties. The micelles were colloidally stable under physiological conditions and disassembled under acidic pH and upon UV light ( $\lambda = 340$  nm) exposure. Mechanistic studies revealed that degradation was governed by acid-catalyzed hydrolysis and likely E/Z photoisomerization of the benzoic imine linkages, demonstrating the feasibility of employing a single responsive motif for dual-stimulus activation.

Chapter 4 advances this design by integrating extended aromatic imine bonds as crosslinkers within core-crosslinked nanogels. Using CDI-mediated pre-crosslinking in organic media, followed by aqueous dispersion, stable nanogels were generated with carbonate

crosslinked hydrophobic cores and PEG coronas. These nanogels were non-cytotoxic, encapsulated curcumin with 4.6 wt% loading, and showed synergistic disassembly under dual acid/visible light ( $\lambda$  = 440 nm) stimuli. Experimental validation using DFT supported the proposed degradation mechanisms attributed to E/Z isomerization of the conjugated imine. Enhanced curcumin release and intracellular activity in HeLa cells further confirmed their therapeutic promise.

Chapter 5 explores step-growth polycondensation to synthesize conjugated poly(benzoic imine) (M-PC) backbones, incorporating aromatic imines directly within the main chain. The resulting hydrophobic polymers absorbed strongly in the visible region ( $\lambda_{max} = 420$  nm), enabling visible light triggered degradation. These polymers were stabilized with PEG/PVA to form nanocolloids with high colloidal stability. These nanocolloids degraded efficiently under both acidic pH and light ( $\lambda = 440$  nm). This backbone-cleavable system offers a distinct degradation mechanism compared to pendant and crosslinked architectures, expanding the versatility of benzoic imine chemistry in stimuli-responsive platforms.

Together, these three systems, through precise macromolecular engineering and rigorous structure—property evaluation, establish a simplified, chemically coherent strategy for dual-responsive polymeric nanocarriers using a single dynamic covalent linkage, with strong implications for intracellular drug delivery and photo-triggered nanomedicine.



#### 6.2. Future Directions

Building upon the fundamental advances presented in this thesis, each system offers distinct opportunities for further refinement and application. Future work should focus on addressing current limitations and advancing the translational potential of the developed polymeric nanoassemblies. The following outlines specific directions for each research chapter:

In *Chapter 3*, the PEG-b-PCIMA micellar system exhibited dual acid/light-responsive disassembly but failed to encapsulate hydrophobic drugs, presumably because of the rigid PC-Im pendants restricting core flexibility. Future designs should incorporate soft, flexible hydrophobic segments, such as aliphatic chains or biodegradable polyesters, to improve core fluidity and enhance drug loading capacity. Adjusting the density and spatial distribution of PC-Im groups may also optimize core packing for more efficient encapsulation and release.

In *Chapter 4*, Given promising *in vitro* results with cell viability and cellular uptake, *in vivo* evaluation of the core-crosslinked nanogels based on PEG-b-PCIMA and the extended conjugated M3 crosslinker is essential to assess biodistribution, systemic clearance, and therapeutic efficacy. Using fluorescent labeling and drug-loaded formulations will aid in tracking and performance evaluation. Additionally, introducing NIR-absorbing moieties or photosensitizers could enable deeper tissue activation and broaden clinical applicability.

In *Chapter 5*, M-PC-based nanocolloids offer a promising backbone-cleavable platform for dual acid/visible light-responsive delivery. Future work should focus on optimizing nanoemulsion fabrication by tuning polymer molecular weight, and stabilizer composition to improve colloidal stability, size uniformity, and drug loading. Further evaluation with hydrophobic drugs, and testing *in vitro* and *in vivo* cancer models, will be critical for validating their therapeutic potential.

In the long term, advancing benzoic imine-based polymeric systems requires both chemical refinement and translational adaptation. A major focus should be the molecular engineering of conjugated benzoic imine linkages to shift their photo-responsiveness into the NIR range for enhanced tissue penetration and safety. This can be achieved by incorporating electron-donating or withdrawing substituents on the aromatic ring. To improve tumor selectivity and cellular uptake, future systems should also integrate targeting ligands such as folic acid, RGD peptides,

or antibody fragments via covalent conjugation to the PEG corona. These moieties would facilitate receptor-mediated endocytosis and enhance intracellular delivery and clinical translation of these dual-responsive polymeric nanocarriers.

### References

- 1. Shahriari, M.; Zahiri, M.; Abnous, K.; Taghdisi, S. M.; Ramezani, M.; Alibolandi, M., Enzyme responsive drug delivery systems in cancer treatment. *Journal of Controlled Release* **2019**, *308*, 172-189.
- 2. Lu, Z.-R.; Qiao, P., Drug delivery in cancer therapy, quo vadis? *Molecular Pharmaceutics* **2018**, *15*, 3603-3616.
- 3. Kashkooli, F. M.; Soltani, M.; Souri, M., Controlled anti-cancer drug release through advanced nano-drug delivery systems: Static and dynamic targeting strategies. *Journal of controlled release* **2020**, *327*, 316-349.
- 4. Wang, X.; Li, C.; Wang, Y.; Chen, H.; Zhang, X.; Luo, C.; Zhou, W.; Li, L.; Teng, L.; Yu, H., Smart drug delivery systems for precise cancer therapy. *Acta Pharmaceutica Sinica B* **2022**, *12*, 4098-4121.
- 5. Beach, M. A.; Nayanathara, U.; Gao, Y.; Zhang, C.; Xiong, Y.; Wang, Y.; Such, G. K., Polymeric Nanoparticles for Drug Delivery. *Chem Rev* **2024**, *124*, 5505-5616.
- 6. Sur, S.; Rathore, A.; Dave, V.; Reddy, K. R.; Chouhan, R. S.; Sadhu, V., Recent developments in functionalized polymer nanoparticles for efficient drug delivery system. *Nano-Structures Nano-Objects* **2019**, *20*, 100397.
- 7. Ulbrich, K.; Hola, K.; Subr, V.; Bakandritsos, A.; Tucek, J.; Zboril, R., Targeted drug delivery with polymers and magnetic nanoparticles: covalent and noncovalent approaches, release control, and clinical studies. *Chemical reviews* **2016**, *116*, 5338-5431.
- 8. Gagliardi, A.; Giuliano, E.; Venkateswararao, E.; Fresta, M.; Bulotta, S.; Awasthi, V.; Cosco, D., Biodegradable polymeric nanoparticles for drug delivery to solid tumors. *Frontiers in pharmacology* **2021**, *12*, 601626.
- 9. Floyd, T. G.; Gurnani, P.; Rho, J. Y., Characterisation of polymeric nanoparticles for drug delivery. *Nanoscale* **2025**, *17*, 7738-7752.
- 10. Mai, Y.; Eisenberg, A., Self-assembly of block copolymers. *Chemical Society Reviews* **2012**, *41*, 5969-5985.
- 11. Cabral, H.; Kataoka, K., Progress of drug-loaded polymeric micelles into clinical studies. *Journal of Controlled Release* **2014**, *190*, 465-476.
- 12. Szewczyk-Łagodzińska, M.; Plichta, A.; Dębowski, M.; Kowalczyk, S.; Iuliano, A.; Florjańczyk, Z., Recent advances in the application of ATRP in the synthesis of drug delivery systems. *Polymers* **2023**, *15*, 1234.
- 13. Messina, M. S.; Messina, K. M.; Bhattacharya, A.; Montgomery, H. R.; Maynard, H. D., Preparation of biomolecule-polymer conjugates by grafting-from using ATRP, RAFT, or ROMP. *Progress in polymer science* **2020**, *100*, 101186.
- 14. Bawa, K. K.; Oh, J. K., Stimulus-Responsive Degradable Polylactide-Based Block Copolymer Nanoassemblies for Controlled/Enhanced Drug Delivery. *Mol. Pharmaceutics* **2017**, *14*, 2460-2474.
- 15. Andrade-Gagnon, B.; Oh, J. K., Recent advances in the synthesis and shell-sheddable disassembly of acid/glutathione-degradable block copolymer nanoassemblies for drug delivery. *Polymer Chemistry* **2024**, *15*, 3709-3735.

- 16. Zhang, H.; Zhai, Y.; Wang, J.; Zhai, G., New progress and prospects: The application of nanogel in drug delivery. *Materials Science and Engineering: C* **2016**, *60*, 560-568.
- 17. Tadros, T.; Izquierdo, P.; Esquena, J.; Solans, C., Formation and stability of nanoemulsions. *Advances in Colloid and Interface Science* **2004**, *108-109*, 303-318.
- 18. Anton, N.; Vandamme, T. F., Nano-emulsions and micro-emulsions: Clarifications of the critical differences. *Pharmaceutical Research* **2009**, *26*, 914-924.
- 19. Gupta, A.; Eral, H. B.; Hatton, T. A.; Doyle, P. S., Nanoemulsions: Formation, properties and applications. *Soft Matter* **2016**, *12*, 2826-2841.
- 20. Zuleger, S.; Lippold, B. C., Polymer particle erosion controlling drug release. I. Factors influencing drug release and characterization of the release mechanism. *Int J Pharm* **2001**, *217*, 139-152.
- 21. Arifin, D. Y.; Lee, L. Y.; Wang, C. H., Mathematical modeling and simulation of drug release from microspheres: Implications to drug delivery systems. *Adv Drug Deliv Rev* **2006**, *58*, 1274-1325.
- 22. Gomes-Filho, M.; Oliveira, F.; Barbosa, M., Modeling the diffusion-erosion crossover dynamics in drug release. *Physical Review E* **2021**, *105*, 044110.
- 23. Lee, Y.; Thompson, D. H., Stimuli-responsive liposomes for drug delivery. *Wiley Interdiscip Rev Nanomed Nanobiotechnol* **2017**, *9*, e1450.
- 24. Sun, Q.; Wang, Z.; Liu, B.; He, F.; Gai, S.; Yang, P.; Yang, D.; Li, C.; Lin, J., Recent advances on endogenous/exogenous stimuli-triggered nanoplatforms for enhanced chemodynamic therapy. *Coordination Chemistry Reviews* **2022**, *451*, 214267.
- 25. Jazani, A. M.; Oh, J. K., Development and disassembly of single and multiple acidcleavable block copolymer nanoassemblies for drug delivery. *Polymer Chemistry* **2020**, *11*, 2934-2954.
- 26. Mane, S. R.; Sathyan, A.; Shunmugam, R., Biomedical Applications of pH-Responsive Amphiphilic Polymer Nanoassemblies. *ACS Applied Nano Materials* **2020**, *3*, 2104-2117.
- 27. Son, J.; Yi, G.; Yoo, J.; Park, C.; Koo, H.; Choi, H. S., Light-responsive nanomedicine for biophotonic imaging and targeted therapy. *Advanced Drug Delivery Reviews* **2019**, *138*, 133-147.
- 28. Shim, G.; Ko, S.; Kim, D.; Le, Q.-V.; Park, G. T.; Lee, J.; Kwon, T.; Choi, H.-G.; Kim, Y. B.; Oh, Y.-K., Light-switchable systems for remotely controlled drug delivery. *Journal of Controlled Release* **2017**, *267*, 67-79.
- 29. Cheng, C.-C.; Huang, J.-J.; Lee, A.-W.; Huang, S.-Y.; Huang, C.-Y.; Lai, J.-Y., Highly Effective Photocontrollable Drug Delivery Systems Based on Ultrasensitive Light-Responsive Self-Assembled Polymeric Micelles: An in Vitro Therapeutic Evaluation. *ACS Applied Bio Materials* **2019**, *2*, 2162-2170.
- 30. Hu, X.; Zhang, Y.; Xie, Z.; Jing, X.; Bellotti, A., Stimuli-responsive polymersomes for biomedical applications. *Advanced Materials* **2017**, *29*, 1700132.
- 31. Meng, L.; Huang, W.; Wang, D.; Huang, X.; Zhu, X.; Yan, D., Chitosan-Based Nanocarriers with pH and Light Dual Response for Anticancer Drug Delivery. *Biomacromolecules* **2013**, *14*, 2601-2610.
- 32. Jin, Q.; Cai, T.; Han, H.; Wang, H.; Wang, Y.; Ji, J., Light and pH dual-degradable triblock copolymer micelles for controlled intracellular drug release. *Macromolecular rapid communications* **2014**, *35*, 1372-1378.
- 33. Kalva, N.; Parekh, N.; Ambade, A. V., Controlled micellar disassembly of photo-and pH-cleavable linear-dendritic block copolymers. *Polymer Chemistry* **2015**, *6*, 6826-6835.

- 34. Pasparakis, G.; Manouras, T.; Vamvakaki, M.; Argitis, P., Harnessing photochemical internalization with dual degradable nanoparticles for combinatorial photo-chemotherapy. *Nature Communications* **2014**, *5*, 3623.
- 35. Long, Y.-B.; Gu, W.-X.; Pang, C.; Ma, J.; Gao, H., Construction of coumarin-based cross-linked micelles with pH responsive hydrazone bond and tumor targeting moiety. *Journal of Materials Chemistry B* **2016**, *4*, 1480-1488.
- 36. Jia, F.; Wang, Y.; Wang, H.; Jin, Q.; Cai, T.; Chen, Y.; Ji, J., Light cross-linkable and pH de-cross-linkable drug nanocarriers for intracellular drug delivery. *Polymer Chemistry* **2015**, *6*, 2069-2075.
- 37. Chien, J. Y.; Ho, R. J. Y., Drug Delivery Trends in Clinical Trials and Translational Medicine: Evaluation of Pharmacokinetic Properties in Special Populations. *Journal of Pharmaceutical Sciences* **2011**, *100*, 53-58.
- 38. Hoffman, A. S., Stimuli-responsive polymers: Biomedical applications and challenges for clinical translation. *Advanced Drug Delivery Reviews* **2013**, *65*, 10-16.
- 39. Chen, H.; Liu, D.; Guo, Z., Endogenous Stimuli-Responsive Nanocarriers for Drug Delivery. *Chemistry Letters* **2016**, *45*, 242-250.
- 40. Raza, A.; Rasheed, T.; Nabeel, F.; Hayat, U.; Bilal, M., Endogenous and Exogenous Stimuli-Responsive Drug Delivery Systems for Programmed Site-Specific Release. *Molecules* **2019**, *24*, 1117.
- 41. Layer, R. W., The Chemistry of Imines. *Chemical Reviews* **1963**, *63*, 489-510.
- 42. Chakma, P.; Konkolewicz, D. J. A. C. I. E., Dynamic covalent bonds in polymeric materials. *Angewandte Chemie International Edition* **2019**, *58*, 9682-9695.
- 43. Qu, X.; Yang, Z., Benzoic-Imine-Based Physiological-pH-Responsive Materials for Biomedical Applications. *Chemistry An Asian Journal* **2016**, *11*, 2633-2641.
- 44. Hu, X.; Jazani, A. M.; Oh, J. K., Recent advances in development of imine-based acid-degradable polymeric nanoassemblies for intracellular drug delivery. *Polymer* **2021**, *230*, 124024.
- 45. Hu, X.; Oh, J. K., Direct Polymerization Approach to Synthesize Acid-Degradable Block Copolymers Bearing Imine Pendants for Tunable pH-Sensitivity and Enhanced Release. *Macromol Rapid Commun* **2020**, *41*, e2000394.
- 46. Liao, S.-C.; Ting, C.-W.; Chiang, W.-H., Functionalized polymeric nanogels with pH-sensitive benzoic-imine cross-linkages designed as vehicles for indocyanine green delivery. *Journal of Colloid and Interface Science* **2020**, *561*, 11-22.
- 47. Zan, M.; Li, J.; Luo, S.; Ge, Z., Dual pH-triggered multistage drug delivery systems based on host–guest interaction-associated polymeric nanogels. *Chemical Communications* **2014**, *50*, 7824-7827.
- 48. Wang, C.; Chen, X.; Yao, X.; Chen, L.; Chen, X., Dual acid-responsive supramolecular nanoparticles as new anticancer drug delivery systems. *Biomaterials Science* **2016**, *4*, 104-114.
- 49. Kandappa, S. K.; Valloli, L. K.; Ahuja, S.; Parthiban, J.; Sivaguru, J., Taming the excited state reactivity of imines—from non-radiative decay to aza Paternò—Büchi reaction. *Chemical Society Reviews* **2021**, *50*, 1617-1641.
- 50. Coelho, P. J.; Castro, M. C. R.; Raposo, M. M. M., Reversible trans—cis photoisomerization of new pyrrolidene heterocyclic imines. *Journal of Photochemistry and Photobiology A: Chemistry* **2013**, *259*, 59-65.
- 51. Greb, L.; Lehn, J. M., Light-driven molecular motors: imines as four-step or two-step unidirectional rotors. *Journal of the American Chemical Society* **2014**, *136*, 13114-13117.

- 52. Greb, L.; Mutlu, H.; Barner-Kowollik, C.; Lehn, J. M., Photo- and Metallo-responsive N-Alkyl α-Bisimines as Orthogonally Addressable Main-Chain Functional Groups in Metathesis Polymers. *Journal of the American Chemical Society* **2016**, *138*, 1142-1145.
- 53. Thai, L. D.; Guimaraes, T. R.; Spann, S.; Goldmann, A. S.; Golberg, D.; Mutlu, H.; Barner-Kowollik, C., Photoswitchable block copolymers based on main chain α-bisimines. *Polymer Chemistry* **2022**, *13*, 5625-5635.
- 54. Fan, W.; Jin, Y.; Shi, L.; Zhou, R.; Du, W., Developing visible-light-induced dynamic aromatic Schiff base bonds for room-temperature self-healable and reprocessable waterborne polyurethanes with high mechanical properties. *Journal of Materials Chemistry A* **2020**, *8*, 6757-6767.
- 55. Lei, Z. Q.; Xie, P.; Rong, M. Z.; Zhang, M. Q., Catalyst-free dynamic exchange of aromatic Schiff base bonds and its application to self-healing and remolding of crosslinked polymers. *Journal of Materials Chemistry A* **2015**, *3*, 19662-19668.
- 56. Zheng, H.; Wang, S.; Lu, C.; Ren, Y.; Liu, Z.; Ding, D.; Wu, Z.; Wang, X.; Chen, Y.; Zhang, Q., Thermal, near-infrared light, and amine solvent triple-responsive recyclable iminetype vitrimer: shape memory, accelerated photohealing/welding, and destructing behaviors. *Industrial & Engineering Chemistry Research* **2020**, *59*, 21768-21778.
- 57. Jin, Z.; Amili, M.; Guo, S., Tumor microenvironment-responsive drug delivery based on polymeric micelles for precision cancer therapy: Strategies and prospects. *Biomedicines* **2024**, *12*, 417.
- 58. Rapoport, N., Physical stimuli-responsive polymeric micelles for anti-cancer drug delivery. *Progress in Polymer Science* **2007**, *32*, 962-990.
- 59. Wei, D.; Sun, Y.; Zhu, H.; Fu, Q., Stimuli-responsive polymer-based nanosystems for cancer theranostics. *ACS Nano* **2023**, *17*, 5281-5300.
- 60. Luo, Y.; Yin, X.; Chen, A.; Zhao, L.; Zhang, G.; Liao, W.; Huang, X.; Li, J.; Zhang, C., Dual pH/redox-responsive mixed polymeric micelles for anticancer drug delivery and controlled release. *Pharmaceutics* **2019**, *11*, 176.
- 61. Fan, W.; Zhang, L.; Li, Y.; Wu, H., Recent Progress of Crosslinking Strategies for Polymeric Micelles with Enhanced Drug Delivery in Cancer Therapy. *Curr Med Chem* **2019**, *26*, 2356-2376.
- 62. Talelli, M.; Barz, M.; Rijcken, C. J.; Kiessling, F.; Hennink, W. E.; Lammers, T., Core-Crosslinked Polymeric Micelles: Principles, Preparation, Biomedical Applications and Clinical Translation. *Nano Today* **2015**, *10*, 93-117.
- 63. Biswas, S.; Kumari, P.; Lakhani, P.; Ghosh, B., Recent advances in polymeric micelles for anti-cancer drug delivery. *European Journal of Pharmaceutical Sciences* **2016**, *83*, 184-202.
- 64. Lee, I.; Park, M.; Kim, Y.; Hwang, O.; Khang, G.; Lee, D., Ketal containing amphiphilic block copolymer micelles as pH-sensitive drug carriers. *International Journal of Pharmaceutics* **2013**, *448*, 259-266.
- 65. Hao, Y.; He, J.; Li, S.; Liu, J.; Zhang, M.; Ni, P., Synthesis of an acid-cleavable and fluorescent amphiphilic block copolymer as a combined delivery vector of DNA and doxorubicin. *Journal of Materials Chemistry B* **2014**, *2*, 4237-4249.
- 66. Jazani, A. M.; Arezi, N.; Shetty, C.; Hong, S. H.; Li, H.; Wang, X.; Oh, J. K., Tumortargeting intracellular drug delivery based on dual acid/reduction-degradable nanoassemblies with ketal interface and disulfide core locations. *Polymer Chemistry* **2019**, *10*, 2840-2853.

- 67. Sun, J.; Fransen, S.; Yu, X.; Kuckling, D., Synthesis of pH-cleavable poly(trimethylene carbonate)-based block copolymers via ROP and RAFT polymerization. *Polymer Chemistry* **2018**, *9*, 3287-3296.
- 68. Basutkar, N. B.; Geetika, S. S.; Shafi, A. M.; and Ambade, A. V., Visible light and pH-responsive star copolymer and doxorubicin-polymer conjugate micelles for combination drug delivery and bioimaging. *Journal of Macromolecular Science, Part A* **2024**, *61*, 105-116.
- 69. Sonawane, S. J.; Kalhapure, R. S.; Jadhav, M.; Rambharose, S.; Mocktar, C.; Govender, T., AB2-type amphiphilic block copolymer containing a pH-cleavable hydrazone linkage for targeted antibiotic delivery. *International Journal of Pharmaceutics* **2020**, *575*, 118948.
- 70. Andrade-Gagnon, B.; Casillas-Popova, S. N.; Jazani, A. M.; Oh, J. K. J. M. R. C., Design, Synthesis, and Acid-Responsive Disassembly of Shell-Sheddable Block Copolymer Labeled with Benzaldehyde Acetal Junction. *Macromolecular Rapid Communications* **2024**, *45*, 2400097.
- 71. Yang, Q.; Tan, L.; He, C.; Liu, B.; Xu, Y.; Zhu, Z.; Shao, Z.; Gong, B.; Shen, Y.-M., Redox-responsive micelles self-assembled from dynamic covalent block copolymers for intracellular drug delivery. *Acta Biomaterialia* **2015**, *17*, 193-200.
- 72. Huo, M.; Liu, Y.; Wang, L.; Yin, T.; Qin, C.; Xiao, Y.; Yin, L.; Liu, J.; Zhou, J., Redox-Sensitive Micelles Based on O,N-Hydroxyethyl Chitosan–Octylamine Conjugates for Triggered Intracellular Delivery of Paclitaxel. *Molecular Pharmaceutics* **2016**, *13*, 1750-1762.
- 73. Lili, Y.; Ruihua, M.; Li, L.; Fei, L.; Lin, Y.; Li, S., Intracellular Doxorubicin Delivery of a Core Cross-linked, Redox-responsive Polymeric Micelles. *International Journal of Pharmaceutics* **2016**, *498*, 195-204.
- 74. Lu, B.; Xiao, Z.; Wang, Z.; Wang, B.; Zhao, W.; Ma, X.; Zhang, J., Redox-Sensitive Polymer Micelles Based on CD44 and Folic Acid Receptor for Intracellular Drug Delivery and Drug Controlled Release in Cancer Therapy. *ACS Applied Bio Materials* **2019**, *2*, 4222-4232.
- 75. Zhang, A.; Zhang, Z.; Shi, F.; Xiao, C.; Ding, J.; Zhuang, X.; He, C.; Chen, L.; Chen, X., Redox-S ensitive Shell-C rosslinked Polypeptide-block-P olysaccharide Micelles for Efficient Intracellular Anticancer Drug Delivery. *Macromolecular bioscience* **2013**, *13*, 1249-1258.
- 76. Xia, Y.; He, H.; Liu, X.; Hu, D.; Yin, L.; Lu, Y.; Xu, W., Redox-responsive, corecrosslinked degradable micelles for controlled drug release. *Polymer Chemistry* **2016**, *7*, 6330-6339.
- 77. Olszowy, Y.; Wesselmann, J.; Over, S. F.; Pätzold, F.; Weberskirch, R., Synthesis of redox-responsive core–shell nanoparticles: insights into core-crosslinking efficiency. *Polymer Chemistry* **2023**, *14*, 3761-3774.
- 78. Kuang, G.; Zhang, Q.; He, S.; Wu, Y.; Huang, Y., Reduction-responsive disulfide linkage core-cross-linked polymeric micelles for site-specific drug delivery. *Polymer Chemistry* **2020**, *11*, 7078-7086.
- 79. Xu, F.; Li, H.; Luo, Y.-L.; Tang, W., Redox-Responsive Self-Assembly Micelles from Poly(N-acryloylmorpholine-block-2-acryloyloxyethyl ferrocenecarboxylate) Amphiphilic Block Copolymers as Drug Release Carriers. *ACS Applied Materials & Interfaces* **2017**, *9*, 5181-5192.
- 80. Shi, L.; Jin, Y.; Du, W.; Lai, S.; Shen, Y.; Zhou, R., Diselenide-containing nonionic gemini polymeric micelles as a smart redox-responsive carrier for potential programmable drug release. *Polymer* **2020**, *198*, 122551.
- 81. Behroozi, F.; Abdkhodaie, M.-J.; Abandansari, H. S.; Satarian, L.; Molazem, M.; Al-Jamal, K. T.; Baharvand, H., Engineering folate-targeting diselenide-containing triblock

- copolymer as a redox-responsive shell-sheddable micelle for antitumor therapy in vivo. *Acta Biomaterialia* **2018**, *76*, 239-256.
- 82. Wan, D.; Song, Y.; Lu, X.; Huang, Y.; Zhang, J.; Liu, Y.; Liu, Y.; Pan, J., Nanoscale "precision strike": Tumor microenvironment-responsive smart micelles for efficient targeted drug delivery. *Nano Research* **2024**, *17*, 8360-8367.
- 83. Park, J.; Jo, S.; Lee, Y. M.; Saravanakumar, G.; Lee, J.; Park, D.; Kim, W. J., Enzyme-Triggered Disassembly of Polymeric Micelles by Controlled Depolymerization via Cascade Cyclization for Anticancer Drug Delivery. *ACS Applied Materials & Interfaces* **2021**, *13*, 8060-8070.
- 84. Harnoy, A. J.; Buzhor, M.; Tirosh, E.; Shaharabani, R.; Beck, R.; Amir, R. J., Modular Synthetic Approach for Adjusting the Disassembly Rates of Enzyme-Responsive Polymeric Micelles. *Biomacromolecules* **2017**, *18*, 1218-1228.
- 85. Segal, M.; Ozery, L.; Slor, G.; Wagle, S. S.; Ehm, T.; Beck, R.; Amir, R. J., Architectural Change of the Shell-Forming Block from Linear to V-Shaped Accelerates Micellar Disassembly, but Slows the Complete Enzymatic Degradation of the Amphiphiles. *Biomacromolecules* **2020**, *21*, 4076-4086.
- 86. Deepagan, V. G.; Kwon, S.; You, D. G.; Nguyen, V. Q.; Um, W.; Ko, H.; Lee, H.; Jo, D.-G.; Kang, Y. M.; Park, J. H., In situ diselenide-crosslinked polymeric micelles for ROS-mediated anticancer drug delivery. *Biomaterials* **2016**, *103*, 56-66.
- 87. Truong Hoang, Q.; Lee, D.; Choi, D. G.; Kim, Y.-C.; Shim, M. S., Efficient and selective cancer therapy using pro-oxidant drug-loaded reactive oxygen species (ROS)-responsive polypeptide micelles. *Journal of Industrial and Engineering Chemistry* **2021**, *95*, 101-108.
- 88. Ge, C.; Zhu, J.; Wu, G.; Ye, H.; Lu, H.; Yin, L., ROS-Responsive Selenopolypeptide Micelles: Preparation, Characterization, and Controlled Drug Release. *Biomacromolecules* **2022**, *23*, 2647-2654.
- 89. Lotocki, V.; Yazdani, H.; Zhang, Q.; Gran, E. R.; Nyrko, A.; Maysinger, D.; Kakkar, A., Miktoarm Star Polymers with Environment-Selective ROS/GSH Responsive Locations: From Modular Synthesis to Tuned Drug Release through Micellar Partial Corona Shedding and/or Core Disassembly. *Macromolecular Bioscience* **2021**, *21*, 2000305.
- 90. Dai, L.; Yu, Y.; Luo, Z.; Li, M.; Chen, W.; Shen, X.; Chen, F.; Sun, Q.; Zhang, Q.; Gu, H.; Cai, K., Photosensitizer enhanced disassembly of amphiphilic micelle for ROS-response targeted tumor therapy in vivo. *Biomaterials* **2016**, *104*, 1-17.
- 91. Kundu, P.; Das, S.; Chattopadhyay, N., Switching from endogenous to exogenous delivery of a model drug to DNA through micellar engineering. *Journal of Photochemistry and Photobiology B: Biology* **2020**, *203*, 111765.
- 92. Son, S.; Shin, E.; Kim, B.-S., Light-Responsive Micelles of Spiropyran Initiated Hyperbranched Polyglycerol for Smart Drug Delivery. *Biomacromolecules* **2014**, *15*, 628-634.
- 93. Zhang, R.; Min, Y.; Ji, P.; Zhou, G.; Yin, H.; Qi, D.; Deng, H.; Hua, Z.; Chen, T., Light and temperature dual stimuli-responsive micelles from carbamate-containing spiropyran-based amphiphilic block copolymers: Fabrication, responsiveness and controlled release behaviors. *European Polymer Journal* **2023**, *200*, 112493.
- 94. Min, Y.; Zhang, R.; Dong, X.; Zhang, L.; Qi, D.; Hua, Z.; Chen, T., Spiropyran-based polymeric micelles in aqueous solution: light-regulated reversible size alterations and catalytic characteristics. *Polymer Chemistry* **2023**, *14*, 888-897.

- 95. Kim, H.-J.; Lee, H.-i., Polymeric Micelles Based on Light-Responsive Block Copolymers for the Phototunable Detection of Mercury(II) Ions Modulated by Morphological Changes. *ACS Applied Materials & Interfaces* **2018**, *10*, 34634-34639.
- 96. Wei, Z.; Liu, X.; Niu, D.; Qin, L.; Li, Y., Upconversion Nanoparticle-Based Organosilica–Micellar Hybrid Nanoplatforms for Redox-Responsive Chemotherapy and NIR-Mediated Photodynamic Therapy. *ACS Applied Bio Materials* **2020**, *3*, 4655-4664.
- 97. Xiang, J.; Tong, X.; Shi, F.; Yan, Q.; Yu, B.; Zhao, Y., Near-infrared light-triggered drug release from UV-responsive diblock copolymer-coated upconversion nanoparticles with high monodispersity. *Journal of Materials Chemistry B* **2018**, *6*, 3531-3540.
- 98. Chen, G.; Jaskula-Sztul, R.; Esquibel, C. R.; Lou, I.; Zheng, Q.; Dammalapati, A.; Harrison, A.; Eliceiri, K. W.; Tang, W.; Chen, H.; Gong, S., Neuroendocrine Tumor-Targeted Upconversion Nanoparticle-Based Micelles for Simultaneous NIR-Controlled Combination Chemotherapy and Photodynamic Therapy, and Fluorescence Imaging. *Advanced Functional Materials* **2017**, *27*, 1604671.
- 99. Chen, Y.; Ma, T.; Liu, P.; Ren, J.; Li, Y.; Jiang, H.; Zhang, L.; Zhu, J., NIR-Light-Activated Ratiometric Fluorescent Hybrid Micelles for High Spatiotemporally Controlled Biological Imaging and Chemotherapy. *Small* **2020**, *16*, 2005667.
- 100. Sana, B.; Finne-Wistrand, A.; Pappalardo, D., Recent development in near infrared light-responsive polymeric materials for smart drug-delivery systems. *Materials Today Chemistry* **2022**, *25*, 100963.
- 101. Zhao, Y., Light-Responsive Block Copolymer Micelles. *Macromolecules* **2012**, *45*, 3647-3657.
- 102. Yamada, S.; Sasaki, E.; Ohno, H.; Hanaoka, K., Heat-guided drug delivery via thermally induced crosslinking of polymeric micelles. *Communications Chemistry* **2024**, *7*, 1-9.
- 103. Lin, S.; Zhu, L.; Li, Z.; Yue, S.; Wang, Z.; Xu, Y.; Zhang, Y.; Gao, Q.; Chen, J.; Yin, T.; Niu, L.; Geng, J., Ultrasound-responsive glycopolymer micelles for targeted dual drug delivery in cancer therapy. *Biomaterials Science* **2023**, *11*, 6149-6159.
- 104. Liu, X.; Zhao, K.; Cao, J.; Qi, X.; Wu, L.; Shen, S., Ultrasound responsive self-assembled micelles loaded with hypocrellin for cancer sonodynamic therapy. *International Journal of Pharmaceutics* **2021**, *608*, 121052.
- 105. Birhan, Y. S.; Hailemeskel, B. Z.; Mekonnen, T. W.; Hanurry, E. Y.; Darge, H. F.; Andrgie, A. T.; Chou, H.-Y.; Lai, J.-Y.; Hsiue, G.-H.; Tsai, H.-C., Fabrication of redox-responsive Bi(mPEG-PLGA)-Se2 micelles for doxorubicin delivery. *International Journal of Pharmaceutics* **2019**, *567*, 118486.
- 106. Ma, G.; Liu, J.; He, J.; Zhang, M.; Ni, P., Dual-Responsive Polyphosphoester-Doxorubicin Prodrug Containing a Diselenide Bond: Synthesis, Characterization, and Drug Delivery. *ACS Biomaterials Science & Engineering* **2018**, *4*, 2443-2452.
- 107. Jazani, A. M.; Oh, J. K., Dual Location, Dual Acidic pH/Reduction-Responsive Degradable Block Copolymer: Synthesis and Investigation of Ketal Linkage Instability under ATRP Conditions. *Macromolecules* **2017**, *50*, 9427-9436.
- 108. Bawa, K. K.; Jazani, A. M.; Ye, Z.; Oh, J. K., Synthesis of degradable PLA-based diblock copolymers with dual acid/reduction-cleavable junction. *Polymer* **2020**, *194*, 122391.
- 109. Jazani, A. M.; Arezi, N.; Maruya-Li, K.; Jung, S.; Oh, J. K., Facile Strategies to Synthesize Dual Location Dual Acidic pH/Reduction-Responsive Degradable Block Copolymers Bearing Acetal/Disulfide Block Junctions and Disulfide Pendants. *ACS Omega* **2018**, *3*, 8980-8991.

- 110. Hu, X.; Larocque, K.; Piekny, A.; Oh, J. K., Dual acid/glutathione-responsive core-degradable/shell-sheddable block copolymer nanoassemblies bearing benzoic imines for enhanced drug release. *RSC Applied Polymers* **2025**, *3*, 196-208.
- 111. Jäck, N.; Hemming, A.; Hartmann, L., Synthesis of Dual-Responsive Amphiphilic Glycomacromolecules: Controlled Release of Glycan Ligands via pH and UV Stimuli. *Macromolecular Rapid Communications* **2024**, *45*, 2400439.
- 112. Lo, Y.-L.; Tsai, M.-F.; Soorni, Y.; Hsu, C.; Liao, Z.-X.; Wang, L.-F., Dual Stimuli-Responsive Block Copolymers with Adjacent Redox- and Photo-Cleavable Linkages for Smart Drug Delivery. *Biomacromolecules* **2020**, *21*, 3342-3352.
- 113. Jäck, N.; Hemming, A.; Hartmann, L., Synthesis of Dual-Responsive Amphiphilic Glycomacromolecules: Controlled Release of Glycan Ligands via pH and UV Stimuli. *Macromolecular Rapid Communications* **2024**, *45*, 2400439.
- 114. Liu, H.; Lu, H.-H.; Alp, Y.; Wu, R.; Thayumanavan, S., Structural determinants of stimuli-responsiveness in amphiphilic macromolecular nano-assemblies. *Progress in Polymer Science* **2024**, *148*, 101765.
- 115. Owen, S. C.; Chan, D. P. Y.; Shoichet, M. S., Polymeric micelle stability. *Nano Today* **2012**, *7*, 53-65.
- 116. Shi, Y.; Lammers, T.; Storm, G.; Hennink, W. E., Physico-Chemical Strategies to Enhance Stability and Drug Retention of Polymeric Micelles for Tumor-Targeted Drug Delivery. *Macromol Biosci* **2017**, *17*, 1600160.
- 117. Cheng, X.; Li, Q.; Sun, X.; Ma, Y.; Xie, H.; Kong, W.; Du, X.; Zhang, Z.; Qiu, D.; Jin, Y., Well-Defined Shell-Sheddable Core-Crosslinked Micelles with pH and Oxidation Dual-Response for On-Demand Drug Delivery. *Polymers (Basel)* **2023**, *15*, 1990.
- 118. Feng, Y.; Bai, J.; Du, X.; Zhao, X., Shell-Cross-Linking of polymeric micelles by Zn coordination for Photo- and pH Dual-Sensitive drug delivery. *Colloids and Surfaces A: Physicochemical and Engineering Aspects* **2023**, *666*, 131369.
- 119. Song, X.; Yuan, K.; Li, H.; Xu, S.; Li, Y., Dual Pseudo and Chemical Crosslinked Polymer Micelles for Effective Paclitaxel Delivery and Release. *ACS Appl Bio Mater* **2020**, *3*, 2455-2465.
- 120. Kolb, H. C.; Finn, M. G.; Sharpless, K. B., Click Chemistry: Diverse Chemical Function from a Few Good Reactions. *Angewandte Chemie International Edition* **2001**, *40*, 2004-2021.
- 121. Wang, C.; Li, Z.; Ding, Y.; Sun, H.; Li, S.; Lin, Y., Click Chemistry in Materials Science. *Materials Today* **2016**, *19*, 394-402.
- 122. Gulfam, M.; Matini, T.; Monteiro, P. F.; Riva, R.; Collins, H.; Spriggs, K.; Howdle, S. M.; Jérôme, C.; Alexander, C., Bioreducible Cross-Linked Core Polymer Micelles Enhance In Vitro Activity of Methotrexate in Breast Cancer Cells. *Biomaterials Science* **2017**, *5*, 532-550.
- 123. Zhang, S.; Chen, F.; Yang, Y.; Chen, H.; Du, J.; Kong, J., "A~A+B3~" strategy to construct redox-responsive core-crosslinked copolymers as potential drug carrier. *Reactive and Functional Polymers* **2019**, *138*, 122-128.
- 124. Yi, X.-Q.; Zhang, Q.; Zhao, D.; Xu, J.-Q.; Zhong, Z.-L.; Zhuo, R.-X.; Li, F., Preparation of pH and redox dual-sensitive core crosslinked micelles for overcoming drug resistance of DOX. *Polymer Chemistry* **2016**, *7*, 1719-1729.
- 125. Siboro, S. A. P.; Salma, S. A.; Kim, H.-R.; Jeong, Y. T.; Gal, Y.-S.; Lim, K. T., Diselenide Core Cross-Linked Micelles of Poly(Ethylene Oxide)-b-Poly(Glycidyl Methacrylate) Prepared through Alkyne-Azide Click Chemistry as a Near-Infrared Controlled Drug Delivery System. *Materials* **2020**, *13*, 2846.

- 126. Wang, D.; Wang, S.; Xia, Y.; Liu, S.; Jia, R.; Xu, G.; Zhan, J.; Lu, Y. J. C.; Biointerfaces, S. B., Preparation of ROS-responsive core crosslinked polycarbonate micelles with thioketal linkage. *Colloids and Surfaces B: Biointerfaces* **2020**, *195*, 111276.
- 127. Huang, Y.; Sun, R.; Luo, Q.; Wang, Y.; Zhang, K.; Deng, X.; Zhu, W.; Li, X.; Shen, Z. J. J. o. P. S. P. A. P. C., In situ fabrication of paclitaxel-loaded core-crosslinked micelles via thiolene "click" chemistry for reduction-responsive drug release. *Journal of Polymer Science Part A: Polymer Chemistry* **2016**, *54*, 99-107.
- 128. Wang, Y.; Luo, Q.; Zhu, W.; Li, X.; Shen, Z. J. P. C., Reduction/pH dual-responsive nano-prodrug micelles for controlled drug delivery. *Polymer Chemistry* **2016**, *7*, 2665-2673.
- 129. Binder, W. H.; Sachsenhofer, R., 'Click' Chemistry in Polymer and Materials Science: Quo Vadis? *Macromolecular Rapid Communications* **2008**, *29*, 952-981.
- 130. Nicolaou, K. C.; Snyder, S. A.; Montagnon, T.; Vassilikogiannakis, G., The Diels–Alder Reaction in Total Synthesis. *Angewandte Chemie International Edition* **2002**, *41*, 1668-1698.
- 131. Salma, S. A.; Le, C. M. Q.; Kim, D. W.; Cao, X. T.; Jeong, Y. T.; Lim, K. T., Synthesis and Characterization of Diselenide Crosslinked Polymeric Micelles via Diels—Alder Click Reaction. *Molecular Crystals and Liquid Crystals* **2018**, *662*, 188-196.
- 132. Liu, B.; Thayumanavan, S., Substituent Effects on the pH Sensitivity of Acetals and Ketals and Their Correlation with Encapsulation Stability in Polymeric Nanogels. *Journal of the American Chemical Society* **2017**, *139*, 2306-2317.
- 133. Nuhn, L.; Van Herck, S.; Best, A.; Deswarte, K.; Kokkinopoulou, M.; Lieberwirth, I.; Koynov, K.; Lambrecht, B. N.; De Geest, B. G., FRET Monitoring of Intracellular Ketal Hydrolysis in Synthetic Nanoparticles. *Angew Chem Int Ed Engl* **2018**, *57*, 10760-10764.
- 134. Cao, X. T.; Cuong, N. V.; Duy, N. T.; Van-Dat, D.; Trang, T. T. K.; and Lim, K. T., Ketal core cross-linked micelles for pH-triggered release of doxorubicin. *Molecular Crystals and Liquid Crystals* **2020**, *707*, 29-37.
- 135. Wang, X.; Wang, L.; Yang, S.; Zhang, M.; Xiong, Q.; Zhao, H.; Liu, L., Construction of multifunctionalizable, core-cross-linked polymeric nanoparticles via dynamic covalent bond. *Macromolecules* **2014**, *47*, 1999-2009.
- 136. Azuma, Y.; Terashima, T.; Sawamoto, M., Precision Synthesis of Imine-Functionalized Reversible Microgel Star Polymers via Dynamic Covalent Cross-Linking of Hydrogen-Bonding Block Copolymer Micelles. *Macromolecules* **2017**, *50*, 587-596.
- 137. Lê, D.; Liénafa, L.; Phan, T. N. T.; Deleruyelle, D.; Bouchet, R.; Maria, S.; Bertin, D.; Gigmes, D., Photo-Cross-Linked Diblock Copolymer Micelles: Quantitative Study of Photochemical Efficiency, Micelles Morphologies and their Thermal Behavior. *Macromolecules* **2014**, *47*, 2420-2429.
- 138. Gohy, J. F.; Zhao, Y., Photo-responsive block copolymer micelles: design and behavior. *Chem Soc Rev* **2013**, *42*, 7117-7129.
- 139. van Nostrum, C. F., Covalently cross-linked amphiphilic block copolymer micelles. *Soft Matter* **2011**, *7*, 3246-3259.
- 140. Wan, Z.; An, N.; Xu, C.; Zheng, M.; Yuan, J., Polymerization-induced self-assembly nanomaterials based on dynamic covalent bonds. *Polymer Chemistry* **2025**, *16*, 636.
- 141. Zhang, X.; Wang, Y.; Li, G.; Liu, Z.; Liu, Z.; Jiang, J. J. M. R. C., Amphiphilic Imbalance and Stabilization of Block Copolymer Micelles on-Demand through Combinational Photo-Cleavage and Photo-Crosslinking. *Macromolecular Rapid Communications* **2017**, *38*, 1600543.

- 142. Alemdar, M.; Tuncaboylu, D. C.; Batu, H. K.; Temel, B. A., Pluronic based injectable smart gels with coumarin functional amphiphilic copolymers. *European Polymer Journal* **2022**, *177*, 111378.
- 143. Cheng, X.; Li, H.; Sun, X.; Xu, T.; Guo, Z.; Du, X.; Li, S.; Li, X.; Xing, X.; Qiu, D., Visible-Light-Induced Diselenide-Crosslinked Polymeric Micelles for ROS-Triggered Drug Delivery. *Molecules* **2024**, *29*, 3970.
- 144. Baysoy, B. S.; Günaydın, İ.; Batu, H. K.; Civelek, D. O.; Temel, B. A. J. M. C.; Physics, Fabrication of Core-Crosslinked Polymer Micelles via Photoinduced Azide Crosslinking. *Macromolecular Chemistry and Physics* **2025**, 2400473.
- 145. Weber, P.; Dzuricky, M.; Min, J.; Jenkins, I.; Chilkoti, A., Concentration-independent multivalent targeting of Cancer cells by genetically encoded Core-crosslinked elastin/Resilin-like polypeptide micelles. *Biomacromolecules* **2021**, *22*, 4347-4356.
- 146. Wan, W.-M.; Hong, C.-Y.; Pan, C.-Y., One-pot synthesis of nanomaterials via RAFT polymerization induced self-assembly and morphology transition. *Chemical Communications* **2009**, *39*, 5883-5885.
- 147. Xu, S.; Yeow, J.; Boyer, C., Exploiting wavelength orthogonality for successive photoinduced polymerization-induced self-assembly and photo-crosslinking. *ACS Macro Letters* **2018**, *7*, 1376-1382.
- 148. Zhang, W.-J.; Hong, C.-Y.; Pan, C.-Y., Efficient fabrication of photosensitive polymeric nano-objects via an ingenious formulation of RAFT dispersion polymerization and their application for drug delivery. *Biomacromolecules* **2017**, *18*, 1210-1217.
- 149. Huang, J.; Li, D.; Liang, H.; Lu, J., Synthesis of Photocrosslinkable and Amine Containing Multifunctional Nanoparticles via Polymerization-Induced Self-Assembly. *Macromolecular Rapid Communications* **2017**, *38*, 1700202.
- 150. Canning, S. L.; Smith, G. N.; Armes, S. P. J. M., A critical appraisal of RAFT-mediated polymerization-induced self-assembly. *Macromolecules* **2016**, *49*, 1985-2001.
- 151. Warren, N. J.; Armes, S. P., Polymerization-induced self-assembly of block copolymer nano-objects via RAFT aqueous dispersion polymerization. *Journal of the American Chemical Society* **2014**, *136*, 10174-10185.
- 152. Zhao, Z.; Fan, L.; Song, G.; Huo, M., Micelle-Cross-Linked Hydrogels with Strain Stiffening Properties Regulated by Intramicellar Cross-Linking. *Chemistry of Materials* **2024**, *36*, 1436-1448.
- 153. Shahrokhinia, A.; Scanga, R. A.; Biswas, P.; Reuther, J. F., PhotoATRP-Induced Self-Assembly (PhotoATR-PISA) Enables Simplified Synthesis of Responsive Polymer Nanoparticles in One-Pot. *Macromolecules* **2021**, *54*, 1441-1451.
- 154. Park, J.; Ahn, N. Y.; Seo, M., Cross-linking polymerization-induced self-assembly to produce branched core cross-linked star block polymer micelles. *Polymer Chemistry* **2020**, *11*, 4335-4343.
- 155. Wei, H.; Zhuo, R.-X.; Zhang, X.-Z., Design and development of polymeric micelles with cleavable links for intracellular drug delivery. *Prog. Polym. Sci.* **2013**, *38*, 503-535.
- 156. Rijcken, C. J. F.; Soga, O.; Hennink, W. E.; van Nostrum, C. F., Triggered destabilization of polymeric micelles and vesicles by changing polymers polarity: An attractive tool for drug delivery. *Journal of Controlled Release* **2007**, *120*, 131-148.
- 157. Alvarez-Lorenzo, C.; Concheiro, A., Smart drug delivery systems: from fundamentals to the clinic. *Chem. Commun.* **2014**, *50*, 7743-7765.

- 158. Loomis, K.; McNeeley, K.; Bellamkonda, R. V., Nanoparticles with targeting, triggered release, and imaging functionality for cancer applications. *Soft Matter* **2011**, *7*, 839-856.
- 159. Mura, S.; Nicolas, J.; Couvreur, P., Stimuli-responsive nanocarriers for drug delivery. *Nat. Mater.* **2013**, *12*, 991-1003.
- 160. Delplace, V.; Nicolas, J., Degradable vinyl polymers for biomedical applications. *Nat. Chem.* **2015**, *7*, 771-784.
- 161. Harada, A.; Kataoka, K., Supramolecular assemblies of block copolymers in aqueous media as nanocontainers relevant to biological applications. *Prog. Polym. Sci.* **2006**, *31*, 949-982.
- 162. Mikhail, A. S.; Allen, C., Block copolymer micelles for delivery of cancer therapy: Transport at the whole body, tissue and cellular levels. *Journal of Controlled Release* **2009**, *138*, 214-223.
- 163. Nishiyama, N.; Kataoka, K., Nanostructured devices based on block copolymer assemblies for drug delivery: designing structures for enhanced drug function. *Adv. Polym. Sci.* **2006**, *193*, 67-101.
- 164. Xiong, X.-B.; Falamarzian, A.; Garg, S. M.; Lavasanifar, A., Engineering of amphiphilic block copolymers for polymeric micellar drug and gene delivery. *Journal of Controlled Release* **2011**, *155*, 248-261.
- 165. Ding, J.; Chen, L.; Xiao, C.; Chen, L.; Zhuang, X.; Chen, X., Noncovalent interaction-assisted polymeric micelles for controlled drug delivery. *Chem. Commun.* **2014**, *50*, 11274-11290.
- 166. Wang, Y.; Xu, H.; Zhang, X., Tuning the Amphiphilicity of Building Blocks: Controlled Self-Assembly and Disassembly for Functional Supramolecular Materials. *Advanced Materials* (Weinheim, Germany) **2009**, *21*, 2849-2864.
- 167. Jackson, A. W.; Fulton, D. A., Making polymeric nanoparticles stimuli-responsive with dynamic covalent bonds. *Polym. Chem.* **2013**, *4*, 31-45.
- 168. Zhang, Q.; Ko, N. R.; Oh, J. K., Recent advances in stimuli-responsive degradable block copolymer micelles: synthesis and controlled drug delivery applications. *Chem. Commun.* **2012**, *48*, 7542-7552.
- 169. Tannock, I. F.; Rotin, D., Acid pH in tumors and its potential for therapeutic exploitation. *Cancer Research* **1989**, *49*, 4373-4384.
- 170. Watson, P.; Jones, A. T.; Stephens, D. J., Intracellular trafficking pathways and drug delivery: fluorescence imaging of living and fixed cells. *Adv. Drug Deliv. Rev.* **2005**, *57*, 43-61.
- 171. Bazban-Shotorbani, S.; Hasani-Sadrabadi, M. M.; Karkhaneh, A.; Serpooshan, V.; Jacob, K. I.; Moshaverinia, A.; Mahmoudi, M., Revisiting structure-property relationship of pHresponsive polymers for drug delivery applications. *J. Control. Release* **2017**, *253*, 46-63.
- 172. Binauld, S.; Stenzel, M. H., Acid-degradable polymers for drug delivery: a decade of innovation. *Chem. Commun.* **2013**, *49*, 2082-2102.
- 173. Kocak, G.; Tuncer, C.; Butun, V., pH-Responsive polymers. *Polymer Chemistry* **2017**, *8*, 144-176.
- 174. Qu, X.; Yang, Z., Benzoic-Imine-Based Physiological-pH-Responsive Materials for Biomedical Applications. *Chemistry An Asian Journal* **2016**, *11*, 2633-2641.
- 175. Zhao, H.; Sterner, E. S.; Coughlin, E. B.; Theato, P., o-Nitrobenzyl Alcohol Derivatives: Opportunities in Polymer and Materials Science. *Macromolecules* **2012**, *45*, 1723-1736.
- 176. Zhao, Y., Light-Responsive Block Copolymer Micelles. *Macromolecules* **2012**, *45*, 3647-3657.

- 177. Jazani, A. M.; Oh, J. K., Development and disassembly of single and multiple acidcleavable block copolymer nanoassemblies for drug delivery. *Polymer Chemistry* **2020**, *11*, 2934-2954.
- 178. Jin, Q.; Cai, T.; Han, H.; Wang, H.; Wang, Y.; Ji, J., Light and pH dual-degradable triblock copolymer micelles for controlled intracellular drug release. *Macromol. Rapid Commun.* **2014**, *35*, 1372-1378.
- 179. Jazani, A. M.; Oh, J. K., Synthesis of multiple stimuli-responsive degradable block copolymers via facile carbonyl imidazole-induced postpolymerization modification. *Polymer Chemistry* **2022**, *13*, 4557-4568.
- 180. Qu, X.; Yang, Z., Benzoic-Imine-Based Physiological-pH-Responsive Materials for Biomedical Applications. *Chem. Asian J.* **2016**, *11*, 2633-2641.
- 181. Liguori, A.; Hakkarainen, M., Designed from Biobased Materials for Recycling: Imine-Based Covalent Adaptable Networks. *Macromol Rapid Commun* **2022**, *43*, e2100816.
- 182. Greb, L.; Lehn, J. M., Light-driven molecular motors: imines as four-step or two-step unidirectional rotors. *J Am Chem Soc* **2014**, *136*, 13114-13117.
- 183. Greb, L.; Mutlu, H.; Barner-Kowollik, C.; Lehn, J. M., Photo- and Metallo-responsive N-Alkyl alpha-Bisimines as Orthogonally Addressable Main-Chain Functional Groups in Metathesis Polymers. *J Am Chem Soc* **2016**, *138*, 1142-1145.
- 184. Thai, L. D.; Guimaraes, T. R.; Spann, S.; Goldmann, A. S.; Golberg, D.; Mutlu, H.; Barner-Kowollik, C., Photoswitchable block copolymers based on main chain α-bisimines. *Polymer Chemistry* **2022**, *13*, 5625-5635.
- 185. Fan, W.; Jin, Y.; Shi, L.; Zhou, R.; Du, W., Developing visible-light-induced dynamic aromatic Schiff base bonds for room-temperature self-healable and reprocessable waterborne polyurethanes with high mechanical properties. *Journal of Materials Chemistry A* **2020**, *8*, 6757-6767.
- 186. Zheng, H.; Wang, S.; Lu, C.; Ren, Y.; Liu, Z.; Ding, D.; Wu, Z.; Wang, X.; Chen, Y.; Zhang, Q., Thermal, Near-Infrared Light, and Amine Solvent Triple-Responsive Recyclable Imine-Type Vitrimer: Shape Memory, Accelerated Photohealing/Welding, and Destructing Behaviors. *Industrial & Engineering Chemistry Research* **2020**, *59*, 21768-21778.
- 187. Hu, X.; Oh, J. K., Direct Polymerization Approach to Synthesize Acid-Degradable Block Copolymers Bearing Imine Pendants for Tunable pH-Sensitivity and Enhanced Release. *Macromolecular Rapid Communications* **2020**, *41*, 2000394.
- 188. Jazani, A. M.; Shetty, C.; Movasat, H.; Bawa, K. K.; Oh, J. K., Imidazole-Mediated Dual Location Disassembly of Acid-Degradable Intracellular Drug Delivery Block Copolymer Nanoassemblies. *Macromolecular Rapid Communications* **2021**, *42*, 2100262.
- 189. Zhao, J.; Zhou, Y.; Zhou, Y.; Zhou, N.; Pan, X.; Zhang, Z.; Zhu, X., A straightforward approach for the one-pot synthesis of cyclic polymers from RAFT polymers via thiol—Michael addition. *Polymer Chemistry* **2016**, *7*, 1782-1791.
- 190. Mutlu, H.; Barner-Kowollik, C., Green chain-shattering polymers based on a self-immolative azobenzene motif. *Polymer Chemistry* **2016**, *7*, 2272-2279.
- 191. Heller, S. T.; Sarpong, R., On the reactivity of imidazole carbamates and ureas and their use as esterification and amidation reagents. *Tetrahedron* **2011**, *67*, 8851-8859.
- 192. Knopke, L. R.; Spannenberg, A.; Bruckner, A.; Bentrup, U., The influence of substituent effects on spectroscopic properties examined on benzylidene aniline-type imines. *Spectrochim Acta A Mol Biomol Spectrosc* **2012**, *95*, 18-24.

- 193. J. E. Johnson, N. M. M., A. M. Gorczyca, D. D. Dolliver and M. A. McAllister, Mechanisms of Acid-Catalyzed Z/E Isomerization of Imines. *Journal of Organic Chemistry* **2001**, *66*, 7979-7985.
- 194. Beach, M. A.; Nayanathara, U.; Gao, Y.; Zhang, C.; Xiong, Y.; Wang, Y.; Such, G. K., Polymeric Nanoparticles for Drug Delivery. *Chem Rev* **2024**,
- 195. Allen, C.; Maysinger, D.; Eisenberg, A., Nano-engineering block copolymer aggregates for drug delivery. *Colloids Surf.*, *B* **1999**, *16*, 3-27.
- 196. Taurin, S.; Nehoff, H.; Greish, K., Anticancer nanomedicine and tumor vascular permeability; Where is the missing link? *J. Controlled Release* **2012**, *164*, 265-275.
- 197. Zhang, L.; Li, Y.; Yu, J. C., Chemical modification of inorganic nanostructures for targeted and controlled drug delivery in cancer treatment. *J. Mater. Chem. B* **2014**, *2*, 452-470.
- 198. Nichols, J. W.; Bae, Y. H., Odyssey of a cancer nanoparticle: From injection site to site of action. *Nano Today* **2012**, *7*, 606-618.
- 199. Bae, Y. H.; Park, K., Targeted drug delivery to tumors: Myths, reality and possibility. *Journal of Controlled Release* **2011**, *153*, 198-205.
- 200. Farokhzad, O. C.; Langer, R., Impact of Nanotechnology on Drug Delivery. *ACS Nano* **2009**, *3*, 16-20.
- 201. Prokop, A.; Davidson, J. M., Nanovehicular intracellular delivery systems. *J. Pharm. Sci.* **2008**, *97*, 3518-3590.
- 202. Cabral, H.; Matsumoto, Y.; Mizuno, K.; Chen, Q.; Murakami, M.; Kimura, M.; Terada, Y.; Kano, M. R.; Miyazono, K.; Uesaka, M.; Nishiyama, N.; Kataoka, K., Accumulation of sub-100 nm polymeric micelles in poorly permeable tumors depends on size. *Nat. Nanotechnol.* **2011**, *6*, 815-823.
- 203. Wang, J.; Mao, W.; Lock, L. L.; Tang, J.; Sui, M.; Sun, W.; Cui, H.; Xu, D.; Shen, Y., The Role of Micelle Size in Tumor Accumulation, Penetration, and Treatment. *ACS Nano* **2015**, *9*, 7195-7206.
- 204. Cook, A. B.; Decuzzi, P., Harnessing Endogenous Stimuli for Responsive Materials in Theranostics. *ACS Nano* **2021**, *15*, 2068-2098.
- 205. Huo, M.; Yuan, J.; Tao, L.; Wei, Y., Redox-responsive polymers for drug delivery: from molecular design to applications. *Polymer Chemistry* **2014**, *5*, 1519-1528.
- 206. Ding, Y.; Kang, Y.; Zhang, X., Enzyme-responsive polymer assemblies constructed through covalent synthesis and supramolecular strategy. *Chem. Commun.* **2015**, *51*, 996-1003.
- 207. Kongkatigumjorn, N.; Crespy, D., Strategies to prepare polymers with cleavable linkages releasing active agents in acidic media. *Polymer Chemistry* **2024**, *15*, 4491-4518.
- 208. Bairagi, K.; Liu, J. T.; Thinphang-nga, A.; Oh, J. K., Synthesis and Dual-Acid/Light-Responsive Disassembly of Amphiphilic Block Copolymer Nanoassemblies Bearing Conjugated Benzoic Imine Pendants. *Macromolecules (Washington, DC, United States)* **2023**, *56*, 4307-4317.
- 209. El-Sawy, H. S.; Al-Abd, A. M.; Ahmed, T. A.; El-Say, K. M.; Torchilin, V. P., Stimuli-Responsive Nano-Architecture Drug-Delivery Systems to Solid Tumor Micromilieu: Past, Present, and Future Perspectives. *ACS Nano* **2018**, *12*, 10636-10664.
- 210. Oh, J. K., Disassembly and tumor-targeting drug delivery of reduction-responsive degradable block copolymer nanoassemblies. *Polymer Chemistry* **2019**, *10*, 1554-1568.
- 211. Altinbasak, I.; Alp, Y.; Sanyal, R.; Sanyal, A., Theranostic nanogels: multifunctional agents for simultaneous therapeutic delivery and diagnostic imaging. *Nanoscale* **2024**, *16*, 14033-14056.

- 212. Hu, J.; He, J.; Cao, D.; Zhang, M.; Ni, P., Core cross-linked polyphosphoester micelles with folate-targeted and acid-cleavable features for pH-triggered drug delivery. *Polymer Chemistry* **2015**, *6*, 3205-3216.
- 213. Zhang, Z.; Yin, L.; Tu, C.; Song, Z.; Zhang, Y.; Xu, Y.; Tong, R.; Zhou, Q.; Ren, J.; Cheng, J., Redox-Responsive, Core Cross-Linked Polyester Micelles. *ACS Macro Lett.* **2013**, *2*, 40-44.
- 214. Zhu, W.; Wang, Y.; Cai, X.; Zha, G.; Luo, Q.; Sun, R.; Li, X.; Shen, Z., Reduction-triggered release of paclitaxel from in situ formed biodegradable core-cross-linked micelles. *Journal of Materials Chemistry B: Materials for Biology and Medicine* **2015**, *3*, 3024-3031.
- 215. Liu, B.; Thayumanavan, S., Substituent Effects on the pH Sensitivity of Acetals and Ketals and Their Correlation with Encapsulation Stability in Polymeric Nanogels. *J. Am. Chem. Soc.* **2017**, *139*, 2306-2317.
- 216. Lee, S.-J.; Min, K.-H.; Lee, H.-J.; Koo, A.-N.; Rim, H.-P.; Jeon, B.-J.; Jeong, S.-Y.; Heo, J.-S.; Lee, S.-C., Ketal Cross-Linked Poly(ethylene glycol)-Poly(amino acid)s Copolymer Micelles for Efficient Intracellular Delivery of Doxorubicin. *Biomacromolecules* **2011**, *12*, 1224-1233.
- 217. Chen, W.; Zheng, M.; Meng, F.; Cheng, R.; Deng, C.; Feijen, J.; Zhong, Z., In Situ Forming Reduction-Sensitive Degradable Nanogels for Facile Loading and Triggered Intracellular Release of Proteins. *Biomacromolecules* **2013**, *14*, 1214-1222.
- 218. Yang, H. Y.; Li, Y.; Jang, M.-S.; Fu, Y.; Wu, T.; Lee, J. H.; Lee, D. S., Green preparation of pH-responsive and dual targeting hyaluronic acid nanogels for efficient protein delivery. *European Polymer Journal* **2019**, *121*, 109342.
- 219. Hartlieb, M.; Bus, T.; Kubel, J.; Pretzel, D.; Hoeppener, S.; Leiske, M. N.; Kempe, K.; Dietzek, B.; Schubert, U. S., Tailoring Cellular Uptake and Fluorescence of Poly(2-oxazoline)-Based Nanogels. *Bioconjug Chem* **2017**, *28*, 1229-1235.
- 220. Raghupathi, K.; Li, L.; Ventura, J.; Jennings, M.; Thayumanavan, S., pH responsive soft nanoclusters with size and charge variation features. *Polymer Chemistry* **2014**, *5*, 1737-1742.
- 221. Chai, J. D.; Head-Gordon, M., Systematic optimization of long-range corrected hybrid density functionals. *J Chem Phys* **2008**, *128*, 084106.
- 222. Frisch, M. J.; Pople, J. A.; Binkley, J. S., Self-consistent molecular orbital methods 25. Supplementary functions for Gaussian basis sets. *The Journal of chemical physics* **1984**, *80*, 3265-3269.
- 223. Tahaoglu, D.; Usta, H.; Alkan, F., Revisiting the Role of Charge Transfer in the Emission Properties of Carborane-Fluorophore Systems: A TDDFT Investigation. *J Phys Chem A* **2022**, *126*, 4199-4210.
- 224. Frisch, M.; Trucks, G.; Schlegel, H.; Scuseria, G.; Robb, M.; Cheeseman, J.; Scalmani, G.; Barone, V.; Petersson, G.; Nakatsuji, H., Gaussian 16 Revision C. 01, 2016. *Gaussian Inc. Wallingford CT* **2016**, *1*, 572.
- 225. Dhillon, N.; Aggarwal, B. B.; Newman, R. A.; Wolff, R. A.; Kunnumakkara, A. B.; Abbruzzese, J. L.; Ng, C. S.; Badmaev, V.; Kurzrock, R., Phase II trial of curcumin in patients with advanced pancreatic cancer. *Clin Cancer Res* **2008**, *14*, 4491-4499.
- 226. Zoi, V.; Galani, V.; Lianos, G. D.; Voulgaris, S.; Kyritsis, A. P.; Alexiou, G. A., The Role of Curcumin in Cancer Treatment. *Biomedicines* **2021**, *9*, 1086.
- 227. Gupta, K. K.; Bharne, S. S.; Rathinasamy, K.; Naik, N. R.; Panda, D., Dietary antioxidant curcumin inhibits microtubule assembly through tubulin binding. *FEBS J* **2006**, *273*, 5320-5332.

- 228. Rashmi, R.; Prakash, N.; Narayanaswamy, H.; Swamy, M. N.; Rathnamma, D.; Ramesh, P.; Sunilchandra, U.; Santhosh, C.; Dhanalakshmi, H.; Nagaraju, N.; Vanishree, H., Cytotoxicity screening of curcumin on HeLa cancer cell lines. *Journal of Entomology and Zoology Studies* **2020**, *8*, 267-269.
- 229. Kamaly, N.; Yameen, B.; Wu, J.; Farokhzad, O. C., Degradable Controlled-Release Polymers and Polymeric Nanoparticles: Mechanisms of Controlling Drug Release. *Chemical Reviews (Washington, DC, United States)* **2016**, *116*, 2602-2663.
- 230. Kost, J.; Langer, R., Responsive polymeric delivery systems. *Advanced Drug Delivery Reviews* **2012**, *64*, 327-341.
- 231. Stuart, M. A. C.; Huck, W. T. S.; Genzer, J.; Muller, M.; Ober, C.; Stamm, M.; Sukhorukov, G. B.; Szleifer, I.; Tsukruk, V. V.; Urban, M.; Winnik, F.; Zauscher, S.; Luzinov, I.; Minko, S., Emerging applications of stimuli-responsive polymer materials. *Nature Materials* **2010**, *9*, 101-113.
- 232. Qin, X.; Li, Y., Strategies To Design and Synthesize Polymer-Based Stimuli-Responsive Drug-Delivery Nanosystems. *ChemBioChem* **2020**, *21*, 1236-1253.
- 233. Liu, Y.; Chen, L.; Shi, Q.; Zhao, Q.; Ma, H., Tumor Microenvironment-Responsive Polypeptide Nanogels for Controlled Antitumor Drug Delivery. *Front Pharmacol* **2021**, *12*, 748102.
- 234. Wang, Y.; Starvaggi, N.; Pentzer, E., Capsules with responsive polymeric shells for applications beyond drug delivery. *Polymer Chemistry* **2023**, *14*, 4033-4047.
- 235. Liu, H.; Lu, H. H.; Alp, Y.; Wu, R.; Thayumanavan, S., Structural Determinants of Stimuli-Responsiveness in Amphiphilic Macromolecular Nano-assemblies. *Prog Polym Sci* **2024**, *148*,
- 236. Blum, A. P.; Kammeyer, J. K.; Rush, A. M.; Callmann, C. E.; Hahn, M. E.; Gianneschi, N. C., Stimuli-responsive nanomaterials for biomedical applications. *J Am Chem Soc* **2015**, *137*, 2140-2154.
- 237. Ding, H.; Tan, P.; Fu, S.; Tian, X.; Zhang, H.; Ma, X.; Gu, Z.; Luo, K., Preparation and application of pH-responsive drug delivery systems. *J Control Release* **2022**, *348*, 206-238.
- 238. Jia, F.; Wang, Y.; Wang, H.; Jin, Q.; Cai, T.; Chen, Y.; Ji, J., Light cross-linkable and pH de-cross-linkable drug nanocarriers for intracellular drug delivery. *Polym. Chem.* **2015**, *6*, 2069-2075.
- 239. Long, Y.-B.; Gu, W.-X.; Pang, C.; Ma, J.; Gao, H., Construction of coumarin-based cross-linked micelles with pH responsive hydrazone bond and tumor targeting moiety. *Journal of Materials Chemistry B: Materials for Biology and Medicine* **2016**, *4*, 1480-1488.
- 240. Pasparakis, G.; Manouras, T.; Vamvakaki, M.; Argitis, P., Harnessing photochemical internalization with dual degradable nanoparticles for combinatorial photo-chemotherapy. *Nature Communications* **2014**, *5*, 4623/4621-4623/4629.
- 241. Bairagi, K.; Shamekhi, M.; Tountas, I.; Letourneau, N.; Peslherbe, G. H.; Piekny, A.; Oh, J. K., Development of Dual Acid/Visible Light-Degradable Core-Crosslinked Nanogels with Extended Conjugate Aromatic Imines for Enhanced Drug Delivery *Journal of Materials Chemistry B* **2025**, *doi.org/10.1039/D5TB00734H*,
- 242. Martin, T. R.; Rynearson, L.; Kuller, M.; Quinn, J.; Wang, C.; Lucht, B.; Neale, N. R., Conjugated Imine Polymer Synthesized via Step-Growth Metathesis for Highly Stable Silicon Nanoparticle Anodes in Lithium-Ion Batteries. *Advanced Energy Materials* **2023**, *13*, 2203921.

- 243. Knop, K.; Hoogenboom, R.; Fischer, D.; Schubert, U. S., Poly(ethylene glycol) in drug delivery: pros and cons as well as potential alternatives. *Angew Chem Int Ed Engl* **2010**, *49*, 6288-6308.
- 244. Bera, A.; Ojha, K.; Mandal, A., Synergistic Effect of Mixed Surfactant Systems on Foam Behavior and Surface Tension. *Journal of Surfactants and Detergents* **2013**, *16*, 621-630.

# **Appendices**

## A1. Supporting Information for Chapter 3

Figure S3.1. <sup>1</sup>H-NMR spectrum of A1 in CDCl<sub>3</sub>.

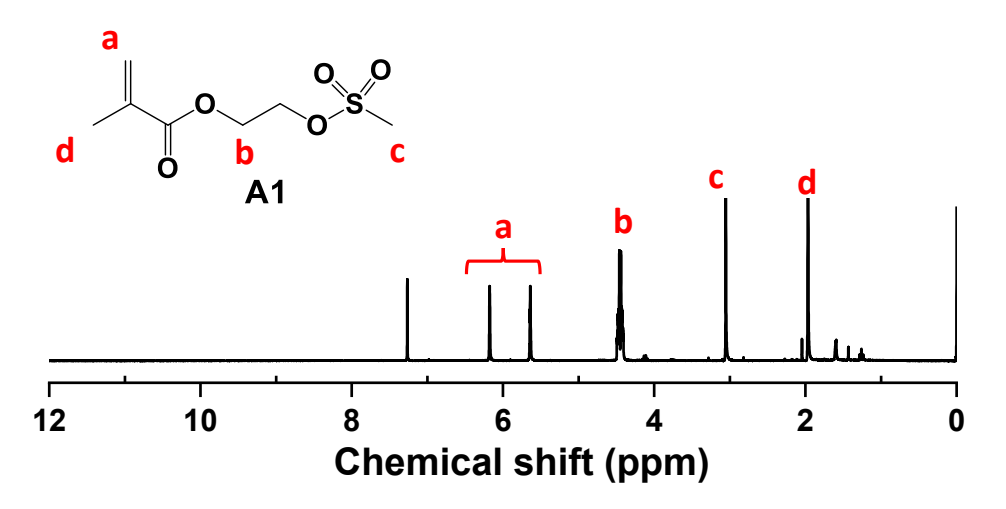


Figure S3.2. <sup>1</sup>H-NMR spectrum of A2 in CDCl<sub>3</sub>.

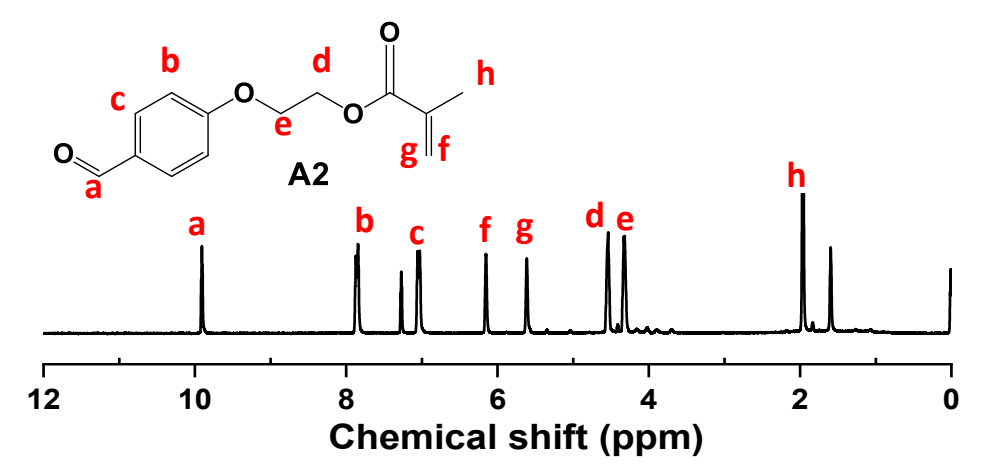
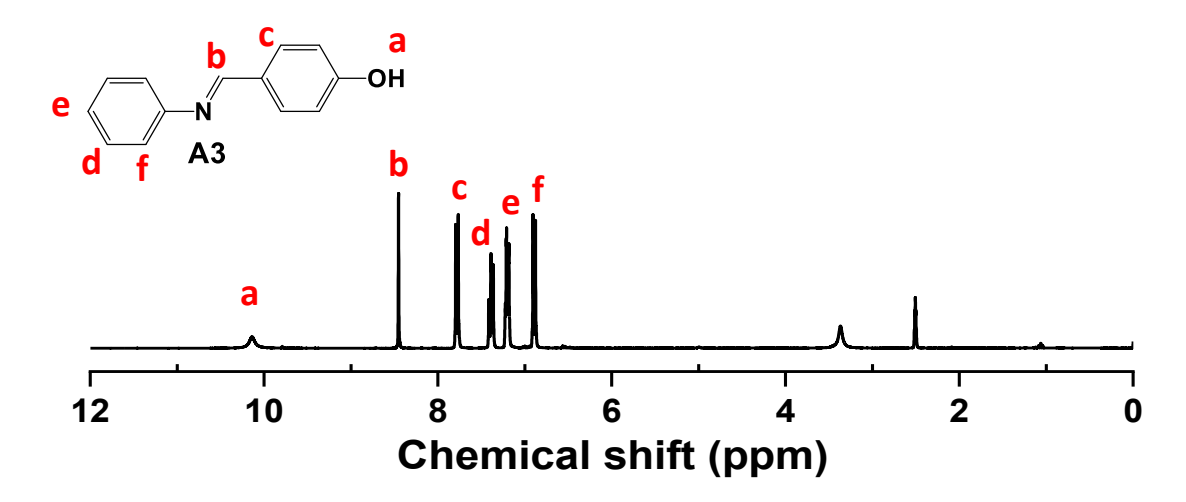
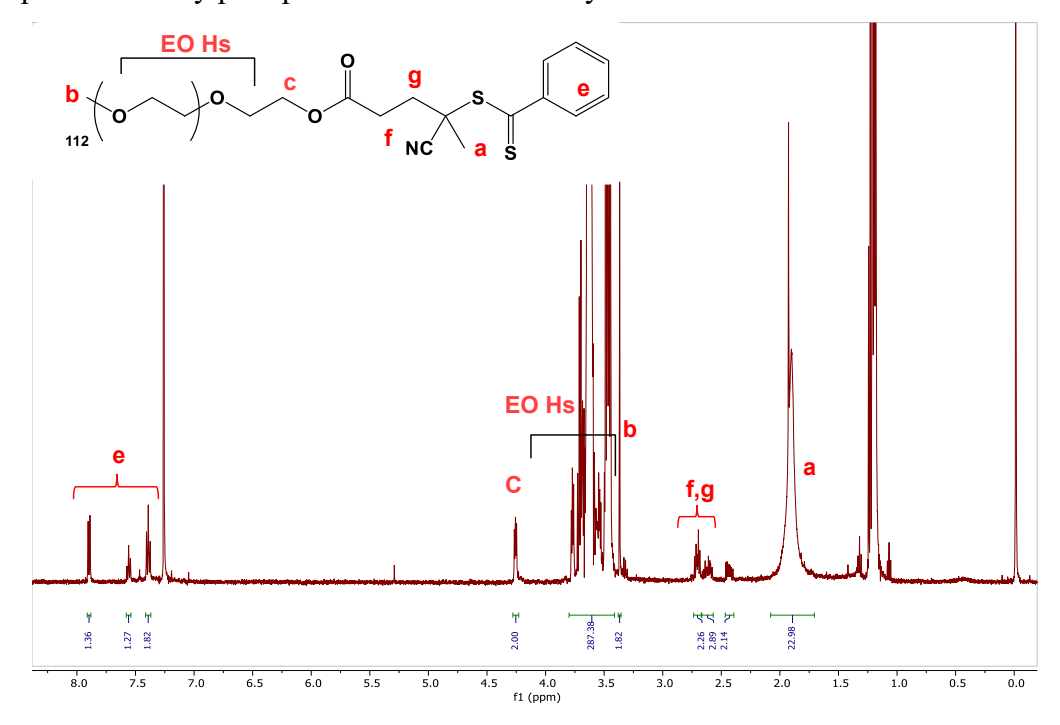


Figure S3.3. <sup>1</sup>H-NMR spectrum of A3 in CDCl<sub>3</sub>.



**Figure S3.4**. <sup>1</sup>H-NMR spectrum in CDCl<sub>3</sub> of a PEG-based macro-RAFT mediator after purification by precipitation from cold diethyl ether.



(The peaks at 7.0-8.0 ppm correspond to aromatic protons in RAFT moieties and the new peak at 4.2 ppm corresponds to methylene protons adjacent to ester groups. Their integral values are quantitative, confirming successful synthesis of PEG-RAFT agent.)

**Figure S3.5**. <sup>1</sup>H-NMR spectrum in CDCl<sub>3</sub> for RAFT polymerization of M2 in the presence of PEG-RAFT mediator after 20 hrs, indicating no polymerization (no conversion of M2 to polymer).

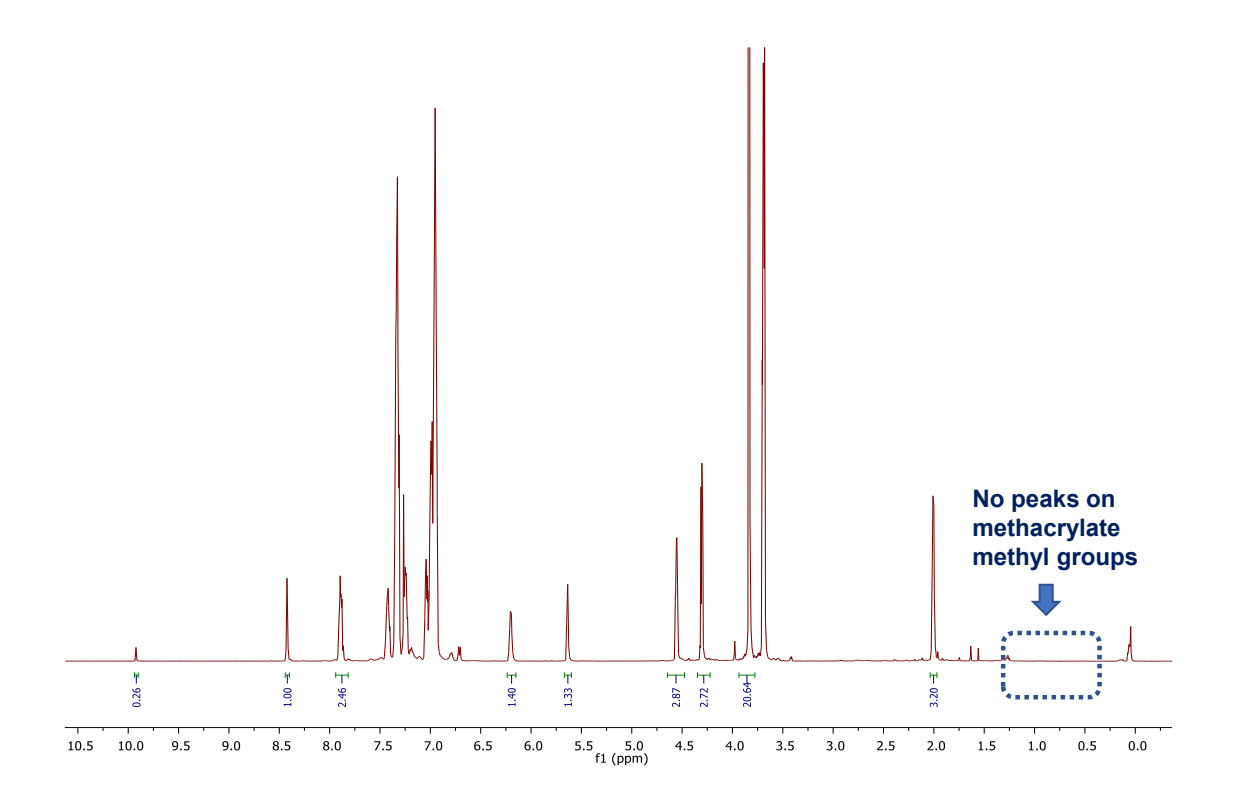


**Figure S3.6**. <sup>1</sup>H-NMR spectrum in CDCl<sub>3</sub> for RAFT polymerization of MMA in the presence of CTA after 4.5 hrs.

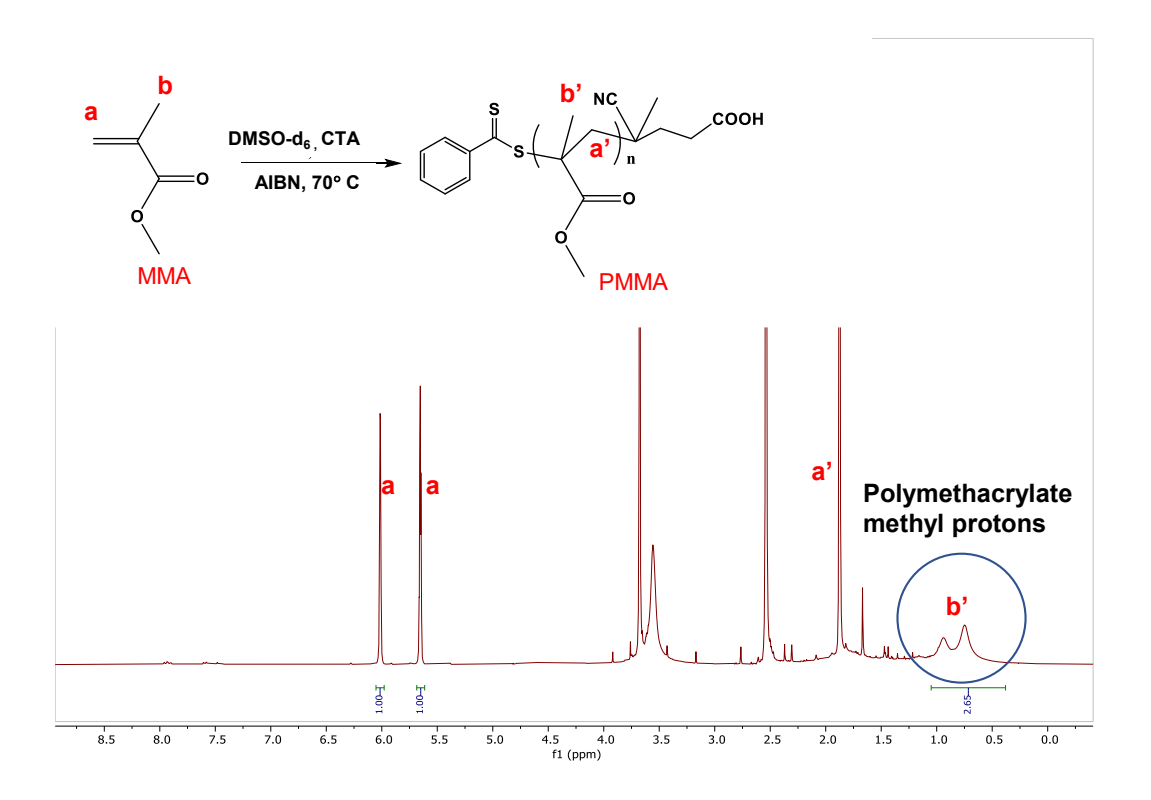


**Figure S3.7**. <sup>1</sup>H-NMR spectrum in CDCl<sub>3</sub> for RAFT polymerization of MMA in the presence of A3 after 20 hrs.

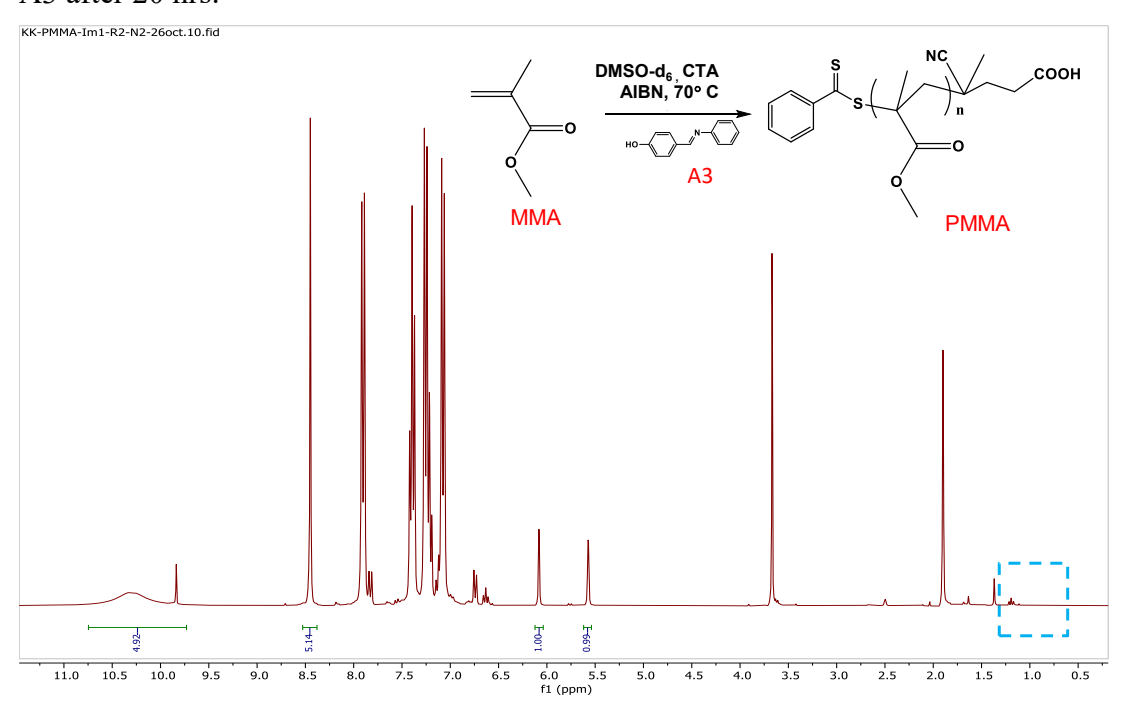
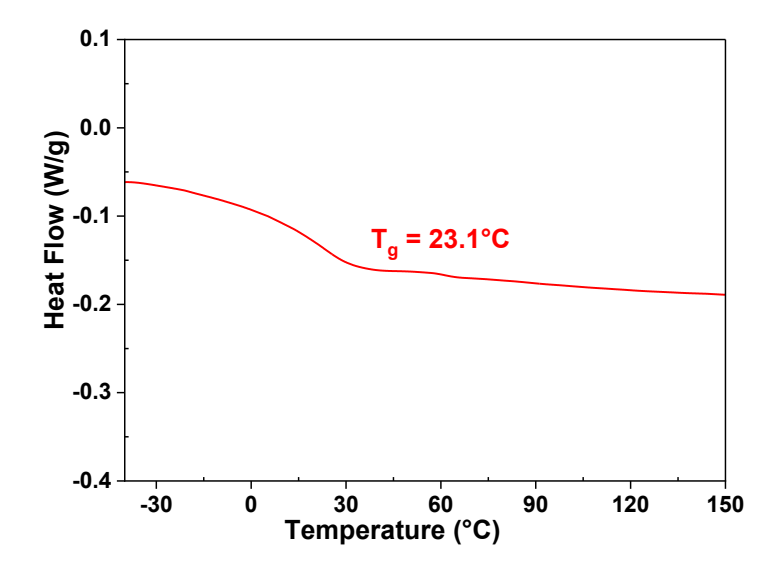
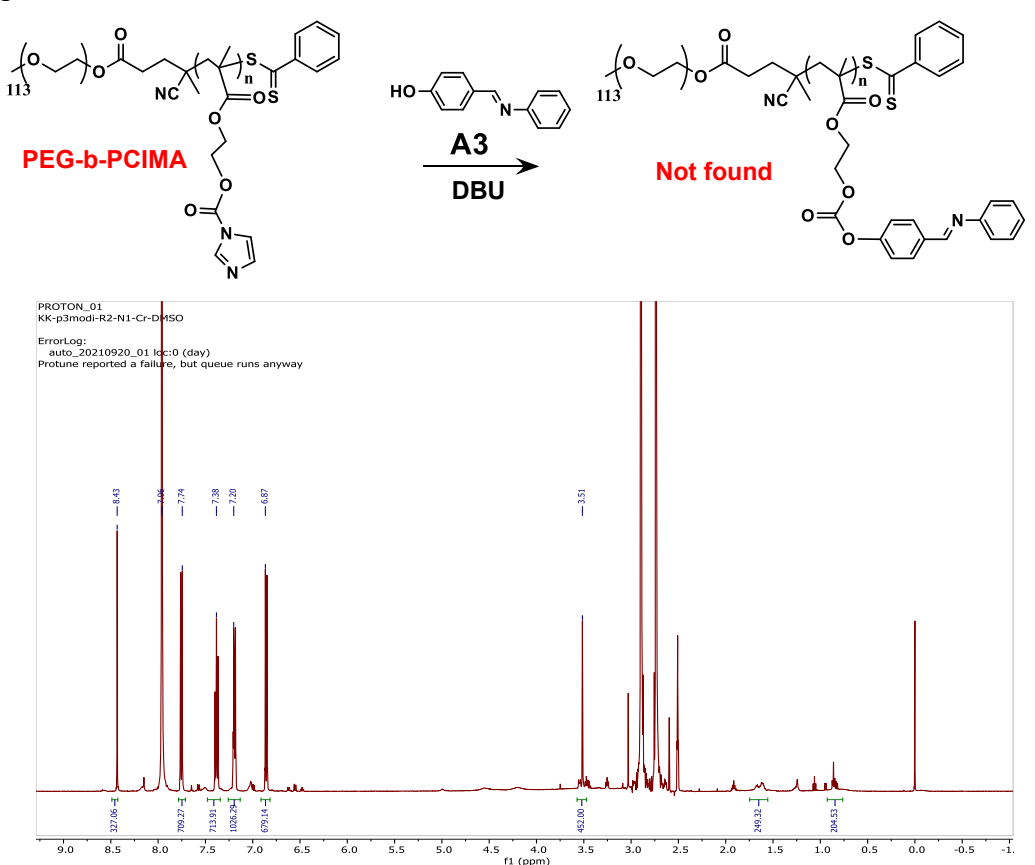


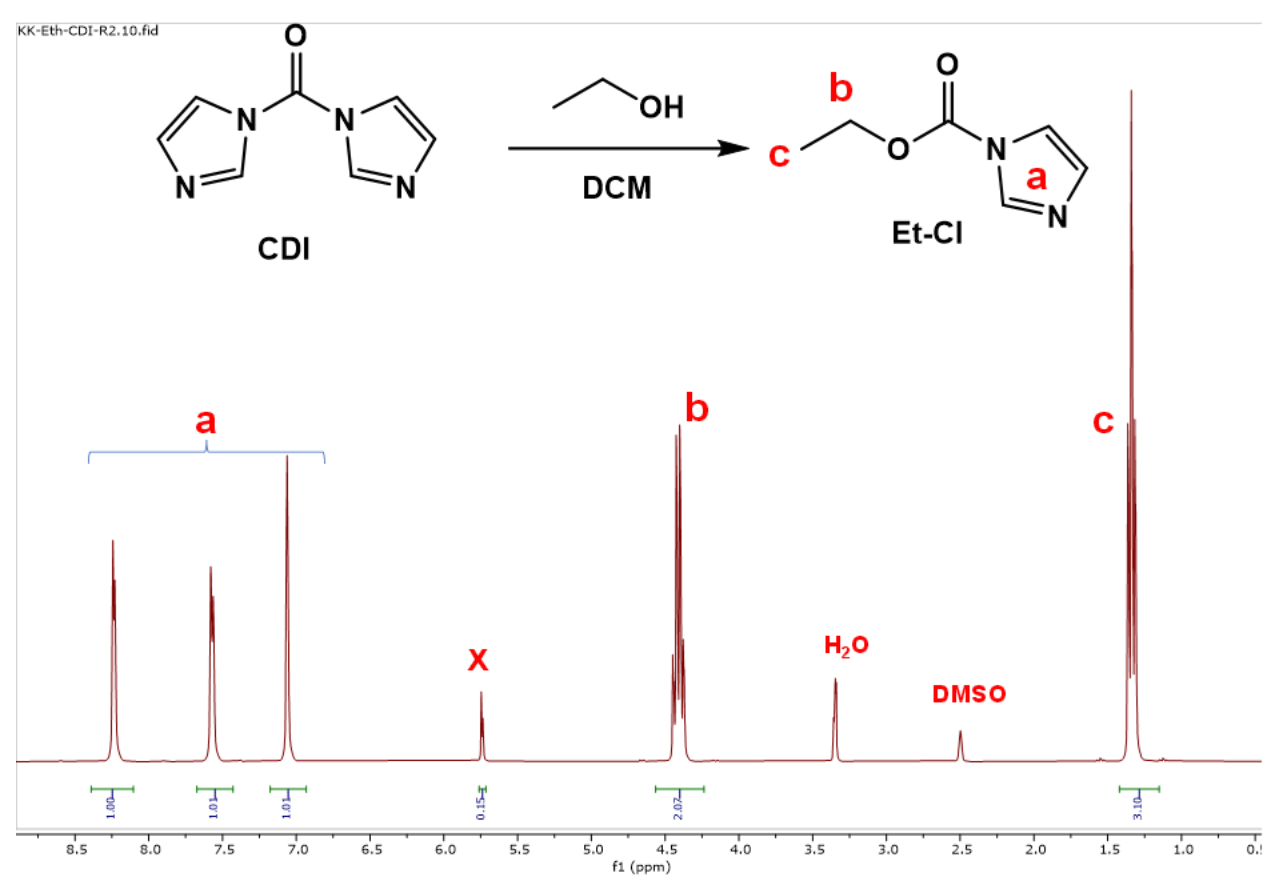
Figure S3.8. DSC thermogram of P-Im.



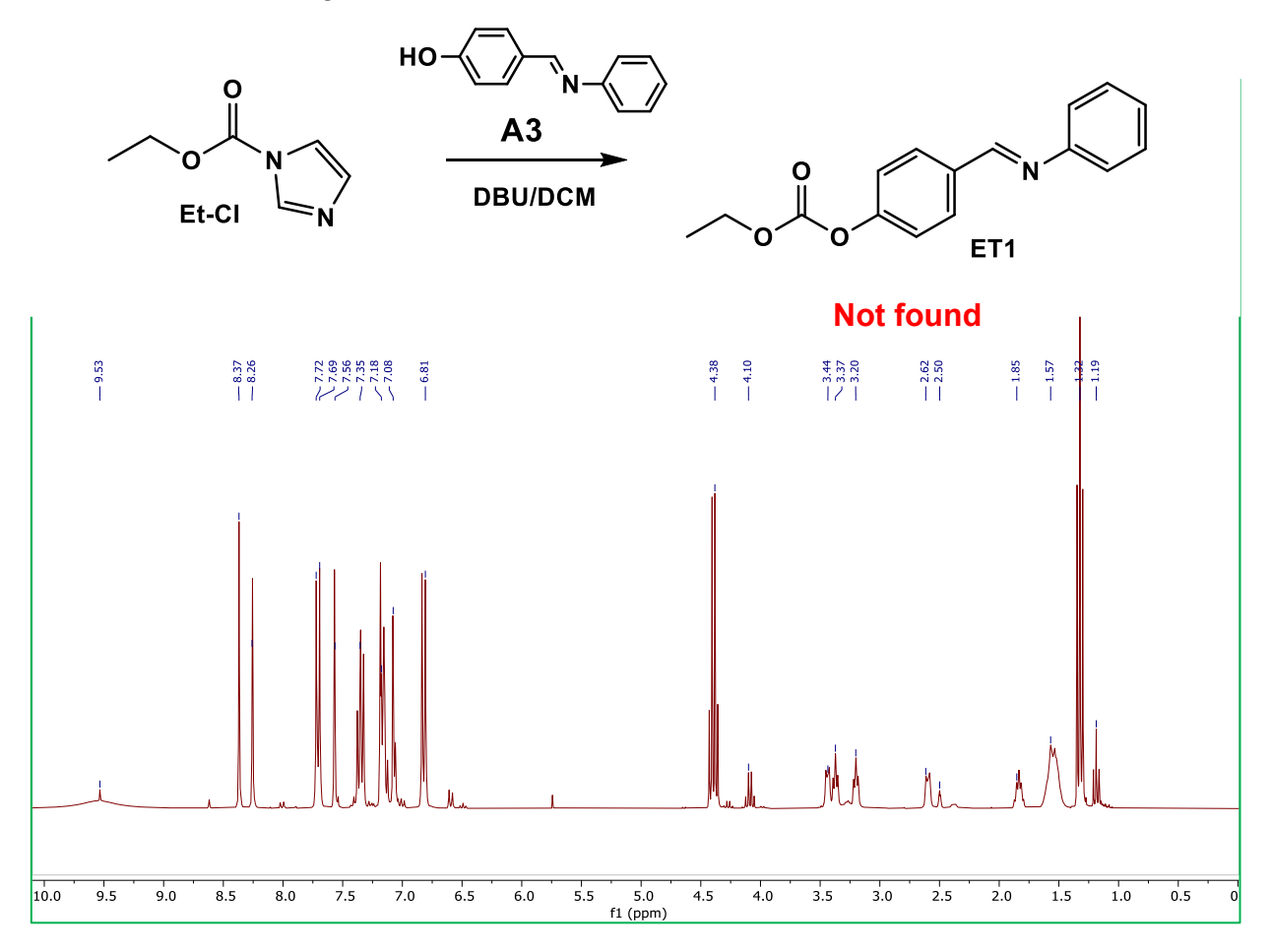
**Figure S3.9**. <sup>1</sup>H-NMR spectrum in CDCl<sub>3</sub> for reaction mixture of PEG-b-PCIMA with A3 precursor.



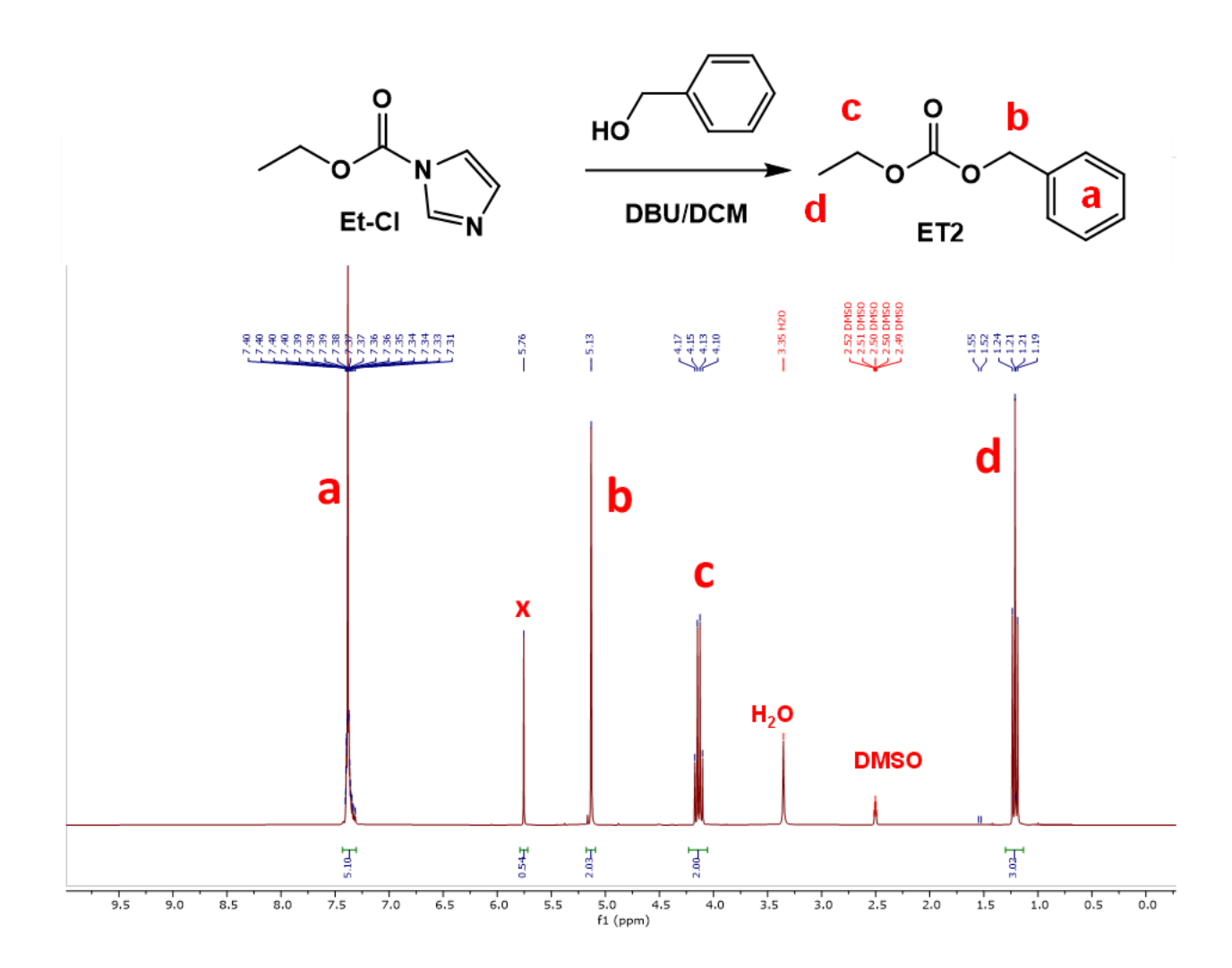
**Figure S3.10**. <sup>1</sup>H-NMR spectrum in DMSO-d<sub>6</sub> of Et-CI synthesized by CDI-mediated coupling reaction of EtOH. x denotes impurity.



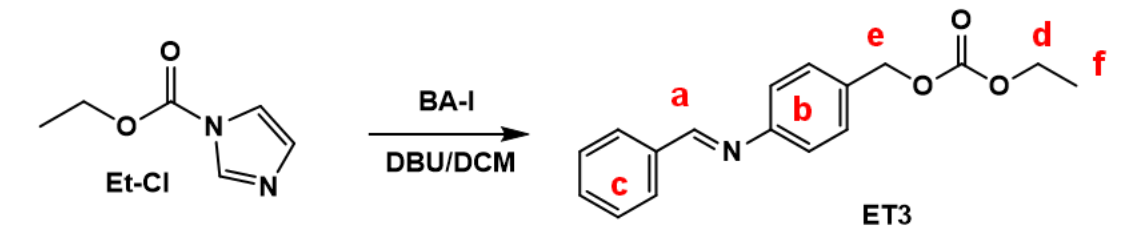
**Figure S3.11**. <sup>1</sup>H-NMR spectrum in DMSO-d<sub>6</sub> of ET1 synthesized by CDI-mediated coupling reaction of Et-CI with A3.



**Figure S3.12**. <sup>1</sup>H-NMR spectrum in DMSO-d<sub>6</sub> of ET2 synthesized by CDI-mediated coupling reaction of Et-CI with benzyl alcohol. x denotes impurity.



**Figure S3.13**. <sup>1</sup>H-NMR spectrum in DMSO-d<sub>6</sub> of ET3 synthesized by CDI-mediated coupling reaction of Et-CI with BA-I. x denotes impurity.



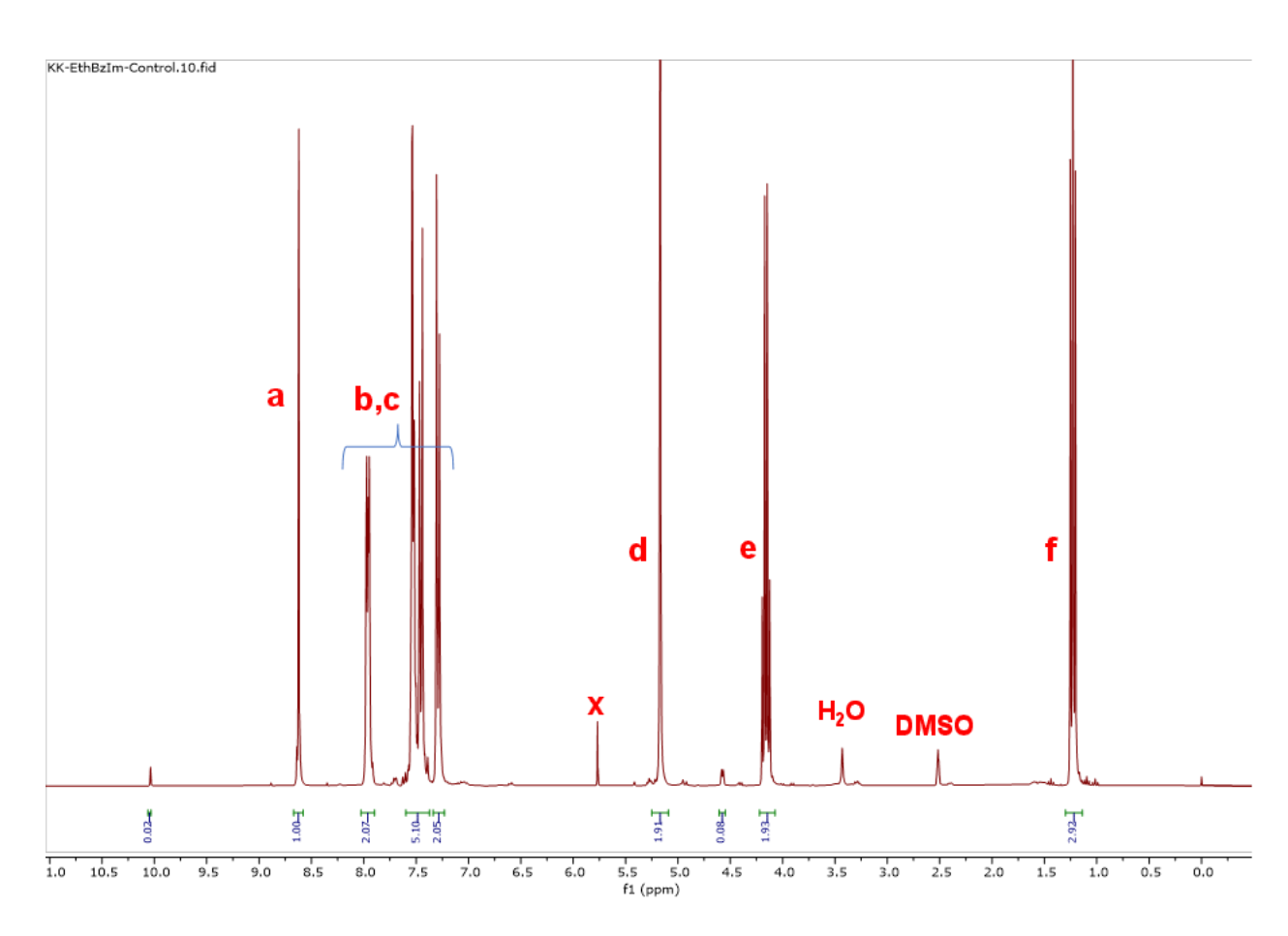


**Figure S3.14**. Overlaid UV/Vis spectra (a) and absorbance at  $\lambda_{max} = 285$  nm (b) of M2 over concentration in DMF.

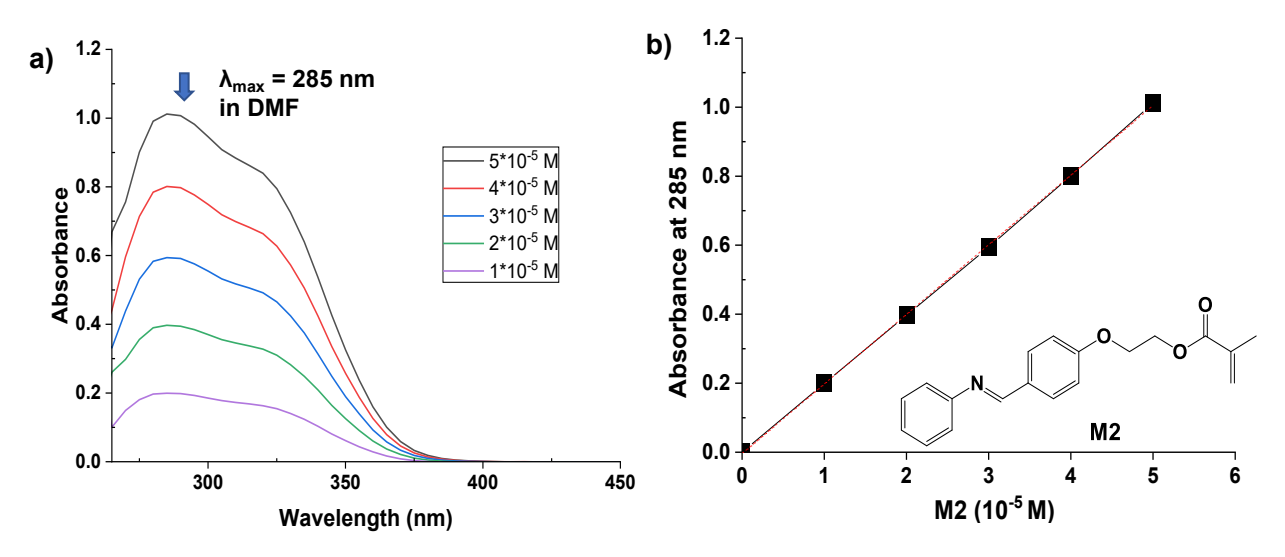


**Figure S3.15**. Overlaid UV/Vis spectra (a) and absorbance at  $\lambda_{max} = 270$  nm (b) of M1 over concentration in DMSO.

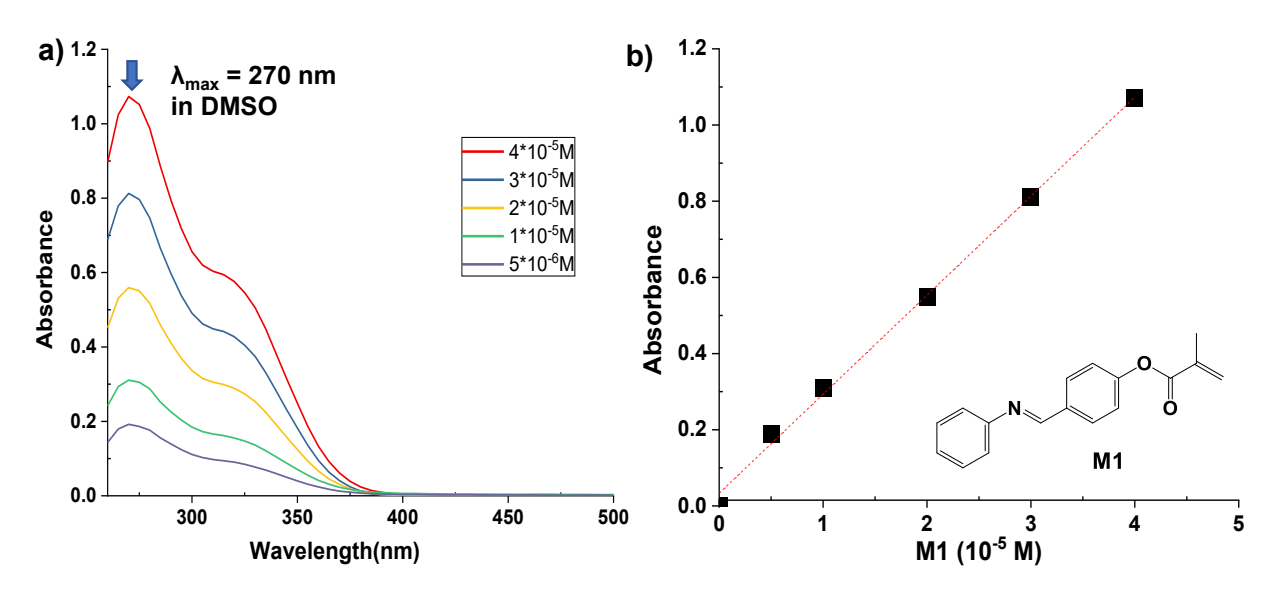


**Figure S3.16**. Overlaid UV/Vis spectra (a) and absorbance at  $\lambda_{max} = 255$  nm (b) of M-HX over concentration in DMF.

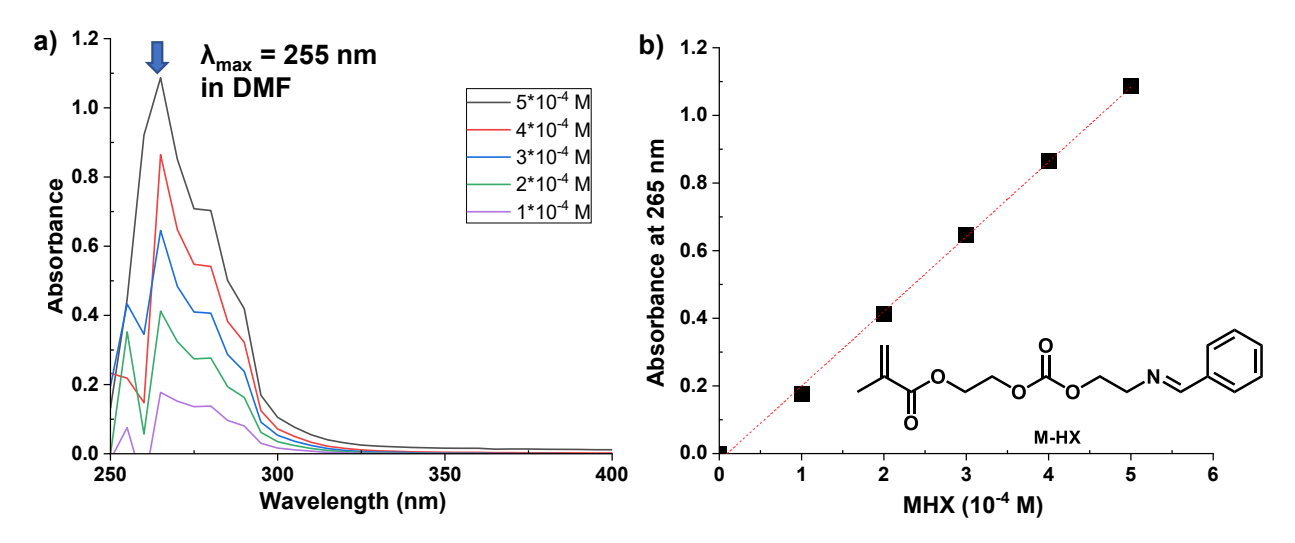


**Figure S3.17**. Overlaid UV/Vis spectra (a) and absorbance at  $\lambda_{max} = 270$  nm (b) of BA-I over concentration in DMSO.

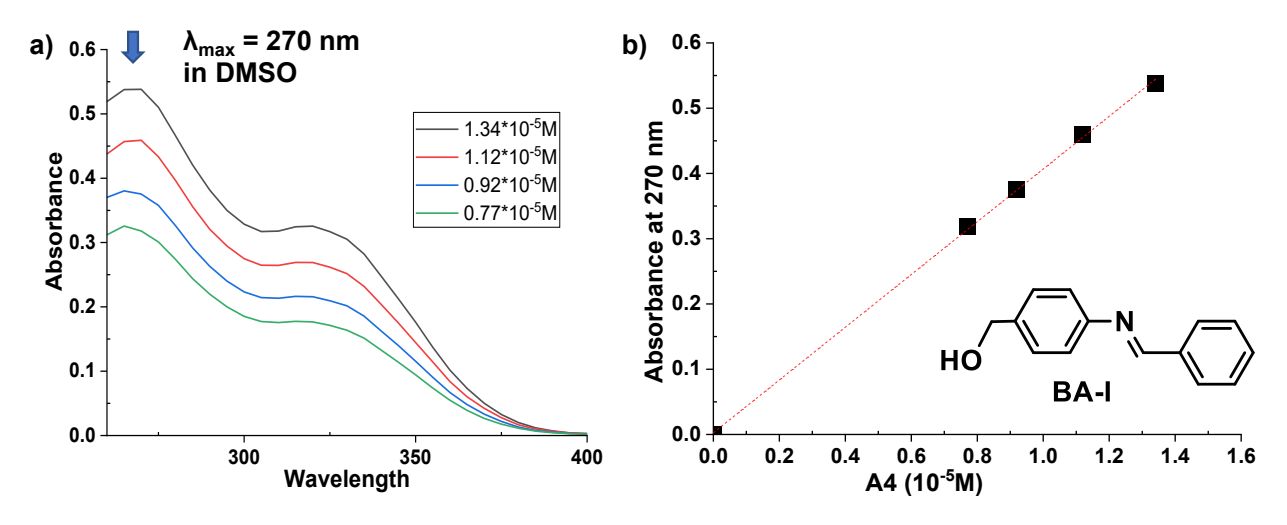


**Figure S3.18**. Overlaid  $^1H$ -NMR spectra (a) and %hydrolysis of M2 over stirring time in a mixture of  $3/1 \text{ v/v CD}_3\text{CN/D}_2\text{O}$  at pD = 6.8.

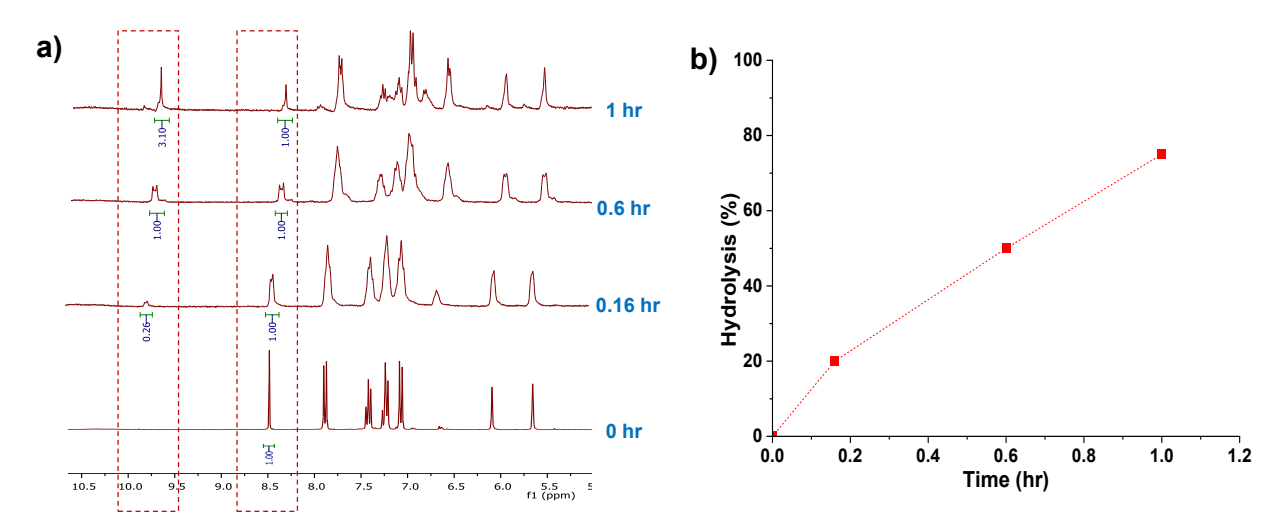


**Figure S3.19**. Overlaid  ${}^{1}H$ -NMR spectra (a) and %hydrolysis of M2 over stirring time in a mixture of  $3/1 \text{ v/v CD}_{3}\text{CN/D}_{2}\text{O}$  at pD = 7.4.

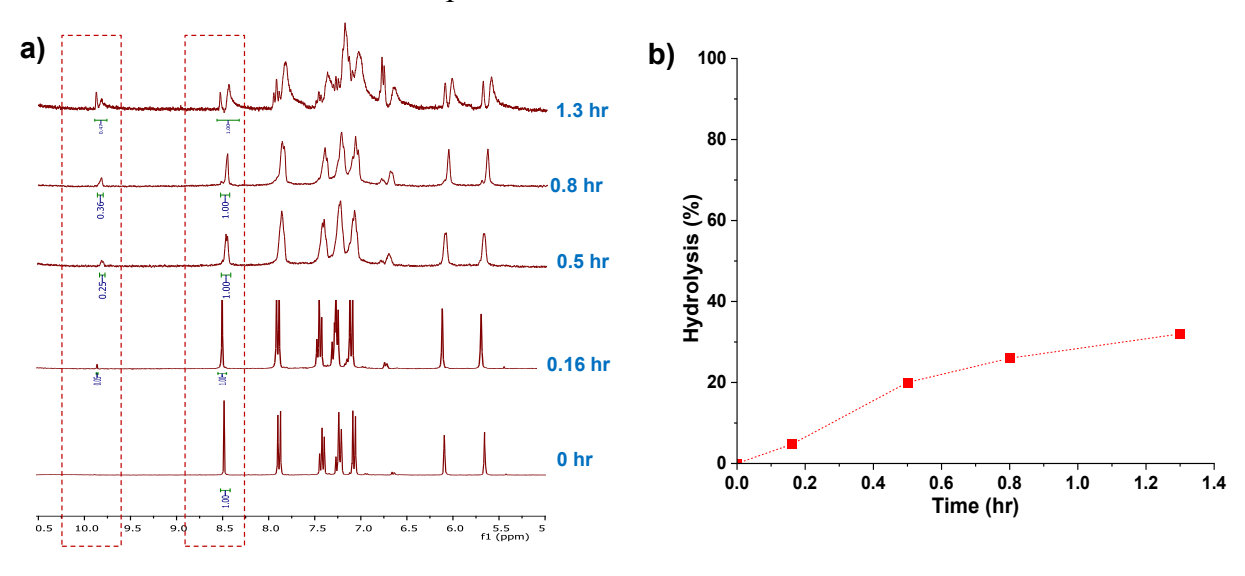
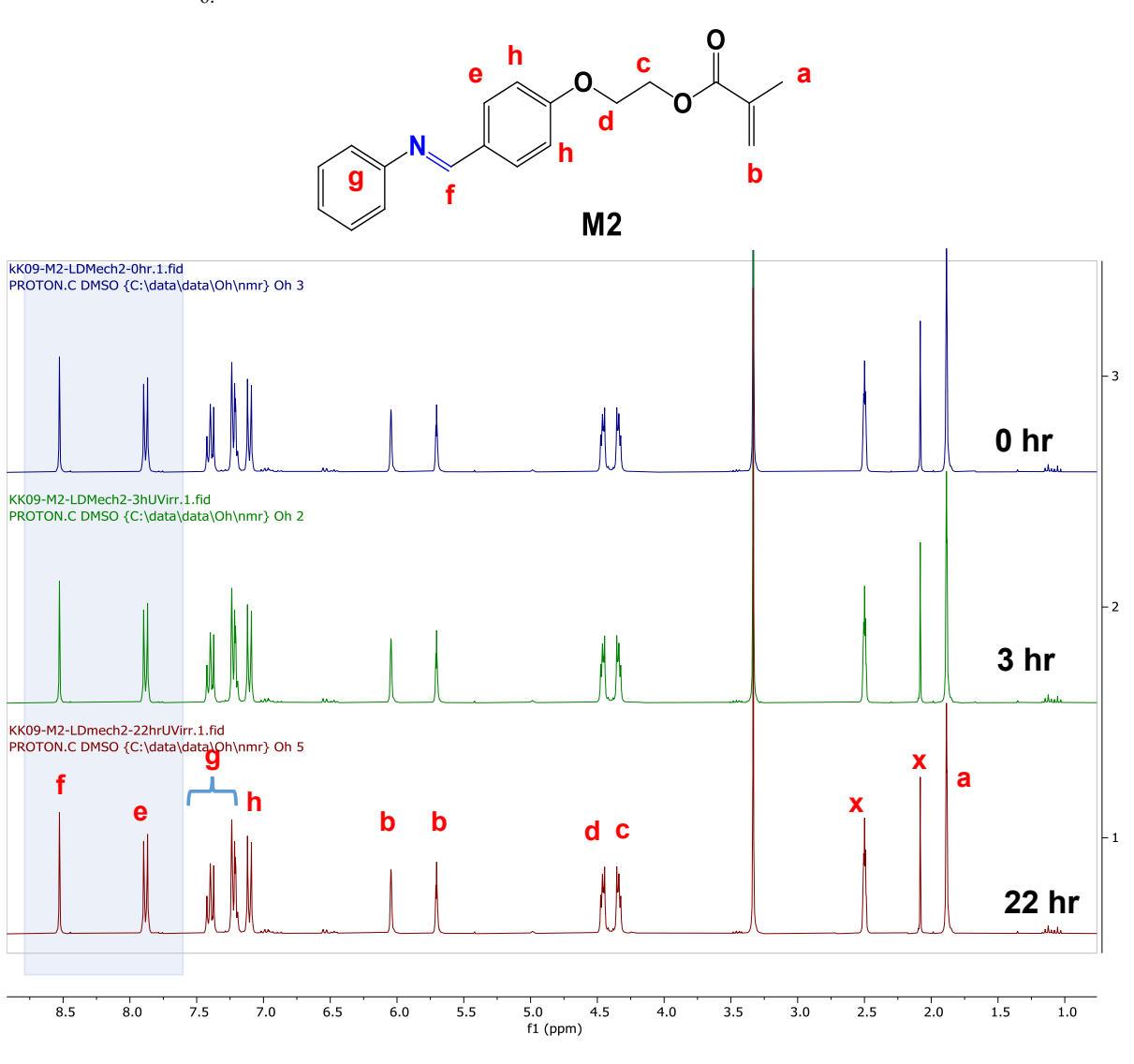


**Figure S3.20**. Overlaid <sup>1</sup>H-NMR spectra of M2 over irradiation time under UV light at  $\lambda = 340$  nm in DMDO-d<sub>6</sub>.



### A2. Supporting Information for Chapter 4

Figure S4.1. <sup>13</sup>C NMR spectrum of M3 in DMSO-d<sub>6</sub>.

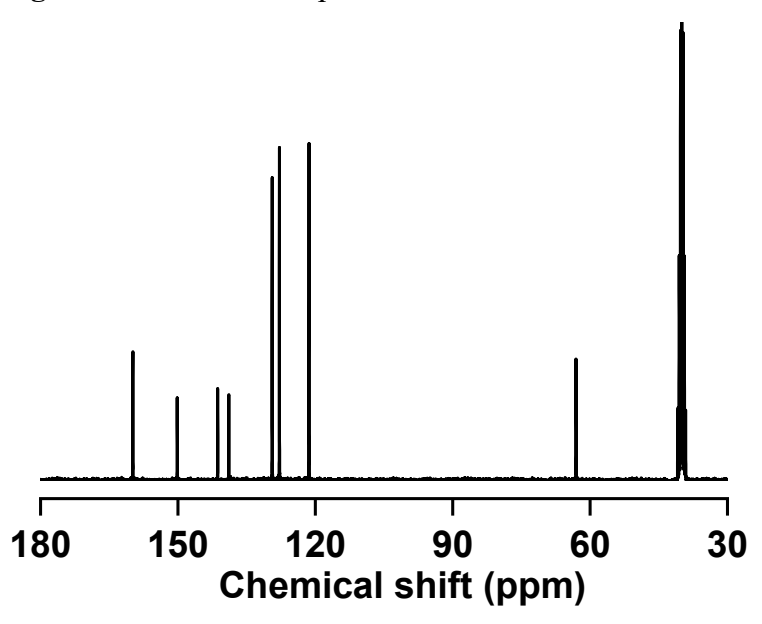


Figure S4.2. HR-MS spectrum of M3.

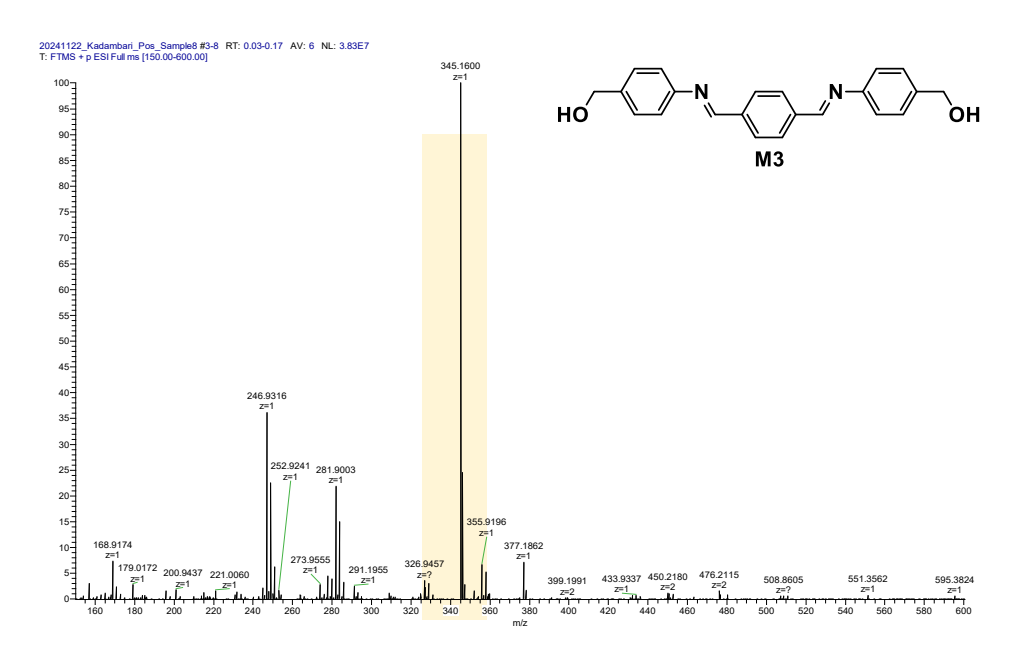
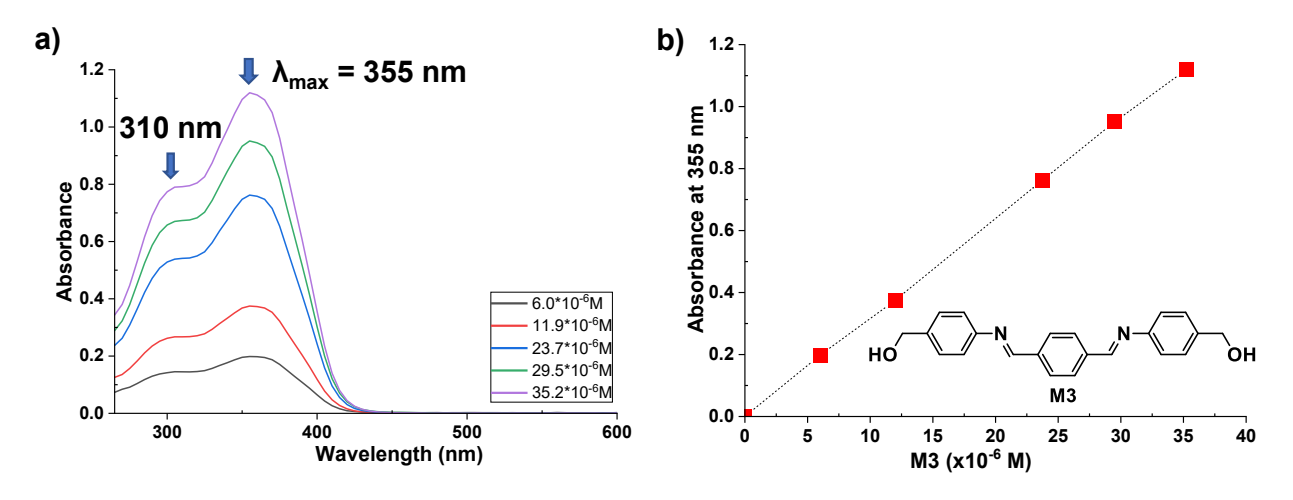
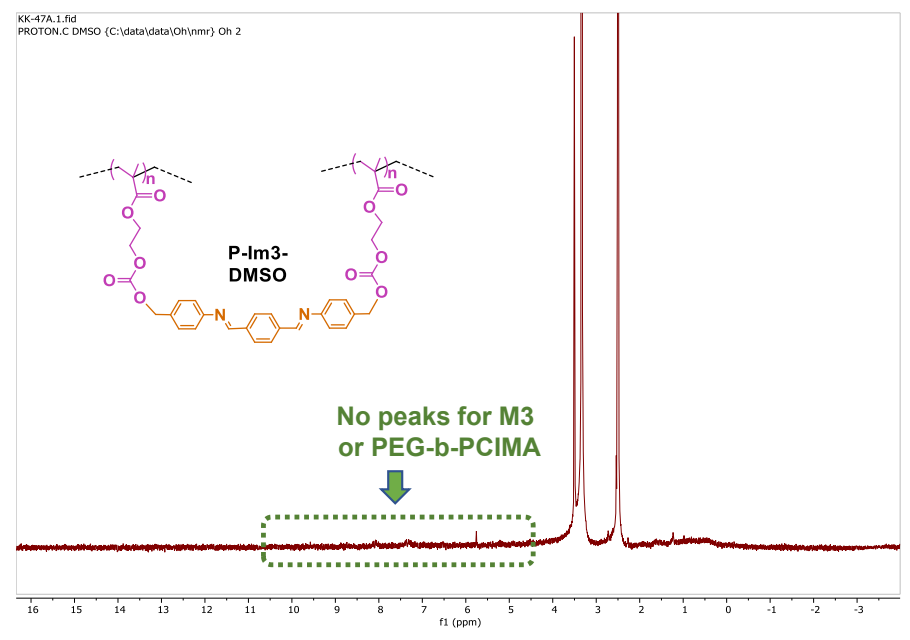


Figure S4.3. Overlaid UV/Vis spectra (a) and absorbance at  $\lambda_{max} = 355$  nm (b) of M3 over its concentration in DMSO.



**Figure S4.4**. <sup>1</sup>H NMR spectrum of P-Im3-DMSO swollen in DMSO-d<sub>6</sub>. The spectrum shows no peaks presenting M3 and PEG-b-PCIMA.



**Figure S4.5**. <sup>1</sup>H NMR spectrum of the supernatant in DMSO-d<sub>6</sub> after P-Im3-DMSO was precipitated from cold diethyl ether. The spectrum shows peaks presenting free imidazole as a side product that is generated by CDI-mediated crosslinking reactions.

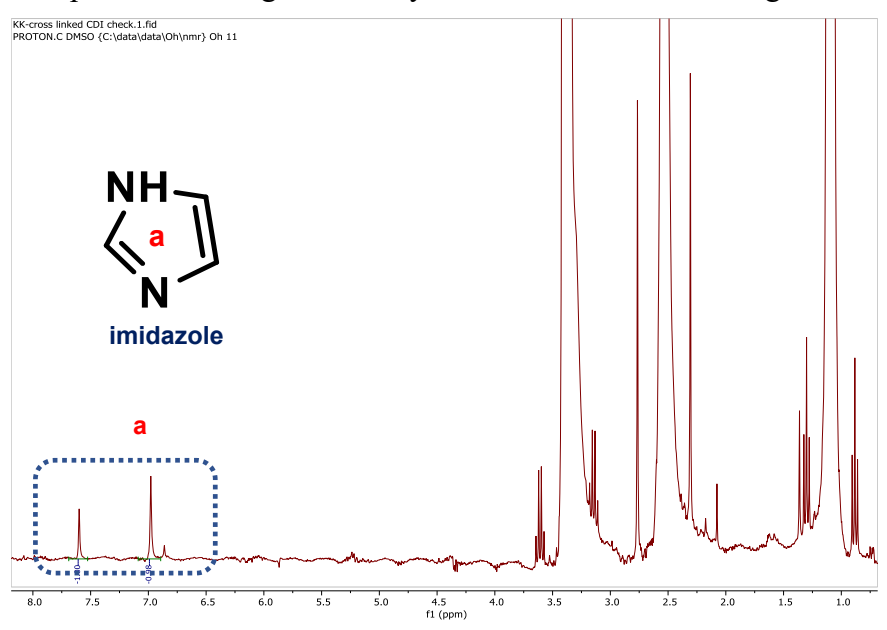


Figure S4.6. DSC thermogram of P-Im3-DMSO.

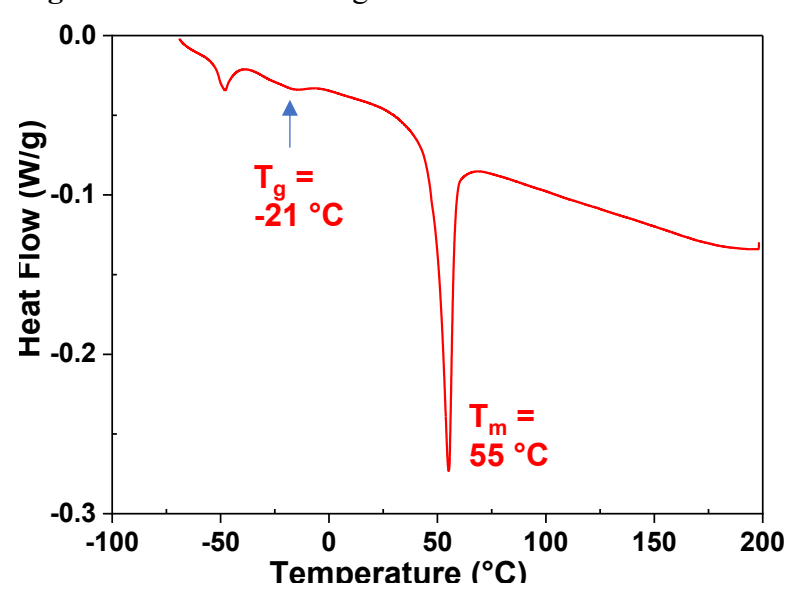
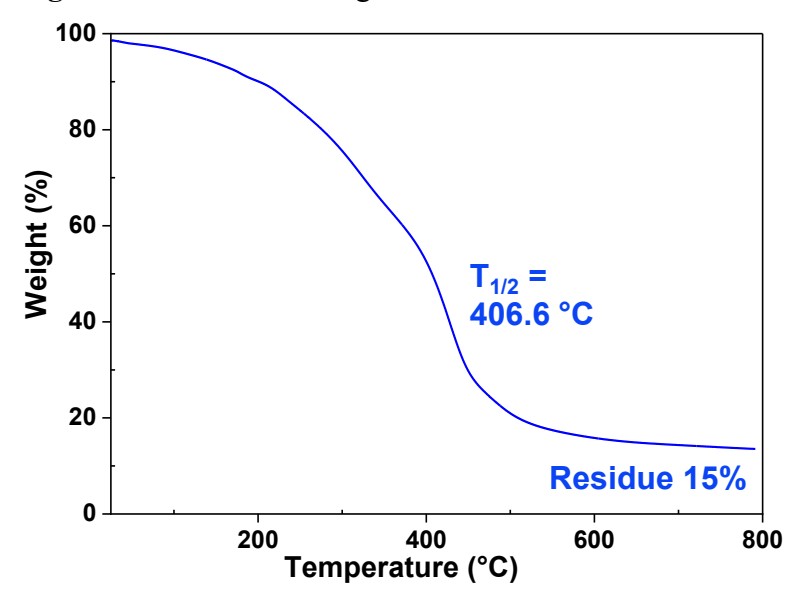
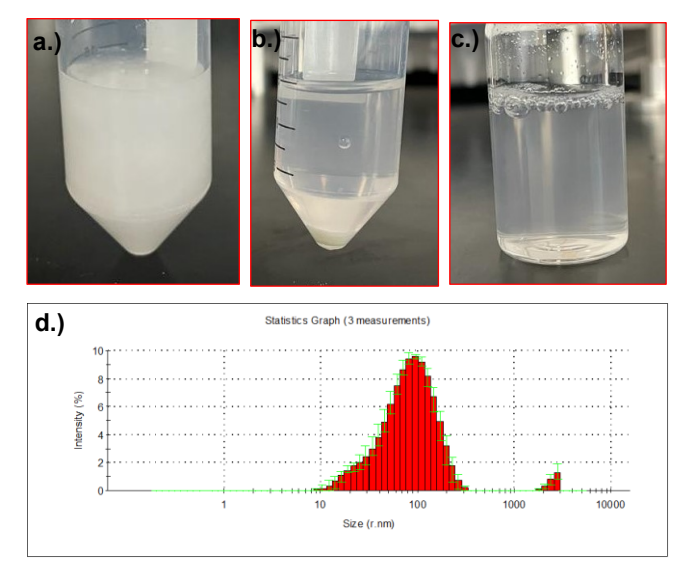


Figure S4.7. TGA thermogram of P-Im3-DMSO.



**Figure S4.8**. Digital images of aqueous dispersion fabricated through a conventional *in situ* crosslinking approach before (a) and after (b) dialysis, followed by filtration (c); DLS diagram of the dispersion after dialysis and filtration (d).



**Figure S4.9**. Schematic presentation for acid-catalyzed hydrolysis of benzoic imine bond in P-Im3-DMSO crosslinked polymer (a) and overlaid <sup>1</sup>H NMR spectra of the polymer in DMSO-d<sub>6</sub> before (b) and after (c) treatment with HCl. Insets: digital images of NMR tubes.

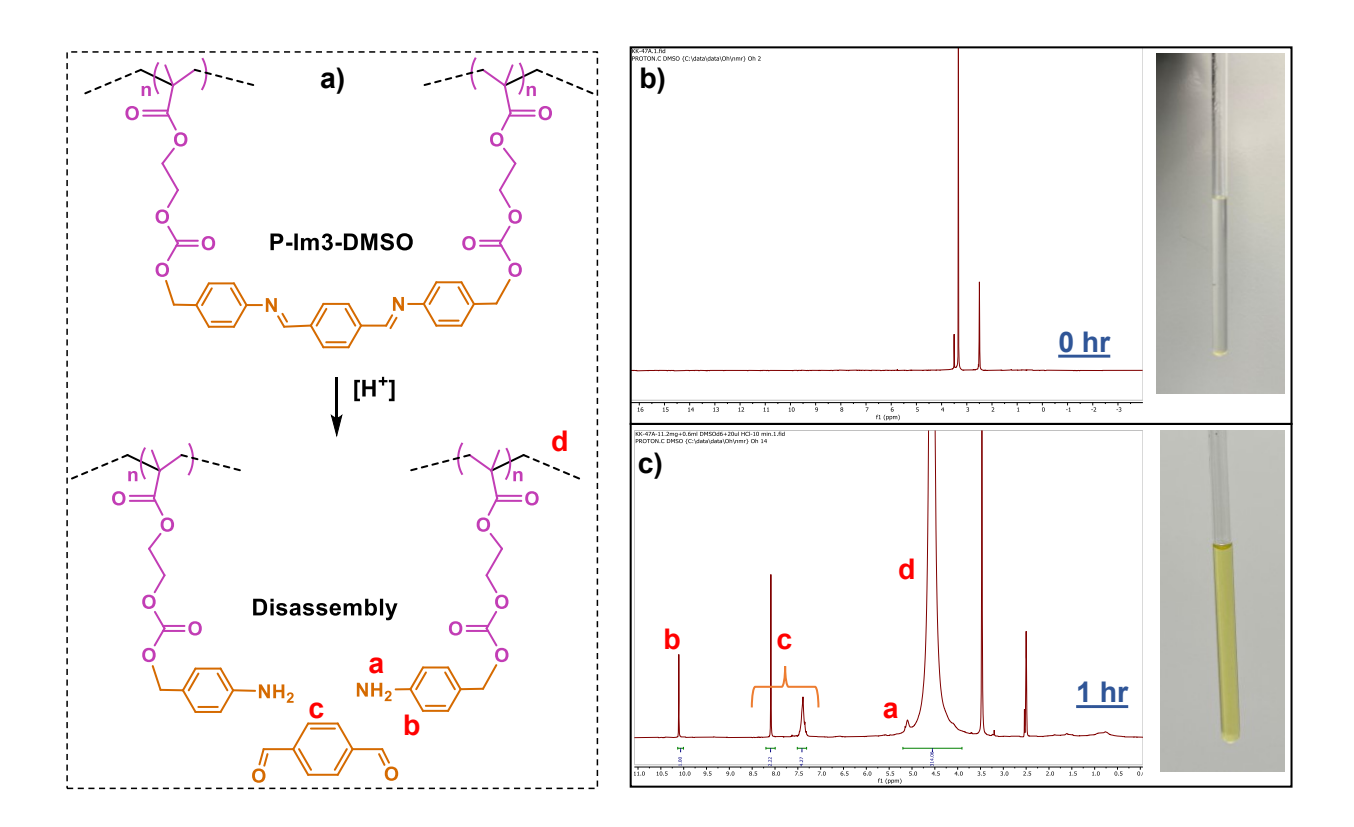


**Figure S4.10**. Overlaid DLS diagrams of aqueous P-Im3-Aq nanogels upon irradiation of visible light at  $\lambda = 420$  nm over 10 hrs (a) and their TEM images before (scale bar = 500 nm) (b) and after (scale bar = 100 nm) (c) irradiation of light.

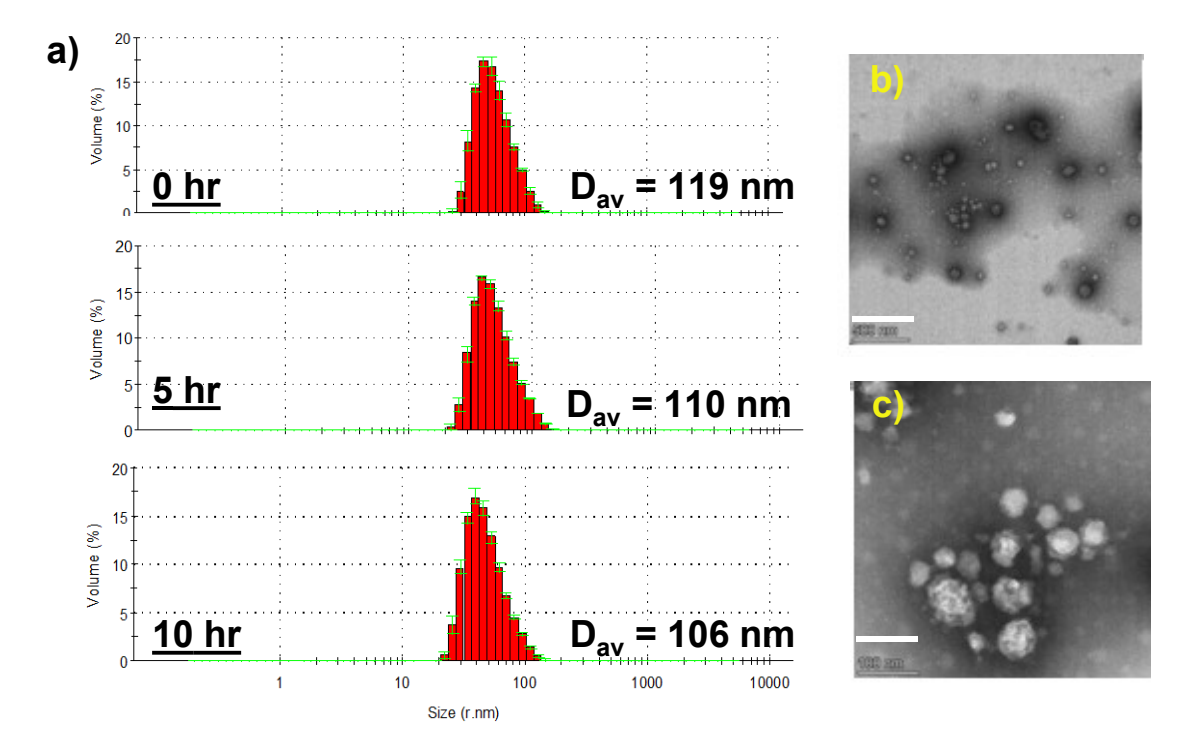


**Figure S4.11**. Relative free energy profile of EE to EZ and EZ to ZZ isomerization. TS denotes the transition state.

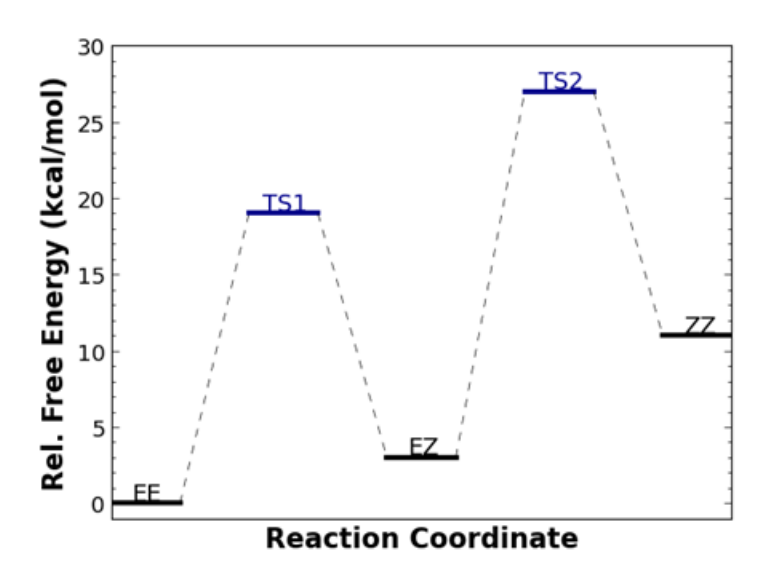
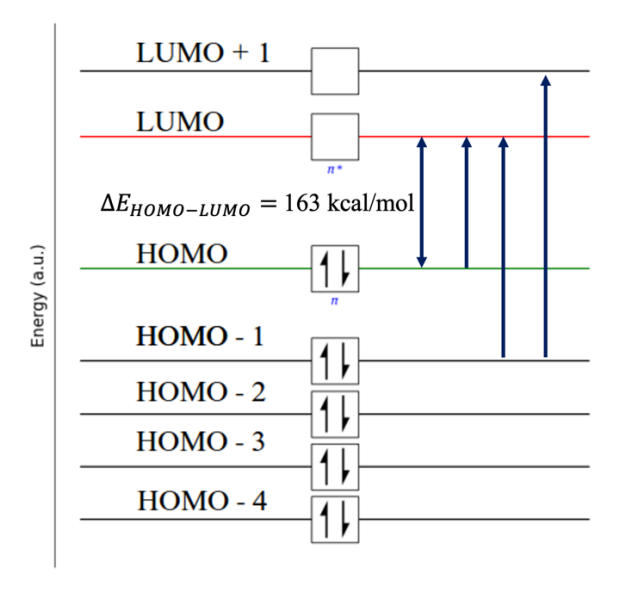
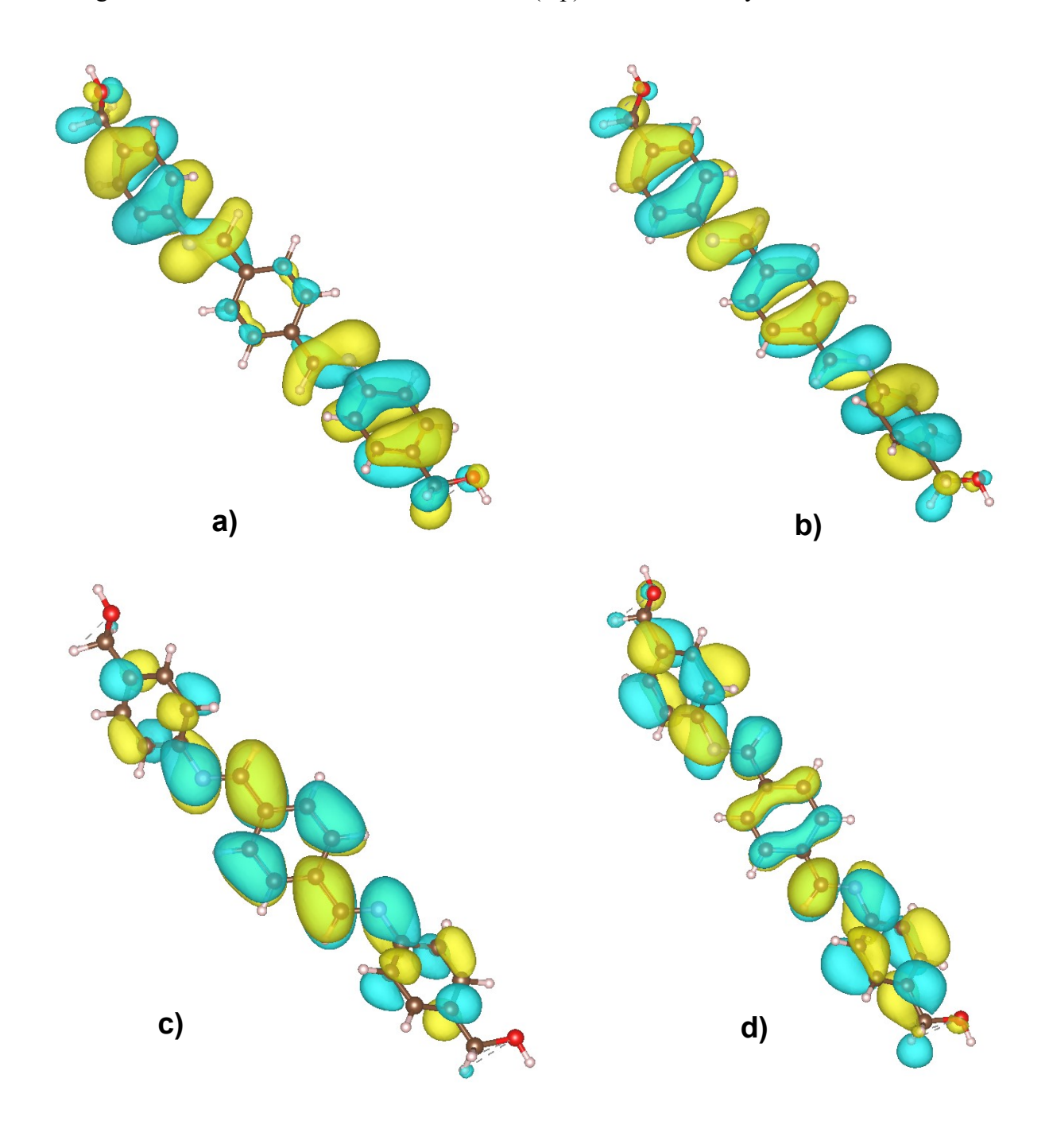


Figure S4.12. M3 molecular orbital configuration with possible electron transitions.



**Figure S4.13**. The FMOs, HOMO-1 (a), HOMO(b), LUMO(c) and LUMO+1 (d), of EE configuration obtained via the  $\omega B97/6-311++G(d,p)$  model chemistry.



**Figure S4.14**. Optimized structures for different conformers of M2. The E isomer (a), transition state (b), and the Z isomer (c)

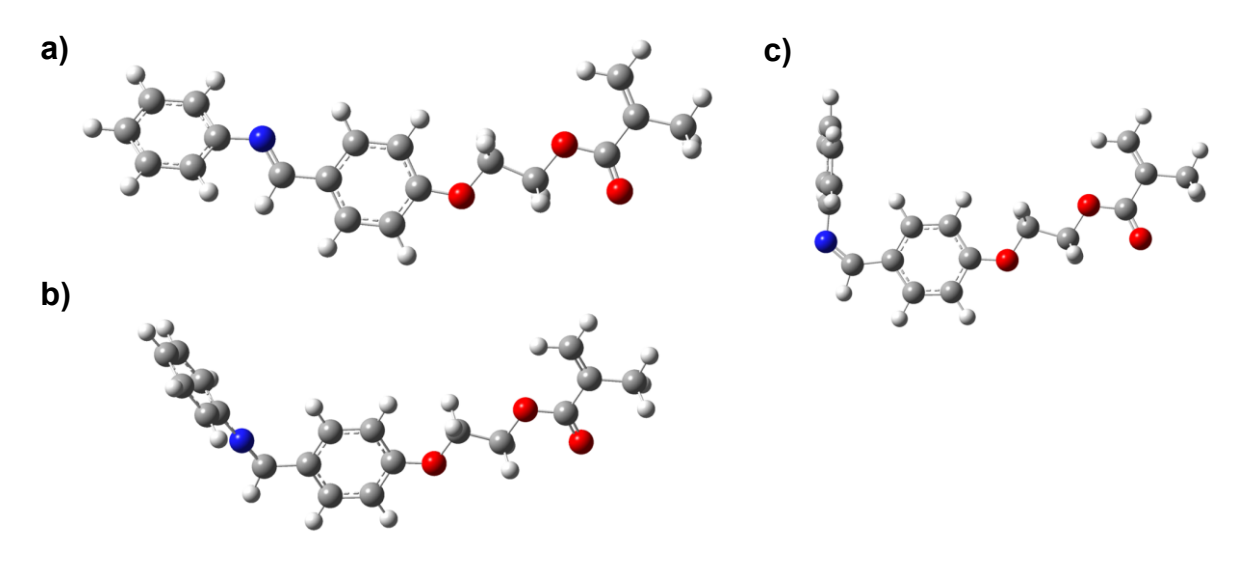


**Figure S4.15**. Relative enthalpy with free energies (in parenthesis) diagram of M2 E/Z isomerization with the transition state and the activation energy.

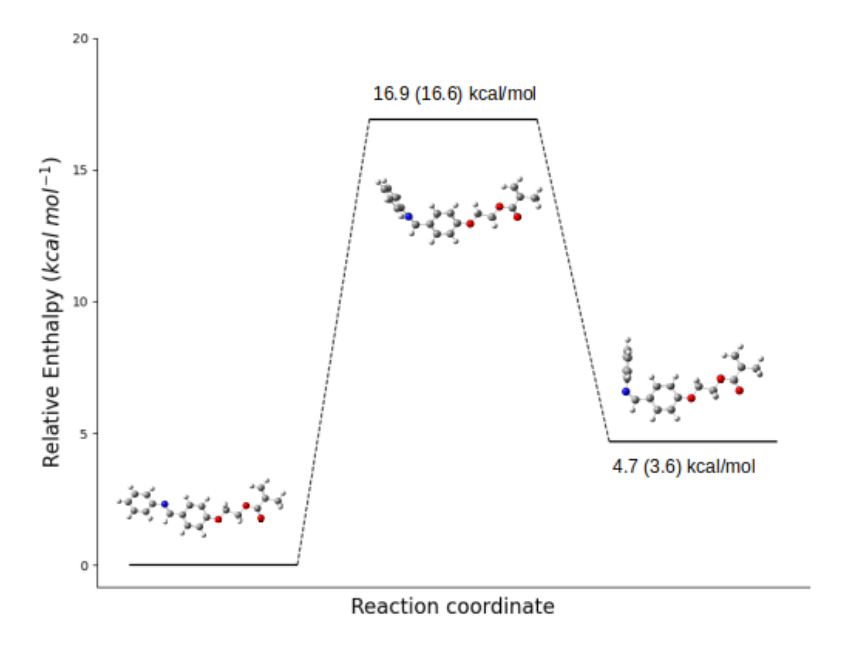


**Figure S4.16**. M2 molecular orbital configuration with possible electron transitions (a) and UV/Vis spectra of E (blue) and Z (red) isomers of M2 (b).

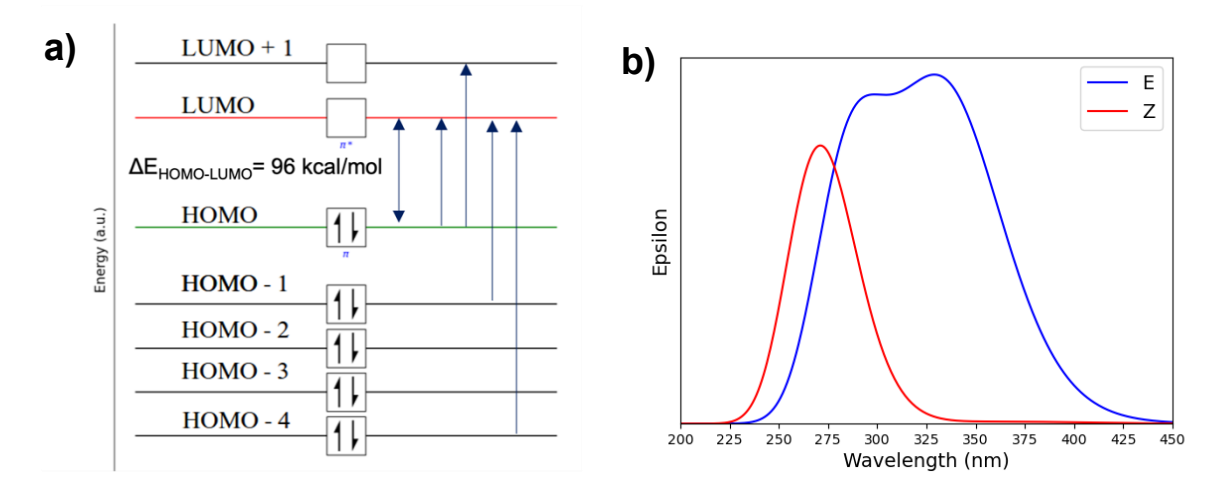


**Figure S4.17**. Molecular orbital diagrams of HOMO-4 (a), HOMO-1 (b), HOMO (c), LUMO (d) and LUMO+1 (e) for E isomer of M2.

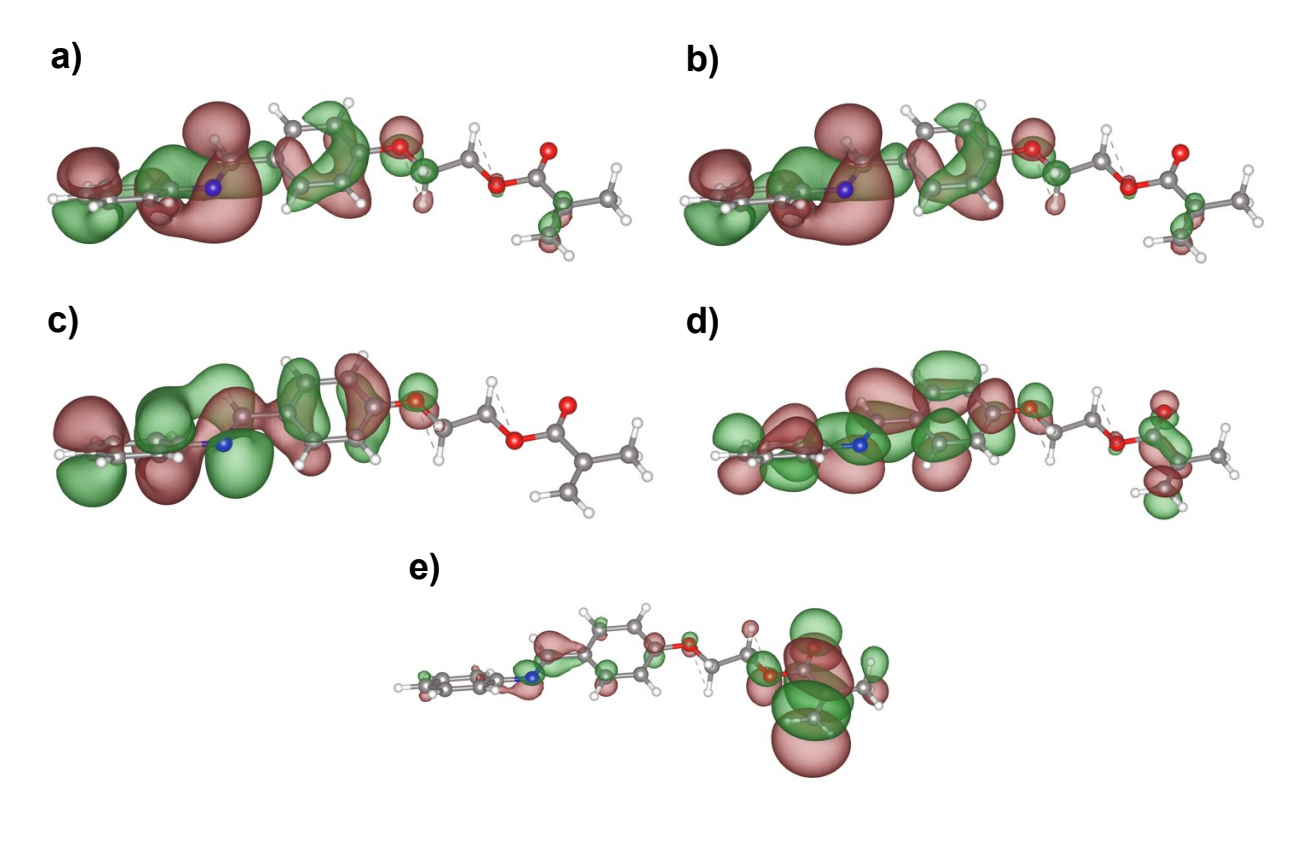
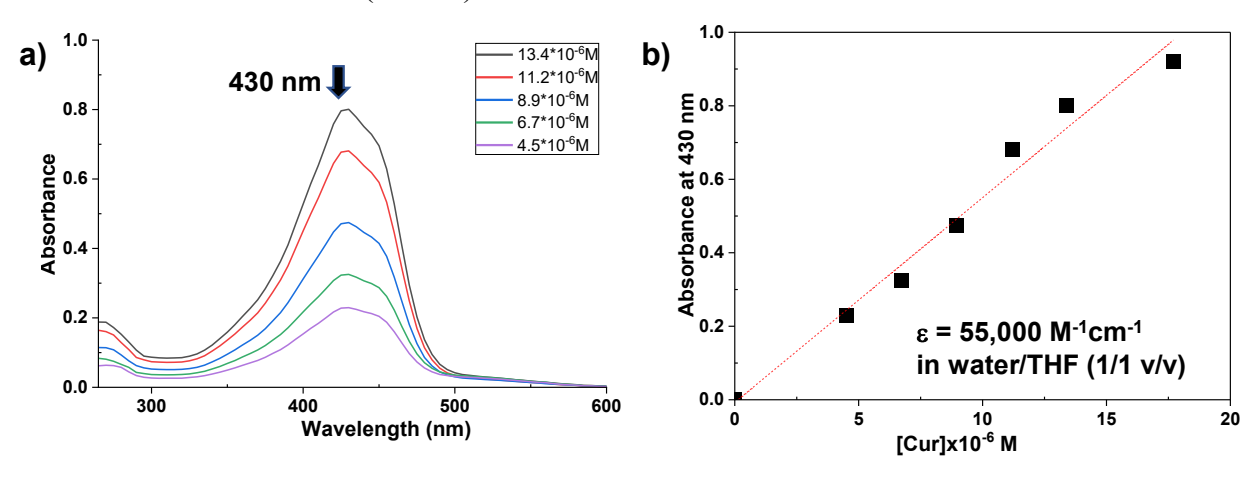
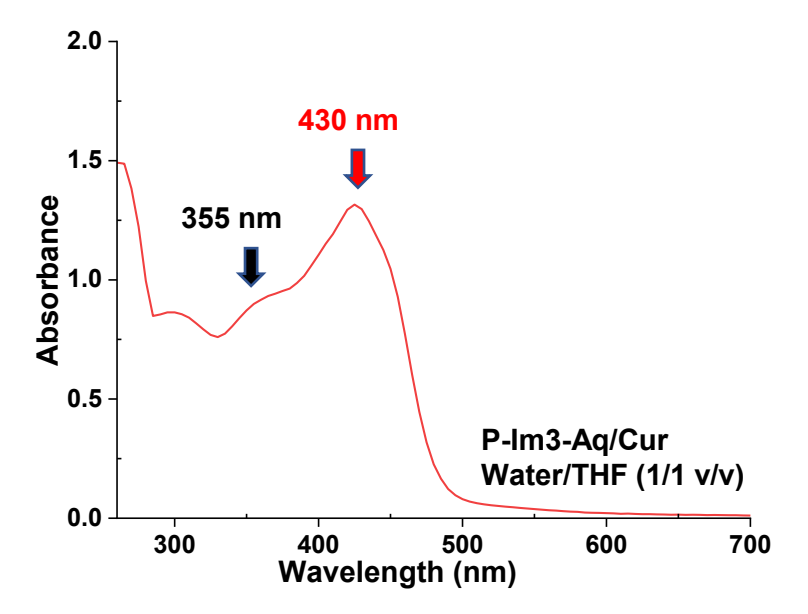


Figure S4.18. Overlaid UV/Vis spectrum (a) and absorbance at  $\lambda_{max} = 430$  nm (b) of Cur over its concentration in water/THF (1/1 v/v).



**Figure S4.19**. UV/Vis spectrum of aqueous P-Im3-Aq/Cur nanogels at 0.27 mg/mL in water/THF (1/1 v/v).



**Figure S4.20**. Overlaid UV/Vis spectra for release of Cur from aqueous P-Im3-Aq/Cur nanogels under visible light at  $\lambda = 420$  nm (a) and in dark as a control (b).

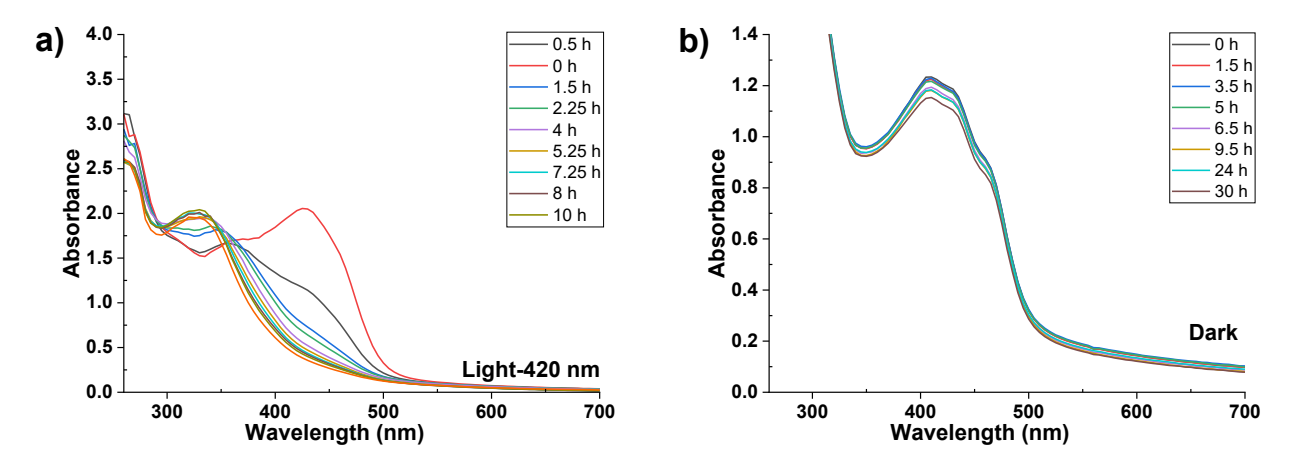


**Figure S4.21**. Overlaid UV/Vis spectra for the release of Cur from P-Im3-Aq/Cur nanogels in pH = 7.4 (a) and acidic pH = 5.0 (b).

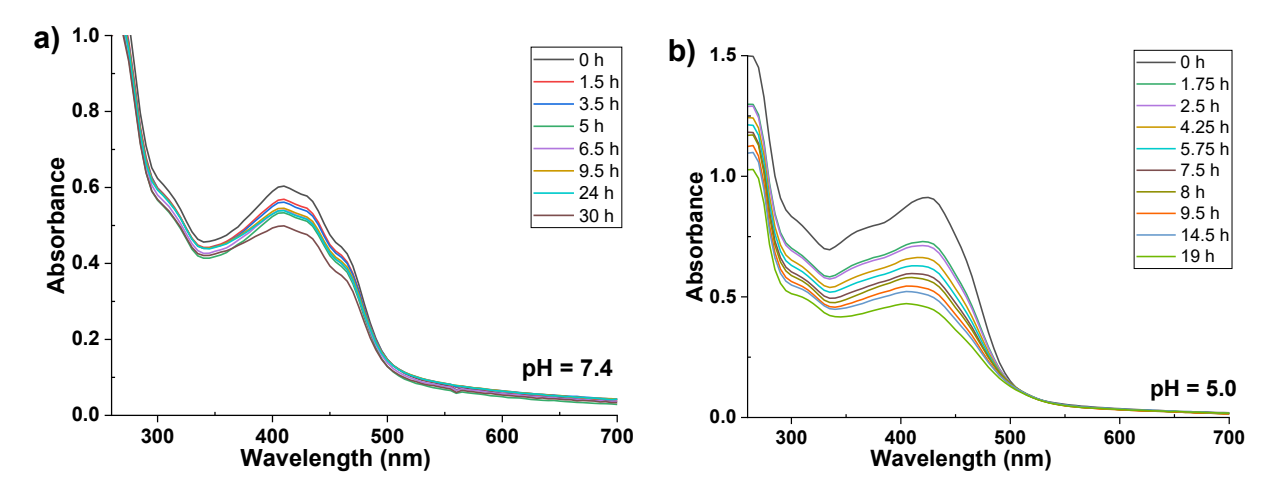


**Figure S4.22**. Overlaid UV/Vis spectrum for the release of Cur from P-Im3-Aq/Cur nanogels in acidic pH = 5.0 under exposure to visible light at  $\lambda = 420$  nm.

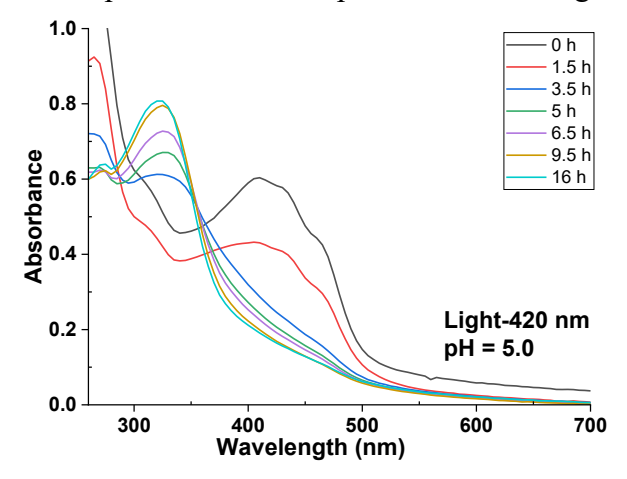


**Table S4.1**. Recipes for a series of aqueous P-Im3-Aq nanogels.

Entry	M3	PEG-b-PCIMA	DBU	DMSO	Water
	(mg)	(mg)	(mg)	(mL)	(mL)
P-Im3-aq	1.7	3.5	0.3	2	10
P-Im3-aq-A	1.7	3.5	0.3	3	9
P-Im3-aq-B	1.7	3.5	0.3	4	8
P-Im3-aq-C	1.7	3.5	0.3	5	7
P-Im3-aq-D	1.1	3.5	0.2	2	10
P-Im3-aq-E	0.8	3.5	0.1	2	10

**Table S4.2**. Calculated thermochemistry values with electronic energy ( $E_{DFT}$ ), zero-point energy (ZPE), thermal enthalpy correction ( $H_{corr}$ ) and thermal correction to free energy  $G_{corr}$  (all units are in kcal/mol).

Isomer	E <sub>DFT</sub>	ZPE	Hcorr	$G_{corr}$
EE	-696665	234	249	198
TS1	-696644	232	248	196
EZ	-696661	234	249	197
TS2	-696636	232	248	196
ZZ	-696654	234	249	198

$$\Delta H^{o}(298) = \Sigma (E_{DFT} + H_{corr})_{product} - \Sigma (E_{DFT} + H_{corr})_{reactants}$$
(1)

$$\Delta G^{o}(298) = \Sigma (E_{DFT} + G_{corr})_{products} - \Sigma (E_{DFT} + G_{corr})_{reactants}$$
 (2)

Note:  $E_{DFT}$  refers to the electronic energy calculated via DFT, while  $H_{corr}$  and  $G_{corr}$  represent the thermal corrections to enthalpy and Gibbs free energy at room temperature, respectively

**Table S4.3**. Excited state,  $\lambda_{max}$ , excitation energy (E), oscillator strength (f) and electronic configurations for EE, EZ and ZZ conformers of M3.

Conformer		l oscillator		transition	MO <sub>contribution</sub> *
Comormer	eV	nm	strength (f)	component	141 Contribution
EE	3.68	337	1.2	H®L	75%
EZ	3.7	334	0.18	$H \otimes L$	65%
ZZ	3.73	331	0.11	H ® L	56%

 $MO_{contribution} = 2 \times (C_{H \to L})^2$  where  $C_{H \to L}$  is the coefficient of the excited state wavefunction in terms of the highest occupied molecular orbital (HOMO) and lowest unoccupied molecular orbital (LUMO)

Table S4.4. Cartesian coordinates of calculated structures (M3)

11	1

C	-1.39413600	-0.84454200	0.06289700
C	-0.63823100	0.30771100	-0.16135800
Н	-1.15218900	1.25068200	-0.30407900
C	0.74337400	0.23120300	-0.19722200
Н	1.32871900	1.12902600	-0.37080900
C	1.39656600	-0.99088400	-0.01264000
C	2.86585400	-1.03622400	-0.05807700
Н	3.37007900	-0.07857500	-0.24858900
N	3.52056100	-2.10877200	0.12462800
C	4.92341400	-2.08314700	0.01589700
C	5.67139900	-2.79369200	0.95728800
Н	5.15047600	-3.32751700	1.74360900
C	7.05438100	-2.79134900	0.89298100
Н	7.62283500	-3.32905700	1.64660400
C	7.72412700	-2.11868700	-0.12991100
C	9.22862300	-2.18216600	-0.20076400
Н	9.64184200	-2.02914100	0.80549200
Н	9.52742900	-3.18690600	-0.53234000
O	9.71237600	-1.20106500	-1.09722300
Н	10.64820500	-1.34388600	-1.23482300
C	6.97801200	-1.43838600	-1.08476600
Н	7.49092800	-0.92359200	-1.88756100
C	5.58985200	-1.41756000	-1.01348400
Н	5.01854500	-0.90562500	-1.78049800
C	0.64060600	-2.14336400	0.21031200
Н	1.15453200	-3.08654600	0.35180900
C	-0.74095700	-2.06659900	0.24775500
Н	-1.32629200	-2.96425100	0.42250600

C	-2.86343400	-0.79833700	0.10816100
Н	-3.36876200	-1.75898500	0.28098600
N	-3.51526400	0.28260700	-0.02833500
C	-4.92194000	0.24323200	-0.02151100
C	-5.60808100	1.23886500	0.67326200
Н	-5.03625700	2.00171200	1.18894400
C	-6.99475800	1.24395600	0.71356200
Н	-7.52214900	2.01366000	1.26292800
C	-7.72633300	0.27681400	0.02895300
C	-9.23300600	0.24896000	0.07397900
Н	-9.61884700	0.00644600	-0.92536000
Н	-9.55308800	-0.55183400	0.75617900
O	-9.72687700	1.49894400	0.51460100
Н	-10.66715100	1.42055600	0.67243100
C	-7.04047400	-0.69178500	-0.69992900
Н	-7.59524500	-1.43318100	-1.26801700
C	-5.65347200	-0.71768700	-0.72453700
Н	-5.13505500	-1.45965200	-1.32213700

# TS1

C	1.42604300	-1.51787500	0.23622300
C	1.14819300	-0.17541000	-0.01690000
Н	1.97023100	0.52174500	-0.13787000
C	-0.16577100	0.25140100	-0.11061500
Н	-0.38191500	1.29672100	-0.30835300
C	-1.22018600	-0.65251500	0.04664900
C	-2.60567700	-0.16733400	-0.05785700
Н	-2.72547500	0.90833500	-0.24733900
N	-3.60588000	-0.94155900	0.04912800
C	-4.90361200	-0.39983600	-0.01160500 142

C	-5.87297900	-1.09137500	-0.74123500
Н	-5.59297600	-2.00996300	-1.24360800
C	-7.16080200	-0.59192900	-0.83502600
Н	-7.89771200	-1.12838300	-1.42604300
C	-7.52545200	0.58121200	-0.17310000
C	-8.95014600	1.06754200	-0.25296200
Н	-9.29629200	0.99373800	-1.29286400
Н	-9.58576300	0.40836000	0.35542400
O	-9.03240300	2.40086700	0.21089900
Н	-9.95423500	2.64659500	0.28152000
C	-6.56831500	1.25116800	0.57958100
Н	-6.84740500	2.15554700	1.10556600
C	-5.26735600	0.76801600	0.65946200
Н	-4.53718900	1.28535100	1.27266600
C	-0.93979200	-1.99685400	0.30060200
Н	-1.76477900	-2.68854900	0.42176200
C	0.37434500	-2.42242400	0.39318400
Н	0.59301400	-3.46764400	0.59069600
C	2.82665800	-2.00053000	0.34284200
Н	2.92379400	-3.08252900	0.54323500
N	3.83103200	-1.28321600	0.22371300
C	4.91476800	-0.50389100	0.09540600
C	5.50741200	-0.30105900	-1.16468000
Н	5.08267100	-0.78733700	-2.03459500
C	6.62206000	0.51171000	-1.28022000
Н	7.06891400	0.64955600	-2.26029800
C	7.18479200	1.14984400	-0.17669000
C	8.41800900	1.99077900	-0.31365900
Н	8.43779600	2.46073100	-1.30595400
Н	8.40694000	2.79046900	0.43888000
O	9.56875800	1.16631600	-0.13730600
			143

Н	10.34937200	1.71535000	-0.22511500
C	6.59001400	0.94172500	1.06624400
Н	7.01164800	1.42019900	1.94516600
C	5.47507500	0.13534400	1.21697600
Н	5.02528800	-0.01316100	2.19128200

## EZ

C	-1.12355100	-0.70959000	-0.15680500
C	-0.31451400	0.33710000	-0.60703700
Н	-0.75343400	1.26671700	-0.94305600
C	1.06344100	0.18620100	-0.63518200
Н	1.68173900	1.00407200	-0.99179900
C	1.66504100	-0.99832800	-0.20922300
C	3.13095100	-1.11684100	-0.24203000
Н	3.67569700	-0.24053800	-0.61984600
N	3.73711800	-2.15940100	0.15470800
C	5.13918400	-2.22113700	0.04855500
C	5.85734900	-2.76642700	1.11496600
Н	5.31567300	-3.11011200	1.98851900
C	7.23865100	-2.84104800	1.05796000
Н	7.78499000	-3.24564800	1.90530800
C	7.93417200	-2.41527200	-0.07440100
C	9.43364200	-2.56207800	-0.12501400
Н	9.85820900	-2.23975200	0.83546000
Н	9.68299000	-3.62459500	-0.25762400
Ο	9.95891800	-1.79387600	-1.18993100
Н	10.88557800	-2.00654400	-1.29572400
C	7.21618000	-1.90250800	-1.14818400
Н	7.74878900	-1.58077600	-2.03440000
C	5.83090200	-1.80328700	-1.08884800
			144

Н	5.28054900	-1.42659800	-1.94442500
C	0.85920400	-2.05089800	0.23008600
Н	1.32955400	-2.97305500	0.54965700
C	-0.51596800	-1.90706600	0.24149400
Н	-1.13836600	-2.73393500	0.56949900
C	-2.60715300	-0.66222600	-0.11317800
Н	-3.07894200	-1.64688200	-0.16932200
N	-3.40723700	0.31783900	-0.01575000
C	-2.96544000	1.64319800	0.15280600
C	-3.19899000	2.57966100	-0.85447800
Н	-3.68986700	2.26043800	-1.76687300
C	-2.78461600	3.89400700	-0.69635900
Н	-2.93962100	4.61088000	-1.49405300
C	-2.15928400	4.30843800	0.47799700
C	-1.75747400	5.74647200	0.67493400
Н	-2.61465200	6.31053800	1.06988800
Н	-0.95331900	5.80027000	1.42045800
Ο	-1.33855900	6.29780700	-0.56243300
Н	-1.26408400	7.24699600	-0.46542400
C	-1.95998100	3.37523000	1.49169100
Н	-1.47423200	3.67769400	2.41486500
C	-2.36207100	2.05570000	1.34046200
Н	-2.19109100	1.33341100	2.13063600

# TS2

C	-1.64848400	-0.87286000	0.96413000
C	-1.07285500	0.39421000	1.09206900
Н	-1.67151900	1.28495800	0.95752900
C	0.27597200	0.51618900	1.38894100
Н	0.71662800	1.50380200	1.48500300
			145

C	1.07057600	-0.61383200	1.57075200
C	2.50997800	-0.45150600	1.90089900
Н	2.84542400	0.59782300	1.98276500
N	3.30080600	-1.38985700	2.07722700
C	4.15759300	-2.40237600	2.27630400
C	4.89075100	-2.94292500	1.20378200
Н	4.76221100	-2.52797700	0.21133900
C	5.76396400	-3.99388600	1.42524200
Н	6.31643200	-4.40065700	0.58351400
C	5.94816400	-4.54243600	2.69294200
C	6.86326000	-5.71038100	2.90537800
Н	7.69932000	-5.66057300	2.19521800
Н	7.27961800	-5.67513700	3.92082300
O	6.12978300	-6.91952700	2.71649200
Н	6.72553800	-7.65778800	2.85281100
C	5.21768600	-3.99876300	3.74766900
Н	5.33731000	-4.40935500	4.74582000
C	4.33620400	-2.94784100	3.56098200
Н	3.77822500	-2.53689200	4.39369200
C	0.50456800	-1.88059600	1.43155700
Н	1.12779000	-2.75835600	1.56406200
C	-0.83722600	-2.00357000	1.11839300
Н	-1.27221800	-2.99063400	0.99680300
C	-3.07600700	-1.10985500	0.62591900
Н	-3.25642500	-2.06487600	0.12551800
N	-4.10652100	-0.39764200	0.82673400
C	-4.06257200	0.81694700	1.53671000
C	-4.38895600	2.00363300	0.88324600
Н	-4.63940000	1.97573800	-0.17100000
C	-4.35809200	3.20702400	1.57519100
Н	-4.58393400	4.12810100	1.04586400
			146

C	-4.05005100	3.24800700	2.93240700
C	-4.08193200	4.55288200	3.68371900
Н	-3.91711000	5.38078600	2.98181900
Н	-5.07782700	4.68876000	4.12926100
Ο	-3.09044300	4.54317300	4.69720500
Н	-3.24296500	5.28492100	5.28245200
C	-3.76525900	2.05181100	3.58809600
Н	-3.51964300	2.07247900	4.64329400
C	-3.76939800	0.84756500	2.90138900
Н	-3.53254900	-0.07786700	3.41442200

# ZZ

C	-1.75054200	-0.58992900	-0.21472200
C	-0.94621700	0.39369400	0.36728000
Н	-1.38795600	1.28425600	0.79364400
C	0.42995200	0.23964900	0.38744300
Н	1.04454900	1.01930300	0.82624400
C	1.04121900	-0.90484700	-0.13176500
C	2.52278500	-0.97775100	-0.05161400
Н	3.01091600	-0.00066400	-0.00661400
N	3.30183900	-1.97860600	-0.01925400
C	2.82711000	-3.30327100	0.02247500
C	3.09532100	-4.16295100	-1.04252800
Н	3.64004500	-3.78484100	-1.90025200
C	2.64801500	-5.47584600	-1.01088400
Н	2.83114100	-6.13165700	-1.85374800
C	1.95468500	-5.96614600	0.09380500
C	1.51544500	-7.40552300	0.15719100
Н	2.33032200	-8.01353200	0.57577400
Н	0.65526000	-7.49319300	0.83382200
			147

Ο	1.18459700	-7.86084200	-1.14386900
Н	1.08642900	-8.81249100	-1.12004300
C	1.72056000	-5.11092800	1.16726300
Н	1.18233900	-5.47376900	2.03813700
C	2.15450600	-3.79327300	1.14168100
Н	1.95665400	-3.13164600	1.97742700
C	0.23906500	-1.87739100	-0.73489700
Н	0.68184000	-2.76102300	-1.17468000
C	-1.13415100	-1.70547300	-0.78831900
Н	-1.74399700	-2.45859500	-1.27732500
C	-3.23007900	-0.50788700	-0.31612500
Н	-3.64547600	-1.06957100	-1.15696000
N	-4.07968800	0.09386300	0.40927200
C	-3.71956900	0.78548400	1.58113200
C	-3.92069800	2.16274400	1.65282300
Н	-4.32017800	2.68475000	0.79090600
C	-3.57899300	2.85401900	2.80715800
Н	-3.71179700	3.93159300	2.83785500
C	-3.07773100	2.18761600	3.92250500
C	-2.77249700	2.94516800	5.18816300
Н	-2.52026800	3.98395900	4.93772000
Н	-3.67086900	2.96544500	5.82177100
O	-1.70386400	2.31649900	5.87504000
Н	-1.64138400	2.69096800	6.75349500
C	-2.91773300	0.80524100	3.85720600
Н	-2.52413200	0.27743800	4.71771300
C	-3.23309500	0.10839500	2.70066500
Н	-3.09210100	-0.96559600	2.65126700

## A3. Supporting Information for Chapter 5

**Figure S5.1**. Overlaid UV/vis absorption spectra of M-PC in DMSO over polycondensation time.

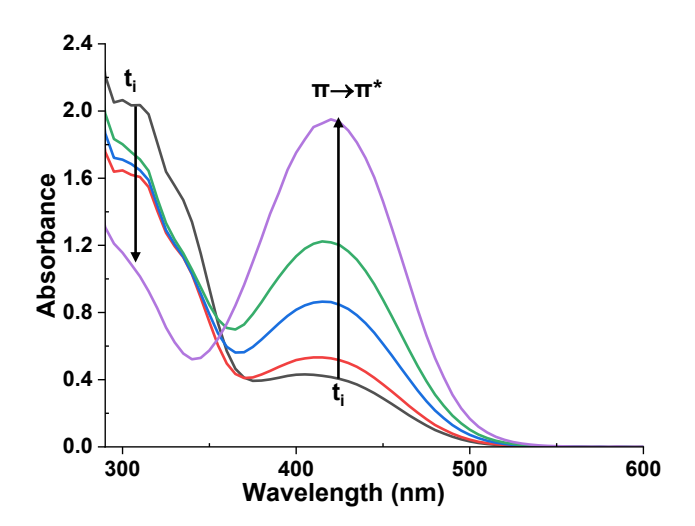


**Figure S5.2**. Table summarizing Mass Spectroscopy analysis and chemical structures suggested for M-PC.

Entry	Intensity	Theoretical m/z value	Observed m/z value	Mass error (ppm)
[M-PC-5+H] <sup>+</sup>	3.86E3	637.2710	637.2692	-1.8
[M-PC-4+H] <sup>+</sup>	9.31E4	521.2448	521.2435	-2.5
$[M-PC-3+H]^{+}$	8.22E5	431.1866	431.1858	-1.9
[M-PC-1+H] <sup>+</sup>	1.12E7	225.1022	225.1009	-1.3

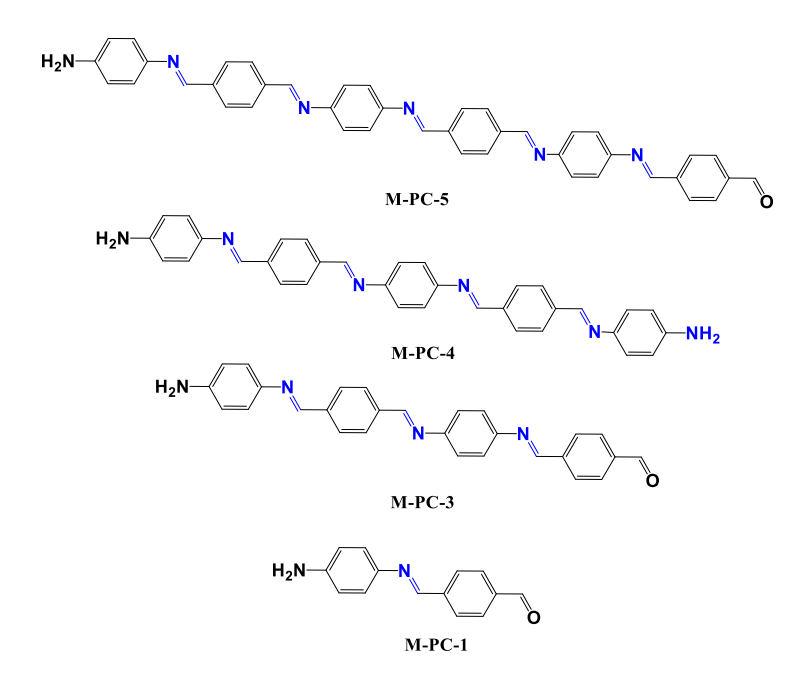


Table S5.1. Recipe to synthesize a series of conjugated poly(benzoic imine)s (M-PCs).

Entry	PPD	TDA	NH <sub>2</sub> /CHO	DMSO	(PPD+TDA)/DMSO	$\lambda_{max}$
	(mg)	(mg)	ratio	(mL)	(mg/mL)	
M-PC	2	2.48	1	6.4	0.7	420
M-PC-A	50	77	0.8	5	25.4	405
М-РС-В	50	49	1.25	5	20	425
M-PC-C	60	52	1.4	5	22.4	425

### **Summary of Achievements**

### **Publications**

- Kadambari Bairagi, Jiang Tian Liu, Anna Thinphang-nga, and Jung Kwon Oh. Synthesis and Dual Acid/Light-Responsive Disassembly of Amphiphilic Block Copolymer Nanoassemblies Bearing Conjugated Benzoic Imine Pendants, Macromolecules, 2023, 56, 4307–4317.
- 2. **Kadambari Bairagi**, Mehdi Shamekhi, Ioanna Tountas, Natasha Letourneau, Gilles H. Peslherbe, Alisa Piekny and Jung Kwon Oh. Development of Dual Acid/Visible Light-Degradable Core-Crosslinked Nanogels with Extended Conjugate Aromatic Imines for Enhanced Drug Delivery, *J. Mater. Chem. B*, 2025, DOI: 10.1039/D5TB00734H.
- 3. **Kadambari Bairagi**, Alondra Camacho and Jung Kwon Oh. Synthesis and Dual Acid/Visible Light-Responsive Degradation of Step-Growth Conjugated Poly(benzoic imine) Nanocolloids, *Journal of Polymer Science*, 2025 (Under review).

### **Oral and Poster Presentations**

- Kadambari K. and Jung Kwon Oh. Conjugated Benzoic Imine-Based Dual Acid/Light-Responsive Polymeric Nanocarriers for Enhanced Drug Delivery: Synthesis and Degradation. CBGRC-2024, Montreal. (Oral)
- 2. **Kadambari K.** and Jung Kwon Oh. Synthesis and Degradation of Conjugated Benzoic Imine-Based Dual Acid/Light-Responsive Polymeric Nanoassemblies for Enhanced Drug Delivery. Canadian Society for Chemical Engineering (CSChE)-2024, Toronto. (Poster)
- 3. **Kadambari K.** and Jung Kwon Oh. Dual Acid/Light-Responsive Degradable Block Copolymer Bearing Conjugated Benzoic Imine Pendants: Synthesis, Aqueous Self-Assembly, and Degradation. Canadian Chemistry Conference and Exhibition (CSC)-2023, Vancouver. (Oral)
- 4. **Kadambari K.** and Jung Kwon Oh. Dual Acid/Light Disassembly of Conjugated Imine-based Block Copolymer Nanoassemblies for Enhanced Drug Delivery. MACRO-2022, Winnipeg. (Oral)

### **Awards and Honours**

- 1. Concordia University Graduate Fellowship D FAS (Jan 2021-Dec 24, \$56,000)
- 2. Concordia University International Tuition Award Excellence PhD (Jan 2021-Aug 23, \$40,656)
- 3. Concordia University Conference and Exposition Award (2023, \$750)
- 4. FAS Graduate Student Conference award (2023, \$200)
- 5. FAS Graduate Student Conference award (2024, \$200)
- 6. Conference Funding Assistance Subsidy Program Graduate Students Association (GSA) (2024, \$243)

### **Others**

- 1. Graduate trainee, PoND (Polymer Nanoparticles for Drug Delivery) CREATE Program (Jan 2021-March 2024)
- 2. Research intern, Jubilant Radiopharma, Montreal (Sept 2023-May 2024), 8-month PoND industrial internship.